

AD-A050 773

MICHIGAN UNIV ANN ARBOR LASER PLASMA INTERACTION LAB
CRITICAL LAYER PENETRATION IN A COLD Z-PINCH PLASMA BY HIGH-INT--ETC(U)

F/G 20/9

SEP 77 J G ACKENHUSEN

AFOSR-77-3349

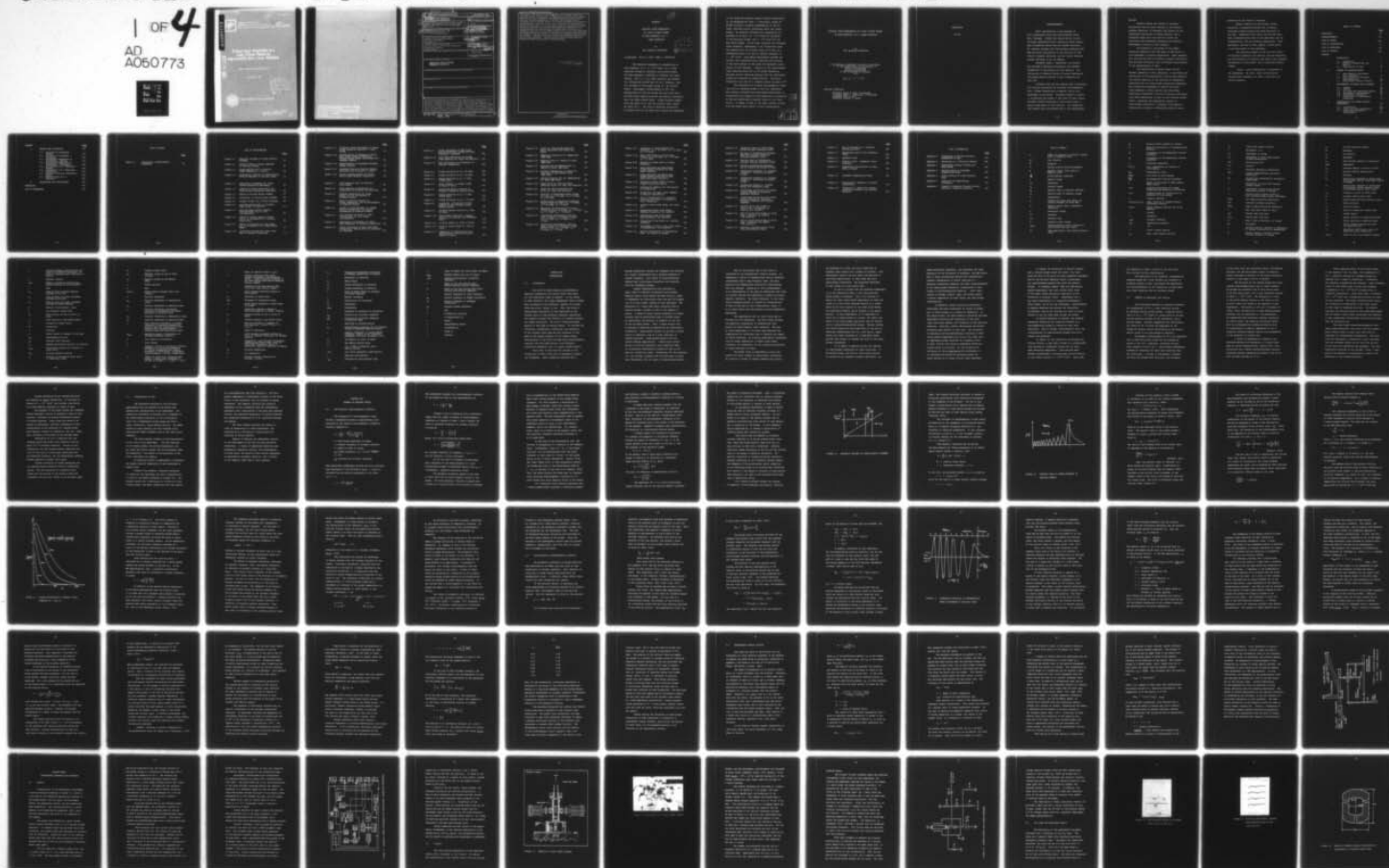
UNCLASSIFIED

LPIL-TR-100

AFOSR-TR-78-0352

NL

1 OF 4
AD
A060773



**ical Layer Penetration in a
Cold Z-Pinch Plasma by
Intensity 10.6μ Laser Radiation**

JOHN GOODYEAR ACKENHUSEN

September, 1977

**D
R
MA**

AIR FORCE OFFICE OF SPECIAL INVESTIGATION
SECTION OF TRANSMISSIONS TO THE
This technical report has been prepared and is
approved for public release and is hereby
distributed in unlimited quantities.
A. F. O. S. I.
Technical Information Office

UNCLASSIFIED

SECURITY CLASSIFICATION OF THIS PAGE (When Data Entered)

REPORT DOCUMENTATION PAGE		READ INSTRUCTIONS BEFORE COMPLETING FORM	
1. REPORT NUMBER	2. GOVT ACCESSION NO.	3. RECIPIENT'S CATALOG NUMBER	
AFOSR-TR-78-0352		Doctoral thesis	
4. TITLE (and Subtitle)	5. TYPE OF REPORT & PERIOD COVERED		
CRITICAL LAYER PENETRATION IN A COLD Z-PINCH PLASMA BY HIGH-INTENSITY 10.6 MICRONS LASER RADIATION.	Interim		
6. AUTHOR(s)	7. PERFORMING ORG. REPORT NUMBER	8. CONTRACT OR GRANT NUMBER(s)	
John Goodyear/Ackenhusen	LPII-TR-1001	AFOSR-77-3349	
9. PERFORMING ORGANIZATION NAME AND ADDRESS		10. PROGRAM ELEMENT, PROJECT, TASK AREA & WORK UNIT NUMBERS	
Aerospace and Nuclear Engineering University of Michigan Ann Arbor, MI		2301 A2 17 61102F	
11. CONTROLLING OFFICE NAME AND ADDRESS		12. REPORT DATE	
Air Force Office of Scientific Research/NP Bolling AFB, Bldg.#410 Wash DC 20332		11 Sep 77 12	
14. MONITORING AGENCY NAME & ADDRESS (if different from Controlling Office)		13. NUMBER OF PAGES	
		358	
		15. SECURITY CLASS. (of this report)	
		Unclassified	
		15a. DECLASSIFICATION/DOWNGRADING SCHEDULE	
16. DISTRIBUTION STATEMENT (of this Report)			
Approved for public release; distribution unlimited.			
17. DISTRIBUTION STATEMENT (of the abstract entered in Block 20, if different from Report)			
18. SUPPLEMENTARY NOTES			
19. KEY WORDS (Continue on reverse side if necessary and identify by block number)			
20. ABSTRACT (Continue on reverse side if necessary and identify by block number)			
<p>The intensity dependence of transmission of high-intensity 10.6 microns laser radiation through an overdense cold Z-pinch plasma has been measured to determine a threshold for transmission. The 10.6 microns laser radiation was focused to a diffraction-limited spot of 125 microns diameter, radially incident on the plasma column of 1 mm critical radius. Holographic interferometry at 347.2 nm, perpendicular to both the column axis and laser axis, provided radial density profiles and density information about the laser-induced shock. Plasma electron temperature was about 20 eV, and the critical scale length was about</p>			

DD FORM 1 JAN 73 1473

EDITION OF 1 NOV 65 IS OBSOLETE

UNCLASSIFIED

410 584

SECURITY CLASSIFICATION OF THIS PAGE (When Data Entered)

150 microns. The ratio of electron oscillatory to thermal velocity was about one, placing the experiment in the regime for possible density profile modification by the ponderomotive force. A holographic cinema of plasma evolution, obtained independently of the CO2 laser, provided initial information about the target plasma. An intensity threshold for transmission was measured to be about 2.5×10 to the 11 W/sq cm for incidence on the pre-pinch plasma, and 2×10 to the eleven W/sq cm for the post-pinch plasma. As the laser intensity was increased above threshold, compression of the transmitted pulse was observed from its incident width of 38 nsec to a trasmitted width of 15 nsec at maximum intensity of 4×10 to the eleven W/cm. Coincidence measurements between the incident and transmitted pulse indicated the blockage of the first portion of the pulse and subsequent transmission of the remainder. Analysis of the laser-induced shock indicated about 60 to 70 percent energy absorption. Enhanced optical continuum emission from the interaction volume was attributed to plasma heating.

UNCLASSIFIED
UNCLASSIFIED

UNCLASSIFIED

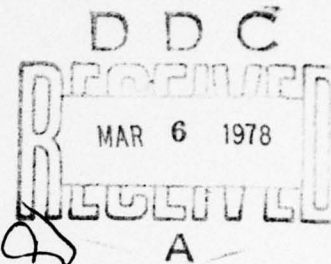
2

ABSTRACT

CRITICAL LAYER PENETRATION
IN A COLD Z-PINCH PLASMA
BY HIGH-INTENSITY 10.6μ
LASER RADIATION

by

John Goodyear Ackenhusen



Co-Chairmen: David R. Bach, James J. Duderstadt

The intensity dependence of transmission of high-intensity ($0.2 - 4 \times 10^{11} \text{ W/cm}^2$) 10.6μ laser radiation through an overdense cold Z-pinch plasma has been measured to determine a threshold for transmission. The $10.6 \mu \text{ CO}_2$ laser radiation was focused to a diffraction-limited spot of 125μ diameter, radially incident on the plasma column of 1 mm critical radius. Holographic interferometry at 347.2 nm, perpendicular to both the column axis and laser axis, provided radial density profiles and density information about the laser-induced shock. Plasma electron temperature was about 20 eV, and the critical scale length was about 150μ . The ratio of electron oscillatory to thermal velocity was about one, placing the experiment

in the regime for possible density profile modification by the ponderomotive force. A holographic cinema of plasma evolution, obtained independently of the CO₂ laser, provided initial information about the target plasma. An intensity threshold for transmission was measured to be about 3.5×10^{11} W/cm² for incidence on the pre-pinch plasma, and 2×10^{11} W/cm² for the post-pinch plasma. As the laser intensity was increased above threshold, compression of the transmitted pulse was observed from its incident width of 38 nsec to a transmitted width of 15 nsec at maximum intensity of 4×10^{11} W/cm². Coincidence measurements between the incident and transmitted pulse indicated the blockage of the first portion of the pulse and subsequent transmission of the remainder. Analysis of the laser-induced shock indicated about 60% to 70% energy absorption. Enhanced optical continuum emission from the interaction volume was attributed to plasma heating. Fractional backscatter into the f/6.3 focusing optics was about 10^{-4} .

The interaction of intense electromagnetic radiation with an overdense plasma is not well understood. The intensity threshold and pulse-shape modification in transmission are evidence of nonlinearities not predicted by the well-established classical theory at low intensities. An appeal is made to the newer theories arising with the laser-fusion effort in data interpretation.

DISTRIBUTION/AVAILABILITY CODES		
Meta Section	<input checked="" type="checkbox"/>	
Ref Section	<input type="checkbox"/>	
DISTRIBUTION/AVAILABILITY CODES		
Dist.	AVAIL. SEC. or SPECIAL	
A		

CRITICAL LAYER PENETRATION IN A COLD Z-PINCH PLASMA
BY HIGH-INTENSITY 10.6 μ LASER RADIATION

by
John Goodyear Ackenhusen

A dissertation submitted in partial fulfillment
of the requirements for the degree of
Doctor of Philosophy
(Nuclear Engineering)
in The University of Michigan
1977

AFOSR 77-3349

Doctoral Committee:

Professor David R. Bach, Co-Chairman
Professor James J. Duderstadt, Co-Chairman
Professor Rudi S. Ong
Professor Richard K. Osborn

DEDICATION

To Kay

ACKNOWLEDGMENTS

Great contributions to the progress of this investigation have come from Professor David Bach, chairman. Without his unique ability to sort out major observations from a myriad of minor details, many interesting results may have passed unnoticed. His personal interest and instructional technique have been the major contributors to the evolution of the author's research abilities, and his unusual physical insight continues to set an example.

Professor James J. Duderstadt, co-chairman, has provided illuminating discussions and frequent suggestions in the progress of this research. His instruction in numerous fields of nuclear engineering and plasma physics provided a basic foundation for this work.

Professor Rudi Ong has supplied many interesting and relevant discussions on nonlinear electromagnetic wave - plasma interactions in general, and on this experiment in particular. Professor Richard K. Osborn, in introducing the author to the field of laser fusion, provided valuable knowledge in the diverse areas of physics applicable to this research. His suggestions and research have contributed much to the experimental

program.

Grateful thanks are offered to Professor William Kerr for his early interest in the author's graduate education, to Professor Ziya Akcasu for his stimulating instruction in plasma physics, and to Professors Glenn Knoll and Dietrich Vincent for instruction and discussion concerning the radiation measurements utilized in this research.

The interest of Joe Kindel of Los Alamos Scientific Laboratory and Fred Mayer of KMS Fusion in this experiment is greatly appreciated. These researchers, and William Kruer of Lawrence Livermore Laboratory, have provided information that contributed significantly to the interpretation of data.

The contribution of Duncan Steel and Paul Rockett, graduates of this laboratory, in the design and construction of the experimental facility made possible the orderly operation of the multitude of diagnostics associated with the laser plasma interaction experiment and allowed this experiment to achieve the large scope necessary to fully monitor the interaction. Stimulating, delightful, and often hilarious discussions with these researchers, as well as with graduate Dwight Duston, concerning the experimental physics of laser-plasma interaction, holography, and numerical modeling were valuable in determining physical inter-

pretation and the course of research.

Special thanks go to Dave Brower, whose assistance in preparing drawings and in reading holograms allowed accurate and rapid evaluation of the data. Discussions with David Voss and Don Kania have illuminated many areas of the experiment and its interpretation, and are sincerely appreciated. Their assistance, and that of Matt Lambert, proved useful in the preparation of the experiment.

The financial support of the Air Force Office of Scientific Research, the National Science Foundation, and the University of Michigan have made a most necessary contribution to this effort, and is gratefully acknowledged.

Finally, loving appreciation is expressed to Kay Ackenhusen. Her love, cheer, and sacrifice, contributions exceeding all others, have made this sojourn possible.

TABLE OF CONTENTS

	<u>Page</u>
DEDICATION	ii
ACKNOWLEDGMENTS	iii
LIST OF TABLES	viii
LIST OF ILLUSTRATIONS	xi
LIST OF APPENDICES	xvi
LIST OF SYMBOLS	xvii
 CHAPTER	
1. INTRODUCTION	1
1.1 Orientation	1
1.2 Summary of Experiment and Results	7
1.3 Organization of Text	11
2. SUMMARY OF RELEVANT THEORY	13
2.1 Low-Intensity Electromagnetic Radiation	13
2.2 High-Intensity Electromagnetic Radiation	29
2.3 Hydrodynamic Energy Transfer	45
3. EXPERIMENTAL APPARATUS AND PROCEDURE	52
3.1 Summary	52
3.2 Z-Pinch	56
3.3 CO ₂ Laser and Associated Optics	62
3.4 Holographic Interferometer	79
3.5 Experimental Procedure	81
3.6 Calculation of Experimental Parameters	93
4. DETERMINATION OF PLASMA ELECTRON TEMPERATURE	100
4.1 Introduction	100
4.2 X-Ray Continuum Measurement	102
4.3 Probe Beam Absorption Measurements	119

CHAPTER		<u>Page</u>
5.	RESULTS AND DISCUSSION	135
5.1	Evolution of Discharge - Results	135
5.2	Evolution of Discharge - Discussion	156
5.3	Holographic Appearance of Interaction - Results	173
5.4	Holographic Appearance of Interaction - Discussion	184
5.5	Transmitted 10.6 μ Radiation - Results	216
5.6	Transmitted 10.6 μ Radiation - Discussion	235
5.7	Radiation from the Interaction Region	256
5.8	Backscattered 10.6 μ Radiation	263
6.	CONCLUSIONS AND IMPLICATIONS	269
	APPENDICES	278
	LIST OF REFERENCES	327

LIST OF TABLES

	<u>Page</u>
Table 3.1 Calculation of Experimental Parameters	95

LIST OF ILLUSTRATIONS

		<u>Page</u>
Figure 2.1	Radiation Incident on Linear Density Increase	18
Figure 2.2	Electric Field in Linear Approach to Critical Density	20
Figure 2.3	Plasma Modification of Electric Field Strength vs. L and θ_e	24
Figure 2.4	Alternating Direction of Ponderomotive Force in Approach to Critical Layer	33
Figure 3.1	Laboratory Arrangement for Laser-Plasma Interaction Experiment	51
Figure 3.2	Diagram of Timing Electronics for Laser-Plasma Interaction Experiment	55
Figure 3.3	Sketch of Z-Pinch Target Chamber	57
Figure 3.4	Photograph of Z-Pinch Target Chamber	58
Figure 3.5	Trigger Circuit for Z-Pinch Discharge	61
Figure 3.6	Gain-Switched Portion of Incident Laser Pulse (50 nsec/div)	63
Figure 3.7	Four CO ₂ Laser Pulses, Showing Non-Reproducibility of Tail (100 nsec/div)	64
Figure 3.8	Sketch of Annular Spatial Distribution of Illumination of Incident Laser Pulse	65
Figure 3.9	Effect of Dispersion of NaCl Wedge and its Correction with Compensating Wedge	70
Figure 3.10	Diffraction-Limited CO ₂ Laser Focal Spot at Several Intensities	72

		<u>Page</u>
Figure 3.11	Alignment Streak Photograph of Plasma Column Imaged on Graticle - 2 μ sec Streak	76
Figure 3.12	Reconstruction of Hologram of Alignment Target Showing Diffraction Fringes Around Target Associated with Improper Imaging	81
Figure 3.13	Reconstruction of Alignment Hologram, Imaged Properly	82
Figure 3.14	Fractional Error in Electron Density Extracted from Hologram vs. Radius	84
Figure 3.15	Optical Imaging System for Plasma Focal Volume Emission Diagnostics	88
Figure 4.1	X-Ray Detector Used on Exploding Wire Plasma	106
Figure 4.2	X-Ray Absorption Coefficient vs. Wavelength for Aluminum and Beryllium	109
Figure 4.3	Detector Sensitivity vs. X-Ray Energy for Two Thicknesses of Aluminum Windows	111
Figure 4.4	Ratio of Detector Signals vs. Plasma Temperature for Two Thicknesses of Aluminum Windows	112
Figure 4.5	Output of X-ray Detector vs. Plasma Electron Temperature for Several Thicknesses of Aluminum Windows	113
Figure 4.6	X-ray Pulses and dI/dt vs. Time for Exploding Li Wire Plasma (500 nsec/div)	115
Figure 4.7	Experimental Arrangement of Probe-Beam Experiment to Determine Absorption	120
Figure 4.8	Streak Photograph of HeNe Probe Beam Transmission through Evolving Discharge-Not Centered	123

		<u>Page</u>
Figure 4.9	Streak Photograph of HeNe Probe Beam Transmission through Evolving Discharge - Centered	124
Figure 4.10	Probe Beam Absorption and Plasma Light Emission vs. Time (500 nsec/div)	125
Figure 4.11	Saha Calculation of Ionization vs. Electron Temperature	130
Figure 5.1	Plasma Evolution at $t_h = 90$ nsec	138
Figure 5.2	Plasma Evolution at $t_h = 46$ nsec	139
Figure 5.3	Plasma Evolution at $t_h = 0$ nsec (Pinch Time)	140
Figure 5.4	Axial Gradient in Plasma Column at Time of Pinch	141
Figure 5.5	Normalized Density Profiles at Various Z-Values at Time of Pinch	143
Figure 5.6	Plasma Evolution at $t_h = 0$ nsec (Pinch Time)	145
Figure 5.7	Plasma Evolution at $t_h = -32$ nsec	146
Figure 5.8	Comparison of Fractional Fringe Reading to Half-Integer Fringe Reading Method	149
Figure 5.9	Electron Density Profile vs. Time to Pinch	150
Figure 5.10	Shot-to-Shot Variation - Density Profiles at Pinch for Two Different Shots	152
Figure 5.11	Critical Radius vs. Time to Pinch	153
Figure 5.12	Critical Scale Length vs. Time to Pinch	154
Figure 5.13	Comparison of Theoretically and Experimentally Obtained Electron Density Profiles	157

		<u>Page</u>
Figure 5.14	dI/dt vs. Time Showing Positive Spike Associated with Spark Gap Noise	159
Figure 5.15	Effective Ionization vs. Temperature (MHD Code)	161
Figure 5.16	Magnetic Field vs. Radius at Pinch (MHD Code)	162
Figure 5.17	Electron and Ion Temperatures vs. Radius at Pinch (MHD Code)	163
Figure 5.18	Electron Temperature vs. Radius at Pinch and 10 nsec Before Pinch (MHD Code)	164
Figure 5.19	Average Electron and Ion Temperatures vs. Time (MHD Code)	165
Figure 5.20	Light Pulse vs. Time and Axial Position; dI/dt vs. Time (100 nsec/div)	169
Figure 5.21	Spark Gap Optical Emission and dI/dt vs. Time (500 nsec/div)	170
Figure 5.22	Blow-Out of Underdense Target Plasma by Laser ($t_h = 66$ nsec; $t_i = 76$ nsec; $t_l = 10$ nsec)	176
Figure 5.23	Constriction of Marginally-Overdense Target Plasma by Laser ($t_h = 32$ nsec; $t_i = 36$ nsec; $t_l = 4$ nsec)	177
Figure 5.24	Beginning of Perturbation by Laser - Twitch at Right of Column ($t_h = 6$ nsec; $t_i = 16$ nsec; $t_l = -10$ nsec)	178
Figure 5.25	Cavity-Like Perturbation from CO ₂ Laser Incident on Overdense Plasma ($t_h = 0$ nsec; $t_i = 0$ nsec; $t_l = 0$ nsec)	180
Figure 5.26	Cavity-Like Perturbation from CO ₂ Laser Incident on Overdense Plasma Before Pinch ($t_h = 24$ nsec; $t_i = 24$ nsec; $t_l = 0$ nsec)	181

	<u>Page</u>
Figure 5.27 Relaxation of Laser-Induced Perturbation ($t_h = -15$ nsec; $t_i = 17$ nsec; $t_l = 32$ nsec)	182
Figure 5.28 Laser Perturbation on Post-Pinch Plasma ($t_h = -60$ nsec; $t_i = -27$ nsec; $t_l = 33$ nsec)	183
Figure 5.29 Geometry of Shock Front in Reconstruction	187
Figure 5.30 Laser-Perturbed and Unperturbed Plasma Density Profiles at Peak Laser Intensity	192
Figure 5.31 Laser-Perturbed and Unperturbed Plasma Density Profiles 20 nsec After Peak Laser Intensity	194
Figure 5.32 Features of Shock Front in Laser-Plasma Interaction Region	196
Figure 5.33 Cylindrical Geometry for Calculation of Fringe Shift	210
Figure 5.34 Fringe Plot for Small Axial Segment of Density Perturbation	214
Figure 5.35 Plot of Transmission vs. Incident Intensity and Time of Incidence of 10.6μ Radiation	219
Figure 5.36 Incident Laser Pulse Shape (100 nsec/div)	221
Figure 5.37 Transmitted Laser Pulse Shape, Moderate Intensity (100 nsec/div)	222
Figure 5.38 Transmitted Laser Pulse Shape, High Intensity (100 nsec/div)	224
Figure 5.39 Transmitted Pulse Width vs. Incident Intensity	225
Figure 5.40 Enhancement of Tail of CO_2 Laser Pulse in Transmission (100 nsec/div)	227
Figure 5.41 Annular Distribution of Transmitted Beam - No Plasma in Chamber	229

	<u>Page</u>
Figure 5.42 Concentric Rings on Pulse Transmitted Through Overdense Plasma	230
Figure 5.43 Hot-Spot in Transmission Burnspot from High Incident Intensity Through Overdense Plasma	231
Figure 5.44 Vertical Bars on Transmission Burnspot through Overdense Plasma	232
Figure 5.45 Multiple Transmission Burnspots Due to Several Transmitted Pulses	234
Figure 5.46 Transmitted Intensity vs. Incident Intensity - Pre-Pinch Overdense Plasma	241
Figure 5.47 Transmitted Intensity vs. Incident Intensity - Post-Pinch Overdense Plasma	242
Figure 5.48 Transmitted Energy vs. Incident Energy for Overdense Plasma	245
Figure 5.49 Pulse-Shape Distortion from Transmission through an Intensity-Dependent Absorber	247
Figure 5.50 Pulse-Shape Distortion from Transmission through an Intensity-Dependent Absorber with Delayed Response	249
Figure 5.51 Optical Pulse from Plasma at Pinch Time - No Aperture or Imaging (200 nsec/div)	257
Figure 5.52 Optical Pulse from Plasma at Pinch Time - Aperture, No Imaging (200 nsec/div)	258
Figure 5.53 Optical Pulse from Plasma at Pinch Time - Apertured and Imaged (200 nsec/div)	259
Figure 5.54 Enhanced, Narrowed Optical Pulse from Laser-Heated Plasma	261

		<u>Page</u>
Figure C.1	The x,t Diagram for a Centered Rarefaction Wave	288
Figure C.2	Rarefaction Wave at Two Different Times	291
Figure C.3	Hugoniot Curve	295
Figure C.4	Hugoniot Curve - Geometric Interpretation	296
Figure C.5	Temperature Distribution of Shock Wave in Plasma	302
Figure D.1	Alignment Compensating Wedge	305
Figure G.1	Calculational Geometry of Fresnel Diffraction	319
Figure G.2	Intensity vs. Radius for Fresnel Diffraction Pattern from Circular Aperture	320

LIST OF APPENDICES

		<u>Page</u>
Appendix A	Propagation of EM Wave Through a Homogeneous Plasma	278
Appendix B	Refraction in a Continuous Medium	284
Appendix C	Hydrodynamic Energy Transfer and Shock Waves	287
Appendix D	Optical Design of Alignment Compensating Wedge	306
Appendix E	Source Listing of X-Ray Analysis Code	308
Appendix F	Checklist for Experimental Procedures	311
Appendix G	Fresnel Diffraction Through Circular Aperture - Numerical Analysis	315

LIST OF SYMBOLS

A	Number of nucleons in nucleus; initial point on Hugoniot curve
Ai	Airy function
$\overset{O}{A}$	Angstrom
b	Density profile fitting parameter
B	Magnetic field; final point on Hugoniot curve
\mathcal{B}	Fourier-Bessel transform
c	Speed of light
cm	Centimeter
c _o	Acoustic speed
c _p	Specific heat at constant pressure
c _v	Specific heat at constant volume
C	Capacitance
d	Distance of chord from center of circle; diameter of focal spot
D	Speed of shock front; convective derivative
e	Electronic charge
e ⁻	Electron
eV	Electron volt
E	Electric field; energy
E _{max}	Maximum electric field strength at point before critical layer
E _o	Peak amplitude of oscillating electric field

E_v	Electric field strength in vacuum
E_v	Spectral distribution of bremsstrahlung emission
f_x	x-frequency in two-dimensional Fourier transform
f_y	y-frequency in two-dimensional Fourier transform
F	Fractional absorption
$F(E,t)$	Foil transmission as function of x-ray energy
F_{NL}	Ponderomotive force
$FWHM$	Full width at half maximum
\mathcal{F}	Two-dimensional Fourier transform
g	Number of particles in Debye sphere; Gaunt factor
$G(\alpha)$	Intensity correction to inverse bremsstrahlung absorption coefficient
$G(E)$	Stopping power of scintillator as function of x-ray energy
h	Planck's constant
$h(x_0, y_0, x_1, y_1)$	Green function in Huygens-Fresnel diffraction formula
$H(E,t)$	Energy response function for x-ray detector
i	Current
I	Intensity
I_{INC}	Incident intensity
I_{TR}	Transmitted intensity
j	$\sqrt{-1}$
J	Joule; current density
J_0	Zero - order Bessel function

J_1	First-order Bessel function
k	Wavenumber, $2\pi/\lambda$
k_0	Wavenumber in vacuum
k_1	Wavenumber of first-order plasma surface perturbation
keV	Kiloelectron volt
kV	Kilovolt
K	Radiation absorption coefficient
K^{IB}	Inverse bremsstrahlung absorption coefficient
K_s	Scintillator photoelectric absorption coefficient
l	Pathlength of object beam through plasma; length
l_0	Pathlength of object beam through unperturbed portion of plasma
L	Critical scale length; border of path through plasma column; inductance
LASL	Los Alamos Scientific Laboratory
LLL	Lawrence Livermore Laboratory
LPIL	Laser Plasma Interaction Laboratory
ℓ	Mean free path; depth of field
ℓ_{th}	Thermal mean free path
ℓ_{vis}	Viscous mean free path
m	Meter; mass of electron; an integer
mm	Millimeter
n	Electron density; exponent of dependence of thermal conductivity on temperature
\bar{n}	Electron density averaged between critical surfaces of column

n_c	Critical electron density
nH	Nanohenry
n_i	Ion density
nm	Nanometer
n_o	Peak electron density at centerline
$nsec$	Nanosecond
n_0	Electron density in front of shock
n_1	Electron density behind shock
p	Pressure
p_o	Fringe shift imparted to object beam from passage through unperturbed region of plasma
p'	Fringe shift imparted to object beam from passage through density border of perturbed region (shock front)
P_0	Pressure in front of shock front
P_1	Pressure behind shock front
Q	Energy deposited from external source
r	Radial position
r_c	Critical radius
r_f	Radius of spherical thermal wave
r_o	Plasma radius
r_0	Radial position at observation plane
r_1	Radial position at aperture plane
r_{01}	Vector between observation point and aperture point
R	Reflection coefficient; radius of spherical shock; resistance
$R(\theta_e)$	Ratio of two x-ray detector signals

s	Distance between aperture plane and center of wavefront curvature; $1/e$ width of Gaussian axial variation in density
S	Eikonal; entropy
$S(E)$	Number of electrons emitted from photocathode per x ray of energy E
t	Time
t_h	Time by which hologram exposure precedes pinch time
t_i	Time by which CO_2 laser incidence precedes pinch time
t_l	Time by which CO_2 laser incidence precedes hologram exposure
T	Period of oscillations; tesla
u	Gas velocity; scalar wave
u_0	Flow velocity of gas in front of shock
u_1	Flow velocity of gas behind shock
U	Strength of scalar field
UV	Ultraviolet
v	Velocity
\mathbf{v}	Vector normal to tangent of ray path
v_{br}	Wavebreaking velocity
v_e	Electron drift velocity
v_o	Maximum oscillatory velocity of electron
v_{osc}	Oscillatory velocity of electron in laser field
v_{th}	Electron thermal velocity
v_l	Velocity of gas behind shock front in laboratory frame

V_f	Volume of shock front
V_0	Specific volume of gas in front of shock
V_1	Specific volume of gas behind shock
w	Piston velocity
W	Watt
$W(\theta, t)$	Output signal strength from x-ray detector
x	Position coordinate
x_0	Position coordinate in observation plane
x_1	Position coordinate in aperture plane
y	Position coordinate; horizontal direction on holography film plate; direction of electric field
y_0	Position coordinate in observation plane
y_1	Position coordinate in aperture plane
z	Axial position coordinate in plasma; direction of radiation propagation; vertical position coordinate on holography plate; distance between aperture plane and observation plane
z_{\max}	Maximum distance of penetration of obliquely-incident radiation
\hat{z}	Unit vector in z-direction
Z	Ionic charge
α	Exponent of time in similarity variable; parameter for intensity-dependence of inverse bremsstrahlung; damping parameter of oscillation; holographic angle parameter = $-\frac{1}{2}\delta\cos\theta$, wedge angle
β	Number of order unity characterizing energy in Maxwellian; parameter of EM wave in plasma = $1 - (\omega_p^2/(\omega^2 + \nu_{ei}^2))$

γ	Ratio of specific heats = c_p/c_v
δ	Change in reference beam angle between holographic interferometry shots; a small quantity; distance of ray from optical axis before entering optical element
δ'	Distance of ray from optical axis after exit from optical element
Δ	Ratio between successive maxima in oscillations
Δx	Thickness of shock front
Δx_R	Thickness of relaxation region
$\Delta\phi$	Phase change imparted to object beam by plasma
ϵ	Dielectric constant; degree of axial perturbation on column density
ϵ_0	Internal energy in gas in front of shock
ϵ_1	Internal energy in gas behind shock
ζ	Position variable in argument of Airy function = $(\omega L/c)^{1/3}(z/L - 1 + jvei/\omega)$
η	Index of refraction
η_0	Field strength parameter defined by ratio of electron oscillatory to thermal velocity
θ	Temperature; angle between holographic reference and object beam; angle of laser beam divergence; angle of refraction; angle of radiation incidence
θ_e	Electron temperature
θ_i	Ion temperature
κ	Electron thermal conductivity; constant = $n_0/2n_c$

κ_0	Temperature-independent multiplier of thermal conductivity of Spitzer
λ	Wavelength of radiation
λ_D	Debye length
λ_0	Vacuum wavelength of radiation
λ_v	Vacuum wavelength of radiation
Λ	Ratio of Debye length to distance of closest approach
μ	Micron; viscosity
μ_0	Permittivity of free space
μF	Microfarad
μsec	Microsecond
ν	Frequency of radiation in cycles/sec
ν_{ei}	Electron-ion collision frequency
ν_{ei}^0	Electron-ion collision frequency at critical layer
ξ	Amplitude of electron motion
ξ_0	Multiplicative constant for self-similar motion of expanding spherical shock
ρ	Density; frequency in Fourier-Bessel transform; radius of ray curvature; parameter of EM wave in plasma = $\omega L/c$
ρ_0	Gas density in front of shock
ρ_1	Gas density behind shock
σ	$1/e$ - width of Gaussian radial density profile
$\sigma(E)$	Foil x-ray absorption cross-section
Σ	Aperture cross-section
τ_{eq}	Electron-ion equilibration time

ϕ	Angle of wedge tilt from normal incidence
ϕ_{\max}	Maximum energy flux out of region
$\chi(E)$	Spectral distribution of emitted radiation
ψ	Angle of ray with optical axis before entering optical component
ψ'	Angle of ray with optical axis after exiting from optical component
ω	Angular frequency of laser radiation
ω_d	Angular frequency of damped oscillation
ω_0	Angular frequency of undamped oscillation
ω_p	Electron plasma frequency
Ω	Ohm
∇	Differential operator
\propto	Is proportional to
$=$	Equals
\approx	Approximately equals
\equiv	Is defined as
\rightarrow	Tends to
∞	Infinity

CHAPTER ONE

INTRODUCTION

1.1 Orientation

The field of high-intensity electromagnetic radiation interaction with matter draws from nearly all the traditional areas of physics. In the regime of high intensity, the target immediately forms a plasma upon ionization by the radiation, whether its initial state was solid, liquid, or gas. Thus, the study of laser-plasma interaction is also applicable to the broader field of high-intensity radiation interaction with matter following the fraction of a second required for target ionization. The work of radiation-plasma physics is the study of ensuing events. It involves the reflection, transmission, scattering, and absorption of the incident laser beam and the influence of this beam on the dynamic behavior of the target plasma. Contributions to the field are made from electrodynamics, classical and non-linear optics, fluid dynamics, statistical mechanics, and, of course, plasma physics.

Early work in the field was related to the interaction of radio waves with an atmospheric plasma, the ionosphere. Radio Luxembourg observed that a

program transmitted through the ionosphere was received as a signal intermingled with a program broadcast at another frequency. This effect of cross-modulation implied that a non-linear interaction was occurring with the ionospheric plasma.

Present communication work continues to apply ideas of radiation interaction with plasmas. Adaptive optics, which modify the beam leaving a laser to compensate for distortions along the path of propagation or at the target, operate on this principle. The modulation of a laser beam after scattering from or passing through a plasma is used in the shaping of pulses. A method of space vehicle propulsion of recent interest uses an earth-bound laser to provide thrust by vaporization and ablation of material at the tail of the air-borne vessel. Thus, a space vehicle with no engines on board may be powered by the laser-plasma interaction. Laser-heated targets can provide a pulsed source of radiation, such as x rays, neutrons, or charged particles. Laser-plasma physics also has several defense applications. A small-scale confirmation of this was achieved in this laboratory when an investigator inadvertently placed his hand in the beam of a pulsed CO₂ laser. Fortunately for the investigator, the incident intensity was not sufficient to place that interaction into the realm of laser-plasma physics.

Most of the current work in the field is stimulated by the thermonuclear research program. By compressing a pellet of thermonuclear fuel by spherical illumination from a high-intensity laser, the high densities and temperatures required for thermonuclear burn are achieved. Essential to this accomplishment is an understanding of the physical mechanisms that allow (or forbid) heating and compressing a plasma by electromagnetic radiation. The theory developed by the laser fusion research program is invoked for interpretation of much of the data in this investigation; hence, it is to laser fusion that the results are most immediately applicable.

The experimental work in laser fusion may be divided into two categories. The first group includes the spherical illumination of thermonuclear fuel pellets by high-intensity laser radiation. The goal of these experiments is to attain high densities and temperatures for sufficient time to maximize the number of fusion reactions. By altering experimental parameters, such as target composition, incident pulse shape, intensity, and wavelength, an ever-increasing production of fusion neutrons is sought.

The second class of experiments is more concerned with basic studies of laser-target interaction. By firing at a target of simpler geometry and varying

one parameter at a time, the basic mechanisms of coupling laser energy into a plasma are studied. Such experimental results are more easily extrapolated to non-fusion applications, as they study the basic laser-plasma interaction. The experiment described in this volume is of the second type.

By use of a plasma that was produced independently of the interacting laser, a well-characterized target plasma is obtained. This is in contrast to nearly all other laser-target experiments in which the target is a solid which requires heating to a plasma state by the first portion of the laser pulse before any interaction effects can be studied in the second portion. In such experiments, it is impossible to start with a known plasma as a target, and thence the study of the laser-plasma interaction must be carried out on a poorly-characterized plasma. Whereas studies with solid targets are more applicable to the goal of achieving thermonuclear burn in a fuel pellet, experiments with laser incidence on a ready-made plasma provide less factors to confuse the study of the laser-plasma interaction.

It is useful to mention briefly the research in laser-plasma interaction at other facilities. In the United States, the bulk of laser fusion efforts is carried out by Lawrence Livermore Laboratory, Los

Alamos Scientific Laboratory, the Laboratory for Laser Energetics of the University of Rochester, and KMS Fusion. Most of these institutions perform both thermonuclear research (maximization of fusion reactions in a spherical irradiation geometry) and basic characterization of the laser-plasma interaction (irradiation of slab targets of non-thermonuclear material). Other laboratories in Germany, France, Japan, and Russia pursue a similar combination of laser fusion and laser-plasma investigations.

In addition, several facilities exclusively investigate the basic interaction by firing at plasma, gas, or solid targets in a variety of geometries. In the United States, the Naval Research Laboratory performs experiments involving the interaction of CO₂ laser light with solid targets, with diagnosis of the resulting radiation. Similarly, Sandia Laboratories and Harvard University have efforts in that area. The University of Washington and the Massachusetts Institute of Technology perform experiments by firing a CO₂ laser into an underdense plasma contained in a magnetic field. At UCLA, similar work using an underdense vacuum arc plasma source is occurring. At the University of California at Davis, experiments with microwaves on an overdense hot-cathode DC discharge plasma are being carried out to study critical layer phenomena.

In Canada, the University of British Columbia uses a Z-pinch plasma source and fires a CO₂ laser along the axis of the pinch to study parametric phenomena. Work at the National Research Council investigates CO₂ laser-produced plasmas from solid and gaseous targets. In Varennes, Quebec, IREQ and INRS Energie perform experiments that most closely match those of the Laser Plasma Interaction Laboratory of the University of Michigan (LPIL). Researchers fire a CO₂ laser transversely on a marginally-overdense Z-pinch plasma, but do not use holographic interferometry to measure densities and monitor the interaction. Furthermore, they do not indicate any study of transmission of the CO₂ laser beam through the plasma.

At Culham Laboratory in England, the Langmuir turbulence induced by CO₂ radiation incident on a high-temperature plasma is studied by ruby laser scattering. Also at Culham, interferometric and x-ray investigations of laser-produced plasmas from solid targets are performed.

In France, at the Laboratoire de Physique des Milieux Ionises, a ruby laser focused on a polyethylene slab provides an independent plasma for CO₂ laser beam absorption experiments. Time-resolved Mach-Zehnder interferometry indicates peak electron density of just below critical ($9 \times 10^{18} \text{ e}^-/\text{cm}^3$). Their peak

CO₂ intensity is about a factor of ten lower than that utilized in this investigation.

The combination of an overdense, independently-prepared plasma and a high incident CO₂ intensity is evidently unique to LPIL, and affords the opportunity for characterization of the interaction of high-intensity laser radiation with an overdense plasma.

1.2 Summary of experiment and results

This experiment measured an intensity threshold for transmission of 10.6 μ laser radiation through an overdense helium Z-pinch plasma. Intensity varied from 0.2 to 4×10^{11} W/cm² at a pulse width of 38 nsec, and was radially incident on the cylindrical, fully ionized plasma. Electron temperature was sufficiently low (about 20 eV) to place the experiment in the regime for density profile modification by the ponderomotive force of the high-intensity radiation.

Holographic interferometry at 347.2 nm, perpendicular to both the plasma column and the propagation vector of the 10.6 μ radiation, indicated critical scale lengths of 100 to 200 μ , and provided hydrodynamic information concerning the shock wave resulting from the interaction. A series of hydrodynamic arguments utilizing the thermal mean free path, the thickness

of the shock front and relaxation region, the Hugoniot relation, and the Taylor-Sedov theory of spherical shocks, provided an estimate of the energy absorption fraction in the range of 60 to 70 percent.

The evolution of the Z-pinch plasma was investigated interferometrically with no laser incident. The plasma was overdense from 50 nsec before pinch to 80 nsec after pinch, with a peak centerline density of about $4 \times 10^{19} \text{ e}^-/\text{cm}^3$. The formation of a step in the radial density profile in the region of the critical radius was unique to the approach to peak compression. The plateau in the plot of density vs. radius, which occurred only at times before maximum pinching, was not predicted in a one-dimensional, two-temperature MHD Lagrangian computer simulation. At time of pinch, the numerical simulation agreed with the holographically-determined density plot. An investigation of density dependence in the z-direction indicated general density wave propagation in the direction of current flow.

A series of experiments to observe x-ray continuum emission and absorption of a probe laser beam by inverse bremsstrahlung, coupled with a Saha calculation and a Bennett pressure-balance relation, indicated electron temperatures between 10 and 40 eV, with the best estimate at 20 eV.

After characterization of the target plasma in the absence of the CO₂ laser, the transmission of 10.6 μ radiation through the overdense plasma was measured over a range of intensities. A threshold for intensity transmission was observed. Laser incidence within 35 nsec before time of pinch and exceeding a threshold of 3.5×10^{11} W/cm² provided about 1% intensity transmission. After pinch time, a threshold of 2×10^{11} W/cm² and a transmission fraction of about 3% were indicated. The higher threshold before pinch was attributed to differences in the target plasma at that stage of discharge evolution. The density step near the critical radius in the unperturbed plasma and the general inward motion associated with approach to peak compression distinguished the pre-pinch plasma from the post-pinch one.

The pulse shape transmitted through the overdense plasma exhibited a very rapid rise and reached peak intensity about 30 nsec later than would be predicted for instantaneous transmission. The pulse width was decreased in transmission, which indicated that the overdense plasma cut out the first portion of the pulse and transmitted the remainder. The self-modelocking structure on the incident pulse (7 nsec period) was enhanced in transmission to nearly 100% modulation of the transmitted pulse.

Further shortening of the transmitted pulse was observed at higher intensities. At the peak intensity of 4×10^{11} W/cm², the incident laser pulse of 38 nsec FWHM was shortened to about 15 nsec.

The burnspot of the pulse through the overdense plasma displayed a series of concentric rings of high contrast, indicative of Fresnel diffraction through a circular aperture. These rings were noted in an earlier investigation, and were interpreted in that investigation as the signature of a smooth-walled hard aperture, similar in diameter to the 125 μ focal spot, produced in the plasma by the incident beam.

Backscatter of 10.6 μ radiation into the focusing optics was linear with intensity, and was about 10^{-4} of incident intensity. Monitor of the backscatter into the focusing optics comprised only 0.27% of the total 2π solid angle associated with the backwards direction, and the experimental geometry forbade sampling a greater solid angle.

Another indication of energy absorption was the enhanced optical emission from the interaction region. This was monitored by a detector which viewed only the portion of the plasma column that coincided with the focal volume of the incident laser.

1.3 Organization of text

The discussion contained in the following pages begins with an overview of the theory that entered into interpretation of the experiment. The theoretical discussion is divided into a treatment of the laser-plasma interaction in the low-intensity limit with a homogeneous target plasma and with a target containing a linear density profile. The added effects of high intensity are then analysed using some physical models commonly used in the laser fusion community.

The third chapter contains a brief description of the tools of the experiment. The main features of the target plasma, the related diagnostics, the CO₂ laser and optical system, and the holography setup are summarized. The method of data-gathering is set forth, concluding the chapter.

An auxiliary series of experiments to determine the plasma electron temperature is next described in Chapter Four.

Chapter Five presents a detailed discussion of results of the experiment and their interpretation in terms of the models presented in Chapter Two. The chapter begins with a description of evolution of the Z-pinch plasma, and makes comparisons with the results

of a one-dimensional MHD code simulation. The holographic appearance of hydrodynamic effects of the interaction is next described, with an estimate of energy absorption. The temporal structure and intensity dependence of the transmitted beam are subsequently presented, with a description of the burn spot observed. Finally, the associated diagnostics of optical emission and integrated backscatter of 10.6μ radiation conclude the chapter.

The final chapter examines the results in light of observations of other researchers, and concludes with a discussion of implications and direction of future research.

Removal of material not immediately related to the development of the text has been practiced extensively. A series of appendices treats the electromagnetic dispersion relation, the hydrodynamics of shock waves, the design of some optical components, an experimental procedure checklist, and a listing of the computer codes used in this endeavor.

CHAPTER TWO

SUMMARY OF RELEVANT THEORY

2.1 Low-intensity electromagnetic radiation

The propagation of electromagnetic waves through a homogeneous plasma is approximately characterized by the familiar electromagnetic dispersion relation (Appendix A):

$$k^2 = \frac{\omega^2}{c^2} \left(1 - \frac{\omega_p^2 (1 - j\nu_{ei}/\omega)}{\omega^2 + \nu_{ei}^2} \right)$$

k = wave vector magnitude in plasma

ω = angular frequency of incident radiation

c = speed of light in vacuum

ω_p = plasma frequency; $\omega_p = 5.64 \times 10^4 \sqrt{n(\text{cm}^{-3})}$

$j = \sqrt{-1}$

ν_{ei} = electron-ion collision frequency

Some simplifying assumptions provide the cold collisionless expression of the refractive index, η , which is obtained from the previous expression in the limit $\nu_{ei}/\omega \ll 1$.

$$\eta = \sqrt{1 - (\omega_p/\omega)^2}$$

The attenuation constant for electromagnetic radiation in the plasma is given in this approximation by

$$K = \left(\frac{\omega_p}{\omega} \right)^2 \frac{\nu_{ei}}{\eta c}$$

Fresnel's law of reflection from a dielectric states that for normal incidence of electromagnetic radiation on a medium of index η from a vacuum, the ratio of reflected intensity to incident intensity is given by

$$R = \frac{I_r}{I_o} = \left(\frac{\eta - 1}{\eta + 1} \right)^2$$

Hence, for a cold collisionless plasma model,

$$R = \left(\frac{\sqrt{1 - (\omega_p/\omega)^2} - 1}{\sqrt{1 - (\omega_p/\omega)^2} + 1} \right)^2$$

For incident radiation of frequency $\omega = \omega_p$, $R = 1$ and the radiation is fully reflected.

So for the case of incidence of electromagnetic radiation on the sharp boundary of a cold, collisionless plasma of sufficient density that $\omega_p > \omega$ ("overdense"), complete reflection occurs.

The preceding discussion applies to the case in which there are no static magnetic fields in the plasma. For electromagnetic radiation incident upon a plasma in a Z-pinch device, the direction of propaga-

tion is perpendicular to the constricting magnetic field lines running parallel to the plasma-vacuum interface. For this situation, a distinction is made between "ordinary" waves with electric vector parallel to magnetic field lines, and "extraordinary" waves with electric vector perpendicular to the magnetic field. The more complicated case of propagation vector parallel to the magnetic field is not considered likely to occur in this experimental geometry, and is not treated here. For ordinary waves, there is no effect of the magnetic field, and the analytical treatment previously described is still applicable.

In the case of the extraordinary wave, the velocity of propagation is a function of the magnetic field. Furthermore, a plot of ω vs. k (the dispersion plot) for the extraordinary wave has three branches, so that waves of a given k in the plasma may be at one of three frequencies. Various "stop" and "pass" bands occur, so that propagation through the plasma may occur in the extraordinary mode for $\omega < \omega_p$, in contrast to the case of no magnetic field. Thus, the above analysis may break down for appropriately polarized electromagnetic radiation on a Z-pinch plasma with axial magnetic fields in the plasma.

As a transition from radiation impinging upon a sharp plasma-vacuum interface to radiation propaga-

ting through a plasma of gradually changing density, the refraction of electromagnetic radiation by a plasma is mentioned.

A plasma that has a density gradient also has a gradient in the index of refraction, as indicated by the cold collisionless dispersion relation mentioned earlier. Just as in the case of a vacuum-glass interface, refraction of electromagnetic radiation is expected for incidence that is not normal to the direction of the gradient. Appendix B presents some considerations of refraction in a continuously-varying medium.

A formula useful for estimates of refraction in a medium with spherical or cylindrical symmetry relates the radius of curvature of a ray, ρ , to the scalar product of the unit normal to the ray, \mathbf{v} , and the gradient of the refractive index:

$$1/\rho = \mathbf{v} \cdot \nabla(\ln \eta)$$

In the special case of small-angle refraction by a plasma of radius r_0 of radiation at a wavelength whose critical density is n_c , where

$$n_c = \frac{1.1 \times 10^{21}}{\lambda^2 (\mu)} \text{ cm}^{-3}$$

the angle of refraction is approximately given by

$$\sin \theta \approx \frac{r_0}{n_c} \frac{dn(r)}{dr}$$

The expression for η in a cold, collisionless plasma indicates that as the electron density increases,

the index of refraction decreases. Thus, a cylindrical plasma acts as a diverging lens to radiation passing through it, and radiation is refracted from regions of high plasma density to regions of lower density.

An interesting observation is made in considering the case of radiation obliquely incident on a plasma slab of slowly increasing density. The ray enters at an angle to the density gradient and is gradually refracted away from regions of high density and is turned out of the plasma. In this geometric optics approximation, no change in polarization is expected during this turning out process.

This should next be compared to obliquely incident radiation on an abrupt plasma-vacuum interface, where the plasma density jumps from zero to over critical in less than a wavelength. Specular reflection causes reflection of the ray off the critical layer in the manner of metallic reflection. For metallic reflection of linearly-polarized radiation, boundary conditions at the conducting surface require the component of the polarization vector tangential to the reflecting plane to be inverted upon reflection. This results in the change of direction of polarization upon reflection, not seen in the previously-mentioned case of geometrical optics.

For a density gradient between the regimes of geometric (slowly-changing) and metallic (infinite

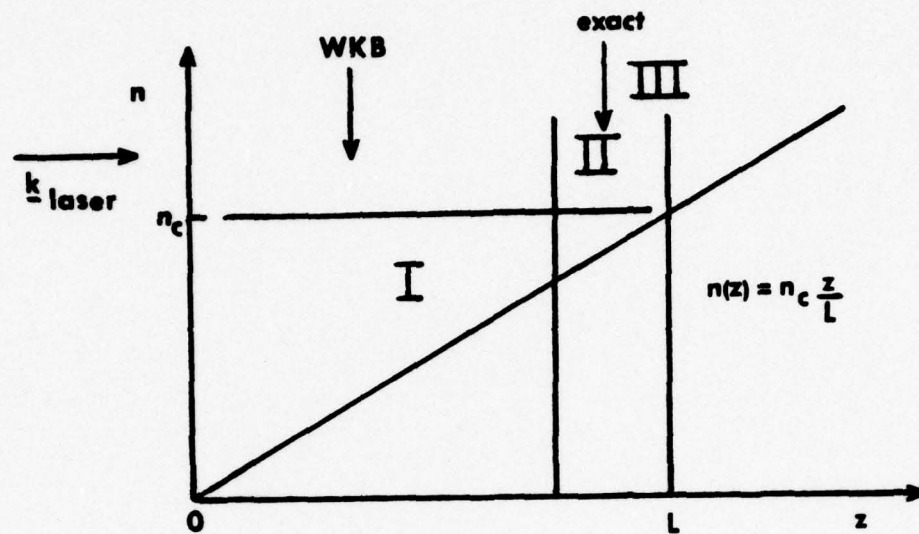


FIGURE 2.1 RADIATION INCIDENT ON LINEAR DENSITY INCREASE

jump), the linearly polarized radiation is changed to elliptical polarization with eccentricity determined by the steepness of the gradient. The use of this change in polarization as an indirect way to measure density gradients in laser pellet plasmas was devised by Phillion and used to infer density scale lengths (Phillion, 1976).

The inclusion of nonhomogeneity is most easily provided for by the assumption of an electron density which is a linearly increasing function of z , the direction of radiation propagation. In this analysis, the density is zero at $z = 0$ and increases linearly to critical density for the wavelength of interest at $z = L$ (Figure 2.1).

From Maxwell's equations may be derived the wave equation for waves propagating in an inhomogeneous medium (Landau & Lifshitz, 1960):

$$\mathbf{E} + \frac{\omega^2}{c^2} \epsilon(\omega, z) \mathbf{E} - \nabla(\nabla \cdot \mathbf{E}) = 0$$

\mathbf{E} = electric field vector

ϵ = dielectric constant; $\epsilon = \eta^2$

In the cold, collisionless plasma, $\epsilon(\omega, z)$ is given by

$$\epsilon = 1 - (\omega_p(z)/\omega)^2$$

which for the case of a linear density gradient becomes

$$\epsilon = 1 - (z/L)$$

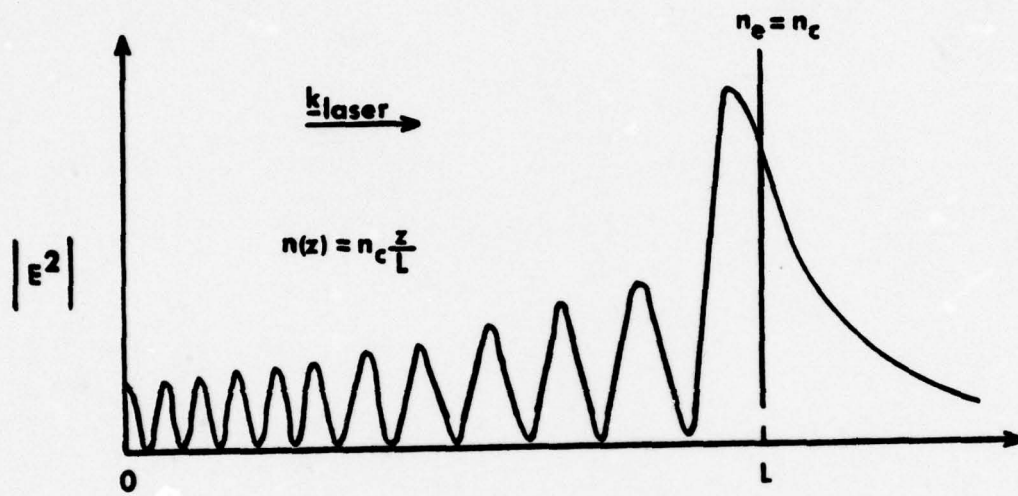


FIGURE 2.2 ELECTRIC FIELD IN LINEAR APPROACH TO
CRITICAL DENSITY

Solution of this equation, after a change of variables, is in terms of the linearly independent Airy functions $Ai(\zeta)$ and $Bi(\zeta)$, where

$$\zeta = (\omega^2/c^2 L)^{1/3} (L - z)$$

for $v_{ei}/\omega \ll 1$ (Osborn, 1975). After determining the multiplicative constants by energy flux arguments, the E-field in the plasma is given by (Kruer, 1976)

$$E(\zeta) = E_v (\omega L/c)^{1/6} 2\sqrt{\pi} Ai(\zeta)$$

where E_v is the free-space value of the electric field. The electric field in the plasma reaches a maximum at a point z_p before the critical layer, given by

$$L - z_p = (c^2 L/\omega^2)^{1/3}.$$

The ratio of this maximum field to its vacuum value is expressed in the absence of collisions as

$$\left| \frac{E_{\max}}{E_v} \right| = 1.9 (\omega L/c)^{1/6}$$

(Ginzburg, 1960)

Thus, the electric field is "swollen" at a point before the critical layer. Conservation of energy in the wave requires that the magnetic field decrease as the electric field increases, so the magnetic field of the wave in the plasma is less than its vacuum value. The field is evanescent beyond the critical layer (Figure 2.2).

The effect of collisional absorption on the electromagnetic wave propagating through a linear gradient may be included by use of the attenuation constant, K , mentioned earlier as taking the form

$$K = (\omega_p/\omega)^2 \frac{\nu_{ei}}{\eta c}; \quad \eta = (1 - z/L)^{1/2}$$

The collision frequency, ν_{ei} , is directly proportional to the square of the electron density, and may be expressed in terms of the electron-ion collision frequency at the critical layer, ν_{ei}^0 . After doing this, the absorption of the electromagnetic wave in its approach to the critical layer is found by integration of K from $z = 0$ to $z = L$:

$$\left| \frac{E}{E_v} \right| = \exp\left(-\frac{1}{2} \int_0^L K(z) dz\right) = \exp\left(\frac{-8 \nu_{ei}^0 L}{15 c}\right)$$

(Rockett, 1977a)

The main idea is that in approaching the critical layer from vacuum, the electric field is attenuated as a result of collisions in the linear gradient approaching the layer, and is enhanced by field swelling. Field swelling arises from the general result applicable in a dielectric, whether plasma or not, that

$$\left| \frac{E(z)}{\sqrt{\eta(z)}} \right| = \text{constant}$$

The general relation that combines field swelling and collisional damping is

$$\left| \frac{E_{\max}}{E_v} \right| \approx 1.9 (\omega L/c)^{1/6} \exp \left(\frac{-8 \nu_{ei}^0 L}{15 c} \right)$$

This numerical expression is only valid in regions preceding the critical layer and is the result of a WKB treatment of electric field strength in a slowly-varying medium. The condition for validity is the WKB restriction that

$$\lambda_v \frac{d\lambda}{dz} \ll 2\pi$$

$$\lambda_v = \text{vacuum wavelength}$$

Since $\lambda = \lambda_v/\eta$, the validity condition may be expressed as a limitation on z to Region I in Figure 2.1:

$$z/L \ll 1 - (\lambda_v/4\pi L)^{2/3}$$

For z near L (Region II in Figure 2.1), the Airy function solution, rather than the WKB approximation, is required.

The maximum value of the electric field at the point near the critical layer is both a function of the critical scale length, L , and the electron-ion collision frequency, ν_{ei} , which, in turn, is a function of the electron temperature. For a variety of electron temperatures and critical scale lengths, the ratio E_{\max}/E_v may be plotted for $n = 1 \times 10^{19} \text{ e}^-/\text{cm}^3$ and

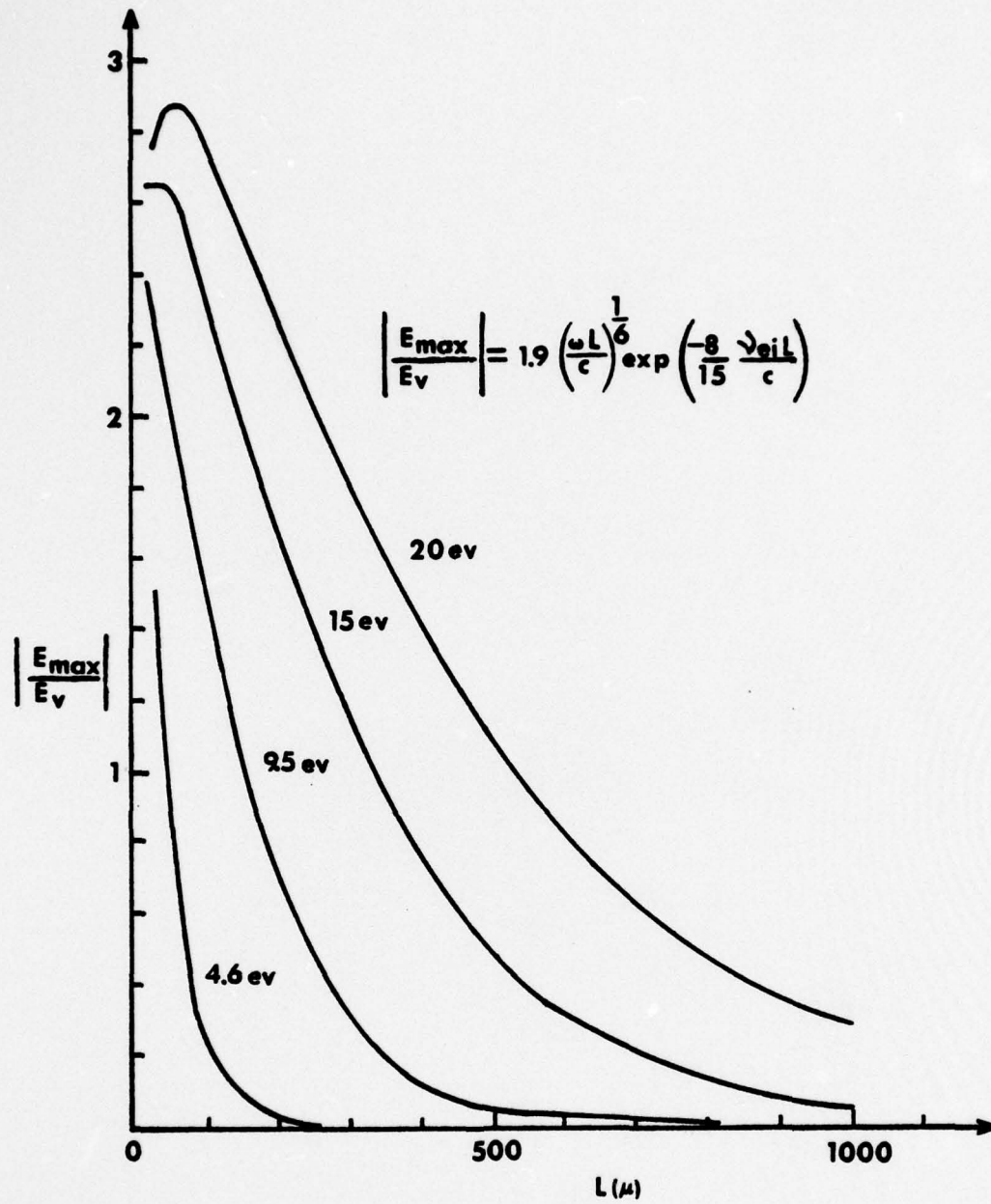


FIGURE 2.3 PLASMA MODIFICATION OF ELECTRIC FIELD STRENGTH VS. L AND θ_e

$\lambda_v = 10.6 \mu$ (Figure 2.3). The field strength is evidently an increasing function of temperature and a decreasing function of scale length. Physically, as the scale length increases, the wave must propagate through a greater length of absorbing plasma before reaching the z-position for which the field is calculated, so a lesser strength remains. As the temperature increases, the collision frequency decreases as a result of the smaller cross-section for coulomb collisions, so less absorption is seen in the approach to the point near the critical layer.

After turning from the critical layer, a reflected ray is further attenuated as it again passes through the linear gradient on the way out. In the WKB approximation, then, a reflection coefficient, defined as the ratio of reflected to incident intensity, is found:

$$R = \exp \left(\frac{-32}{15} \frac{v_{ei}^0 L}{c} \right)$$

In addition to the warning against application of the above approximation near the critical layer, it is noted that this treatment using Maxwell's equations is not the only one possible. Another derivation has been proposed, which uses a photon transport model and predicts more energy absorption in the overdense region, $z > L$, than in the underdense region (Osborn, 1975).

The preceding discussion applies to radiation normally incident on the plasma slab (propagation in direction of density gradient). For the case of oblique incidence, the ray turns outward before reaching the critical layer at a point where the local plasma frequency divided by the cosine of the angle of incidence equals the radiation frequency, or

$$z_{\max}/L = \cos^2 \theta$$

Effects of oblique incidence are dealt with in a very abbreviated fashion, as the investigation under consideration occurred at normal incidence.

The effect of resonance absorption, described by Ginzburg (Ginzburg, 1960), may enhance absorption of radiation at oblique incidence at a particular angle. This results from a component of the incident electric field vector being in the direction of increasing density. For this to occur, the two conditions of oblique incidence and polarization in the plane of incidence must be met. The component of the electric vector that points along the density gradient can drive plasma oscillations at the incident frequency. At the point in the plasma where the local plasma frequency equals that of the incident radiation, a condition of resonance enhances absorption. This effect cannot occur at normal incidence because in that case, no projection of the incident electric field

vector lies along the plasma gradient to excite these waves. Furthermore, at large angles of incidence, the turning point of the radiation, z_{\max} , is far from the critical layer, so the plasma oscillations cannot tunnel in to drive the region of resonance at the critical layer. Thus for some intermediate angle, given by

$$(kL)^{2/3} \sin \theta \approx 0.7 ,$$

absorption by this means is at a maximum (Freidberg et al., 1972).

This discussion has treated two mechanisms of energy transfer from the incident radiation to the plasma. Collisional absorption, resulting from the attenuation of the beam in a manner described by the absorption coefficient, K , is associated with the process of inverse bremsstrahlung by electrons in the field of ions. The absorption coefficient for inverse bremsstrahlung in a fully-ionized plasma may be expressed as a function of the plasma temperature, θ_e , plasma electron density, n , ionic charge, Z , and incident wavelength, λ , as

$$K^{IB} = 2.875 \times 10^{-37} \frac{\lambda^2 n^2 Z (1 - 8.97 \times 10^{-22} n \lambda^2)^{1/2}}{\theta_e^{3/2}}$$

θ_e in eV

λ in μ

n in cm^{-3}

K^{IB} in cm^{-1}

As indicated by the above relation, absorption by this means decreases as temperature increases. So to transfer energy efficiently from electromagnetic radiation to a hot plasma, other mechanisms are necessary.

The coupling of the radiation to the collective modes of plasma oscillation is another means of absorption. An example of this is the resonant absorption mechanism, which couples the oscillating field to plasma oscillations. The parametric excitation of waves in the plasma is also possible. In general, high incident intensities are required for these effects to be appreciable. In parametric excitation, the incident electromagnetic wave may excite two waves in the plasma. If both of these waves are electrostatic, absorption of the incident radiation causes plasma heating as the electrostatic waves are absorbed by plasma damping processes. If one excited wave is electromagnetic, it may leave the plasma and appear as a scattered wave (stimulated scattering).

The theory of parametric excitation is thoroughly treated in the literature (Dubois, 1973; Drake, et al., 1974; Forslund, Kindel, & Lindman, 1975; Nishikawa & Liu, 1975). An earlier investigation for stimulated Brillouin scattering in this laboratory showed no

evidence of this parametric process (Steel, 1976).

In a plasma with a steep density gradient, intensity thresholds for the parametric processes increase over the thresholds for the homogeneous case. The lack of stimulated Brillouin scattering was attributed to the short scale lengths in the plasma. Since the analysis of the experimental results does not include parametric instabilities, this vast area of interest will be dropped at this point.

2.2 High-intensity electromagnetic radiation

The parametric excitation of plasma modes has been mentioned as an effect that may occur at high intensities of incident radiation. More attention is given here to those effects associated with the ponderomotive force. In addition, other effects associated with high intensities are treated.

In the previous section, in obtaining the force experienced by an electron excited by an electromagnetic wave, the magnetic field of the wave was ignored. The full expression of force on the electron is

$$\mathbf{F} = -e(\mathbf{E} + \frac{1}{c}\mathbf{v} \times \mathbf{B})$$

For electrons that oscillate with sufficient

velocity, the magnetic field term produces an additional force on the electron which is orthogonal to both the electric field and the magnetic field of the wave. Thus, this additional term imparts a component of motion parallel or anti-parallel to the k -vector of the incident radiation. By retaining this term in the analysis of the last section, one obtains a force that is nonlinear in the incident field strength and is given by (Hora, 1969):

$$F_{NL} = \frac{-1}{8\pi} \nabla (\bar{E}^2 + \bar{B}^2)$$

(Bars denote time average)

This force acts in the direction opposite to the gradient in E^2 , and may drive particles from regions of high electric field to regions of lower field. This expression, and in fact this entire discussion, is for radiation incident perpendicularly to the plasma layer. Oblique incidence is discussed in the literature (Hora, 1969; Lindl & Kaw, 1971).

Three levels of accuracy may be used to further analyze this force. The lowest-order approximation evaluates the gradient of the field for forward-propagating radiation in the plasma. For the case of a collisionless plasma, the gradient of the E -field in the z -direction arises from the field swelling mentioned in the previous section. The ponderomotive force, F_{NL} ,

in this case is expressed as (Hora, 1969):

$$F_{NL} = \frac{E_V}{16\pi} (\omega_P/\omega\eta)^2 \frac{\partial\eta}{\partial z}$$

The second level of accuracy provides for the standing wave pattern that results from the combined incident radiation and reflected radiation from the critical layer. The standing wave pattern results in alternating regions of high and low field and alternation in the direction of the ponderomotive force between direction parallel and anti-parallel to the incident wave vector.

The solution of the wave equation which yielded the Airy function representation of the electric field in the previous section may be used in the most accurate treatment of the ponderomotive force (Lindl & Kaw, 1971). This method expresses the ponderomotive force in terms of the Airy function and its first derivative. For this case, the ponderomotive force is given by

$$\begin{aligned} F_{NL} = & \hat{z} \frac{\omega}{c} E_V^2 \exp(-2\rho s) \{ (Ai_R' Ai_R' + Ai_I' Ai_I') \\ & + \rho^{-2/3} (Ai_R' (\zeta_R Ai_R - \zeta_I Ai_I) \\ & + Ai_I' (\zeta_I Ai_R + \zeta_R Ai_I)) \} \end{aligned}$$

The subscripts R and I denote the real and imaginary

parts of the quantity to which they are attached, and

$$\begin{aligned} A_{iR} + jA_{iI} &= Ai(\zeta) \\ A'_{iR} + jA'_{iI} &= A'_i(\zeta) \\ \zeta &= (\omega L/c)^{2/3} (\frac{z}{L} - 1 + jv_{ei}/\omega) \\ \rho &= \omega L/c \\ s &= v_{ei}/\omega \end{aligned}$$

In general, evaluation of this expression for the ponderomotive force is difficult, but for the case of evaluation at the critical layer, the real part of ζ goes to zero and the first few terms of the series expansion of the Airy function (Abramowitz & Stegun, 1965) may be used to find

$$\begin{aligned} F_{NL} &\approx \hat{z} \frac{\omega}{c} E_V^2 (6.71 \times 10^{-2}) \exp(-2Lv_{ei}/c) \\ &\times (1.37 + (L/c)^{2/3} \omega^{-4/3} v_{ei}^2) \end{aligned}$$

at $z = L$ (critical layer).

The above form may not be derived from the earlier expression of the electric field in the plasma, which was subject to a WKB validity condition that forbade its application near the critical layer. The effect of collisions in the above expression is to reduce the ponderomotive force at the critical layer. Recalling the absorption of radiation caused by collisions in the approach to the critical layer through a linear

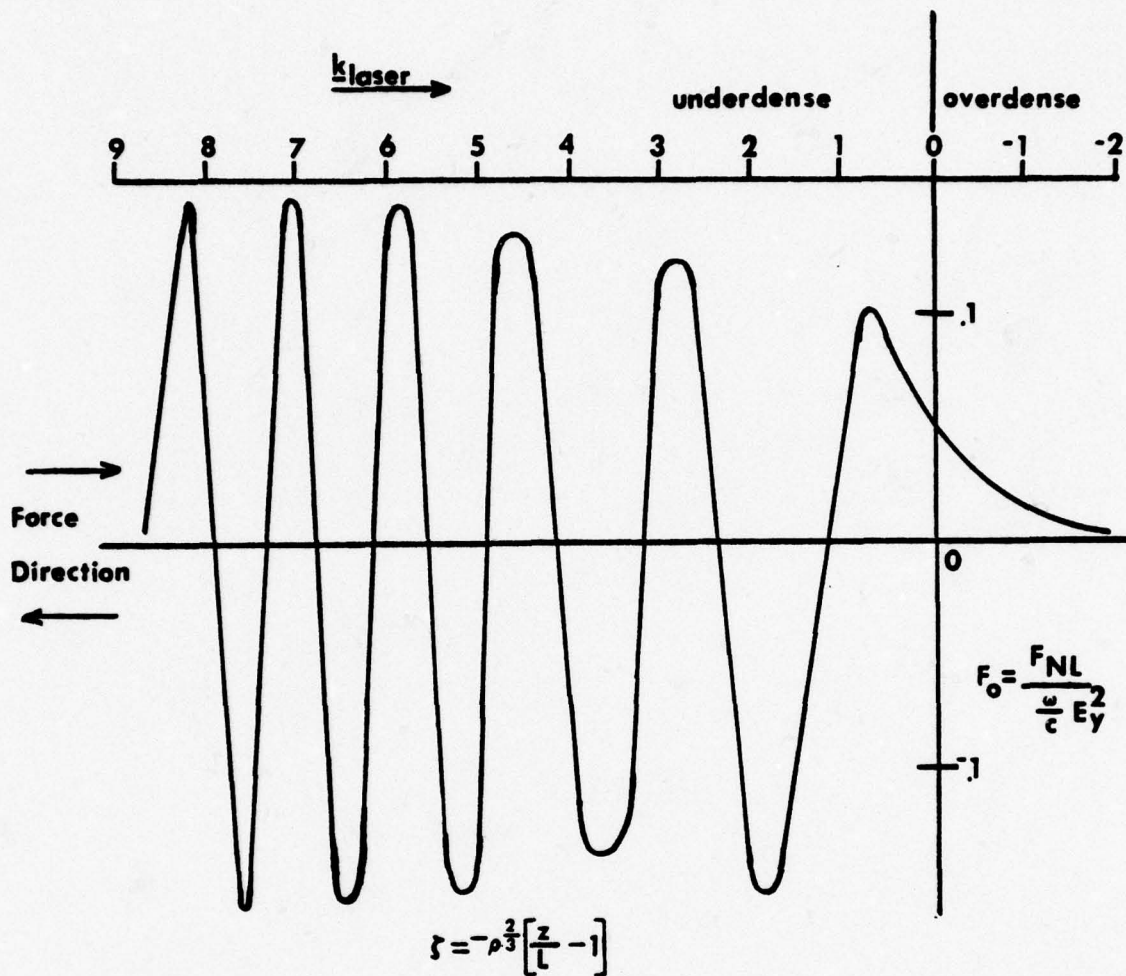


FIGURE 2.4 ALTERNATING DIRECTION OF PONDEROMOTIVE FORCE IN APPROACH TO CRITICAL LAYER

density gradient, it appears physically reasonable that the collisionally-reduced field strength would provide less force.

The bunching effect of the ponderomotive force may be seen from the plot of Figure 2.4 in the region of standing waves. Just before the critical layer, the force reaches a maximum, and then decays as the critical layer is crossed (Lindl & Kaw, 1971).

Thus, as a result of the inclusion of the magnetic field term in the force on an electron, a radiation pressure has been described which is directed toward the regions of decreasing field strength. For the case of a plane wave incident on a slab plasma, a force is exerted on the critical layer in the direction of the propagating beam.

If this radiation pressure is applied to a plasma of low kinetic pressure, actual pushing in of the critical layer and associated steepening of the density gradient in the region of the critical layer is predicted. This effect, called "profile modification," becomes important when the plasma kinetic pressure does not vastly exceed the radiation pressure. The field strength parameter, η_0 , defined as the ratio of the maximum oscillatory velocity of the electron quivering in the incident radiation field to its thermal velocity, is often used to express this condition. In calculation

of the field strength parameter near the critical layer, both the collisional absorption and the electric field swelling should be accounted for. Near the critical layer, η_0 is given by:

$$\eta_0 = \frac{v_{osc}}{v_{th}} = \frac{|eE/m\omega|}{\sqrt{\theta_e/m}}$$

The electric field, E , is to be calculated from its swollen and damped vacuum value in the manner described in the previous section. In the WKB approximation, η_0 is given by the formula

$$\eta_0 \approx 1.6 \times 10^{-6} (I/\theta_e)^{1/2} L^{1/6} \lambda^{5/6} \exp(-5.9 \times 10^{-2} \frac{\ln Z \ln \Lambda}{\theta_e^{3/2}})$$

I = intensity (W/cm^2)

θ_e = electron temperature (eV)

L = scale length (μ)

λ = wavelength of radiation (μ)

n = electron density (cm^{-3})

Z = ionization state

Λ = Spitzer's Λ - ratio of Debye length to distance of closest approach

This formula was obtained by expressing the electric field in the plasma in terms of the field swelling and the collisional attenuation of the incident radiation, and expressing the collision frequency by

$$v_{ei} = \frac{Z \ln \Lambda}{10} \frac{\omega_p}{g}; \quad g = \frac{4}{3} \pi \lambda_D^3$$

The steepening of the density profile by high-intensity laser radiation has been indicated in numerical simulations (Estabrook, Valeo, & Krueer, 1975). The result of the steepened profile is predicted to be the enhancement of resonant absorption at larger angles of incidence and the inhibition of parametric instabilities at the critical surface.

For radiation incident over a finite-sized spot, such as at the focus of a laser beam, a gradient in field points from the edge toward the centerline of the incident beam. A component of the ponderomotive force is thus expected to be directed from the center to the edge of the beam. As a result of this outward force, the plasma may be pushed sideways out of the beam to some extent, again determined by the opposing thermo-kinetic pressure. The beam may then be refracted to the regions of lower plasma density created by this pushing-out process and actually focused in the plasma by this means. This mechanism is given the name of the self-focusing instability. A related phenomenon occurs for radiation incident along density perturbations. The regions of higher density tend to

refract the beam into regions of lower density, breaking the beam into filaments. This effect, the filamentation instability, and the similar self-focusing instability have rather low thresholds compared to the other parametric instabilities. In fact, the only mechanism that provides a threshold at all is the imperfect Debye shielding, which provides an electric field force that must be overcome by the ponderomotive force. The threshold for occurrence of filamentation into striations of wavenumber k_1 , where $k_1 = 2 / (\text{spacing between filaments})$, is

$$(v_{\text{osc}}/c)^2 = 4(1 + \theta_i/\theta_e)k_1^2\lambda_D^2$$

(Chen, 1973)

Application of this formula to the experiment at hand indicates that the intensity utilized was about a factor of ten over this threshold for the lowest order perturbation of the spatial extent of the focal spot. However, the growth rate for this instability is rather low when compared to growth rates for stimulated scattering.

A related effect caused by high incident intensity is the rippling of the critical surface. Numerical simulations suggest that the critical surface may be altered from a planar shape to a series of surface ripples as the profile is steepened (Valeo & Estabrook, 1975; Stark et al., 1976). Thus, a variety of incident

angles arises and therefore, specular reflection is spread out into the entire 2π solid angle of the backward direction. This rippling is indicated for radiation polarized perpendicular to the plane of incidence and occurs on a scale comparable to the vacuum wavelength of the incident radiation.

In the earlier discussion of resonance absorption, no limitations on the energy of the resonantly-driven plasma wave were presented. For the case of a warm plasma, thermal convection limits the wave amplitude. For a cold plasma with no convection out of the heated region, it is conceivable that the amplitude of the electron motion,

$$\xi = \frac{eE}{m(\omega^2 - \omega_p^2(z) - j\nu_{ei}\omega)}$$

could become quite large. In fact, for $\nu_{ei} = 0$ and $\omega = \omega_p$ (at the critical layer), the expression for the amplitude becomes infinite. However, cold-plasma wavebreaking is a means to remove the energy from the heated region.

The formal definition sets the condition for wavebreaking to be when $|d\xi/dz| = 1$. This corresponds to the condition that adjacent particles occupy the same position. Another interpretation is that the oscillatory velocity of the electrons exceeds the velocity

of the plasma waves. A velocity for electron wave-breaking may be expressed by application of the formal wavebreaking condition (Estabrook, Valeo, & Kruer, 1975):

$$v_{br} = (2v_{osc}\omega L)^{\frac{1}{2}}$$

When wavebreaking occurs, the electrons are propelled at velocities of up to $2 v_{br}$ away from the resonant region. Thus, a fraction of the incident laser energy is converted to a high-energy distribution of electrons.

From the standpoint of laser fusion experiments, this high-energy electron distribution can have severe implications. In the attempt to achieve compression of a fuel pellet, a tail of high-energy electrons can deposit some energy in the core of the pellet and heat the core (preheat), thereby reducing compression. A classical analysis predicts that at longer wavelengths, the critical density of the target plasma occurs at a greater distance from peak density, so this acceleration mechanism can preheat a large volume of the plasma inside the critical layer. At shorter wavelengths, the incident radiation will penetrate to higher density before reaching the critical layer and beginning the resonant acceleration mechanism.

However, inclusion of profile steepening by the ponderomotive force can change this (Giovanielli, 1976).

By steepening of the profile, the critical scale length, L , is decreased. The maximum velocity of the hot electrons, $2v_{br}$, is proportional to the square root of the scale length, L , so this energy may be reduced in the event of profile modification. Because the onset of profile modification occurs at lower intensities for longer wavelengths, it is unclear how the hot electron energy behaves as a function of wavelength. This question is under active consideration in the laser fusion community.

Another example of wavebreaking pertains to the ripples mentioned as occurring on the critical surface in the presence of incident laser radiation. The same wavebreaking condition may be applied to predict the occurrence of a distribution of high-energy electrons upon the breaking of the peaks of the ripples into density fingers.

The presence of high-energy electrons may be used as a diagnostic of the resonant acceleration mechanism. An experiment indicates the appearance of high-energy electrons in the plane of polarization and at 60° to the direction of radiation incident on a gaseous target (Kolodner & Yablonovitch, 1976). The application of the cold plasma wavebreaking condition to the electron energy indicates concurrence between the predicted and observed electron energies.

There exists a mechanism for the production of high magnetic fields in a plasma illuminated by laser radiation (Brueckner, 1974). In the event of laser illumination, a pressure gradient is formed, which can cause charge separation and an associated electric field:

$$eEn = -\nabla(n\theta_e)$$

Using Maxwell's equations, one infers that this electric field can contribute a large magnetic field for non-parallel temperature and density gradients:

$$\frac{\partial B}{\partial t} = \frac{c}{en} \nabla \theta_e \times \nabla n$$

The magnetic field arising from this effect may exceed several megagauss in a laser-heated pellet and may modify transport coefficients in the heated region. In particular, thermal conduction across magnetic field lines is severely inhibited, leading to localized hot spots in the plasma which can then lead to hot ions leaving the region (Craxton & Haines, 1975).

Another absorption effect that exhibits intensity dependence is inverse bremsstrahlung (collisional absorption). At low intensities, the energy absorption fraction due to collisions may be expressed as the difference between incident and reflected intensities:

$$F = 1 - R = 1 - \exp\left(-\frac{32 v_{ei} L}{15 c}\right)$$

The electron-ion collision frequency is given in the low intensity limit by the proportionality:

$$v_{ei} \propto n^2/\theta_e^{3/2}$$

In the case of high incident intensity, the oscillation velocity enters into the expression for the collision frequency as it contributes to the expression for the energy per electron:

$$\frac{3}{2} \theta_e \xrightarrow{I \rightarrow \infty} \frac{3}{2} \theta_e + \frac{1}{2} m \langle v_{osc} \rangle^2$$

So in the case of high intensity, the absorption coefficient is multiplied by a factor that depends on η_0 , the ratio of oscillatory velocity to thermal velocity:

$$F = 1 - \exp\left(-\frac{32 v_{ei} L}{15 c} G(\alpha)\right)$$

$$\alpha = \frac{1}{6} \eta_0^2$$

The function G is a decreasing function of α , with a value of one at $\alpha = 0$. The particular form of G varies among various authors, but a typical form (Kruer et al., 1976) has values as indicated:

<u>α</u>	<u>$G(\alpha)$</u>
0.00	1.00
0.17	0.50
0.33	0.30
0.50	0.25
0.67	0.20
0.83	0.15
1.00	0.10

Thus, at high intensities, collisional absorption is decreased by the motion of the oscillating electrons, leading to a nonlinear dependence of the bremsstrahlung absorption coefficient on incident intensity. Furthermore, the profile steepening which is postulated at high frequencies results in a decrease in L and a subsequent reduction of the absorption fraction.

The preceding discussion has treated some effects either predicted or observed at high incident laser intensities. The phrase "high intensities" has been indicated to mean field strengths sufficient to impart a maximum oscillatory velocity to the electrons that approaches or exceeds their thermal velocity. The ponderomotive force, which results from the effects of the electromagnetic wave's magnetic field, may cause density profile steepening in the region of the

critical layer, and it can also push the plasma into density striations to produce filamentation of the beam. The rippling of the critical layer may expose the plasma to a variety of incident angles of radiation, enhancing resonant absorption, and may distribute the backscatter radiation over a wide range of angles. Resonant absorption results in "anomalous" heating, that is, conversion of radiation energy into plasma energy, which, in turn, is converted to particle energy from wave damping. This energy absorption method is distinguished from the classical process of collisional absorption, which has been seen to become less efficient at high intensities. The particles heated by this wave damping may be accelerated greatly, and may carry away much of the incident laser energy in a high-temperature distribution. Intense magnetic fields generated by $\nabla n \times \nabla \theta$ may inhibit thermal conduction and cause hot spots, which may accelerate ions from the region.

Before leaving the discussion of laser-plasma interaction at high intensities, a discussion of hydrodynamic energy transfer, particularly the physics of shock waves, will be presented because of its relevance to the experimental results.

2.3 Hydrodynamic energy transfer

The ideas set forth in this section are the highlights of a more detailed treatment of gas dynamics in general and shock waves in particular, presented in Appendix C and based on the work of Zel'dovich and Raizer (Zel'dovich & Raizer, 1966).

The speed of propagation of an acoustic disturbance in a fluid increases with the pressure. Therefore, if a mechanism, such as a piston or a laser beam, acts to compress an extent of fluid (gas or plasma) suddenly, the pressure at the piston face becomes higher than the equilibrium pressure, and a disturbance begins to propagate at a velocity greater than the acoustic speed. Meanwhile, at a point that is a bit farther away from the piston, the pressure is not so far above equilibrium value, and a disturbance from this point propagates more slowly, and is soon overtaken by the disturbance from the higher pressure region. Thus, the tail of the wave overtakes the head. This results in a shock wave, which is a discontinuous jump in flow variables (density, pressure) over a very short distance.

In the event of nonzero thermal conductivity in this shock front, the front thickness, Δx , for a weak shock is given by

$$\Delta x \approx \frac{\ell_{th}}{(n_1/n_0) - 1}$$

where n_0 is the equilibrium density, n_1 is the higher density behind the shock front, and ℓ_{th} is the thermal mean free path.

The Hugoniot relation expresses the pressure and density on one side of the shock in terms of the pressure and density on the other side. In the event that energy was deposited from an external source, Q , the ratio of equilibrium pressure, p_0 , to final pressure, p_1 , achieved after the shock passes, is given for the ideal gas by

$$\frac{p_1}{p_0} = \frac{(\gamma+1)V_0 - (\gamma-1)V_1 + 2Q/p_0}{(\gamma+1)V_1 - (\gamma-1)V_0}$$

$$V_0 = 1/n_0$$

$$V_1 = 1/n_1$$

$$\gamma = \text{ratio of specific heats}$$

The radius of a shock front propagating from a point of explosive energy deposition of amount Q into a homogeneous infinite medium of density ρ_0 is given as a function of time by the Taylor-Sedov expression for a strong shock:

$$R(t) \approx 1.1(Q/\rho_0)^{1/5} t^{2/5}$$

This expression assumes that observation is made "sufficiently far" from the center.

The preceding statements are general to any gas. For the particular case of a plasma, the ions are heated much more quickly than the electrons during the passage of a shock front, due to their higher viscosity. The electrons are then heated by collisions with the ions after the shock front has passed. This results in a relaxation region behind the shock front, in which the electrons equilibrate with the hotter ions. The thickness of this region is approximated by

$$\Delta x_R \approx D\tau_{eq}$$

D = speed of front propagation

τ_{eq} = electron-ion equilibration time

Also peculiar to a plasma is the temperature-dependent thermal conductivity. This allows the existence of a thermal front, or sharp temperature boundary. In the case of spherically-symmetric expansion from a point of energy deposition in a plasma, the radius of the thermal front, r_f , increases as a function of time:

$$r_f \propto t^{2/19}$$

The thermal wave generally starts out at a velocity far above the acoustic velocity in the medium, and slows as it expands. When the wave has slowed to a point

where its velocity is equal to the acoustic velocity, it can cause fluid motion in the manner of a shock wave.

A number of effects which are associated with the high-intensity irradiation of a solid target in a background gas exhibit many of the physical mechanisms associated with shocks in a plasma. The illumination of a solid target in a background gas can produce a laser-supported detonation wave, which propagates from the solid toward the laser as an ionized, absorbing front. A shock wave, followed by a deflagration wave, may be sent into the target, and subsequent blowoff of a portion of the target that is much larger than the focal spot of the incident beam occurs (Bobin, 1971; Rehm, 1970). The Bouguer number, or $(\text{plasma dimension})/(\text{radiation absorption length})$, and the Boltzmann number, or $(\text{energy flux convected from the interaction region})/(\text{energy flux incident on region})$, characterize the extent of expansion and the manner of velocity scaling to the incident energy (Dyer, 1973). Since many of these effects arise from ionization of the target by the beam and do not apply to a fully-ionized plasma, and since no appreciable background gas surrounded the target plasma, the analysis of the experimental results does not include these mechanisms.

When dealing with large amounts of energy being

quickly deposited in small regions, thermal diffusion out of the region becomes important. The concept of flux-limiting sets an upper bound on the energy flux out of the heated region in terms of the thermal velocity of the electrons in the region. The internal energy in a heated region, $3n\theta/2$, cannot flow out of that region any faster than the electron thermal velocity, $v_{th} = \sqrt{\theta_e/m}$. This statement sets the condition that

$$\phi_{max} = \beta n \theta_e (\theta_e/m)^{1/2}$$

where β is a number of order unity that characterizes the energy carried by a Maxwellian distribution. For temperature in eV and density in e^-/cm^3 ,

$$\phi_{max} = 5.4 \times 10^{-12} n \theta_e^{3/2} \text{ W/cm}^2$$

At high incident intensities, flux-limiting sets a limit upon the amount of energy that can be removed from a heated region by thermal diffusion, whereas at low intensities, the convective flux is approximated by Fourier's Law:

$$\phi = \kappa \nabla \cdot \theta_e$$

κ = thermal conductivity

Summary. - This chapter has presented some physical models to be used in interpretation of the

experimental results. Total reflection of electromagnetic radiation by a critical layer was seen to occur only in the non-physical limit of low intensity, no magnetic field, no collisions, and infinite density gradient. By examination of electromagnetic field properties in a plasma of linear density gradient, the mechanisms of field swelling and collisional damping were represented in a WKB approximation. At high intensities, the appearance of the ponderomotive force was described and quantified, both in the WKB region and at the critical layer. Profile modification by the ponderomotive force was predicted to alter energy absorption from the classical expectation. The effect of profile modification on hot electron production by wavebreaking was discussed, as was the reduction of collisional absorption at high intensity. The spontaneous production of high magnetic fields was seen to affect thermal conductivity. Finally, a discussion of hydrodynamic energy transfer detailed the appearance of a shock front propagating from the point of energy deposition and described the concept of flux-limiting.

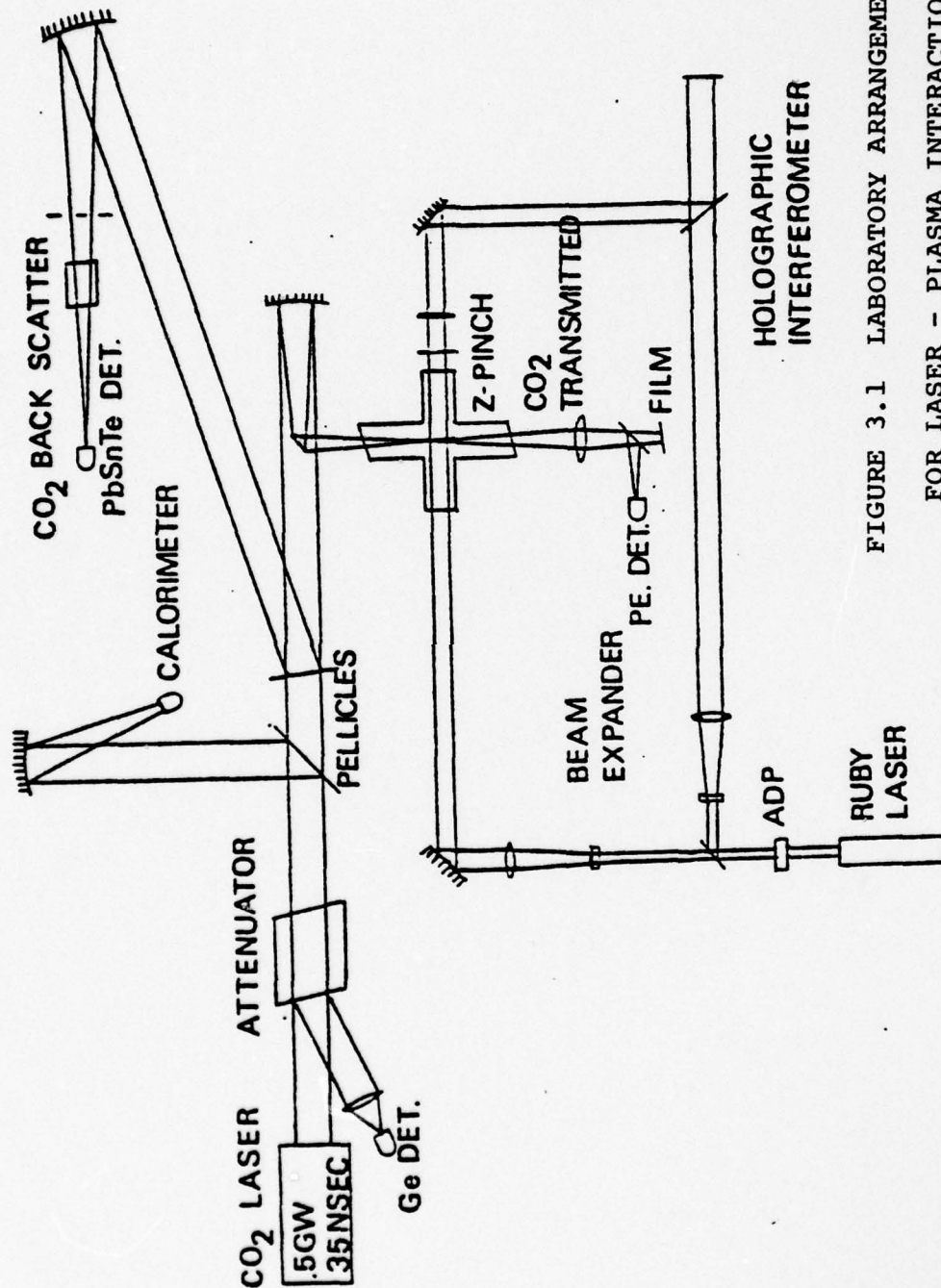


FIGURE 3.1 LABORATORY ARRANGEMENT
FOR LASER - PLASMA INTERACTION
EXPERIMENT

CHAPTER THREE

EXPERIMENTAL APPARATUS AND PROCEDURE

3.1 Summary

A description of the experimental arrangement is most succinctly presented in Figure 3.1, which is a top view of the laboratory showing the location of the plasma source, the CO₂ laser, the holography system, the backscatter optics, and the transmitted beam diagnostics. The following section is a brief summary of the experimental apparatus, with a more detailed description set forth in the remainder of the chapter.

The plasma was produced by a small coaxial linear Z-pinch discharge atop a 13.4 μ F energy storage capacitor. A triggered spark gap provided low-jitter switching, and current paths were designed for minimization of inductance. Around the waist of the vertical column were four arms with optical-quality ports for entrance and exit of the CO₂ and holographic interferometer laser beams.

The CO₂ laser was a Lumonics Model 601A, with a maximum output of 17 J in a gain-switched spike of 78 nsec FWHM. The beam passed through a calibrated

gas-filled attenuation cell and focused radially on the plasma column to a diffraction-limited spot with a central disc diameter of $125\ \mu$. The focusing was obtained with a modified Newtonian imaging system consisting of a large copper focusing mirror and a small flat deflection mirror. The beam left the unstable resonator laser cavity in a nearly annular intensity distribution, with a vertical dimension of 11 cm and a horizontal dimension of 8.5 cm, and a central shadow that was 5.7 cm by 4.5 cm.

Along the optical path to the focusing system were two beamsplitters, one to deflect a portion of the incident CO_2 beam to an energy monitor, and one to send a portion of the returning backscattered radiation to another copper focusing mirror. This mirror focused the backscattered beam onto a lead-tin-telluride infrared radiation detector.

After focusing into the Z-pinch target chamber through a second ZnSe flat, the exiting CO_2 beam was gathered by a KCl lens and refocused. Between the KCl lens and its focus was an NaCl beamsplitter, which sent a fraction of the converging beam to a pyroelectric detector. This pyroelectric detector comprised the transmitted pulse shape monitor. The remainder of the beam, transmitted through the NaCl beamsplitter, was incident on a piece of exposed Polaroid film placed 2 cm

inside the focus. The burnspots on this film comprised the spatial characterization of the transmitted beam.

Holographic interferometry was accomplished by frequency-doubling the output from a modified Korad ruby laser. The pulse width was 16 ns, and modifications to the laser provided increased spatial and temporal coherence to a coherence length of over one meter. The scene beam passed through the waist of the plasma column perpendicular to the incident CO₂ beam, and the plasma was imaged with a lens to a point about 15 cm in front of a 2" x 2" holographic plate to achieve a magnification of three.

Timing monitors included a photon drag detector that determined time of CO₂ beam incidence, a PIN diode that determined time of holography, and a second PIN diode which determined time of plasma pinching.

Optical alignment of the CO₂ beam was achieved by staining the beam path with a HeNe alignment laser beam. The alignment beam allowed proper placement of the Newtonian imaging elements and allowed placement of beam focus. When a perforated mask was placed in the alignment beam, a Fraunhofer pattern was observed on a screen placed at the focal point in the target chamber. The pattern allowed longitudinal placement of the focus. Lateral positioning was effected by firing the discharge and photographing the plasma,

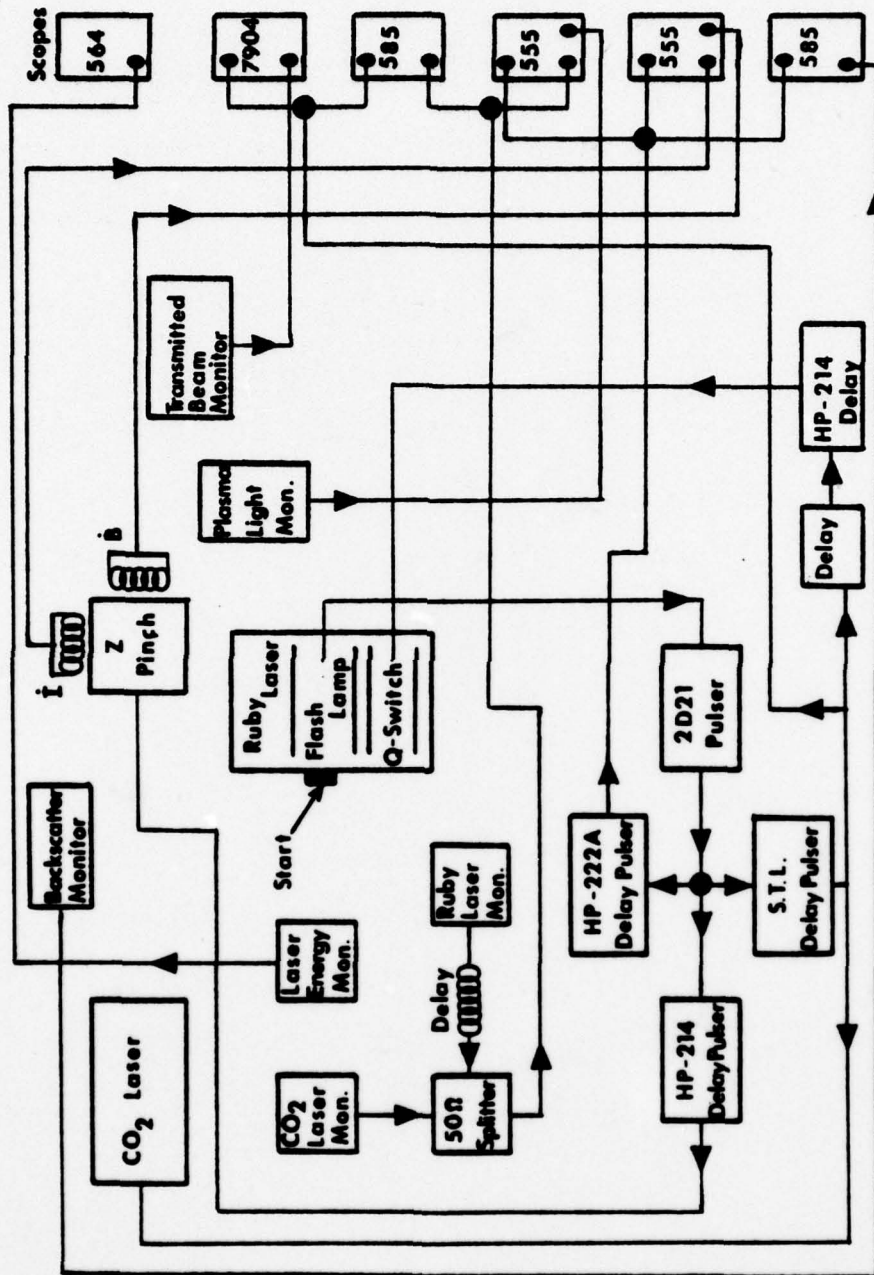


FIGURE 3.2 DIAGRAM OF TIMING ELECTRONICS FOR LASER-PLASMA INTERACTION EXPERIMENT

imaged onto a transparent graticle, with a streak camera viewing the exit CO_2 beam port. An image of the CO_2 focus, obtained by a series of relay lenses, allowed positioning of the focal spot to the plasma location noted on the scale.

Timing of the two lasers, scope triggers, and discharge initiation was achieved electronically. A bank of delay generators and pulsers provided variable timing of CO_2 and holographic beam incidence on the evolving plasma (Figure 3.2). Calibration of the various timing devices was verified before each run and during each run by common optical pulses from the holography laser placed on the two PIN diode detectors. The CO_2 monitor and holography timing monitor, the latter of which was passively delayed by 94 nsec, were mixed and displayed on the same oscilloscope trace.

Having summarized the main points of the experimental arrangement, a more detailed description of the plasma source, the CO_2 optics, the holography procedure, and the method of performing the experiment is presented.

3.2 Z-pinch

The more detailed description of the experiment begins with a treatment of the Z-pinch. The design and construction of the Z-pinch, much of the CO_2 optical

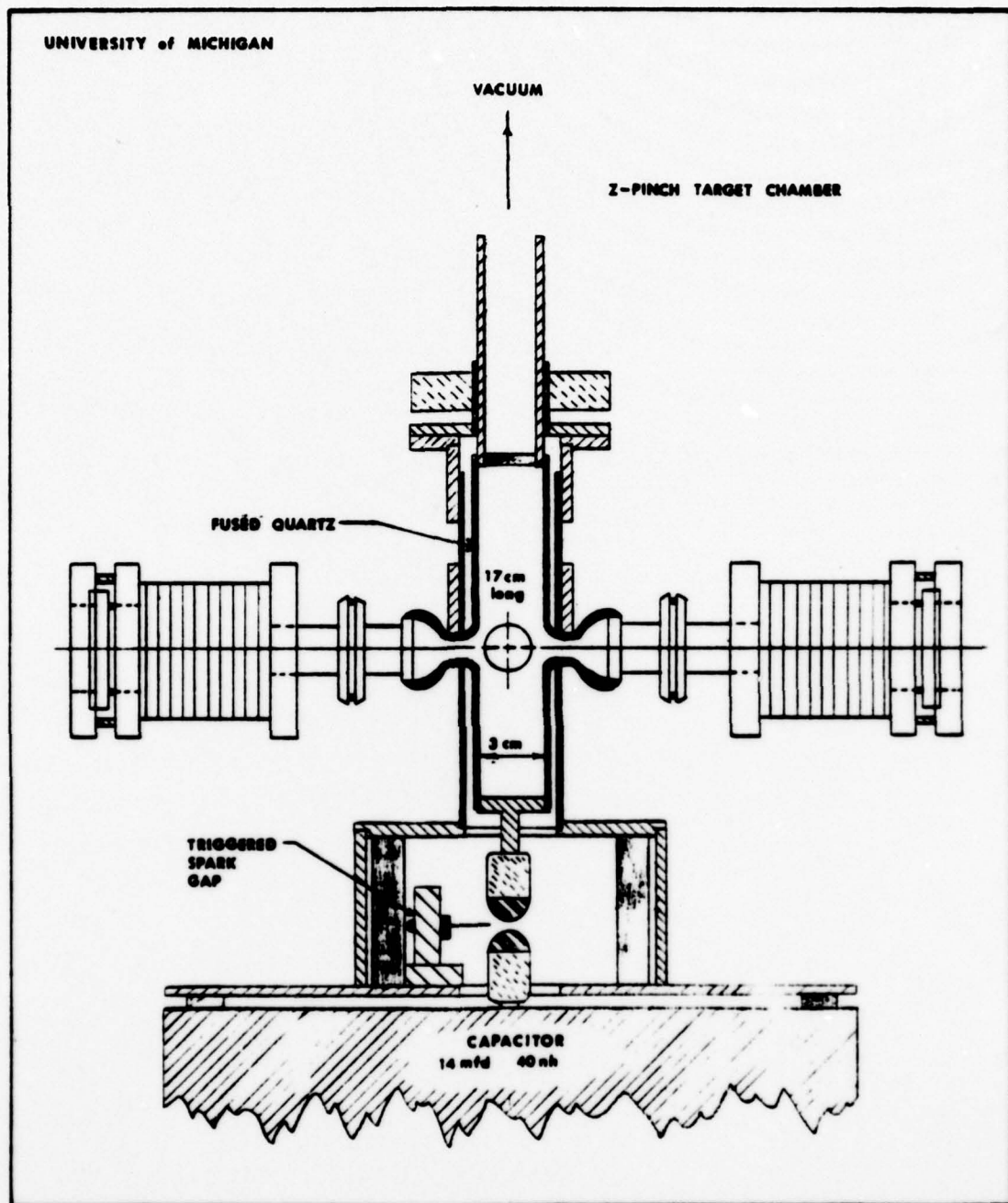


FIGURE 3.3 SKETCH OF Z-PINCH TARGET CHAMBER

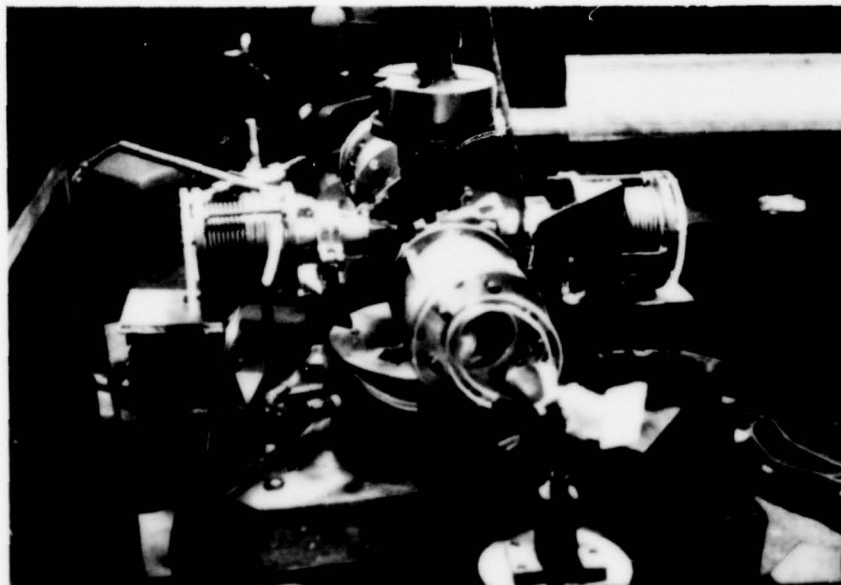


FIGURE 3.4 PHOTOGRAPH OF Z-PINCH TARGET CHAMBER

system, and the holographic interferometer are discussed in great detail elsewhere (Steel, 1976; Rockett, 1977a; Steel et al., 1977), so for improved portability of this volume, elaboration upon these items will be kept to a strict minimum.

The Z-pinch discharge was initiated in a quartz cylinder, 1.5 cm radius by 17 cm length, with four ports equally spaced about the midsection of the column (Figure 3.3). The chamber was mounted upon a Sangamo energy storage capacitor (13.4 μ F, 30 nH, 20 kV max). The discharge was fired by a triggered spark gap coaxially positioned between the capacitor and the bottom electrode of the vertical discharge cylinder. As seen in Figure 3.4, the ports were fabricated from bellows and clamps that facilitated removal of each port. A two-inch optical flat was affixed at the end of each port, allowing beam entrance and exit. For the two ports associated with entrance and exit of the holography beam, optically flat windows of fused silica were used to pass the ultraviolet wavelength, and for the CO₂ beam entrance and exit ports, ZnSe comprised the pair of flats.

The chamber was evacuated from the top by a standard combination of a roughing pump and an oil-diffusion pump. Experiments were run with 1.4 Torr helium as a fill gas, measured by a mechanical-diaphragm

pressure gauge.

The original Z-pinch triggered spark gap exhibited unacceptably large jitter for this experiment, for running the experiment required the timing of two lasers to a point along the plasma discharge evolution. To minimize the 150 nsec uncertainty in time of the firing of the triggered spark gap, a small study was undertaken to first ascertain that it was the spark gap, rather than the triggering electronics, that was providing the uncertainty. After this verification, an attempt to incorporate a commercially-built spark gap (Physics International) into the Z-pinch design met with failure. The commercial pressurized spark gap exhibited deposition of metal vapor from its electrodes inside the pressurized chamber. The deposition, on subsequent shots, provided a current path for premature, untriggered breakdown. This failure mode was believed to result from the high currents and ringing associated with the discharge.

After many attempts to preserve the original configuration of inducing gap breakdown by a voltage pulse capacitively coupled to the upper spark ball, it was concluded to be impossible to improve the temporal reproducibility of that configuration. Then the gap spacing was increased to 0.222" and a tungsten trigger pin was placed midway between the two balls. The high-

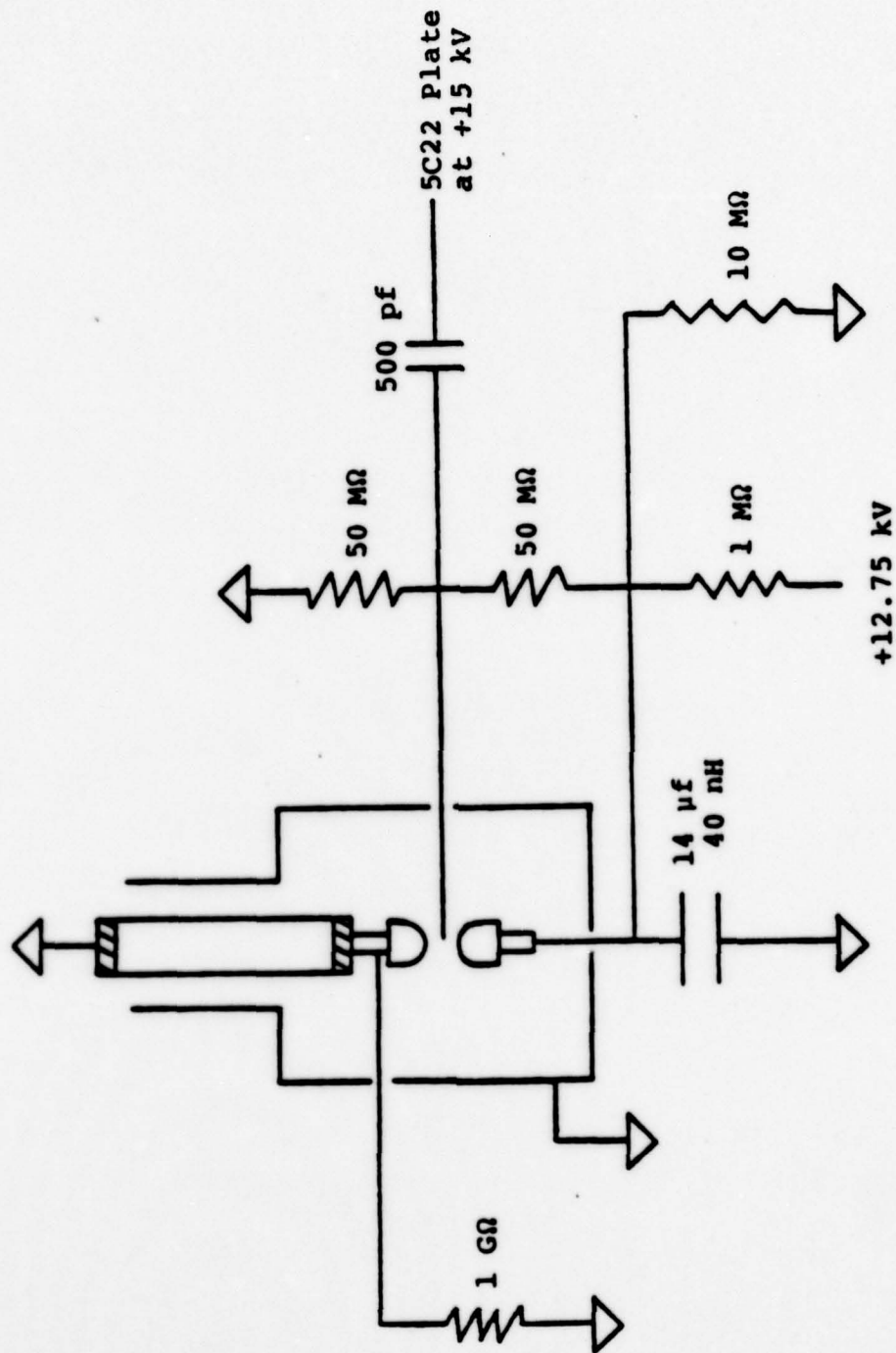


FIGURE 3.5 TRIGGER CIRCUIT FOR Z-PINCH DISCHARGE

voltage negative trigger pulse was then capacitively coupled to the trigger pin, which was biased with a resistive divider midway between the capacitor charging voltage and ground. To further improve reliability, the upper spark ball (lower electrode in chamber) was grounded through a $1\text{ G}\Omega$ resistor. In addition, the spark balls were remachined to a shape more characteristic of the Rogowski shape to minimize local maxima in electric field at the edges.

The combination of these alterations (Figure 3.5) provided a spark gap with a firing uncertainty of only 40 nsec, rather than the 150 nsec of the previous design. A 50 kV trigger pulser would be a suggested improvement for added reproducibility.

3.3 CO_2 laser and associated optics

The description of the experimental equipment continues with a discussion of the CO_2 laser. The laser was a Lumonics Model 601A transverse-excitation atmospheric pressure laser. Throughout the experiments described, the laser was run at a gas flow ratio of 9:9:0.25 $\text{He}:\text{CO}_2:\text{N}_2$. This ratio had been found to minimize the occurrence of a long tail pulse following the 38 nsec gain-switched spike. The pulse was temporally characterized as a triangular gain-switched spike of

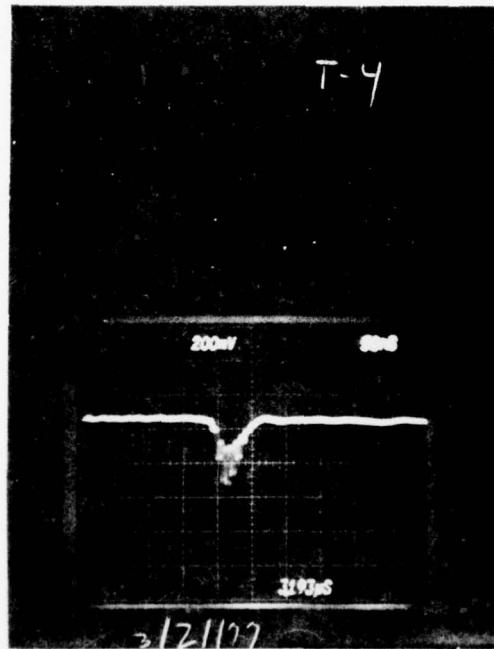


FIGURE 3.6 GAIN-SWITCHED PORTION OF INCIDENT
LASER PULSE (50 nsec/div)

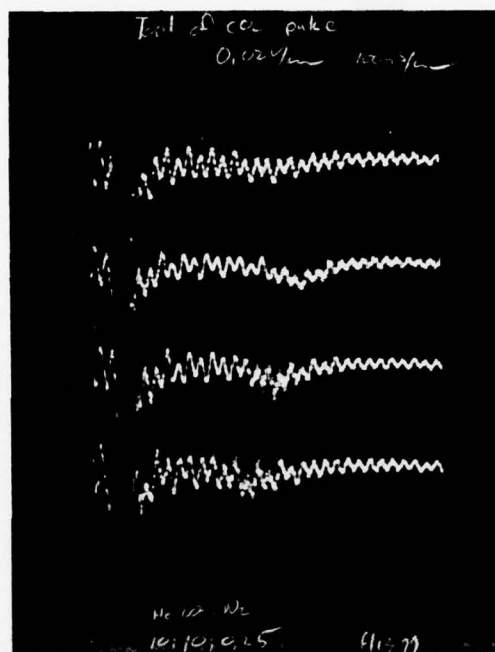


FIGURE 3.7 FOUR CO₂ LASER PULSES, SHOWING
NON-REPRODUCIBILITY OF TAIL
(100 nsec/div)

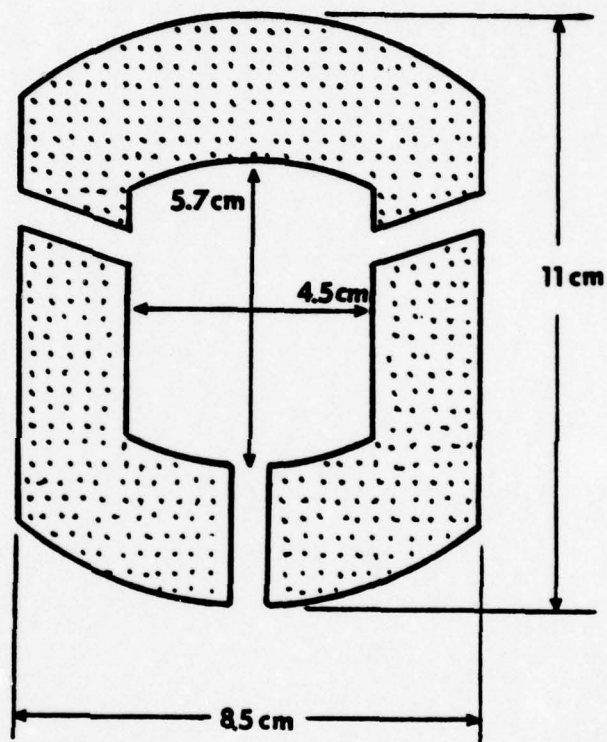


FIGURE 3.8 SKETCH OF ANNULAR SPATIAL DISTRIBUTION OF
ILLUMINATION OF INCIDENT LASER PULSE

AD-A050 773

MICHIGAN UNIV ANN ARBOR LASER PLASMA INTERACTION LAB
CRITICAL LAYER PENETRATION IN A COLD Z-PINCH PLASMA BY HIGH-INT--ETC(U)

F/G 20/9

SEP 77 J G ACKENHUSEN

AFOSR-77-3349

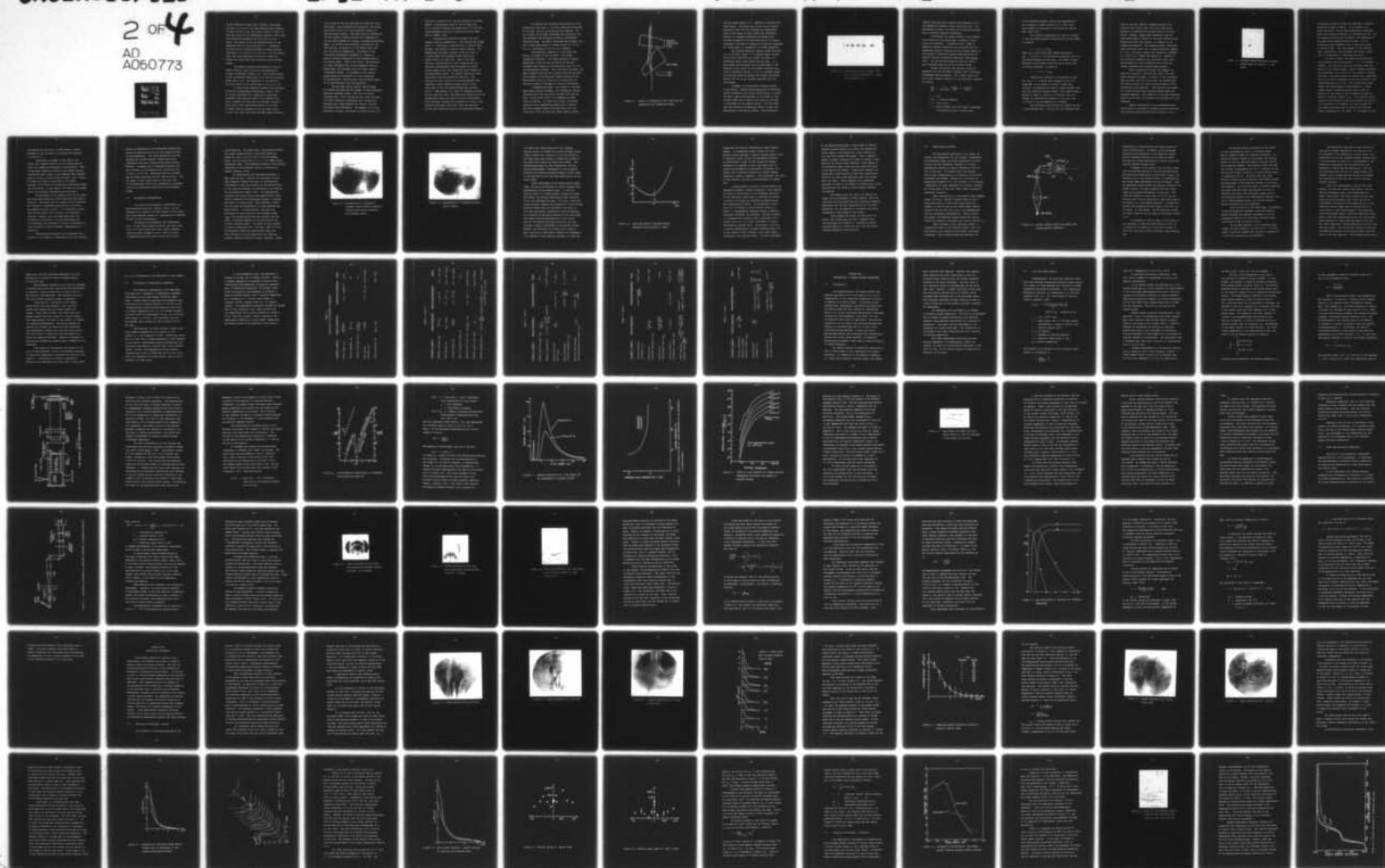
UNCLASSIFIED

LPIL-TR-100

AFOSR-TR-78-0352

NL

2 OF 4
AD
A050773



38 nsec FWHM and 76 nsec base, followed, after about 400 nsec, by a tail of 100 nsec FWHM and peak intensity of about 8% that of the main pulse (Figure 3.6 and 3.7). This tail could not be reproducibly obtained, and in fact went unnoticed throughout the first part of this study. The energy of the gain-switched spike at the specified ratio of flow rates was 17 J. Increasing the flow rate of nitrogen provided an energy increase from about 2 J to over 55 J in the tail, but the greater width and later occurrence of the tail rendered it useless for interaction with the short-lived overdense plasma.

The spatial intensity distribution of the unstable resonator laser cavity was characterized by annular illumination (Figure 3.8). The vertical extent of the illumination region was 11 cm, and the horizontal extent was 8.5 cm. The dimensions of the shadow of the front mirror in the cavity were 5.7 cm by 4.5 cm.

A unique laser alignment procedure was developed during this investigation (Ackenhusen & Steel, 1977). An initial technique was to position a helium-neon alignment laser along the axis of the unstable resonator, coupling the beam into the resonator through a small hole in the large primary mirror at the rear. The HeNe light was expanded by the CO₂ laser cavity to leave the output port with the same spatial distribu-

tion as that of the CO₂ beam when the laser was fired. Previously, crude alignment was effected by deflecting the cavity mirrors in a trial-and-error fashion to maximize output energy. The added accuracy afforded by the new alignment method resulted from inspection of the CO₂ pulse burnspot on a piece of thermally-sensitized paper. By rotating the micrometer adjustment on the front mirror, the position of the shadow within the exit CO₂ beam was symmetrized. Adjustment of the rear mirror micrometers proceeded in a manner to achieve uniform illumination of the burnspot seen on the thermal paper. After a few trials, the direction of mirror adjustment for a given asymmetry could be ascertained, and alignment could be finely tuned in a systematic manner. In alignment by this method, output energy was maximized to a point exceeding the manufacturer's specification, and the pulse length of the gain-switched spike was minimized.

The CO₂ beam optical system, which relayed and focused the beam onto the plasma, is more completely described elsewhere (Steel, 1976) and is briefly discussed here. After leaving the CO₂ laser, the beam was passed through an attenuation cell filled with propylene gas, whose pressure was varied to provide continuous beam attenuation. The chamber, an 8" long horizontal cylinder, was fitted at either end with a 6"

NaCl flat, inclined at 8° , and was mounted on a vacuum system. The reflected image of the CO_2 beam from one of the NaCl surfaces was focused with a 10 cm focal length germanium lens onto a photon drag pulse shape monitor (DeBoo, 1974).

Following the attenuation chamber was an 8" diameter pellicle beamsplitter. The pellicle was formed from 5 μ - thick Mylar, stretched over a circular frame, affixed, then heated to obtain a smooth surface. The beamsplitter directed a portion of the CO_2 beam to a Gentec Model 200 Joulemeter which acted as an energy monitor for each shot. Next in the beam path was a second pellicle, which directed any CO_2 radiation backscattered from the plasma to a gold-coated copper mirror that formed the first element of the backscatter optics. Two severe difficulties were encountered with the backscatter pellicle. The pellicle was very sensitive to the ever-present room vibrations, which imparted sizable motion to the focal spot of the gold-coated backscatter focusing mirror. Additionally, the large (8" diameter) surface was not optically flat, and severe beam distortion of the backscattered image was noted at optical wavelengths. This distortion forbade the attainment of a small, well-defined backscatter focal spot, which was required by the small sensitive area of the backscatter detector.

To minimize the vibration and distortion of the backscatter focal spot, a 1.5° NaCl wedge was positioned in the beam, and the two pellicles were removed. The solid mount of the wedge eliminated the vibrations, and the optically flat surfaces provided an undistorted reflected image. The wedge, purchased from Harshaw, Inc., had a laser-grade polish, a surface figure of $\lambda/10$ at 10.6 μ , a thickness of 0.5", and a 6" diameter.

Unfortunately, dispersion of the wedge made optical alignment of the CO₂ beam to the plasma exceedingly difficult. The wedge imparted an angular deflection to both the CO₂ radiation and the HeNe alignment laser beam, but the deflection angle for the two wavelengths differed. Thus, following the wedge, the HeNe alignment beam was not collinear with the CO₂ beam, and alignment of the Newtonian imaging system and the positioning of the CO₂ focus on the plasma were not directly related to alignment at optical wavelengths.

A compensating wedge, to be placed in the HeNe beam during optical alignment, was designed to deflect the HeNe beam to be once again collinear with the CO₂ path. During actual shots, the compensating wedge would be removed. To obtain this result, the design objective was a compensating wedge angle to deflect the HeNe alignment beam to the same angle with the laser axis as the CO₂ beam made after passing through

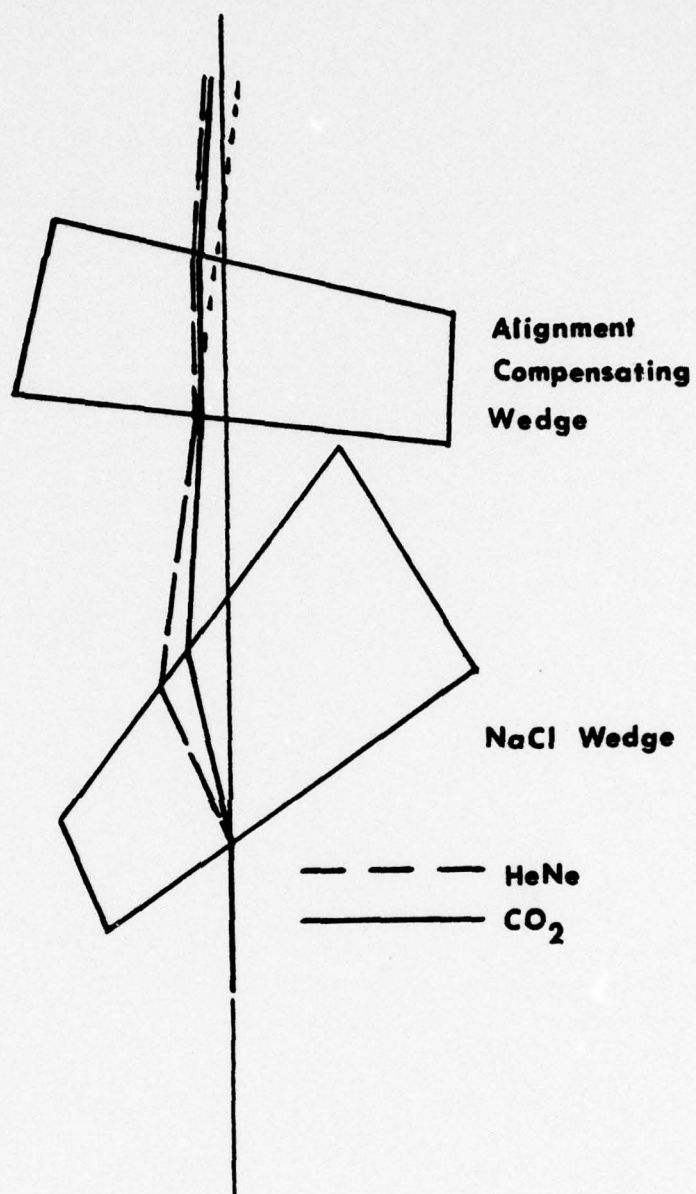


FIGURE 3.9 EFFECT OF DISPERSION OF NaCl WEDGE AND ITS CORRECTION WITH COMPENSATING WEDGE

the NaCl wedge (Figure 3.9). Appendix D discusses the wedge design. Estimates from various optics vendors indicated a cost that far exceeded the experimental worth of the wedge, so this project was terminated. Instead, an alignment technique was devised that involved alignment of the Newtonian optics at visible wavelength, followed by translation of optical components by a known amount to compensate for wedge dispersion.

The modified Newtonian imaging system consisted of a 75 cm focal length 6 in. diameter copper concave mirror which reflected the incident CO_2 beam, in a converging manner, back toward the CO_2 laser. At a point where the converging cone had decreased to the diameter of the "hole" in the incident unstable resonator illumination pattern, a 2.25 in. diameter copper flat was positioned to deflect the further converging beam by 90° out of the incident beam path and into the chamber.

Alignment of the Newtonian focusing system was designed to assure minimum aberration by achieving normal incidence on the large concave mirror, to place the small copper flat precisely in the shadow in the incident beam, and to position the focus of the beam at the center of the plasma location. The CO_2 focal spot was limited by diffraction effects, rather than aberrations in the optical system. The diffraction-

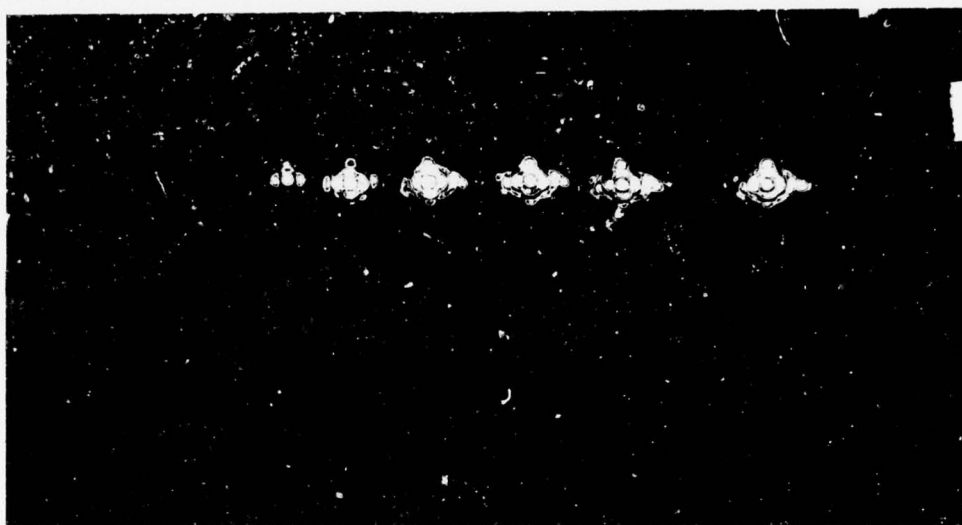


FIGURE 3.10 DIFFRACTION-LIMITED CO₂ LASER FOCAL
SPOT AT SEVERAL INTENSITIES - CENTRAL
DISC DIAMETER OF 125 μ

limited focal spot had a central disc diameter of 125 μ , and exhibited a series of lobes around the disc. The photograph in Figure 3.10 shows the diffraction-limited spot at several different intensities.

To determine the energy fraction in the central disc relative to the entire spot, recourse to calculation was necessary. A simulation by A. Frank of Lawrence Livermore Laboratory had calculated the two-dimensional Fourier transform by the focusing optics of the incident illumination pattern associated with the Lumonics unstable resonator output beam (Frank et al., 1976). His calculations predicted that the central spot contained about 50% of the incident energy.

Further verification was possible using the expression for the far-field intensity from a uniformly-illuminated annular aperture. For a major radius of b and a minor (shadow) radius of a , the far-field intensity is given by

$$\frac{I(x)}{I(0)} = \frac{4}{(1 - \epsilon^2)^2} \left(\frac{J_1(x)}{x} - \epsilon^2 \frac{J_1(\epsilon x)}{\epsilon x} \right)^2$$

$$\epsilon = a/b$$

$$I(0) = \text{on-axis intensity}$$

$$x = (2\pi/\lambda)b \sin \alpha$$

$$\alpha = \text{angle between line from center of aperture to observation point \& optical axis}$$

If the unstable resonator pattern were approximated by an annulus of aspect ratio of 0.5, 50% of the total energy is calculated to lie within the central spot (Judd, 1973).

For uniform illumination of a lens of f-number F , the focal spot diameter containing 85% of the energy is given by

$$d \approx 2.44 \lambda F \theta / \theta_{DL}$$

where θ_{DL} is the diffraction-limited divergence,

$\theta_{DL} = (2.44\lambda/b)$, b is the aperture diameter, and θ is the beam divergence of the laser. The depth of focus, defined by the distance from focus to the first zero in on-axis intensity, is given by

$$l \approx \pm 2 F^2 \lambda \theta / \theta_{DL}$$

Applying the formulas to the problem at hand, for $\theta/\theta_{DL} = 1$, a central disc diameter of 160μ is predicted, so the effect of annular, rather than circular, illumination has been to reduce the spot size but also reduce its energy content. The second formula predicts a depth of field of ± 0.8 mm for the $f/6.3$ system, so longitudinal placement of the focal spot to within 0.5 mm was adequate in alignment.

The converging beam entered the chamber through a zinc-selenide flat. Earlier work had indicated that

this was the only material transmitting both 10.6 μ radiation and visible light that had a high enough strength to withstand the acoustic shock of the discharge. However, copper vapor deposition from the electrodes formed a coating on the inner surface of the entrance and exit ZnSe windows, so cleaning of the windows was required. The cleaning process, performed every ten shots, used 0.06 μ alumina polishing compound in a 90% - 10% water - acetic acid suspension, imbedded in a cloth lap to remove the deposition. Removal of the polishing suspension by a distilled water rinse was followed by a final cleansing with a taut lens tissue, moistened with reagent-grade methanol.

After transmission through the chamber, the beam was collected at the exit port with a KCl lens, which refocused the beam. A portion of the converging beam was split off with a NaCl flat, and focused upon the active surface of a Laser Precision Model kT-1540 pyroelectric pulse detector. This detector was encased in a brass cylinder with a Hewlett-Packard Model 460 wideband amplifier. The bandwidth of the pulse detection system was 150 MHz, and linearity was verified over this bandwidth.

Spatial distribution of the transmitted beam was recorded by incidence on exposed Polaroid black-and-white prints, placed inside the KCl focus by 2 cm. A



FIGURE 3.11 ALIGNMENT STREAK PHOTOGRAPH OF PLASMA
COLUMN IMAGED ON GRATICLE - 2 μ SEC
STREAK

calibration estimate of this film indicated a response threshold of about 10 MW/cm^2 . At an intensity of about 200 MW/cm^2 , the tan burn distribution associated with lower intensity advanced to a yellow-white hue. For an intensity greater than 300 MW/cm^2 , the roughening of the paper due to paper blowoff was seen. All the intensities were incident at the 38 nsec pulse width of the CO_2 laser. The three stages of film response (tan, yellow-white, and roughened) were rather subjective, so calibration by this means was crude.

At time of pinch, the plasma column was about 3 mm diameter, and was positioned in a 3 cm diameter chamber. To locate the focal spot precisely upon the center of the plasma column, a novel alignment technique was discovered. By a series of relay lenses at the CO_2 exit port, the plasma column was imaged with a magnification of 4.6 upon a transparent ruler with vertical lines spaced horizontally by 1 mm. The rule and the plasma column were simultaneously photographed by a streak camera during a discharge of the Z-pinch, and the position of the center of the illuminated column was noted on the scale (Figure 3.11). Thus, the horizontal position of the column on the scale defined the location of the plasma in the chamber, so a beam focused into the chamber was positioned by placing its magnified image, transformed by the lenses, at the proper horizon-

tal position on the scale. In this manner, lateral alignment of the CO₂ beam to the plasma was obtained to within 60 μ .

Longitudinal alignment of the beam to the column first required location of the column position within the chamber by holographic interferometry. Then, a translucent screen was placed at the plasma location. A perforated mask, placed in the expanded HeNe alignment beam at a point in front of the CO₂ laser, cast a series of concentric rings on the screen at the plasma position if the focus of the Newtonian system were located upon the screen. In this manner, the focus of the copper mirror was precisely positioned upon the plasma.

The placement of the diagonal flat and the lateral and longitudinal position of the focus were thus easily attained. Fortunately for the success of this technique, the location of the plasma column did not vary within the chamber from shot to shot. If the pellicle, rather than the NaCl wedge, were in place, this technique sufficed. However, with the wedge positioned, the difference in ray paths at the two wavelengths had to be measured, and alignment at optical wavelengths was then followed by a known adjustment compensating for dispersion.

The backscatter detector was illuminated with a fraction of the radiation backscattered into the focusing

optics, as determined by the backscatter beamsplitter. Either the Mylar pellicle or the salt wedge was used as the beamsplitter. The image provided by the beamsplitter was focused through a second gas-filled attenuation cell onto a lead-tin-telluride infrared detector. Alignment of the backscatter detector was very critical, as the detector had a sensitive area of only $3.6 \times 10^{-3} \text{ cm}^2$. Meaningful data was obtained only on those shots with the NaCl wedge in place. With the wedge in place, positioning of the focal spot on the backscatter mirror was accomplished by maximization of the backscatter signal from an air-breakdown plasma.

3.4 Holographic interferometer

The system for holographic interferometry has been described previously (Rockett, 1977a), so this description is limited to a brief account of the system and a more detailed account of a reconstruction procedure devised in this investigation.

Holographic interferometry was accomplished with a 16 nsec FWHM frequency-doubled ruby laser pulse (347.2 nm) from a Korad ruby laser, whose coherence length had been extended to over 1 meter by use of a temperature-controlled front etalon and an intra-

cavity aperture. The object beam, after passing through the plasma, passed through a lens which imaged the plasma at a point 15 cm in front of the holographic plate. The film plate was a 2 in. x 2 in. Kodak 120-02 holographic plate. The alignment procedure of the optical components in the holography system is described by Rockett (Rockett, 1977a).

In reconstructing the developed holograms, a HeNe laser was used. Because the wavelength of hologram formation differed from that of reconstruction, a difference in both the location and the magnification of the image was expected, as indicated by the formulas for the wavefronts (Smith, 1975). To experimentally ascertain both image location and magnification, after optical alignment of the holography system, a hologram was taken of a known target. This provided a record that was used for determination of image position and magnification. In reconstruction, the plate was positioned to allow viewing of the conjugate image (i.e., the reconstruction beam was directed upon the plate in direction opposite to the direction of the original reference beam). The image was then located by moving a comparator with a very small depth of field longitudinally along the reconstructed image axis until diffraction fringes associated with improper imaging, appearing around the target, vanished. Figure

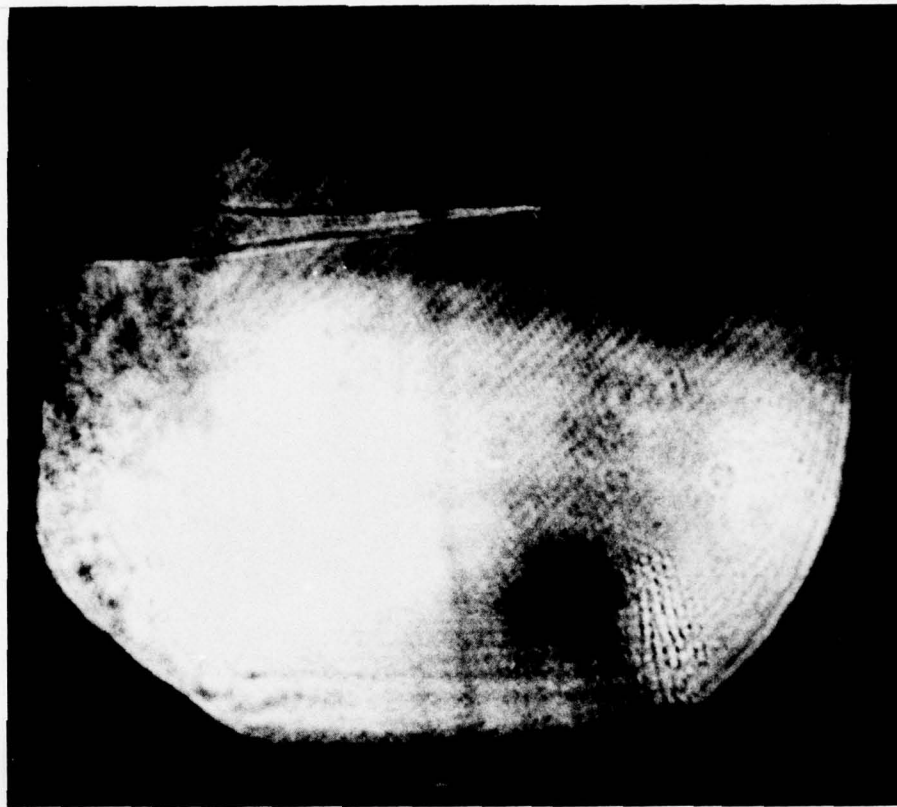


FIGURE 3.12 RECONSTRUCTION OF HOLOGRAM OF
ALIGNMENT TARGET SHOWING DIFFRACTION
FRINGES AROUND TARGET ASSOCIATED
WITH IMPROPER IMAGING

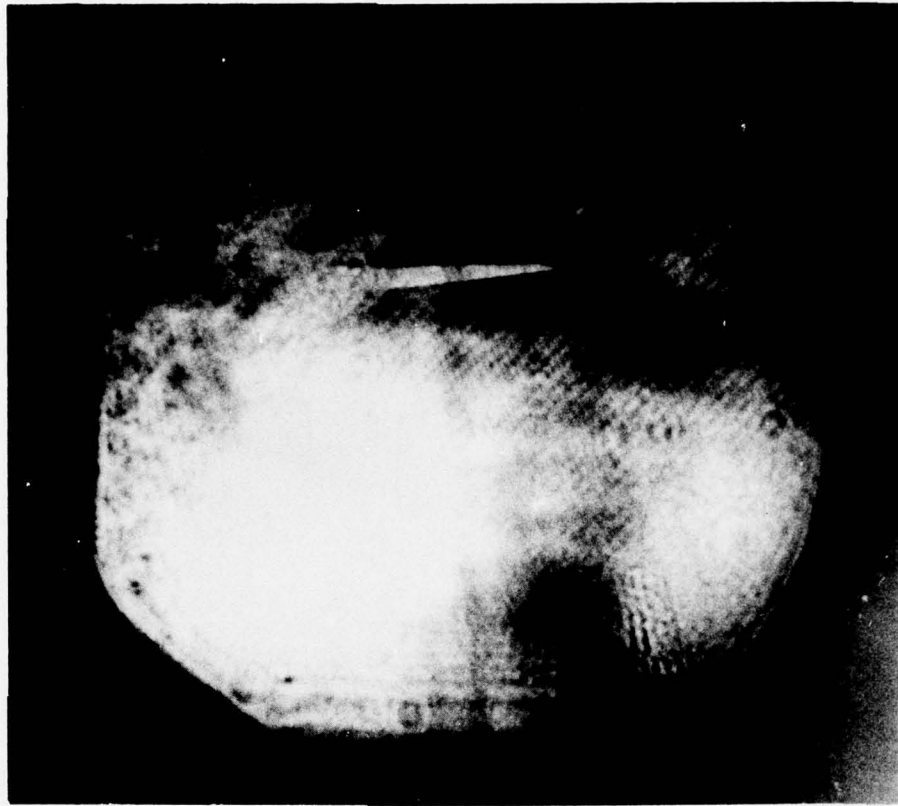


FIGURE 3.13 RECONSTRUCTION OF ALIGNMENT HOLOGRAM,
IMAGED PROPERLY

3.12 shows the fringes associated with improper imaging; Figure 3.13 shows the correctly-imaged target. A small screen with a cross on it was then placed at the image plane just located, a camera was focused on the cross, and finally the screen was removed. The reconstructed image was thus focused onto the film, and was photographed. Replacement of the alignment hologram with plasma holograms produced a plasma image at the same point and of the same magnification as the target image.

After photography of the reconstructed plasma image, the print was enlarged to obtain nineteen times magnification of the plasma column. To read the vertical shift of a fringe passing through the column and extract the electron densities by Abel inversion, one of two techniques was used. The first, fractional fringe reading, required the following of a given fringe from the vacuum region at the edge of the field of view into the plasma, recording its vertical position as a function of horizontal position on the film plate. This method afforded determination of the fringe shift at any desired horizontal position, and thus provided a density measurement at any desired radius. However, the following of a fringe over a range of axial positions in this manner required the assumption of an absence of axial density gradients, so that the

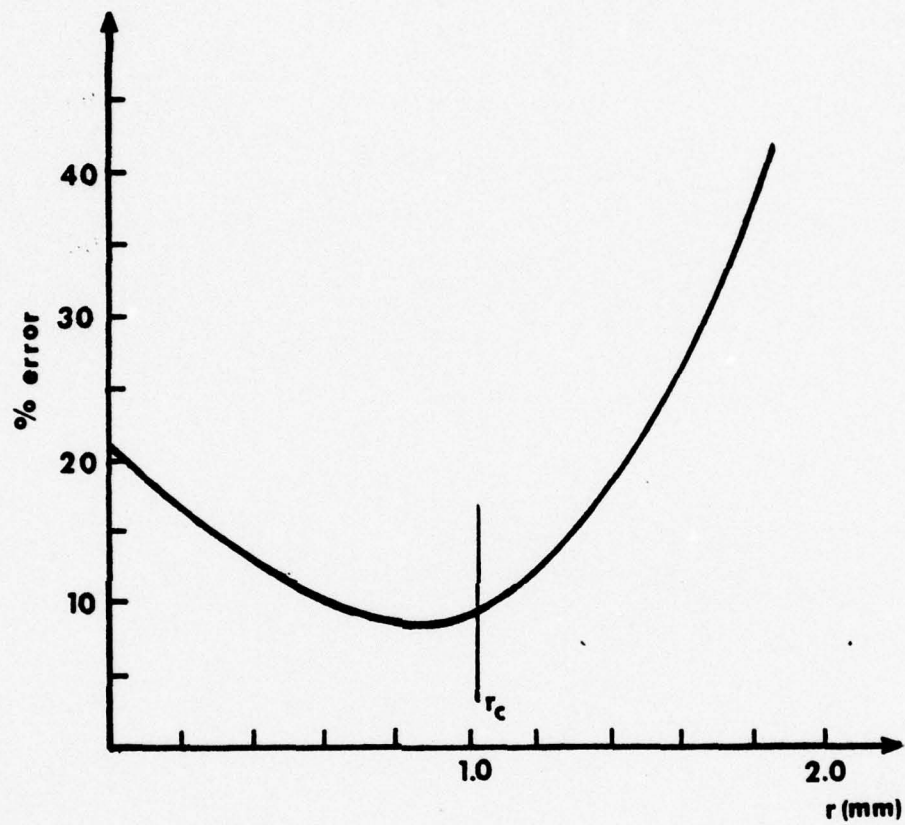


FIGURE 3.14 FRACTIONAL ERROR IN ELECTRON DENSITY
EXTRACTED FROM HOLOGRAM VS. RADIUS

fringe path was entirely determined by radial density changes. An alternative method, called the "half-integer fringe technique," required reading across a line of constant z -value, noting the horizontal positions at which either a light or dark fringe was crossed. Occurring at a constant z -value, the method did not require the assumption of negligible z -gradients, but neither did it provide information at points between maxima and minima in exposure. Both techniques were used in data analysis, and will be distinguished in Chapter Five.

A quantification of error in fringe reading was obtained by reading a fringe "correctly," then changing its value of fringe shift at one horizontal position. In the fractional fringe case, an accuracy of reading to within 0.15 fringe was indicated by magnification and reconstruction quality. By introducing a known error of 0.15 fringe at various radial values of a fringe, a corresponding fractional change in density, after Abel inversion, was obtained. The plot in Figure 3.14 displays the fractional error associated with a reading error of 0.15 fringe, introduced at a point positioned at various radii. Fortuitously, the error in density determination reached a minimum of about 10% at that radius of most interest in the laser-plasma interaction, the critical radius. An error introduced

at the centerline provided a large change in density, because the path length of an object ray through the center region of the plasma was a small fraction of its total path through the plasma. Thus, a specific change in phase, indicated by a shift in fringe, introduced by the center region required a large change in the refractive index, since the path length was small. At the edge of the column, a fixed error imparted to a fringe was a large fraction of the total fringe shift, since at the lower outer densities, the total fringe shift was small. These competing error mechanisms provided a minimum in the effect of reading error, which occurred near the radius at which greatest accuracy was desired.

The reading error was seen to be similar for either of the techniques of fringe reading. The error associated with variation from the cylindrical symmetry associated with the Abel transform was not as easily quantified, but was expected to be smaller than error introduced in the reading of the fringe.

After reading the values of fringe shift vs. radius, the results were put into a computer code that performed the inverse Abel transform to obtain electron density vs. radius by use of the collisionless refractive index relation.

3.5 Experimental procedure

The simultaneous operation of two lasers, the Z-pinch, the diagnostics for the incident, transmitted, and backscatter beam, the timing diagnostics and electronics, and ten information channels by a single experimenter required an orderly progression from one shot to the next. To minimize error and maximize shot-to-shot reproducibility, a checklist of intra-shot procedures was devised. Another list set forth the preparation procedure for a run of shots (6 to 14 shots). A description of these procedures is included, primarily for future users of the LPIL (Laser Plasma Interaction Laboratory) facility.

After installation of a new quartz target chamber (every 100 shots), several alignment shots of the Z-pinch were needed to locate the plasma within the chamber, on the one axis by the streak camera imaging system at the CO₂ exit port, and on the perpendicular axis by holographic interferometry. Having located the plasma, the Newtonian imaging system for the CO₂ system was aligned in the manner set forth in Section 3.3.

After alignment of the holography system, a hologram was taken of the reference target, which was positioned at the location of the plasma, previously determined. This hologram became the reference for

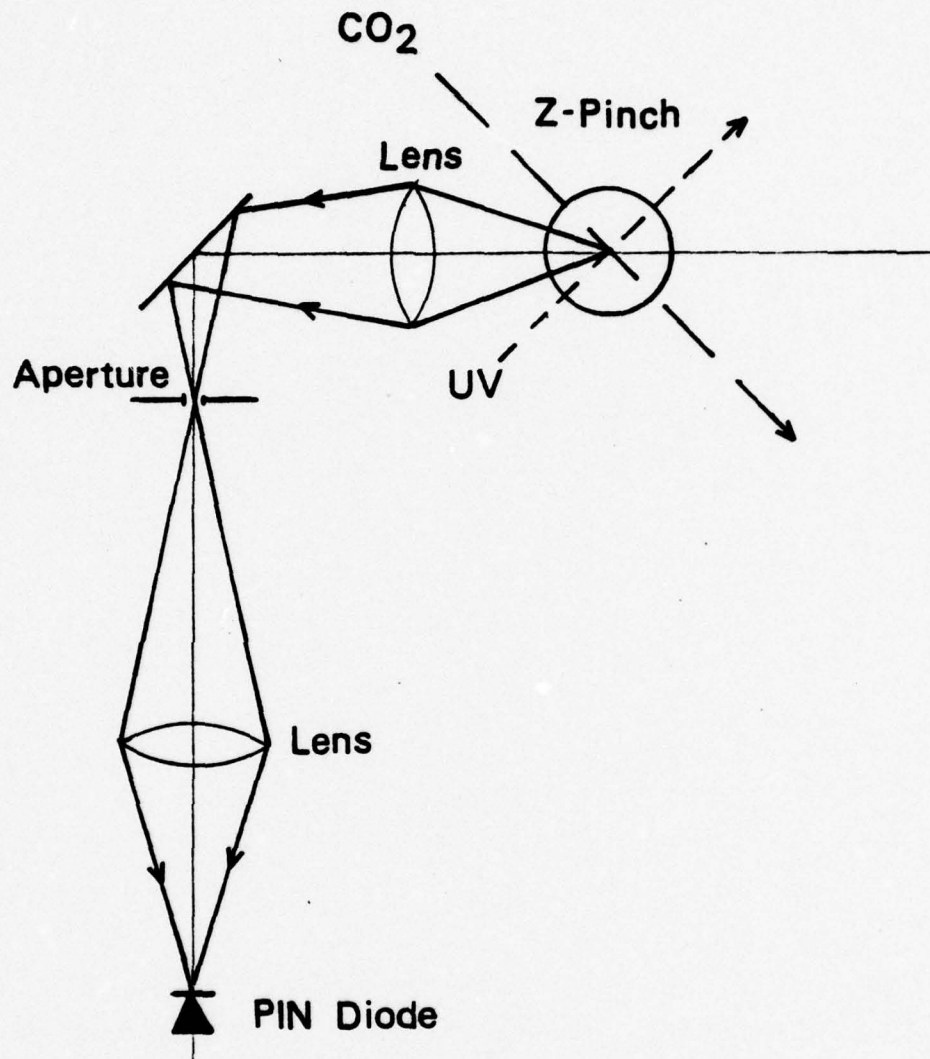


FIGURE 3.15 OPTICAL IMAGING SYSTEM FOR PLASMA FOCAL
VOLUME EMISSION DIAGNOSTICS

determination of magnification and image location in future reconstruction. Alignment of the holography system and the positioning of the Newtonian imaging mirrors remained constant for at least two weeks, although the lateral positioning of the CO_2 focal spot required checking between shots.

Placement of the image of the CO_2 focal volume onto the sensitive surface of the emission-monitoring PIN diode was accomplished by positioning a shiny 1 mm diameter wire at the plasma location, as determined by the streak camera photographs and the holograms. When the Newtonian imaging system was properly aligned to the plasma location, the HeNe alignment beam was transformed to an image in scattering off the wire. This image was formed by a relay lens, at 45° to the CO_2 entrance axis, and was magnified by three and placed at the center of a 1 mm diameter aperture. A second lens relayed this spatially-filtered image to the face of a PIN diode. In this manner, the PIN diode only viewed the focal volume of the CO_2 laser in the plasma (Figure 3.15).

In alignment of the CO_2 beam to the plasma, it was important to leave the ZnSe windows in place for all phases of the operation, since the 14° angle at which the flats were tilted introduced a beam displacement.

The absolute energy calibration of the system was next determined by use of a calibrated energy monitor (Lumonics Model 50D Large-Area Detector). To obtain the energy incident on the plasma, the entrance window for the CO₂ beam was placed in position and the exit window was removed. The entrance window was measured to have a transmission for 10.6 μ radiation of 69%, and the exit window, tilted at a slightly smaller angle, a transmission of 71%. By placing the large area detector outside the exit beam port with window removed, the same energy at the focus was incident on the large area detector. By firing the laser at reduced intensity, the signal from the large area detector was used to calibrate the signal from the GenTec energy monitor. The large area detector was calibrated by Lumonics, Inc., with an NBS-traceable source, and provided absolute energy calibration for the experiment.

Prior to each run of the experiment, the position of the air-supported holography tables was checked. Normal incidence and symmetric placement of the two holographic beams on the film plate indicated proper positioning of the air-floated tables.

The ultimate pressure in the evacuated target chamber was next checked to be less than 5×10^{-5} Torr before filling the chamber with helium to a pressure of 1.4 Torr for operation of the discharge.

The backscatter detector was next filled with the liquid nitrogen required for its operation, and by adjustment of the backscatter focusing mirror, the backscatter from an air breakdown plasma, obtained with a CO_2 beam energy of about 0.1 J, was maximized. The backscatter attenuation cell was then filled with propylene to achieve desired attenuation. With the CO_2 attenuator still set for low output energy, the presence of the transmitted beam through the chamber was ascertained on both the burn film and the pyro-electric detector.

Next, the oscillograms of the two PIN diode signals, one from the Z-pinch light monitor, and one from the holography laser, were synchronized by a common laser pulse. The timing between the CO_2 laser firing and the holography laser firing was set for coincidence, and timing of both lasers was set to the predicted time of pinch, seen in previous shots to occur about 1.2 μsec after trigger of the spark gap. Other oscilloscope traces, providing backscatter information, were next synchronized by use of a fast pulser. After checking all scope rates and sensitivities and all cable connections, the holography plate for the first shot was loaded. The CO_2 beam was laterally aligned to the predicted position of the plasma column, using the scale at the exit beam port. This completed the pre-run

preparation, and the calibrated attenuation cell was pressurized to provide the desired incident energy for the first shot.

The procedure followed for each shot was designed to minimize the errors that could arise from carelessness in operation, such as firing with no film or with an obstruction in the beam path. The checklists for pre-shot and intrashot operation appear in Appendix F.

After each run, calibration of the GenTec energy monitor was again checked. Also, the ZnSe windows were removed from the target chamber and cleaned. After every 25 shots, the fused silica holography windows were also cleaned in a similar manner. After approximately 100 shots of the Z-pinch, the device was completely disassembled. The quartz chamber was annealed and cleaned, the spark balls and electrodes were repolished to remove pits, and every metal interface that formed a current path from the capacitor to ground was carefully polished. Complete realignment of both optical systems was performed upon reassembly of the discharge.

This chapter has presented a description of the tools of the experiment, as well as procedures developed in running the experiment to maximize the accuracy of the results. A calculation of a series of parameters describing the experiment was found useful in data analy-

sis, and is reproduced in the conclusion of this chapter.

3.6 Calculation of experimental parameters

This chapter of description of the experiment concludes with a compendium of experimental parameters associated with the laser-plasma interaction experiment. Unless otherwise specified, the parameters were calculated for an electron density of $1.14 \times 10^{19} \text{ e}^-/\text{cm}^3$ (average density inside critical radius at pinch time), an electron temperature of 20 eV, an incident intensity of $3 \times 10^{11} \text{ W/cm}^2$ at a wavelength of 10.6μ , and a critical scale length, L , of 250μ . Full ionization with $Z=2$ was assumed, and a current at time of pinch of 80 kA was used.

When possible, the units used are "plasma units," which express temperature in eV, density in cm^{-3} , length in μ , and intensity in W/cm^2 . Purists may object, but it is felt that a formula expressed in units familiar to the field of laser-plasma physics provides more compatibility with physical intuition than a more standard system. However, some expressions, such as thermal conductivities, have no traditional units in the literature that specialize to plasma physics, and so are expressed in SI (MKS) units.

In the accompanying table, the parameter of interest is stated, and its symbol provided. Usually, a "general expression" is provided in terms of previously-calculated parameters and physical constants. Next, a "specialized expression" is provided, which allows calculation of the parameter of interest in terms of electron density (cm^{-3}), electron temperature (eV), wavelength (μ), critical scale length (μ), intensity (W/cm^2), magnetic field (T), or velocity (cm/sec). The specialized expression includes the assumption of full ionization ($Z=2$), equal electron and ion temperatures, and a current through the plasma of 80 kA. The final heading, "value," applies to the experimental conditions of scale length, temperature, and density stated at the beginning of the section.

TABLE 3.1
CALCULATION OF EXPERIMENTAL PARAMETERS

<u>Parameter (Symbol)</u>	<u>General Expression</u>	<u>Specialized Expression</u>	<u>Value</u>
Debye length (λ_D)	$\sqrt{\theta_e / 4\pi n e^2}$	$7.43 \times 10^2 \theta_e^{1/2} n^{-1/2}$	0.01μ
Plasma parameter (g)	$\frac{4\pi}{3} n \lambda_D^3$		50
Coulomb logarithm ($\ln \Lambda$)	$\ln \left(\frac{\lambda_D}{e^2 / \theta_e} \right)$		5.0
Mean thermal velocity (v_{th})	$\sqrt{3\theta_e / m}$	$4.2 \times 10^7 \theta_e^{1/2}$	1.9×10^8 cm/sec
Kinetic pressure (p)	$n_e \theta_e + n_i \theta_i$		5×10^7 n/m ²

TABLE 3.1 (con't.)

<u>Parameter (Symbol)</u>	<u>General Expression</u>	<u>Specialized Expression</u>	<u>Value</u>
Magnetic pressure (p_m)	$ B ^2/2\mu_0$	$4 \times 10^5 B^2$	$3.5 \times 10^7 \text{ n/m}^2$
Mass density (ρ)	$m_e n_e + m_i n_i$	$3.3 \times 10^{-21} n_e$	$3.81 \times 10^{-2} \text{ kg/m}^3$
Acoustic speed (c_0)	$\sqrt{\theta_e/m_i}$	$4.9 \times 10^5 \theta_e^{1/2}$	$2.2 \times 10^6 \text{ cm/sec}$
Ratio of specific heats (γ)			5/3
Specific heat @ con. vol. (c_v)	$(c_v) \frac{3}{2}(n_e + n_i)$	$3.11 \times 10^{-17} n$	$3.55 \times 10^2 \text{ J/OK}\cdot\text{m}^3$
Specific heat @ con. pres.	γc_v		$5.91 \times 10^2 \text{ J/OK}\cdot\text{m}^3$
Thermal conductivity (κ)	$1.95 \times 10^{-9} \frac{\theta_e^{5/2}}{Z \ln \Lambda} \epsilon(Z) \delta_T(Z)$	$0.414 \theta_e^{5/2} (\theta \text{ in eV})$ $2.85 \times 10^{-11} \theta_e^{5/2} (\theta \text{ in } ^\circ\text{K})$	$741 \text{ J/sec}\cdot\text{m}$

TABLE 3.1 (con't.)

<u>Parameter (Symbol)</u>	<u>General Expression</u>	<u>Specialized Expression</u>	<u>Value</u>
Thermal mean free path (ℓ_{th})	$\frac{\kappa}{\rho c_p v_{th}}$		18 μ
Spitzer viscosity (μ)	$2.21 \cdot 10^{-15} \frac{\theta^{5/2} A^{3/2}}{Z^4 \ln \Lambda}$	gm/cm \cdot sec	1.43 $\times 10^{-4}$ kg/m \cdot sec
Viscous mean free path (ℓ_{vis})	$\frac{\mu}{\rho v_{th}}$	$5.02 \times 10^{-12} \theta^2$	$2 \times 10^{-3} \mu$
Electron-electron collision frequency (ν_{ee})		$2.91 \times 10^{-6} \frac{n \ln \Lambda}{\theta_e^{3/2}}$	$1.7 \times 10^{12} \text{sec}^{-1}$
Mean free path between electron-electron collisions (λ_{ee})	$\lambda_{ee} v_{th}$	$1.44 \times 10^{17} \frac{\theta_e^2}{n \ln \Lambda}$	0.5 μ

TABLE 3.1 (con't.)

<u>Parameter (Symbol)</u>	<u>General Expression</u>	<u>Specialized Expression</u>	<u>Value</u>
Ion-ion collision frequency (ν_{ii})		$4.8 \times 10^{-8} \frac{n_i \ln \Lambda}{\theta_i^{3/2} A^{1/2}}$	$1.5 \times 10^{10} \text{ sec}^{-1}$
Electron-ion collision frequency (ν_{ei})	$\frac{Z \ln \Lambda}{10} \frac{\omega_p}{g}$		$3.3 \times 10^{12} \text{ sec}^{-1}$
Electron-ion equilibration time (τ_{eq})	$\frac{3.5 \times 10^8 A \theta_e^{3/2}}{n_i Z^2 \ln \Lambda}$		1 nsec
Electric field of CO ₂ beam (in vacuum) (E_V)	$I = \epsilon_0 c \langle E^2 \rangle$	$E_V = 27.5 \sqrt{I}$	$1.5 \times 10^9 \text{ V/m}$
Field swelling & damping factor $\left(\frac{E_{max}}{E_V} \right)$	$1.9 \left[\frac{\omega L}{c} \right]^{1/6} \exp \left(\frac{-8 \nu_{ei} L}{15 c} \right)$	$2.6 (L/\lambda)^{1/6} \times \exp \left(-5.9 \cdot 10^{-2} \frac{L n Z \ln \Lambda}{\theta^{3/2}} \right)$	$1.7 @ L=150 \mu$ $1.3 @ L=200 \mu$ $1.0 @ L=250 \mu$

TABLE 3.1 (con't.)

<u>Parameter (Symbol)</u>	<u>General Expression</u>	<u>Specialized Expression</u>	<u>Value</u>						
Electron oscillatory velocity in plasma-modified E-field (v_{osc})	$v_{osc} = \frac{eE_{max}}{m\omega}$		$1.5 \times 10^8 \text{ cm/s}$						
Field-strength parameter (η_0)	$\frac{v_{osc}}{v_{th}}$	$1.6 \times 10^{-6} (I/\theta_e)^{\frac{1}{2}} L^{1/6} \lambda^{5/6} \\ \times \exp \left[-5.9 \times 10^{-21} \frac{Ln Z \ln \Lambda}{\theta_e^{3/2}} \right]$	$\frac{L(\mu)}{\eta_0}$ <table><tr><td>150</td><td>1.2</td></tr><tr><td>200</td><td>0.9</td></tr><tr><td>250</td><td>0.7</td></tr></table>	150	1.2	200	0.9	250	0.7
150	1.2								
200	0.9								
250	0.7								
Magnetic field of CO ₂ beam (in plasma) (B)		$6.1 \cdot 10^{-6} \sqrt{I(L/\lambda)^{-1/6}} \\ \times \exp \left[-5.9 \times 10^{-21} \frac{Ln Z \ln \Lambda}{\theta_e^{3/2}} \right]$	0.38 T						

CHAPTER FOUR

DETERMINATION OF PLASMA ELECTRON TEMPERATURE

4.1 Introduction

As intimated before, the plasma electron temperature was taken to be in the range of 15 to 25 eV. Temperatures in this range were exceedingly difficult to measure in an helium plasma. Calculations which assumed local thermodynamic equilibrium indicated that the helium plasma was fully ionized at temperatures above 10 eV, so the traditional spectroscopic techniques of measuring line broadening, line ratios, or line-to-continuum ratios were not applicable. The electron temperature was low enough that continuum emission was primarily at energies below 500 eV, so that little x-ray emission was expected. Vacuum ultraviolet spectroscopy methods were eliminated from consideration because the Z-pinch plasma required a considerable background gas pressure, which acted to absorb radiation at these wavelengths.

One possible method of temperature determination used in some plasmas at this temperature was Thomson scattering. By inspection of the spectral broadening of a laser pulse scattered from the plasma, the tempera-

ture could have been obtained. However, such measurements required high laser intensities to bring the scattered light intensity above the plasma background emission at the laser wavelength. The only laser in this laboratory worthy of consideration was the Korad ruby laser. However, to obtain sufficient output power, the intra-cavity aperture had to be removed, which increased beam divergence due to the multimode output. This increased divergence forbade focusing the beam to a small enough spot on the plasma to provide a meaningful measurement.

Two experiments were performed in an attempt to determine plasma temperature. The first to be described was an attempt to measure low-energy x-ray continuum emission, whose spectral distribution is a function of temperature. The second was the measurement of the absorption of a probe laser beam. The transmission of the plasma at the laser wavelength was also a function of electron temperature.

Both these experiments relied upon the temperature dependence of bremsstrahlung, either the emission of radiation from electrons accelerated in the field of ions, or the inverse process of absorption of radiation by electrons.

4.2 X-ray continuum emission

Bremsstrahlung, the free-free transition radiation from electrons scattering from heavy charge centers in a plasma, is often expressed as a function of plasma temperature and emission wavelength. For a Maxwellian distribution function at a temperature θ_e in the high-frequency limit ($\theta_e \ll h\nu$) the emission is given by (Drawin & Felenbok, 1965):

$$E_\nu(\theta_e) = \frac{C n n_i Z^2 g(\nu, Z, \theta_e) \sqrt{3}}{\theta_e^{1/2} \pi} \times \exp(-h\nu/\theta_e) \quad \text{ergs/sec} \cdot \text{cm}^3 \cdot \text{sr}$$

$$C = 6.36 \times 10^{-47} \quad (\text{cgs})$$

$$g = \text{Gaunt factor, set to } \pi/\sqrt{3} \text{ (the "smooth approximation")} \quad (\text{Karzas \& Latter, 1961})$$

$$n = \text{electron density (cm}^{-3}\text{)}$$

$$n_i = \text{ion density}$$

$$\nu = \text{frequency of emitted radiation}$$

$$Z = \text{effective charge state of ions}$$

$$\theta_e = \text{electron temperature}$$

The maximum of this emission in the wavelength domain occurs at a wavelength of

$$\lambda = \frac{6200}{\theta_e (\text{eV})} \quad \text{\AA}$$

which for a temperature of 20 eV is at 310 Å.

To determine the electron temperature, then, "all" that is needed is a measurement of $E_\nu(\theta_e)$, the spectral distribution.

In the optical regime, the determination of the spectral distribution is often achieved with spectrometers. In the x-ray realm, spectrometers also exist, utilizing crystals or diffraction gratings at grazing incidence. These devices spatially disperse the various wavelengths, and are only useful where copious quantities of radiation are available. This was not the case for the Z-pinch plasma.

Another method of spectral determination, often used with γ rays, is differential pulse height measurement from a detector whose voltage output is proportional to the energy of an incident photon. Typically, hundreds of nanoseconds are required to digitally process one pulse, so the attainment of information from the thousands of pulses needed for valid statistics requires hundreds of microseconds. For measurement from a discharge that lasts only a fraction of a microsecond, this is far too long.

Integral measurement of x-ray spectral distribution is typically used on short-lifetime plasmas. A simple example serves to point out the methods used. The functional dependence of $E_\nu(\theta_e)$ is simplified to

the form $E_v(\theta_e) = \exp(-E/\theta_e)$ for this example.

The key to this measurement is the use of two detectors of differing energy response. In this example, one detector is taken to measure all photons whose energy exceeds a certain value, E_1 . The detector responds equally to photons of any energy greater than E_1 , and does not respond at all to photons of energy less than E_1 . The second detector responds to all photons whose energy exceeds E_2 , which is greater than E_1 . For a radiation pulse of a distribution of energies, the response of the first detector will be greater than that of the second, since the first responds over a wider energy range. The response of the first detector to a pulse of the assumed energy distribution $E_v(\theta_e)$, where θ_e is unknown, is found by integrating over all energies greater than its threshold, E_1 . The response of the second detector is found similarly. For simultaneous observation of the same radiation pulse, the ratio of the two detector signals is given by

$$\frac{W_1}{W_2} = \frac{\int_{E_1}^{\infty} dE \exp(-E/\theta_e)}{\int_{E_2}^{\infty} dE \exp(-E/\theta_e)}$$

Performing the integration, the unknown temperature θ_e

is then expressed in terms of the known values of E_1 and E_2 and the measured ratio:

$$\theta_e = \frac{E_1 - E_2}{\ln(W_1/W_2)}$$

This is the idealized example that demonstrates the procedure. In practice, a detector which responds equally to all energies above a threshold is nonexistent. The response of a real-world detector to a photon of energy E is expressed as some function $H(E,t)$, where t is some easily-varied parameter that changes the energy response. The energy response function, $H(E,t)$, may be interpreted as the voltage output of the detector in response to a photon of energy E , when the detector is parameterized by t . Furthermore, the spectral distribution function of the source is most generally represented as an unknown function, $\chi(E)$. In this case, the detector response is given by the integral expression,

$$W(t) = \int_0^{\infty} dE H(E,t) \chi(E)$$

The observed signal, $W(t)$, is a function of the parameter t . Given a series of W values from experiments taken at

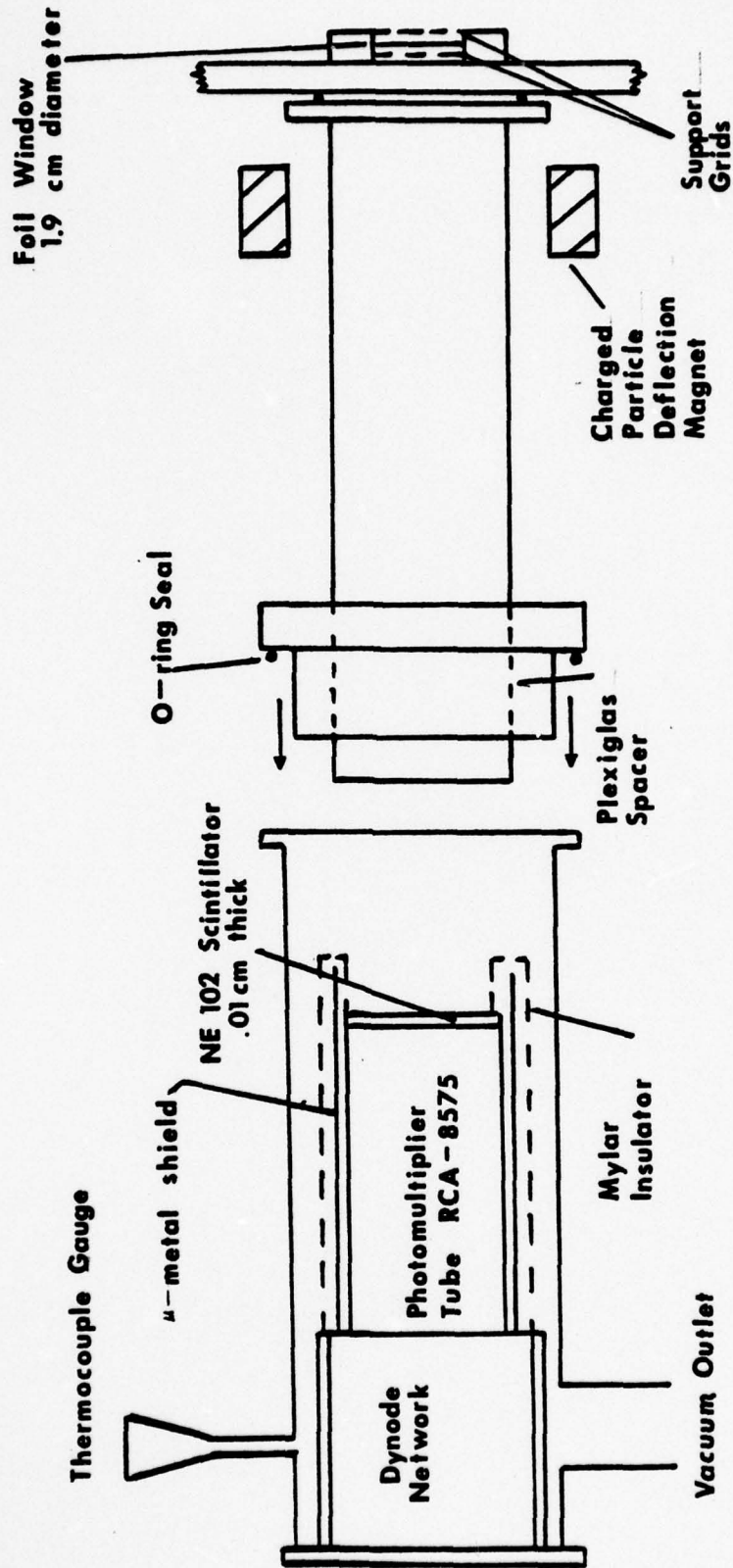


FIGURE 4.1
X-RAY DETECTOR USED ON EXPLODING WIRE PLASMA

different t values, $\chi(E)$ is found for a known $H(E,t)$ using the above integral expression. The determination of $\chi(E)$ from this sort of integral equation is called an inhomogeneous Fredholm problem of the first kind by theorists, and is called impossible by experimentalists. But if the assumption of a Maxwellian distribution of radiators is made, $\chi(E)$ takes on the exponential form shown before, and is characterized by the temperature as a parameter. This makes solution of the problem possible, preserves the integrity of the physics (for the case of a thermal distribution), and allows this method of measurement to succeed in pulsed plasmas of moderate temperature.

For this investigation, an x-ray detector was constructed utilizing the principles outlined by Jahoda and others (Jahoda et al., 1960). The detector (Figure 4.1) was composed of the thin (2 to 35 mg/cm²) foil window, followed by a thin-film plastic scintillator (1×10^{-2} cm; NE-102). This scintillator was optically coupled to the entrance window of a photomultiplier tube (RCA-8575). A certain portion of the x-ray spectrum, as determined by the absorption cross-section and thickness of the foil window and the thin-film scintillator, was stopped in the scintillator and produced a light flash proportional to the incident photon energy. By displaying the output of the photomultiplier tube, which could

temporally resolve x-ray emission to better than 35 nsec, a record of x-ray emission vs. time was obtained. Furthermore, by changing window thickness and/or material, energy information was obtained and was related to the electron temperature of the plasma. This variation of foil absorber thickness on successive shots comprised the variation of the parameter t in the expression for the detector response function.

Just behind the foil entrance window to the detector was placed a 300 G magnet to deflect any charged particles that might enter the scintillator. The interior of the detector was evacuated to a pressure of less than 20 mT to prevent attenuation of x rays on the way to the detector.

To interpret the results and provide energy information, a computer code, KXRAY, was devised. The pulse height from the detector, $W(\theta_e, t)$, resulting from x rays of spectral distribution $\chi(\theta_e, E)$ was determined by the transmission of the foil, $F(E, t)$, the stopping power of the scintillator, $G(E)$, and the light output of the scintillator for incident x rays of energy E , $S(E)$. More specifically,

$$F(E, t) = \exp(-\sigma(E)t; \quad \sigma(E) = \text{absorption cross section as function of energy for foil used;}$$

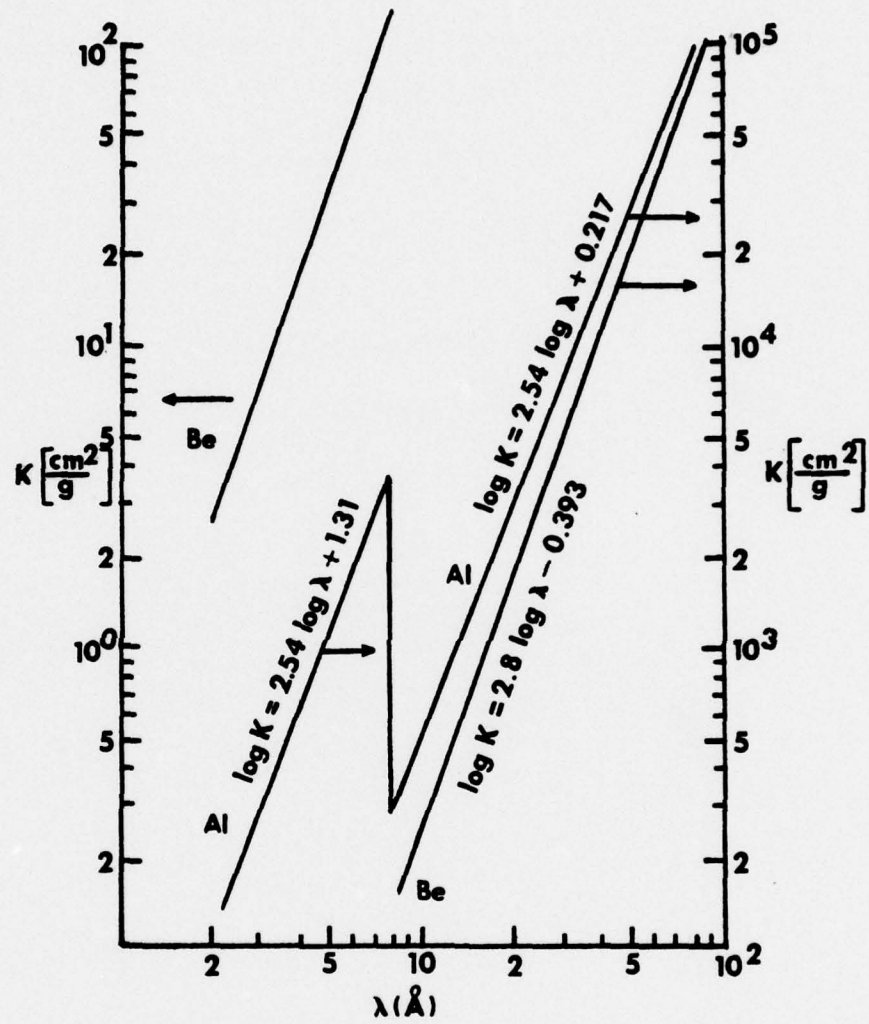


Figure 4.2 X-RAY ABSORPTION COEFFICIENT VS. WAVELENGTH
FOR ALUMINUM AND BERYLLIUM

$$G(E) = 1 - \exp K_S(E)x ; \quad K_S(E) = \text{photoelectric cross section of scintillator}$$

$$t = \text{foil thickness}$$

$$x = \text{scintillator thickness}$$

$$S(E) = \alpha E; \quad \alpha = \text{number of electrons emitted from photocathode of photomultiplier per one 1 keV x ray}$$

The foil absorption cross section, $\sigma(E)$, was represented as a straight line on a plot of $\log \sigma$ vs. $\log \lambda$, where λ is the wavelength associated with an x ray of energy E , given by

$$\lambda(\text{\AA}) = \frac{12.4}{E(\text{keV})}$$

The equation of the straight line was of the form

$$\log \sigma = m \log \lambda + b .$$

In Figure 4.2, values of m and b for aluminum and beryllium are indicated. To account for the discontinuity of the K-edge (at 1.55 keV in aluminum), a discontinuous change in b at the edge energy was accounted for. A similar bi-linear representation was used for calculating $K_S(E)$ to obtain $G(E)$. The linear treatment of the scintillator-photomultiplier tube was found to be accurate, even at these low photon energies (Meyerott, Fisher, & Roethig, 1964). The product $F \times G \times S$ defined the detector response function, $H(E)$, plotted as a

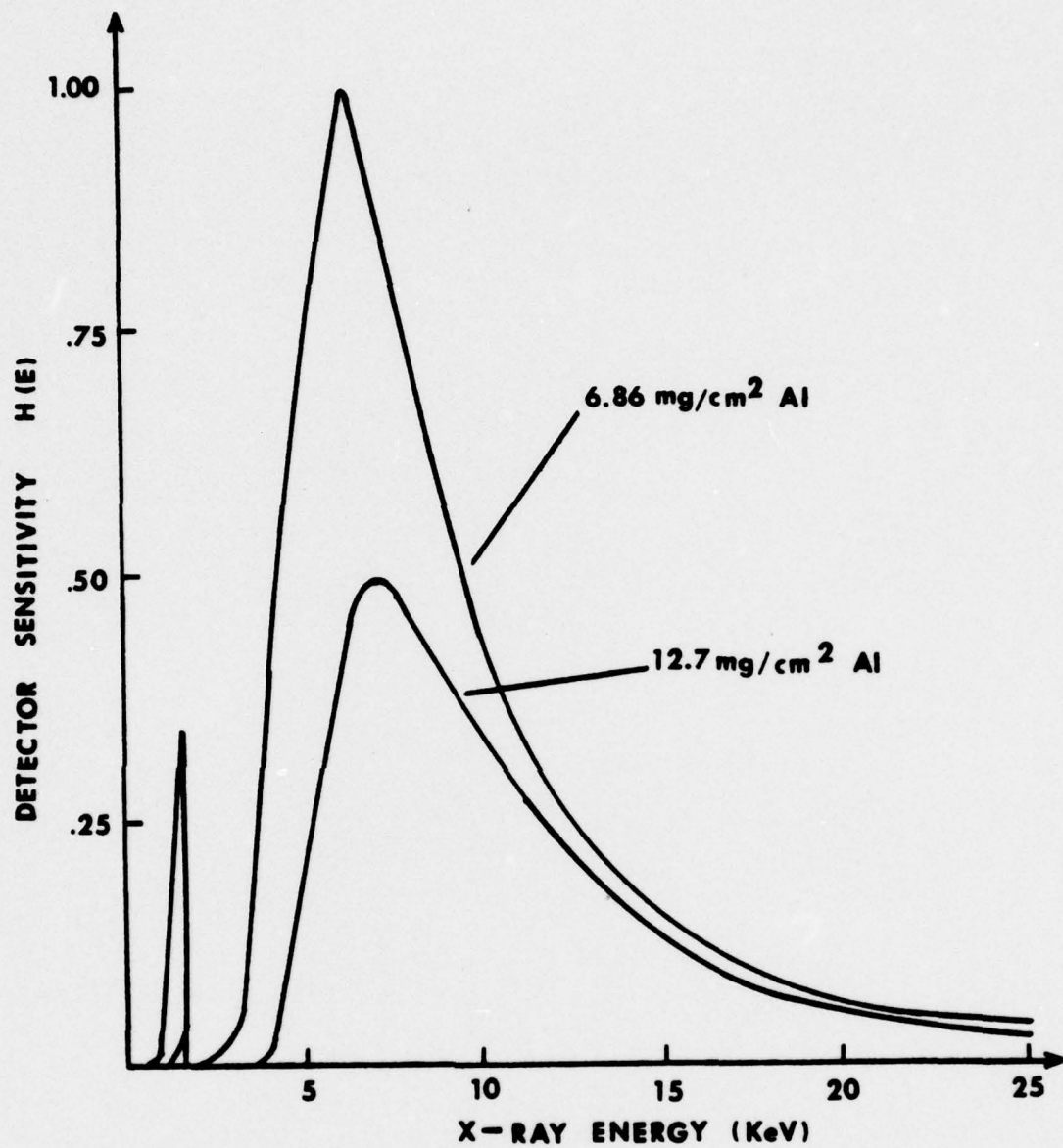


FIGURE 4.3 DETECTOR SENSITIVITY VS. X-RAY ENERGY FOR TWO THICKNESSES OF ALUMINUM WINDOWS

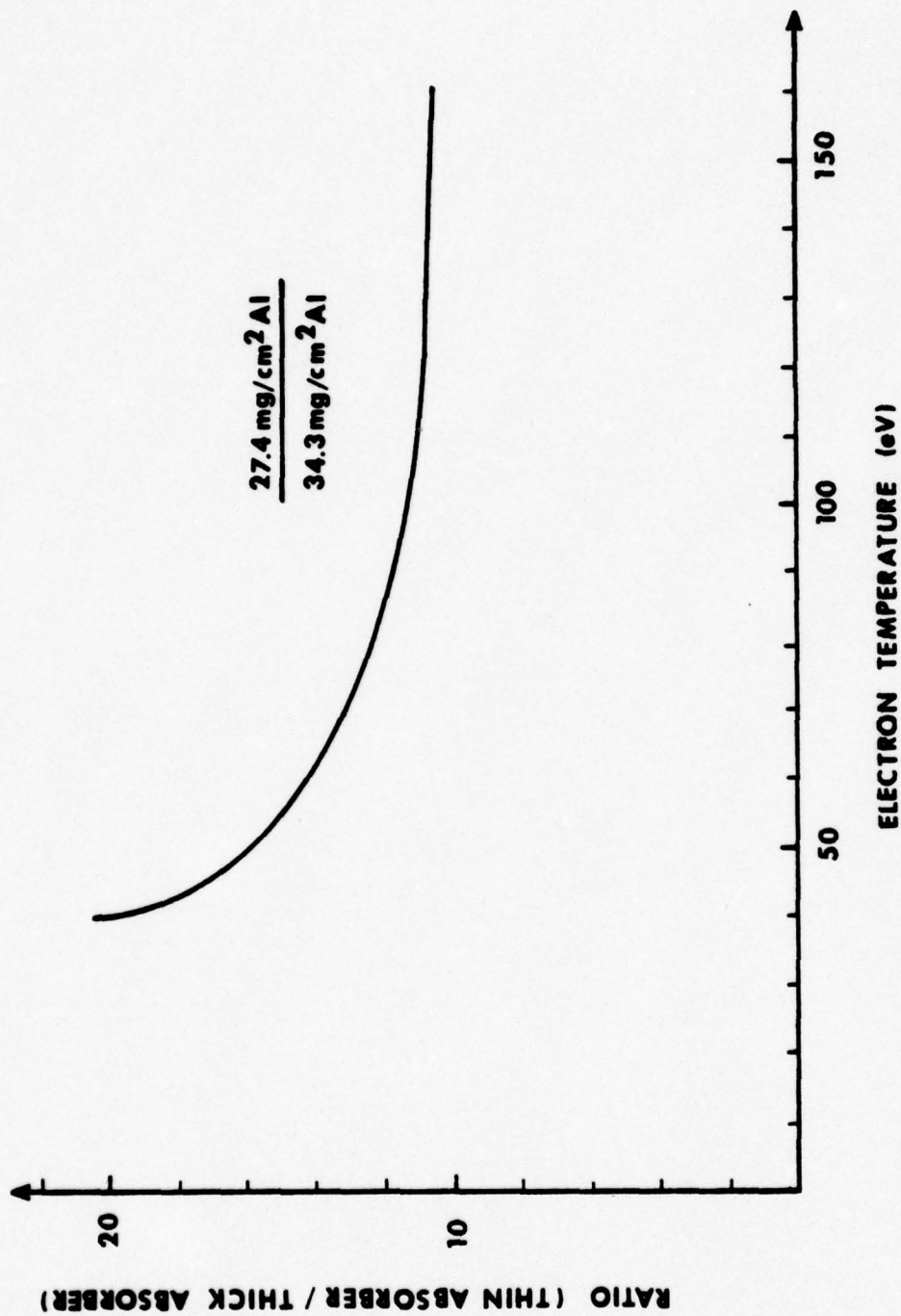


FIGURE 4.4 RATIO OF DETECTOR SIGNALS VS. PLASMA TEMPERATURE FOR TWO THICKNESSES OF ALUMINUM WINDOWS

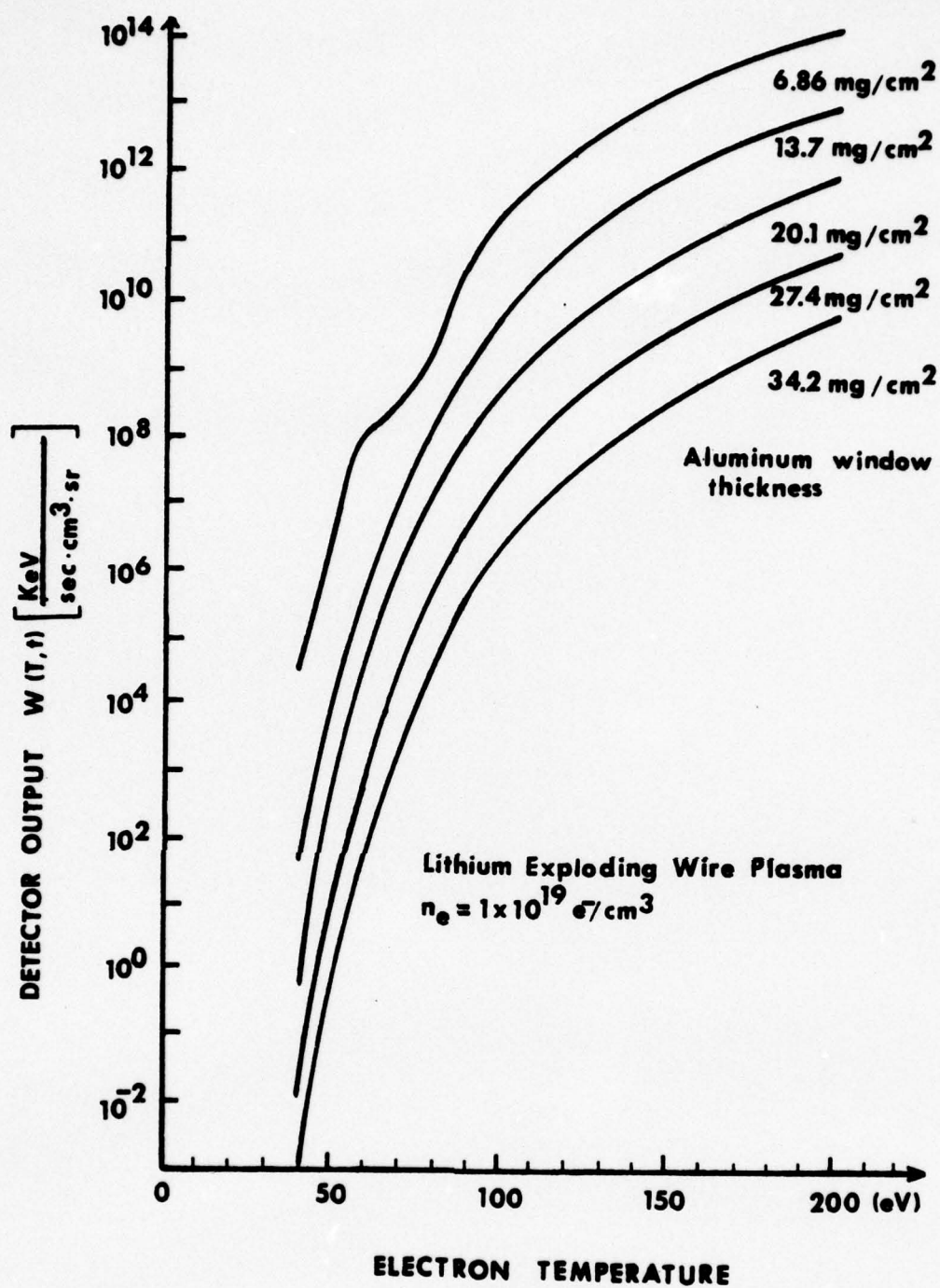


FIGURE 4.5 OUTPUT OF X-RAY DETECTOR VS. PLASMA ELECTRON TEMPERATURE FOR SEVERAL THICKNESSES OF ALUMINUM WINDOWS

function of x-ray energy in Figure 4.3. The output of the detector, $W(\theta_e, t)$ was the product of the detector response function, $H(E)$, and the bremsstrahlung spectral distribution function, $\chi(E, \theta_e)$, integrated over all energies. For high energies compared to the final ionization potential, $\chi(E, \theta_e)$ was proportional to $\exp(-E/\theta_e)$. The program KXRAY computed $W(\theta_e, t)$ by Romberg integration for two thicknesses of foils for a given temperature and found the ratio of $W(\theta_e, t)$ for the two foils. The FORTRAN code KXRAY is listed in Appendix E. Thus, a plot of $W(\theta_e, t_1)/W(\theta_e, t_2)$ versus temperature was made for a number of foil combinations so that an experimentally-determined ratio could be associated with an electron temperature (Figure 4.4). Furthermore, an absolute x-ray energy emission calculation was performed using $W(\theta_e, t)$ and included plasma density, volume, charge state, and solid angle viewed (Figure 4.5). Such a calculation was not as credible as a ratio determination, as the quantities which cancelled out in a ratio measurement were not easily determined.

To verify correct operation of the detector, the first experimental work was performed using the exploding wire plasma device in this laboratory. It was on this plasma that the calculational procedure for temperature and the ability to handle the foils were developed.

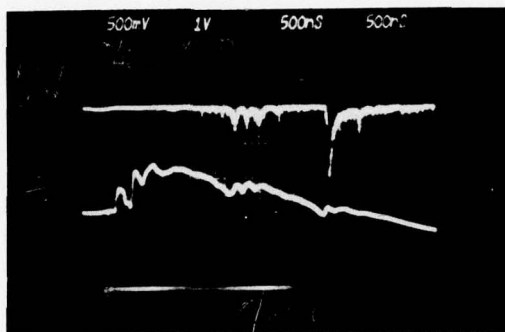


FIGURE 4.6 X-RAY PULSES (TOP TRACE) AND di/dt
(BOTTOM TRACE) VS. TIME FOR EXPLODING
Li WIRE PLASMA (500 nsec/div)

X rays were observed by the detector from the exploding wire in sufficient quantities to saturate the detector for window thicknesses of less than 27.4 mg/cm^2 of aluminum. These x rays occurred in 50 nsec-wide pulses at times of sharp dips in the time derivative of the current through the plasma, dI/dt (Figure 4.6). By using x-ray detector signals for 27.4 mg/cm^2 and 34.3 mg/cm^2 aluminum foil windows, a determination of electron temperature at time of pinch was attempted. Since only one detector was constructed for this pilot study, measurements with different foil thicknesses had to be made on different shots, which depended on the rather tenuous assumption that the evolution was reproducible from shot to shot. By averaging together several shots at each of the two foil thicknesses, a ratio value of 12.5 was used, although shot-to-shot variation gave a range of ratios from 10.4 to 13.0. This yielded an electron temperature at time of pinch of 75 eV, ranging from 70 to 155 eV (Figure 4.4).

To verify that the emission occurred from a Maxwellian distribution, several ratio measurements could have been made with a wider range of foil thicknesses. If all ratios indicated the same temperature, the x-ray spectrum was demonstrated to have occurred from a Maxwellian distribution. The investigation on the wire suggested that enough x rays were present for

imaging with an x-ray pinhole camera.

Having verified detector operation by observing x rays from the exploding wire, the x-ray detector was modified to fit onto one of the four arms of the Z-pinch target chamber to determine whether an x-ray continuum was emitted by the Z-pinch plasma. This was done by removing the tube between the foil window and the scintillator shown in the right portion of the drawing of the detector, moving the foil window much closer to the scintillator and photomultiplier tube. Unfortunately, since the detector was closer to the Z-pinch discharge than it was to the exploding wire, the detector became a path to ground for the discharge current, impeding evolution of the plasma and producing very puzzling signals on the detector output. To prevent this, the brass detector case was subsequently isolated from ground by minor redesign and re-insulation.

X ray emission from the Z-pinch plasma was not detected using aluminum foil windows as thin as 1.65 mg/cm^2 . An attempt was made to fashion absorbers more transparent to low-energy x rays by evaporating 100 to 1000 nm of aluminum onto 1.4 mg/cm^2 polyethylene. This proved unsuccessful, as after evaporation, the aluminum layer was marred with small pinholes which allowed light from the discharge to reach the photomultiplier tube. This gave the false indication of

x rays.

To further lower the temperature detection threshold, beryllium foil (4.7 mg/cm^2 and 2.3 mg/cm^2) was used as the x-ray window. The beryllium was quite brittle, and one foil was slightly damaged by acoustic shock from the discharge.

Initial results were plagued by light leaks in the foil and pickup of electromagnetic noise from the discharge. The leaks and noise gave the misleading impression that x-ray bursts were emitted. As a control check, x-ray wavelengths were blocked from the detector, but optical wavelengths were passed, by covering the foil window with glass of sufficient thickness to block x rays of energy up to 15 keV. The subsequent Z-pinch shots indicated that plasma light and electromagnetic interference were giving false indication of x-ray pulses, since detector pulses were similar to those previously seen.

To reduce the appearance of electromagnetic interference from the discharge on the detector output, the high-voltage power supply for the detector was moved away from the discharge and placed in the shielded screen room with the timing electronics. Also, additional shielding was placed on the detector, and the signal wire within the detector was replaced with shielded 50Ω cable. In addition, a method of visual

inspection was developed that allowed detection of pinholes as small as 5μ diameter.

Subsequent experiments with the foils mentioned indicated no x-ray emission from the plasma within the energy domain of the detector. Using the absolute calibration estimate described earlier, the results indicated an upper limit to the electron temperature of 40 eV.

Generally, even the lack of observable x rays proved to be useful information, as it allowed an upper limit to be set on the Z-pinch plasma electron temperature. This knowledge of a low temperature was very important in the subsequent work in CO_2 radiation - plasma interaction experiments.

4.3 Probe beam absorption experiments

The lack of x rays prevented a temperature determination by a ratio measurement. An experiment was then performed to determine electron temperature by measuring the absorption of a laser probe beam by the Z-pinch plasma.

In this experiment, the relevant physical mechanism was the absorption of radiation in a plasma by inverse bremsstrahlung. The absorption coefficient for inverse bremsstrahlung by electrons in the field of

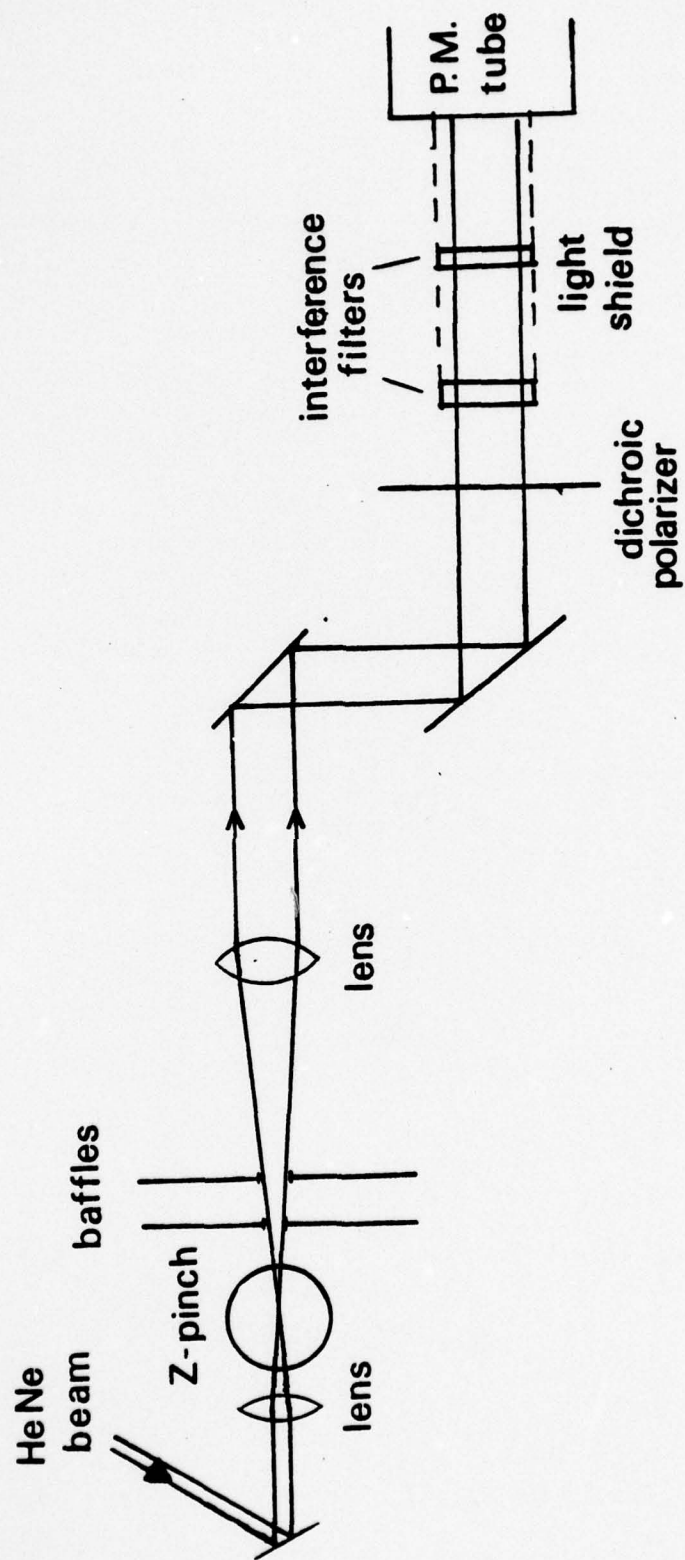


FIGURE 4.7 EXPERIMENTAL ARRANGEMENT OF PROBE-BEAM EXPERIMENT TO DETERMINE ABSORPTION

ions, given by

$$\kappa^{\text{IB}} = 2.875 \times 10^{-37} \frac{\lambda^2 n^2 Z}{\theta_e^{3/2}} (1 - 8.97 \times 10^{-22} n \lambda^2)^{-1/2} \text{ cm}^{-1}$$

λ = wavelength of radiation (μ)

n = electron density (cm^{-3})

θ_e = electron temperature (eV)

Z = effective charge state of ions

is temperature-dependent, so an absorption measurement can be related to an electron temperature.

In some plasmas, inverse bremsstrahlung in the field of neutrals can distort results from those predicted in the previous formula (DeBoo & Bach, 1975). In the fully-ionized Z-pinch plasma, this was not expected to pose a problem. Some question arises as to the applicability of the above formula in a cold, dense plasma, even through fully ionized (Billman & Stallcop, 1976); however, in the domain of this experiment, validity was expected.

Beam refraction was a problem in the absorption measurement. Because of the steep density gradients in the plasma column, it was very difficult to determine whether the plasma had absorbed the beam or whether it had refracted the beam. Both mechanisms would have indicated a similar detector response.

The experimental arrangement was as sketched in Figure 4.7. A 50 W continuous-wave Spectra-Physics

helium-neon laser provided a beam that was focused onto the plasma by a 32 cm focal length lens. The focal spot diameter was 76μ and was centered on the plasma column. Various light baffles were incorporated to block plasma emission from the probe beam detector. The helium-neon beam was sent through two 1-nm-bandwidth interference filters and a dichroic polarizer oriented with pass axis in the direction of beam polarization. This further served to separate the probe beam from plasma emission.

To detect the transmitted beam, a 931A RCA photomultiplier tube was wired to allow high currents through the dynode chain. The probe beam was usually incident on the photomultiplier tube and produced high current output except for the brief period when the plasma discharge pinched down and absorbed the beam. Anode current corresponding to 100% transmission (with no plasma) was one mA, which provided a 50 mV DC voltage into the 50Ω input circuit.

An attempt was made to minimize refraction effects in this experiment. A careful attempt was made to align the probe beam with the plasma centerline using the method of Oktay (Oktay, 1970). By monitoring the transmitted probe beam with a streak camera, beam deflection, indicative of refraction, was monitored. By removing the lens from the camera and impinging

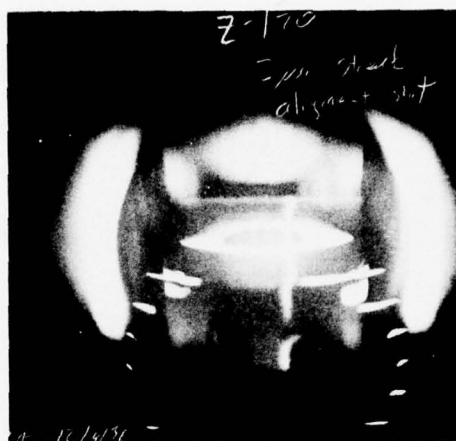


FIGURE 4.8 STREAK PHOTOGRAPH OF HeNe PROBE
BEAM TRANSMISSION THROUGH EVOLVING
DISCHARGE - NOT CENTERED

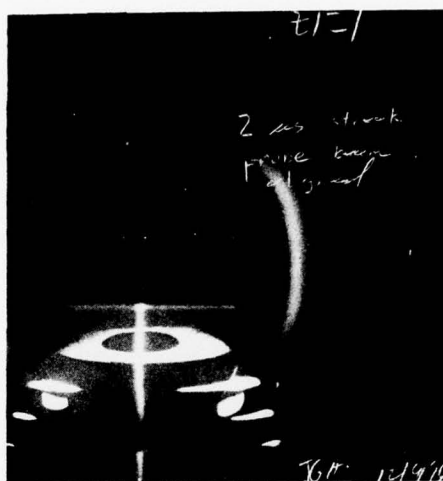


FIGURE 4.9 STREAK PHOTOGRAPH OF HeNe PROBE
BEAM TRANSMISSION THROUGH EVOLVING
DISCHARGE - CENTERED

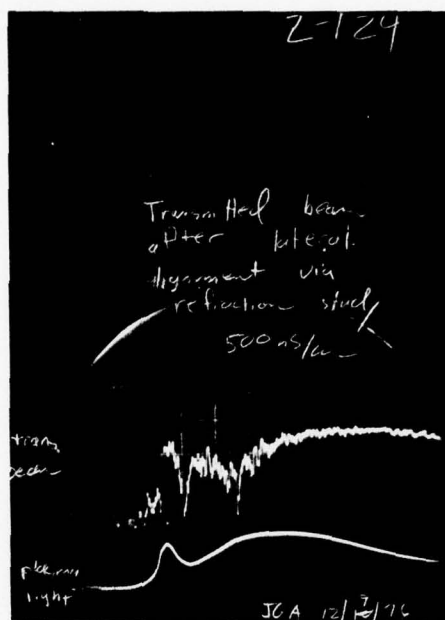


FIGURE 4.10 PROBE BEAM ABSORPTION (TOP) AND PLASMA
LIGHT EMISSION (BOTTOM) VS. TIME
(500 nsec/div)

the probe beam on the slit at the face of the image-intensifier tube, an adjustment to beam alignment was made to minimize deflection when the discharge was fired. Figure 4.8 presents a streak picture in which the beam was not centered on the plasma, and shows beam deflection at pinch time and again slightly after pinch. Figure 4.9 shows the streak picture resulting from the probe beam centered on the discharge column. This streak picture shows the probe beam disappearing at pinch time, but in a centered fashion, with no deflection or widening indicating refraction. Thus, it appeared that the beam disappearance in the streak picture was due to absorption and not refraction.

After aligning the probe beam to the column in this manner, the photomultiplier detector was used to quantify this absorption. The signal from the tube indicated a steady DC level corresponding to 100% transmission until the discharge pinched down, at which time the signal moved toward zero. The detector signal indicating probe beam absorption is shown in Figure 4.10. The calibration indicated that an absorption of at least 90% was seen. Thus, ignoring refraction for the time, absorption of the probe beam was 90% at pinch time, and was assumed due to absorption by inverse bremsstrahlung.

Using the formula at the first of this section and knowing the path length through the plasma and the plasma density profile from holographic interferometry, an estimate of the electron temperature was possible. Absorption along a path through the plasma was a function of position due to the density dependence of the absorption coefficient. In fact, the ratio between incident intensity and transmitted intensity was given by

$$\frac{I_{\text{trans}}}{I_{\text{inc}}} = \exp \left[- \int_{-L}^L dl \, K^{\text{IB}}(l) \right]$$

$$= \exp \left[\frac{-4.7 \times 10^{-57}}{\theta_e^{1/2}} (1 - e^{-h\nu/\theta_e}) \int_0^{r_0} dr n^2(r) \right]$$

To obtain the integral $\int dr n^2(r)$, the density profile of the plasma at time of pinch was used as determined by holographic interferometry. By fitting a Lorentzian function,

$$n(r) = \frac{n_0}{r^2 + b^2}$$

to the density profile shown at pinch time by holography (Figure 5.3), the integral was performed numerically. This was done by use of a ray-tracing code (DeBoo, 1974;

Rockett & DeBoo, 1975) which calculated both the refraction and absorption of a ray passing through the plasma which entered at a specified impact parameter. In this manner, the temperature was found by running the code for the Lorentzian profile at assorted temperatures until arriving at the 10% transmission obtained experimentally.

It was found that an electron temperature of only 5 eV was predicted to give the 10% transmission that was measured. This was lower than was consistent with the observation of full ionization predicted by Saha calculation.

The absorption coefficient depended very strongly on peak density, which occurred on the centerline of the Z-pinch plasma. It was in this region that the holographic interferometry was least able to determine electron density with accuracy, as was discussed in Section 3.4. A difference in centerline density within the 25% error of the inversion procedure changed the integral expression for K^{IB} by the square of the density, and the corresponding exponentiation changed the transmission calculation at a given temperature by as much as 100%.

Thus, several factors could have contributed to this low temperature assessment. The possibility of a high centerline density has been discussed. Beam

refraction may have occurred to direct the probe beam away from the detector, giving the false indication of absorption. Even though the probe beam was directed along a plasma diameter to minimize refraction from radial density gradients, some gradients in the axial or azimuthal direction could have deflected the beam. For small refraction angles, a geometrical argument provides the angle of refraction, θ , in terms of the density gradient, dn/dr , the plasma radius, r_0 , and the critical density associated with the incident ray, n_c :

$$\sin \theta \approx \frac{r_0}{n_c} \frac{dn}{dr}$$

The experimental arrangement was such that a ray deflection of only 0.1 degree would have removed the beam from the face of the photomultiplier tube. The gradient necessary for this deflection was about $2 \times 10^{19} \text{ e}^-/\text{cm}^4$, or a change in electron density of only $2 \times 10^{18} \text{ e}^-/\text{cm}^3$ over a scale of 1 mm. Chapter Five will display density plots that indicate that this change is very small in light of typical density gradients. Thus, even though not apparent in the streak pictures of the probe beam, refraction could have given the appearance of reduced transmission.

These mechanisms could contribute to the indication

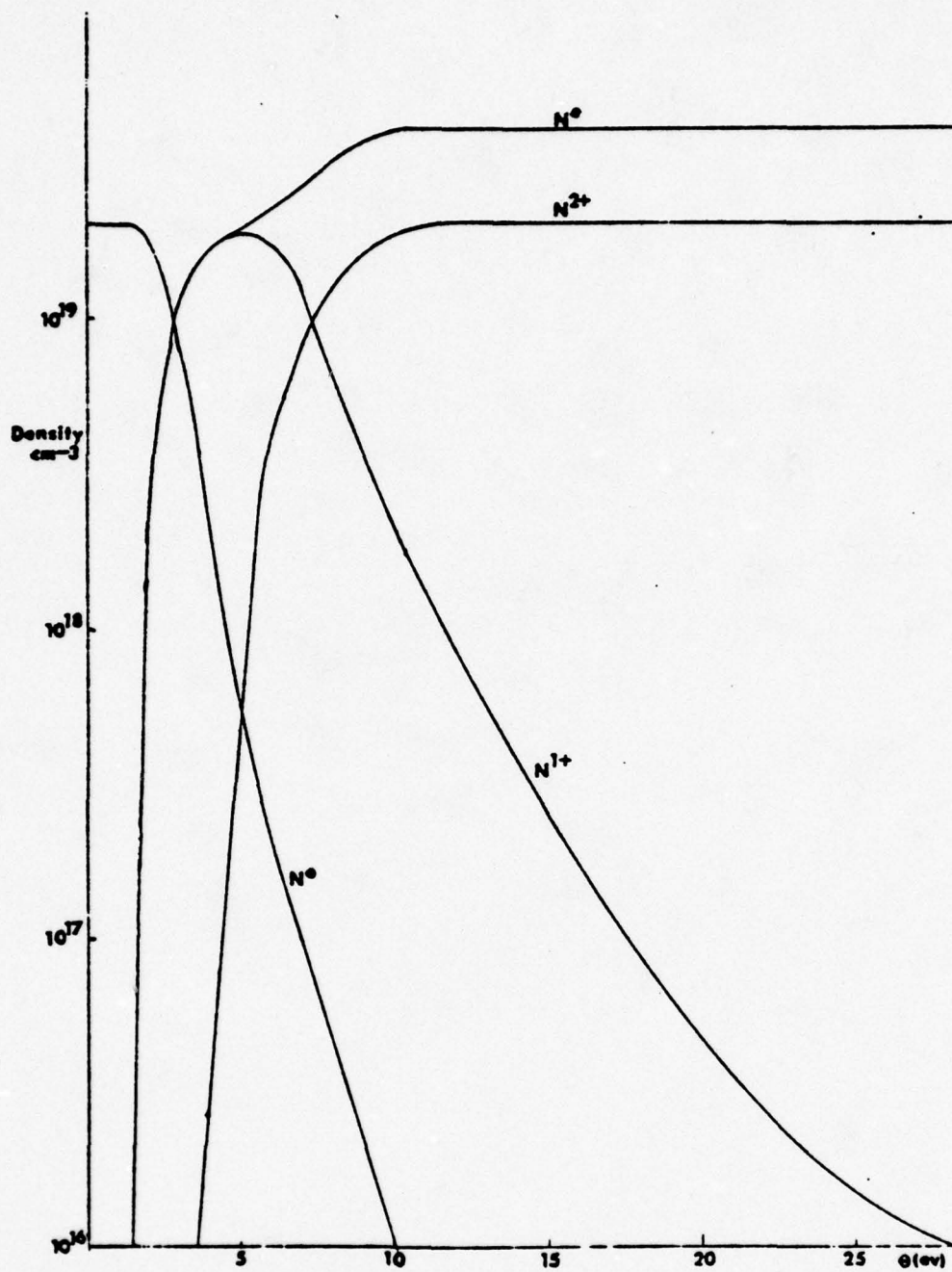


FIGURE 4.11 SAHA CALCULATION OF IONIZATION VS. ELECTRON TEMPERATURE

of a low plasma temperature. Furthermore, the only absorption mechanism was assumed to be inverse bremsstrahlung of electrons in the field of He^{2+} ions. The temperature determination by this method was thus not in agreement with the earlier spectral information indicating complete ionization.

The Saha calculation of ionization (Steel, 1976) is reproduced as Figure 4.11. Population of neutral, singly-ionized and fully-ionized species are plotted vs. electron temperature for a maximum electron density of $2 \times 10^{19} \text{ e}^-/\text{cm}^3$. For temperatures greater than 10 eV, ionization is nearly complete. Thus, a lower temperature limit is indicated by the observation of complete ionization.

Another estimate of temperature may be gained by use of the Bennett relation. The balance of kinetic pressure in the equilibrium plasma column to the current flowing through the column determines the relation (Uman, 1964):

$$i^2 = \frac{8\pi N_1 (\theta_e + \theta_i/Z)}{\mu_0} \quad (\text{MKS})$$

$$N_1 = \text{electrons/m}$$

If the current through the discharge is known, then the sum $\theta_e + \theta_i/Z$ may be determined. If the further assumption of equal ion and electron temperature is

made, then the electron temperature is given by

$$\theta_e = \frac{\mu_0 i^2}{8\pi N_1 (1 + \frac{1}{Z})}$$

To determine the current through the plasma at time of pinch, i , the equation of current vs. time for a damped RLC discharge was used to interpret the pickup coil signals of the current time derivative. This equation also allowed determination of the Z-pinch circuit parameters by inspection of the current trace. The current as a function of time is given by (Leonard, 1972):

$$i(t) = \frac{V_0}{L} e^{-\alpha t} \sin(\omega_d t)$$

$$\alpha = R/2L$$

$$\omega_d^2 = \omega_0^2 - \alpha^2$$

The inductance of the circuit is expressed:

$$L = \frac{1}{C} (T/2\pi)^2 (1 + (\ln\Delta/\pi)^2)^{-1} = 130 \text{ nH}$$

V_0 = charging voltage

C = capacitance (13.4 μF)

T = period of damped oscillation (8.4 μsec)

$$2 C/\omega_0 = T$$

Δ = amplitude ratio of two successive peaks

The resistance is given by

$$R = \frac{1}{C} (T \ln \Delta / \pi^2) (1 + (\ln \Delta / \pi)^2)^{-1} = 3.3 \times 10^{-2} \Omega$$

Knowing the circuit parameters, the time to pinch, and the charging voltage, the current at the time of pinch was found to be about 80 kA. The number of particles per unit length was 1×10^{18} e⁻/cm, determined by integration of the holographically-obtained plot of electron density vs. radius. Then, using the formula for electron temperature, a temperature of about 12.8 eV was calculated. This temperature appeared to be consistent with the lower limit set by Saha calculation of full ionization and the upper limit set by the observation of no x-ray continuum.

To relate the equation for an equilibrium pinch to the dynamic pinch of the experiment may not have been valid; however, combining the x-ray, Saha, and Bennett calculation, an estimate of electron temperature in the range of 10 to 40 eV was inferred. In the calculation of temperature-dependent parameters, the value of $\theta_e = 20$ eV was assumed. Although the electron temperature value remains uncertain, it was apparent that the temperature was low enough to allow the experiment to fall into the regime of "interesting" in terms

studying the high-intensity laser interaction with a plasma. The laser intensity was rather modest in present technology, but the plasma was of sufficiently low temperature to have a kinetic pressure on the order of the radiation pressure of the laser beam.

CHAPTER FIVE

RESULTS AND DISCUSSION

This chapter presents the results of this investigation and discusses the results in terms of physical models previously mentioned. The first two sections describe the evolution of the discharge as determined by holographic interferometry. In Sections 5.3 and 5.4, the holographic appearance of the perturbation on the target plasma produced by the CO_2 laser is described. Some assumptions about the geometry of the perturbation allow extraction of electron densities in the perturbed region, and with this information, hydrodynamic arguments yield an estimate of the fraction of laser energy absorbed. The subsequent two sections describe both the temporal and spatial structure of the CO_2 beam that is transmitted through the overdense plasma, and discuss the intensity dependence of the results. Other observations concerning continuum emission due to laser heating (both x-ray and optical) and backscatter measurements comprise the final sections.

5.1 Evolution of discharge - results

The evolution of the plasma produced by the

Z-pinch, from its formation through its pinching down to a high-density plasma of short scale lengths and continuing on to its disassembly, was important both in interpreting the results of the high-intensity laser interaction and in understanding the dynamics of the Z-pinch device itself. Holographic interferometry provided both quantitative electron density information and qualitative knowledge of plasma evolution.

Each interferogram afforded a 16 nsec snapshot of the plasma at some stage along its evolution, determined by the time the holography laser fired relative to the Z-pinch. As mentioned in Section 3.2, pre-shot adjustments determined the time of an interferogram within about 40 nsec (the jitter in the discharge), but post-shot examination of the oscilloscope photographs set the time of the hologram to within 15 nsec uncertainty. Thus, a succession of shots provided a set of interferograms at various times along the plasma evolution. The necessary assumption in this procedure was that the plasma behaved in a reproducible manner from shot to shot. This was investigated by comparison of several interferograms and associated electron density plots at one particular time along plasma evolution.

All information about plasma evolution was taken from holograms with no CO₂ laser incident or with CO₂ laser firing after the time of the holography laser.

Temporal position of the hologram was determined by comparison to the time of a burst of optical continuum emission which occurred near time of peak plasma densities. As is described in Section 5.7, the pulse shape of this light burst was somewhat a function of the collecting optics, but for the results reported here, it can be regarded as a pulse of about 150 nsec FWHM whose peak was discernable to within 10 nsec.

A qualitative look at the discharge proved useful in preparation for comparison of density distributions with those predicted by an MHD code (Duston, 1977).

In this discussion, t_h refers to the difference between the time that a hologram was made and the time of peak optical emission from the plasma. Positive values of t_h correspond to a holographic record of the plasma before the optical peak, and negative values refer to a hologram made after time of peak optical emission.

For t_h greater than 100 nsec, that is, for holograms taken of the plasma more than 100 nsec before time of peak optical emission, no sign of any plasma was seen. The Moire fringes had no shift associated with them and retained their vacuum appearance as a series of parallel horizontal lines. For times between 100 nsec and 50 nsec before the optical peak ($100 \text{ nsec} > t_h$

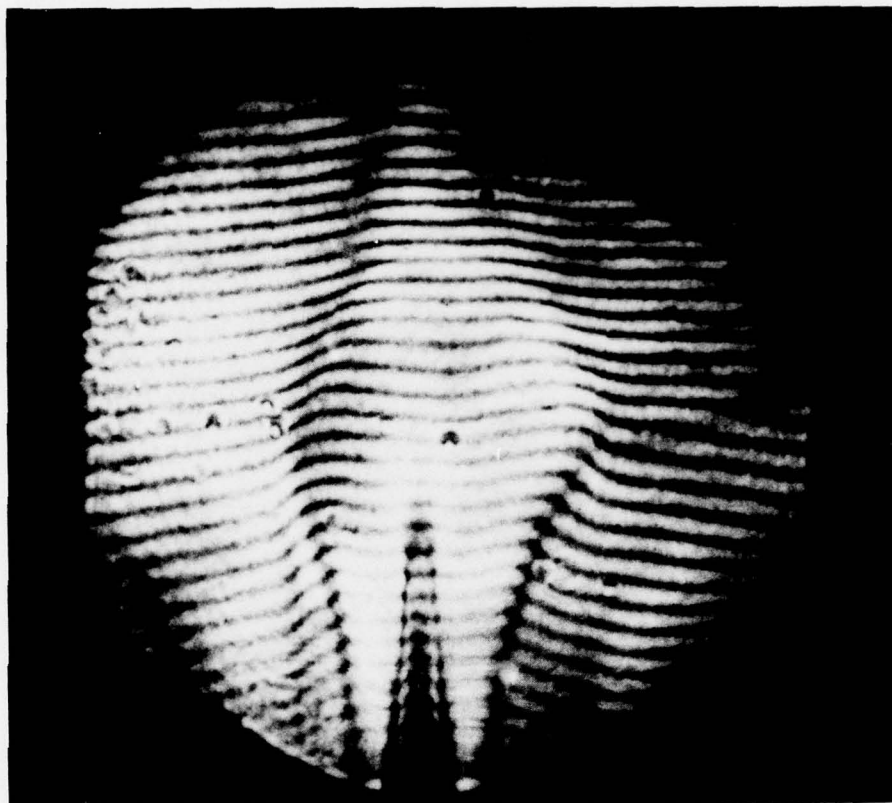


FIGURE 5.1 PLASMA EVOLUTION AT $t_h = 90$ nsec

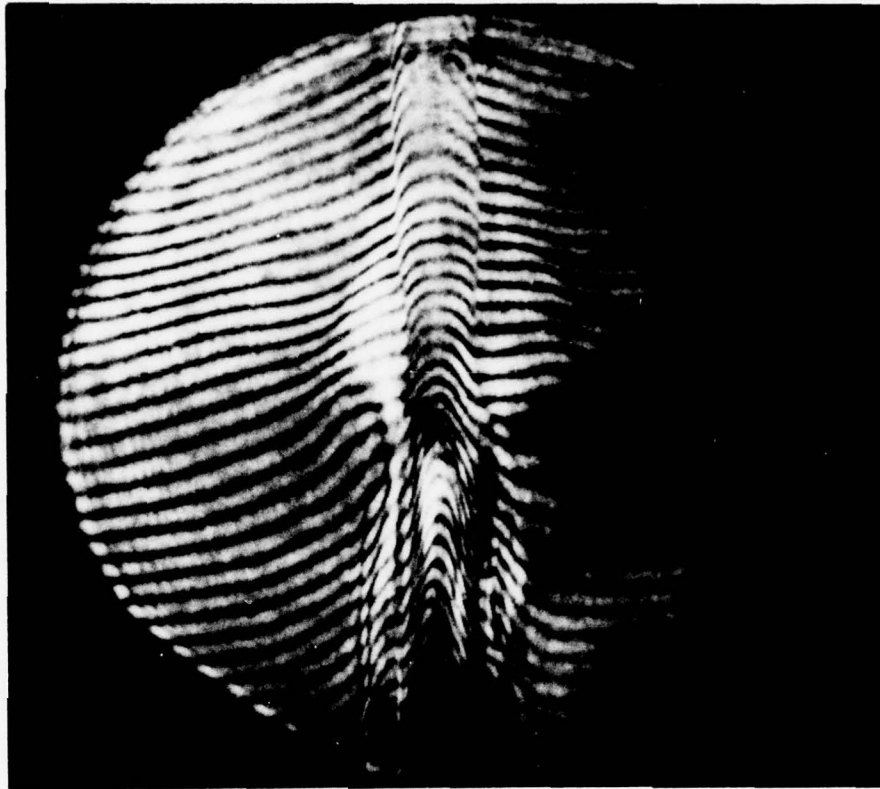


FIGURE 5.2 PLASMA EVOLUTION AT $t_h = 46$ nsec

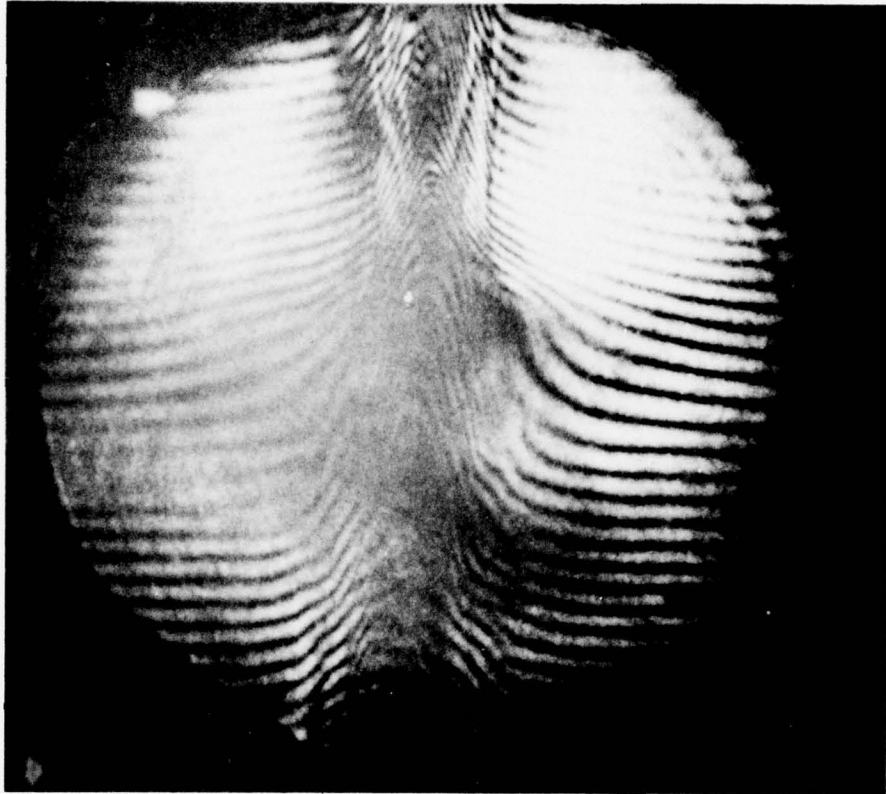
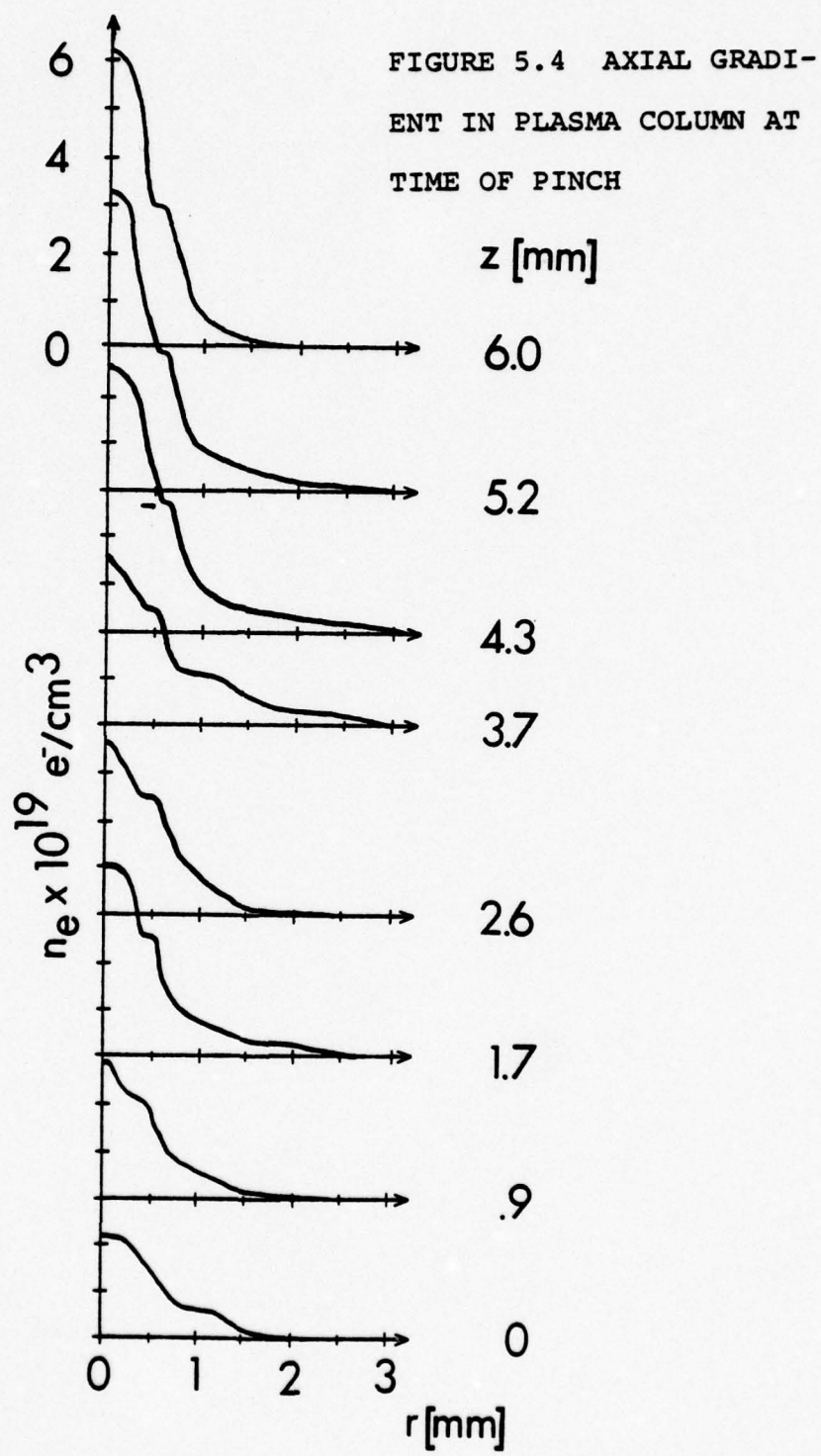


FIGURE 5.3 PLASMA EVOLUTION AT $t_h = 0$ nsec
(PINCH TIME)



> 50 nsec), a center dark finger was seen extending from the bottom of the field of view (Figure 5.1). On either side of the finger, a fringe discontinuity indicated a shell of increased electron density surrounding the central tapered column. The central finger appeared to have little fringe shift associated with it, and was seen more due to its attenuation of the object holography beam than due to phase information imparted to the beam.

This shell evolved to a column in the range $50 \text{ nsec} > t_h > 30 \text{ nsec}$ (Figure 5.2). The column diameter was greater at the bottom of the hologram than at the top, and inspection of the fringe shift indicated a greater density at the bottom than at the top of the column.

Near the time of peak optical emission, often referred to as "time of pinch," that is, $30 \text{ nsec} > t_h > -30 \text{ nsec}$, the apparent diameter of the plasma column grew and the fringe shift across the column greatly increased, as seen in Figure 5.3. This stage of plasma evolution was characterized by an increase in fringe shift and in electron density up the column. On this particular hologram, the electron density at various z -values was extracted by use of the half-integer fringe reading technique described in Section 3.4 (Figure 5.4). The readings indicated a z -gradient toward the top

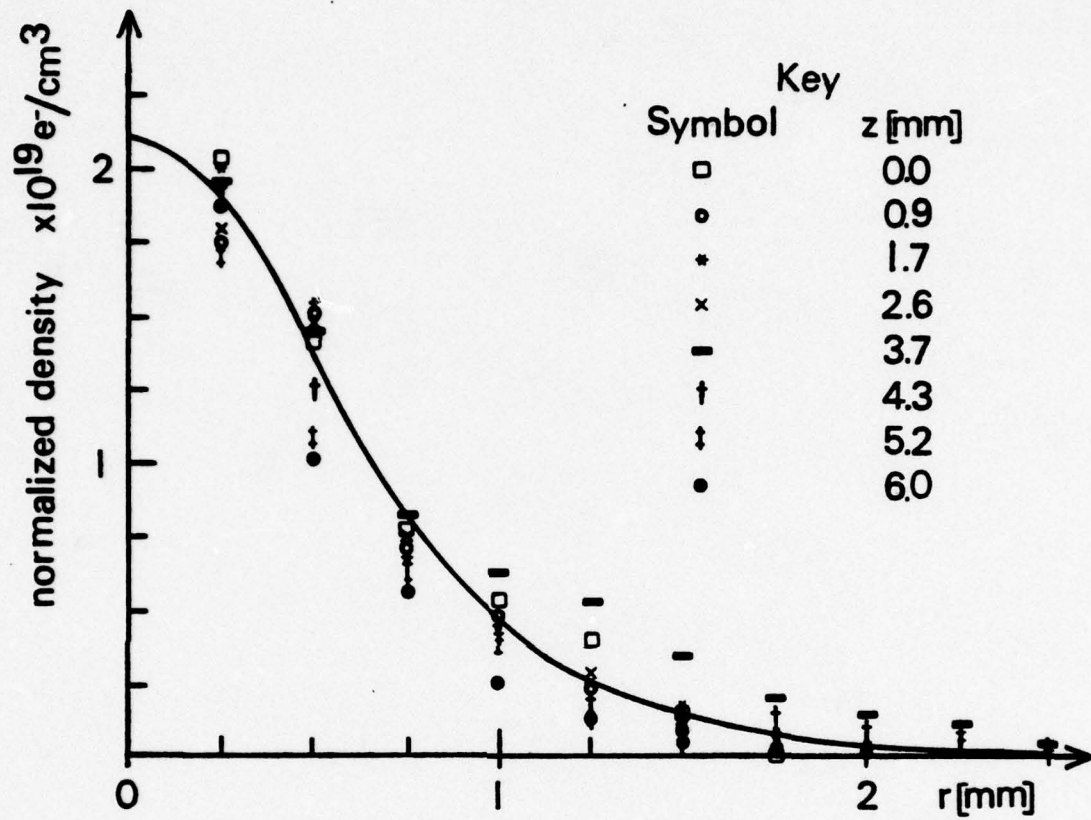


FIGURE 5.5 NORMALIZED DENSITY PROFILES AT VARIOUS z -VALUES AT TIME OF PINCH

of the hologram.

The relative shapes of the electron density profiles as a function of z were compared by normalizing each plot so that the centerline density, n_0 , was the same for each value of z . After multiplying $n(r)$ by the normalization factor associated with each plot, the scaled plots were placed on top of one another for comparison of shapes (Figure 5.5). As seen in the figure, each dot at a given r -value corresponded to one of the eight density profiles in Figure 5.4. The curve drawn through the points corresponded to the best-fitting Bennett distribution (Uman, 1964) associated with the plot. The Bennett relation, derived from the balance of kinetic pressure of the plasma at a given temperature θ with the magnetic pressure from the current-induced magnetic field, predicted a shape of electron density vs. radius for an equilibrium pinch:

$$n(r) = \frac{n_0}{(1 + n_0 b r^2)^2}$$

$$b = \frac{\mu_0 e^2 v_d^2}{8(\theta_e + \theta_i/Z)}$$

v_d = electron drift velocity from current flow

The current through the plasma at time of pinch, 80 kA (Section 4.3) and the plasma density per length yielded a temperature of 12.2 eV for the curve drawn.

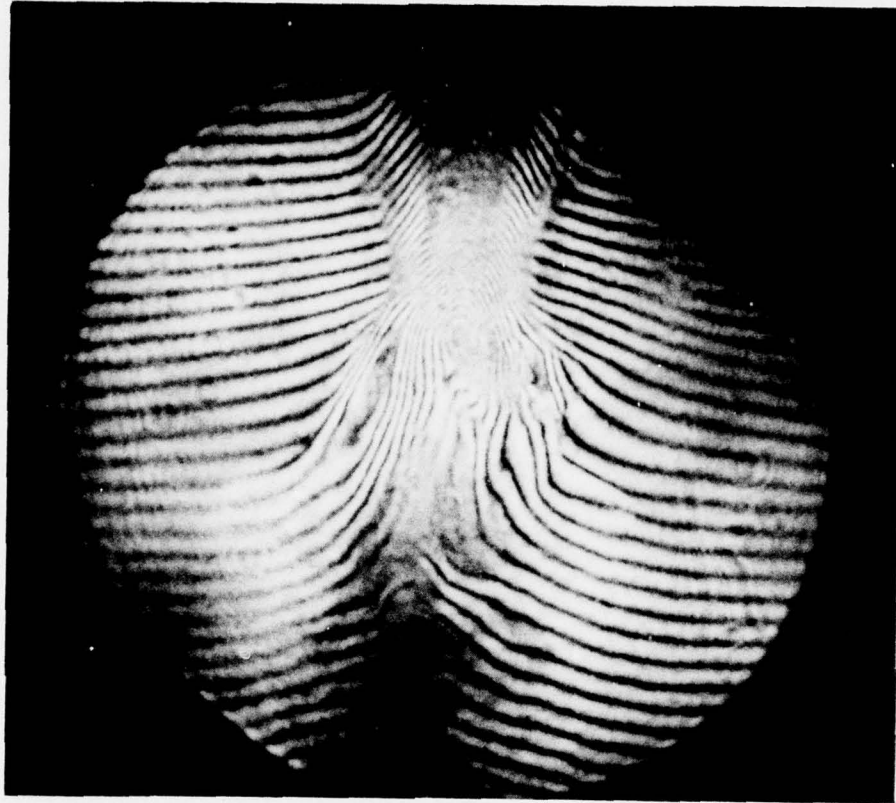


FIGURE 5.6 PLASMA EVOLUTION AT $t_h = 0$ nsec
(PINCH TIME)

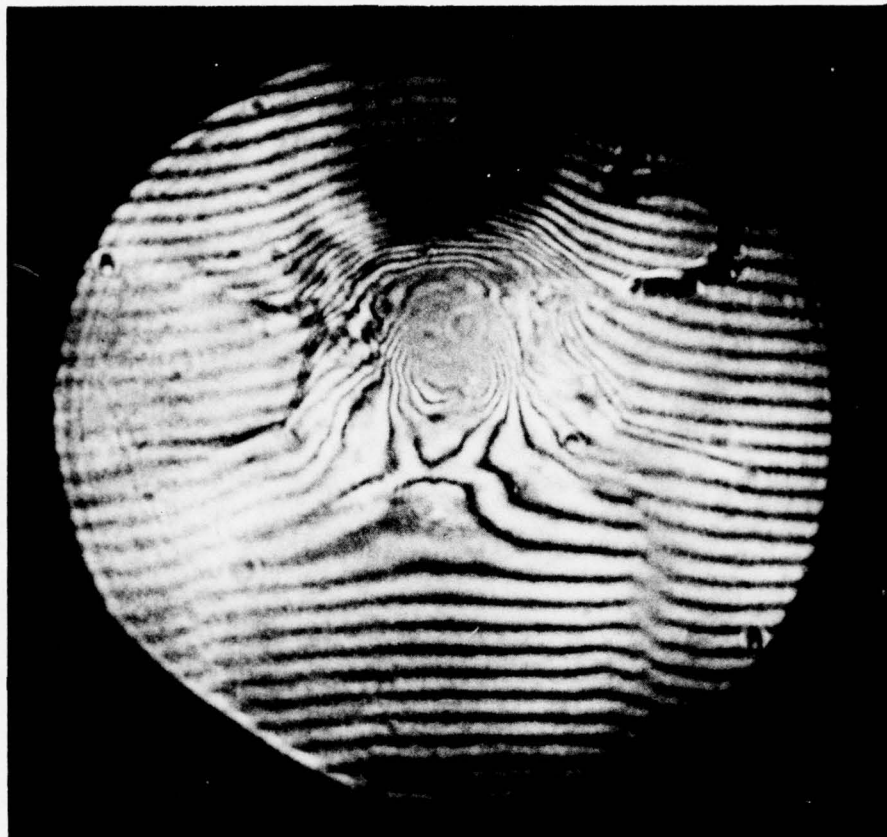


FIGURE 5.7 PLASMA EVOLUTION AT $t_h = -32$ nsec

This was comparable to the temperature found from the Bennett calculation in Section 4.3 which did not include the shape of the density profile, but only used the current and the number per unit length to determine a temperature.

Continuing with the discussion of the qualitative evolution of the column, for times $-30 \text{ nsec} > t_h > -80 \text{ nsec}$, the center fringes across the column swept upwards further until opposite sides of a fringe met at the center. Figure 5.6, at $t_h = 0 \text{ nsec}$, is similar to Figure 5.3, but is a better-quality hologram in which the beginning of this fringe steepening at the center can be seen. This evolved to the state seen in Figure 5.7 ($t_h = -32 \text{ nsec}$), in which the plasma column nearly vanished at the top and bottom of the hologram, leaving a central clump with closely-spaced, circular fringes. These fringes are similar to fringes seen from a spherical phase object, for example, a laser pellet plasma, and suggested the formation of a clump of plasma that remained after disassembly of the column.

For times greater than 80 nsec after time of pinch, irregular fringe shifts across the viewing port indicated a general asymmetric smearing-out of the remaining plasma.

In characterizing qualitative appearance of the

plasma evolution in these stages, difficulties arose in determining the time at which the plasma was said to change from one stage to the next. Indeed, these times were rather arbitrary and could have just as well been shifted by 10 nsec either way. They resulted from the qualitative study of five or more holograms at each state. The main point of the preceding discussion is that there was certainly density variation in the z-direction, both in manner of plasma evolution and in the density profile at any one time.

More useful in interpreting the CO₂ laser-plasma interaction was the evolution of the region of the plasma that was at the focal spot of the laser beam. This region was one-third of the way down the column from the top in the holograms. For this study, fringes were read by the fractional method (Section 3.4). To be valid, this technique required either assumption of no density gradients in the z-direction or knowledge of these gradients, since the method followed one fringe up the plasma column, moving toward the centerline. The greatest effect of a plasma upon an electromagnetic wave occurs where the wave approaches critical density. Thus, the particular fringe read in the target region of the plasma was one that crossed critical density at the height of the CO₂ focal spot. A spot check of the fringe reading by the half-integer method revealed little

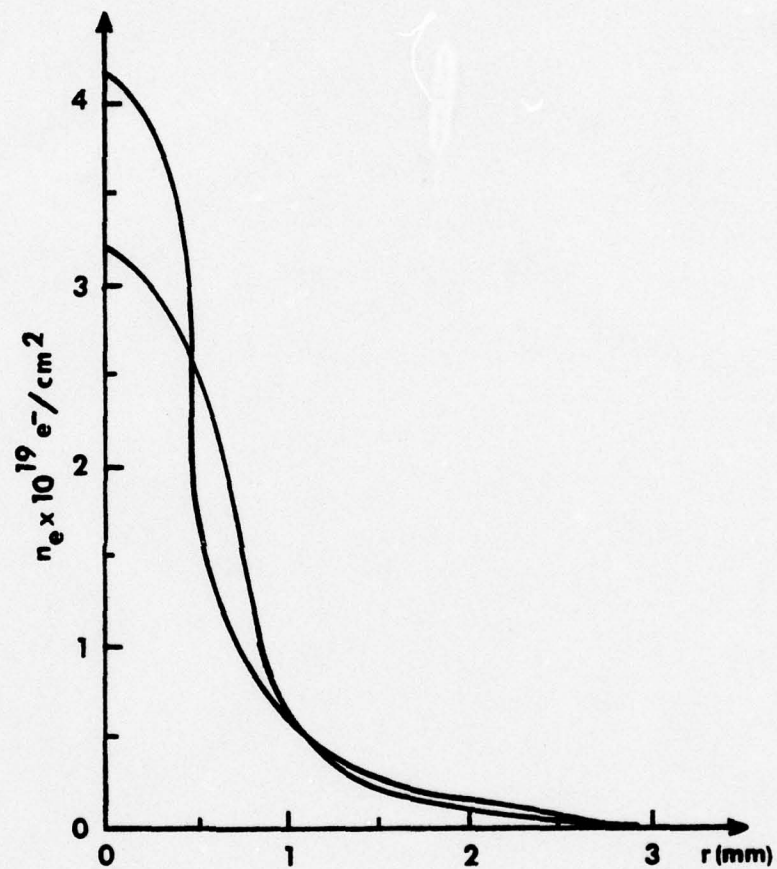


FIGURE 5.8 COMPARISON OF FRACTIONAL FRINGE READING
(HIGHER VALUE AT CENTERLINE) TO HALF -
INTEGER FRINGE READING METHOD

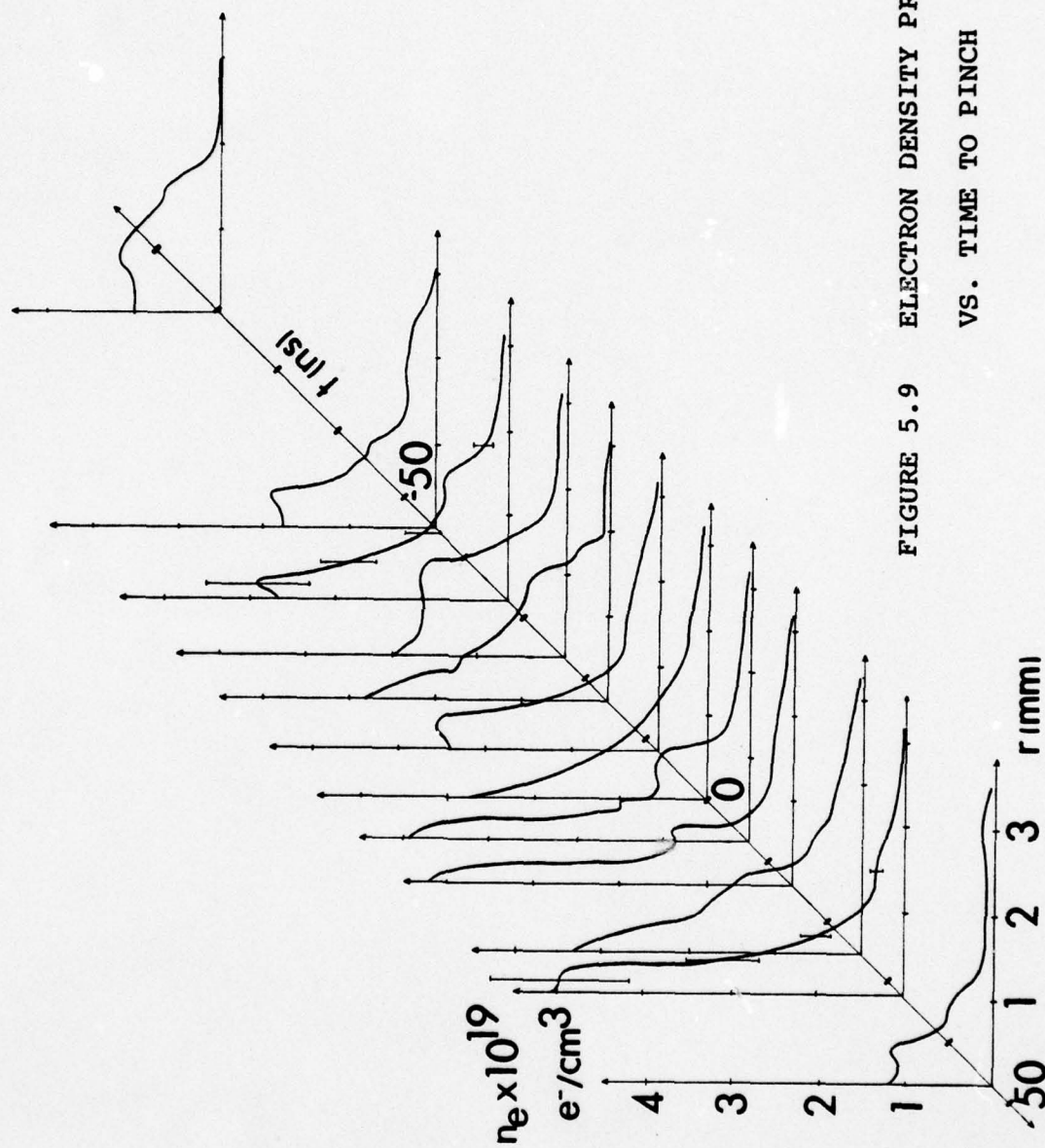


FIGURE 5.9 ELECTRON DENSITY PROFILE
VS. TIME TO PINCH

difference in the profiles obtained (Figure 5.8).

Figure 5.9 is a plot of electron density profile vs. t_h , the time to pinch, in the target portion of the plasma without the CO_2 laser incident. As seen in the plot, the plasma reached critical density at about 50 nsec before time of pinch. Centerline density appeared to peak at about 15 nsec before pinch at 3 to $4 \times 10^{19} \text{ e}^-/\text{cm}^3$. From about 20 nsec before pinch to time of pinch, a steepening of the density plot appeared at densities near $10^{19} \text{ e}^-/\text{cm}^3$ and later disappeared at pinch time. This step was investigated rather thoroughly, as it was the sort of feature expected from the misreading of a fringe in that region. However, the amount of density change associated with the step was greater than the error associated with the fringe reading at that radius (Section 3.4) and was seen in all holograms that corresponded to t_h in that range. The best verification of its validity was that the fringe upon the reconstructed hologram displayed an inflection at the radius corresponding to the step. The presence of the density step entered into the interpretation of CO_2 laser transmission (Section 5.6).

For times following time of pinch at $t_h = 0$ nsec, the centerline density dropped off, and density at $r > 2$ mm dropped noticeably for $t_h < -40$ nsec. The

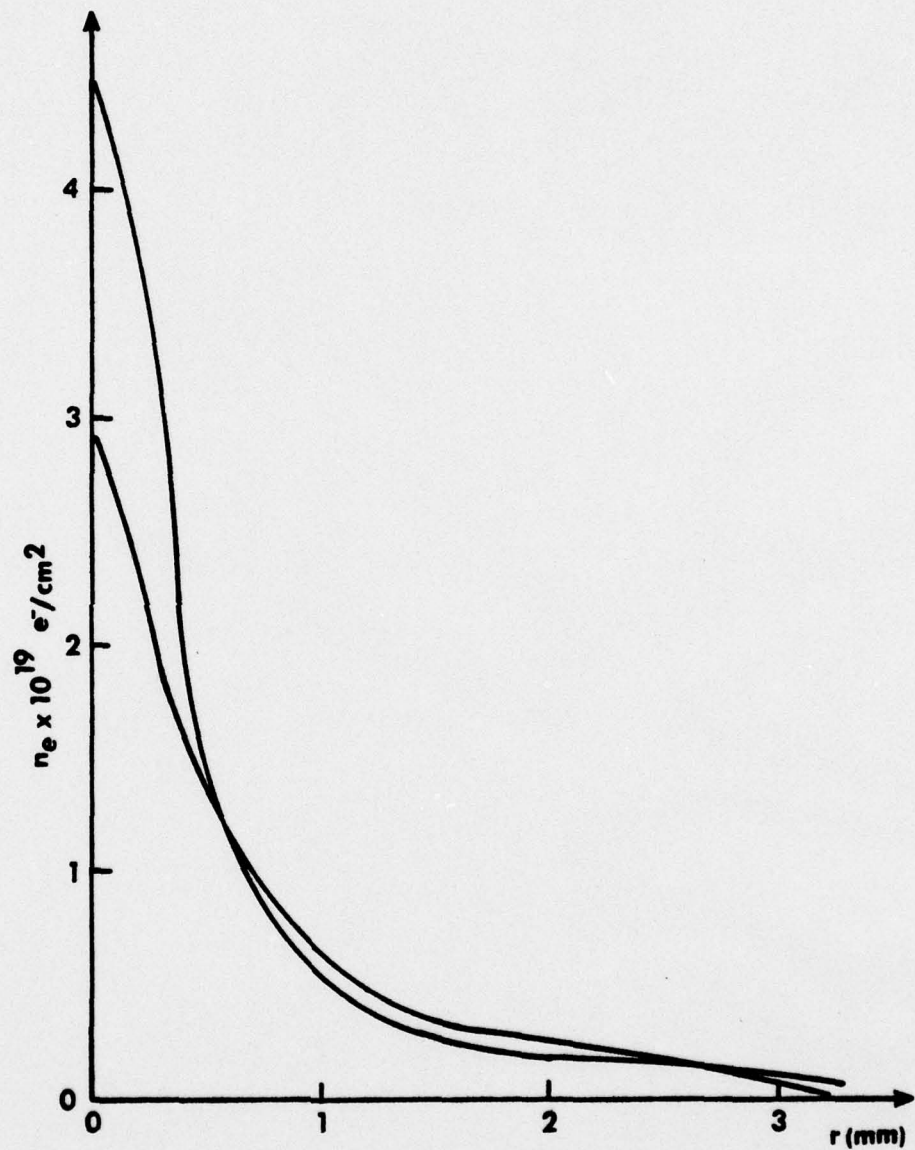


FIGURE 5.10 SHOT-TO-SHOT VARIATION - DENSITY PROFILES
AT PINCH FOR TWO DIFFERENT SHOTS

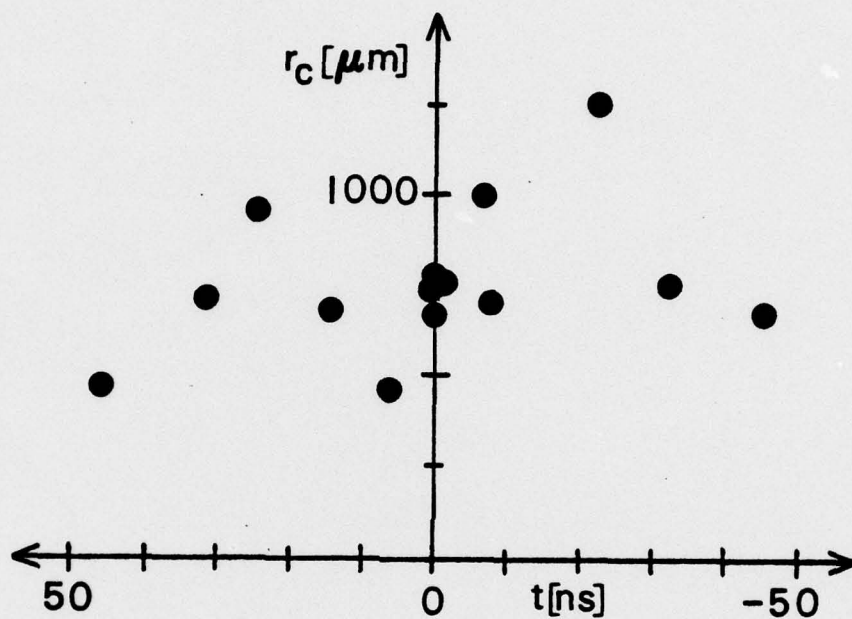


FIGURE 5.11 CRITICAL RADIUS VS. TIME TO PINCH

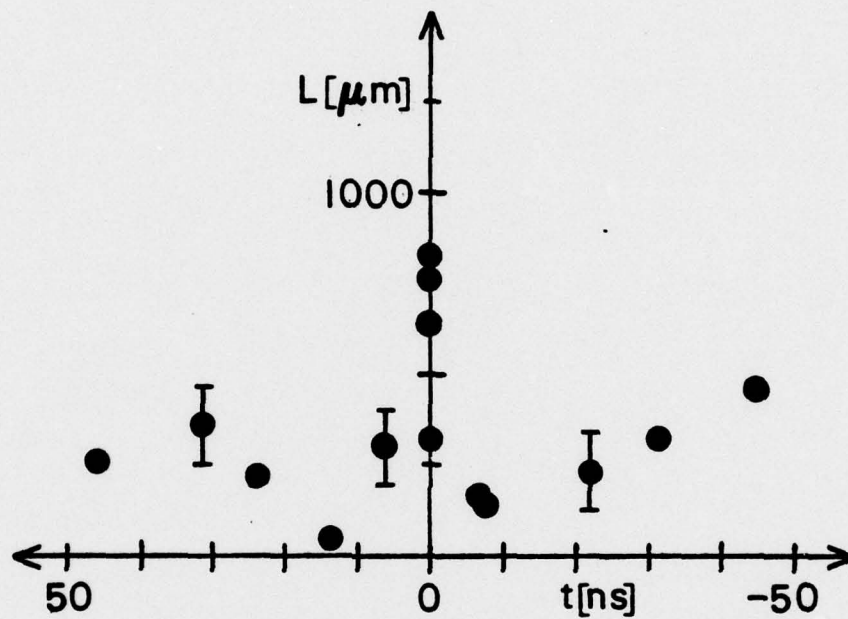


FIGURE 5.12 CRITICAL SCALE LENGTH VS. TIME TO PINCH

shape of the profile for $t_h < 0$ nsec differed from that for $t_h > 0$ nsec in that the centerline density was less and densities at about $r = 1$ mm were greater for $t_h < 0$ nsec. At about 80 nsec after time of pinch, the electron density dropped below critical.

Although each density profile in Figure 5.9 corresponded to one hologram, the shape at a particular t_h was found to be typical of several holograms taken at a particular time. By comparing the density profile extracted from one hologram taken at $t_h = 0$ nsec (Figure 5.3) to another (Figure 5.6), an indication of the shot-to-shot variation of the profile was made. Figure 5.10 plots the density profile of both holograms on a common coordinate system.

Of natural interest in the study of a plasma to be used as a laser target was its critical radius, r_c , and its critical scale length, L , given by

$$L = - \left(\frac{dn}{dr} \Big|_{r=r_c} / n_c \right)^{-1}$$

A plot of critical radius vs. t_h appears as Figure 5.11. This showed no trend except a general increase from $t_h = 10$ nsec to $t_h = -25$ nsec. The critical scale length vs. t_h is displayed in Figure 5.12. Since the critical scale length is a quantity derived from

density points read on either side of the critical radius, the error associated with it was much larger than that associated with the density at such a point. Use of the general error propagation formula,

$$\sigma_u^2 = \sum_{i=1}^n (\partial u / \partial x_i)^2 \sigma_{x_i}^2$$

u = a quantity derived from the measurements x_1, x_2, \dots, x_i ,

σ_{x_i} = uncertainty associated with x_i

σ_u = uncertainty associated with u

indicated an error of $\pm 100 \mu$ associated with L , as shown in the figure. The temporal oscillation in L was a result of the density step near critical density mentioned earlier. At $t_h = 15 \text{ nsec}$ and $t_h = -10 \text{ nsec}$, Figure 5.9 shows the steeper slope than the smooth profile seen at pinch time.

5.2 Evolution of discharge - discussion

The experimental investigation of plasma evolution provided density profiles at various times relative to time of pinch, which, in turn, provided values of critical radius and critical scale length. In addition, time from discharge initiation to time of pinch was found, although only approximately due to uncertainty

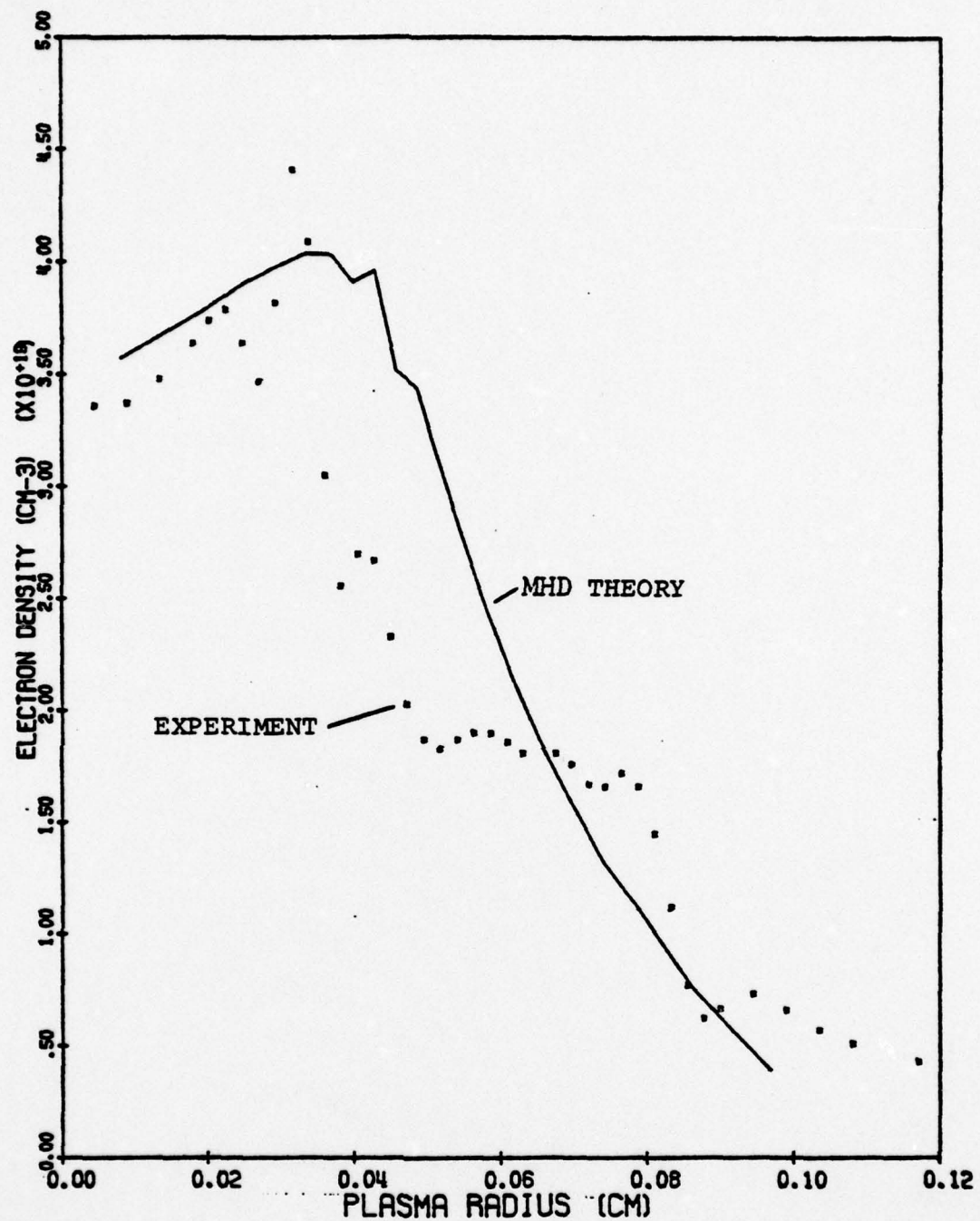


FIGURE 5.13 COMPARISON OF THEORETICALLY AND EXPERIMENTALLY OBTAINED ELECTRON DENSITY PROFILES

in time of current flow initiation.

Comparison of these parameters to a theoretical model was possible. A one-dimensional, two-temperature Lagrangian MHD computer code was developed concurrently with the experimental work (Chapin, Duderstadt, & Bach, 1974; Duston et al., 1977). By using such a code, plasma parameters not readily measurable in experiments, such as effective ionization, electron and ion temperature, and plasma magnetic field, were calculated.

For this modeling to be credible, it had to reasonably model the measurable parameters of the experiment. Since the code was one-dimensional, modeling of the multi-dimensional effects, especially the z-axis dependences mentioned in Section 5.1, was not achieved, but surprisingly good agreement was seen in the comparison of experimental values with the calculation.

Figure 5.13 displays the density profile at time of pinch as calculated by the MHD code (solid curve) and as found by inversion of a fringe read in the fractional manner (points). In the area of interest in this laser-plasma interaction experiment, that is, approaching the critical radius, the agreement was within the error associated with the experimentally-determined density. The density shelf indicated by the points was not reflected in the MHD code calculation, and was

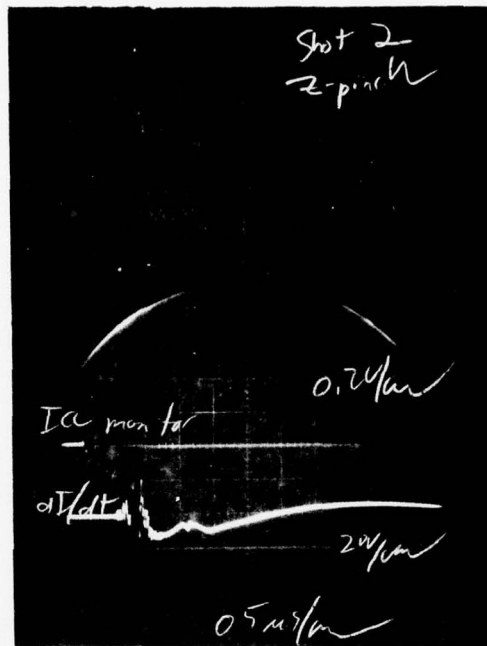


FIGURE 5.14 di/dt VS. TIME (BOTTOM) SHOWING
 POSITIVE SPIKE ASSOCIATED WITH
 SPARK GAP NOISE (500 nsec/div)

perhaps a manifestation of the multi-dimensional nature of the problem. The peaking of the density profile at a point different than the centerline was seen in both cases. However, the error associated with the density extraction procedure at radii less than 0.3 mm was rather large, 15% and approaching 25% at centerline (Section 3.4). Detailed comparison of these two plots, or in fact of any two experimentally obtained density plots, is not valid for the portion of the column for which $r < 0.3\text{mm}$. The critical radius obtained by either method agreed well within experimental error. The critical scale length differed in the experimental value of $90\ \mu$ from that predicted by the code, $220\ \mu$. Since the density step seen in the experimental plot did not appear in the calculated profile, this was not surprising.

Another experimental parameter available for comparison with calculation was the time from initiation of current flow to time of pinch. The code run predicted pinching at about 800 nsec after discharge initiation. Experimental data indicated pinch time not earlier than 900 nsec after discharge began. However, spark gap noise on the current trace made precise determination of discharge initiation time very difficult (Figure 5.14). Also, the term "time of pinch" was not precisely defined on the experimentally determined density plot, and in

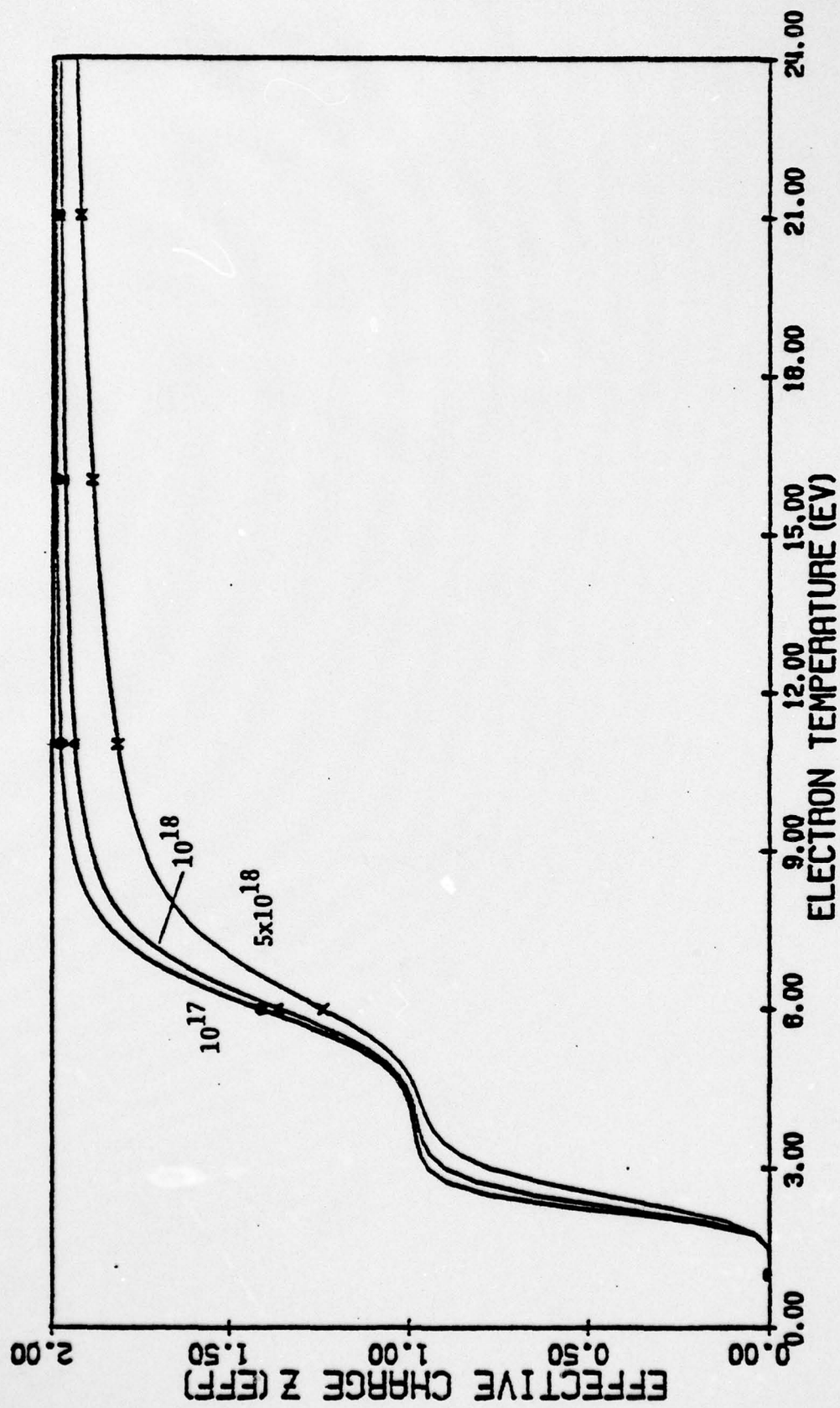


FIGURE 5.15 EFFECTIVE IONIZATION VS. TEMPERATURE (MHD CODE)

AD-A050 773

MICHIGAN UNIV ANN ARBOR LASER PLASMA INTERACTION LAB F/G 20/9
CRITICAL LAYER PENETRATION IN A COLD Z-PINCH PLASMA BY HIGH-INT--ETC(U)
SEP 77 J G ACKENHUSEN AFOSR-77-3349

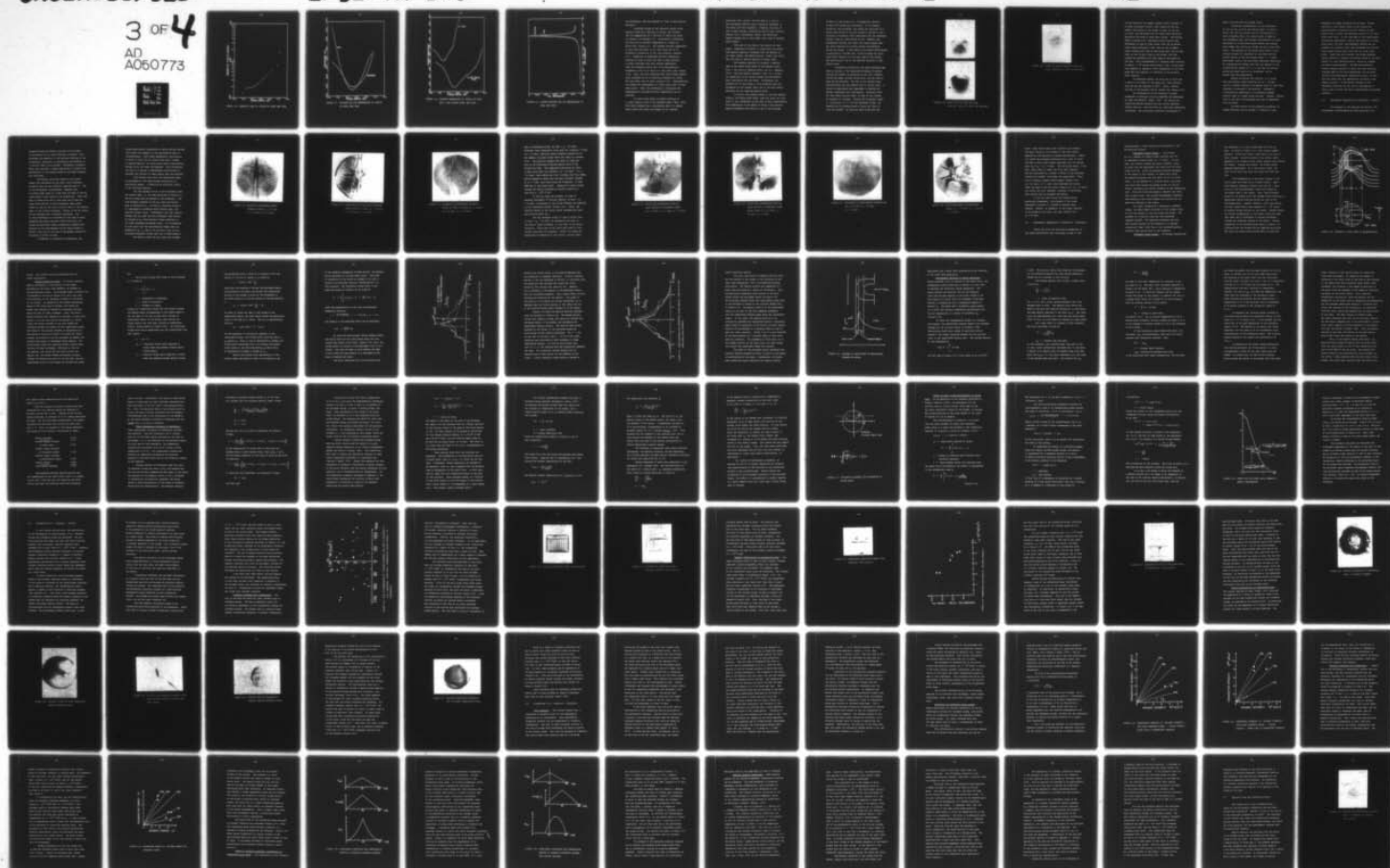
UNCLASSIFIED

LPIL-TR-100

AFOSR-TR-78-0352

NL

3 OF 4
AD
A050773



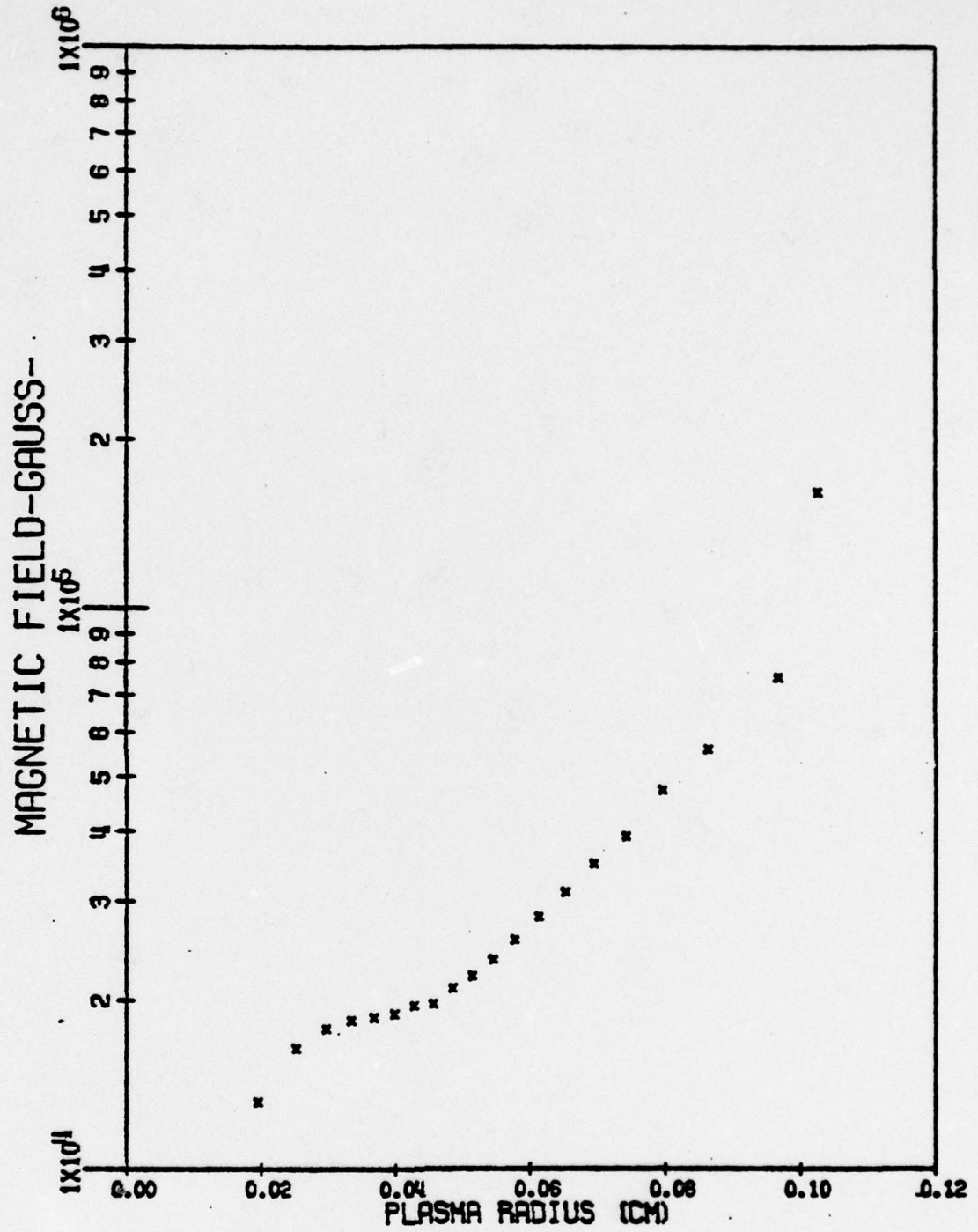


FIGURE 5.16 MAGNETIC FIELD VS. RADIUS AT PINCH (MHD CODE)

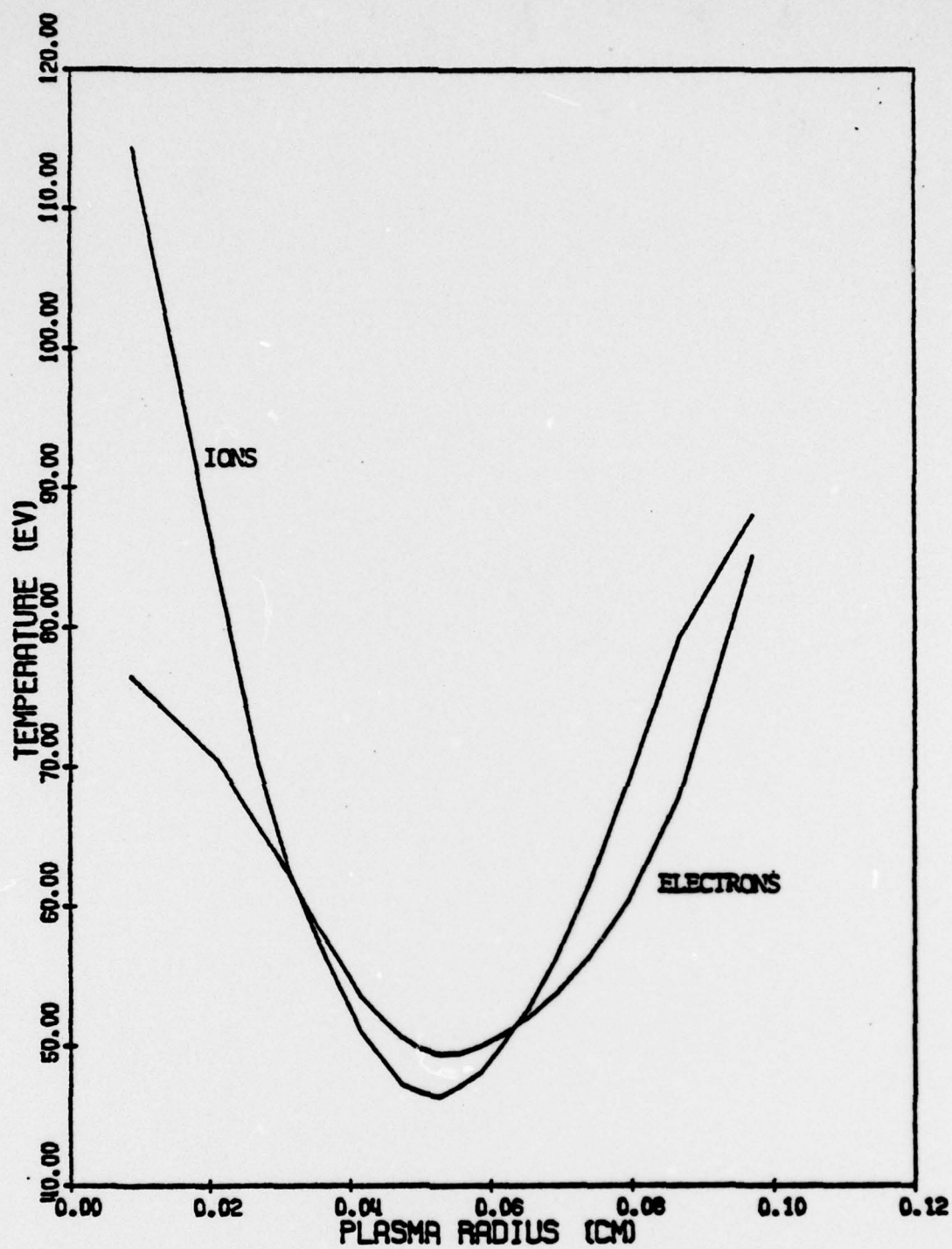


FIGURE 5.17 ELECTRON AND ION TEMPERATURES VS. RADIUS
AT PINCH (MHD CODE)

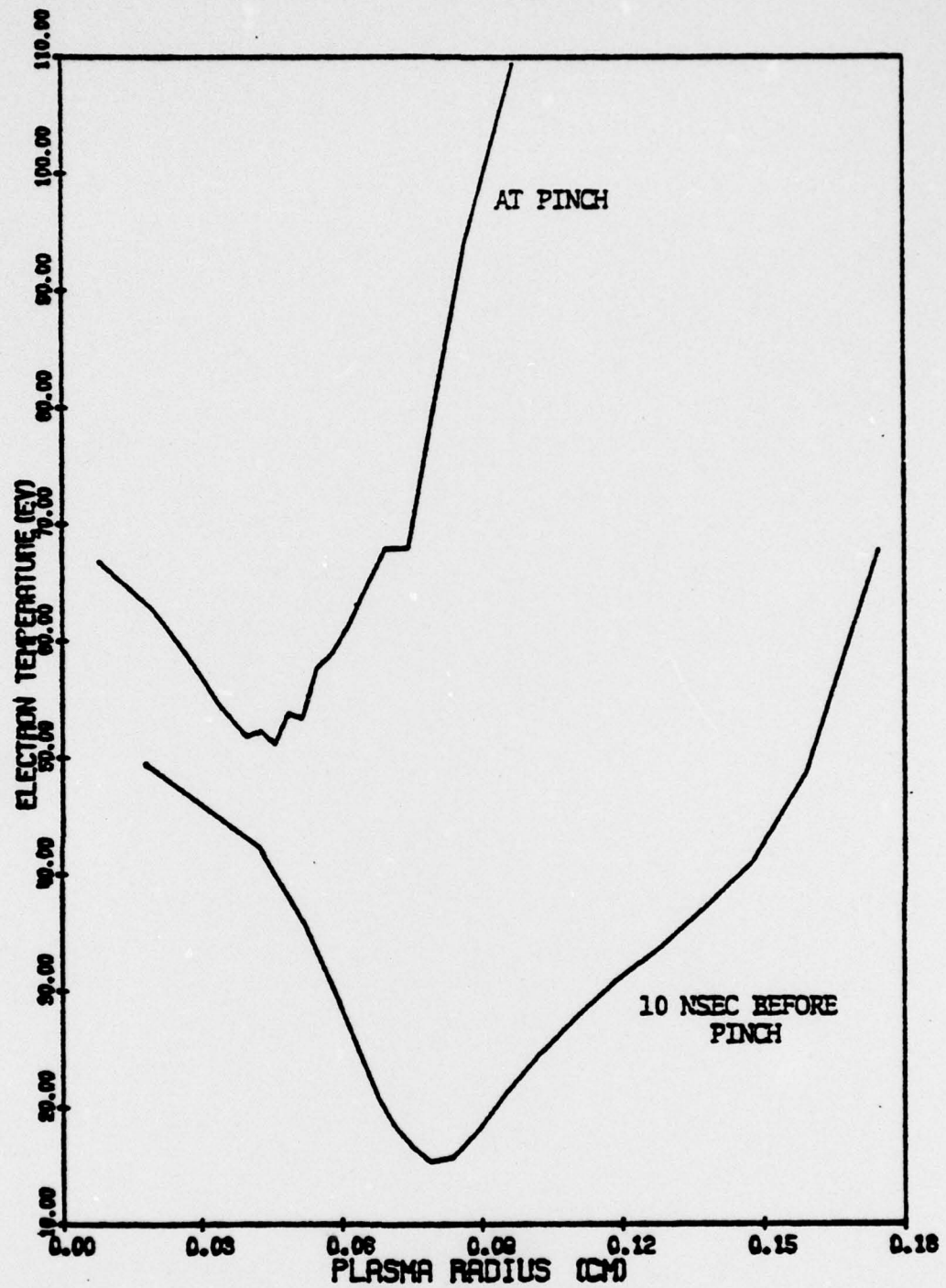


FIGURE 5.18 ELECTRON TEMPERATURE VS. RADIUS AT PINCH
AND 10 NSEC BEFORE PINCH (MHD CODE)

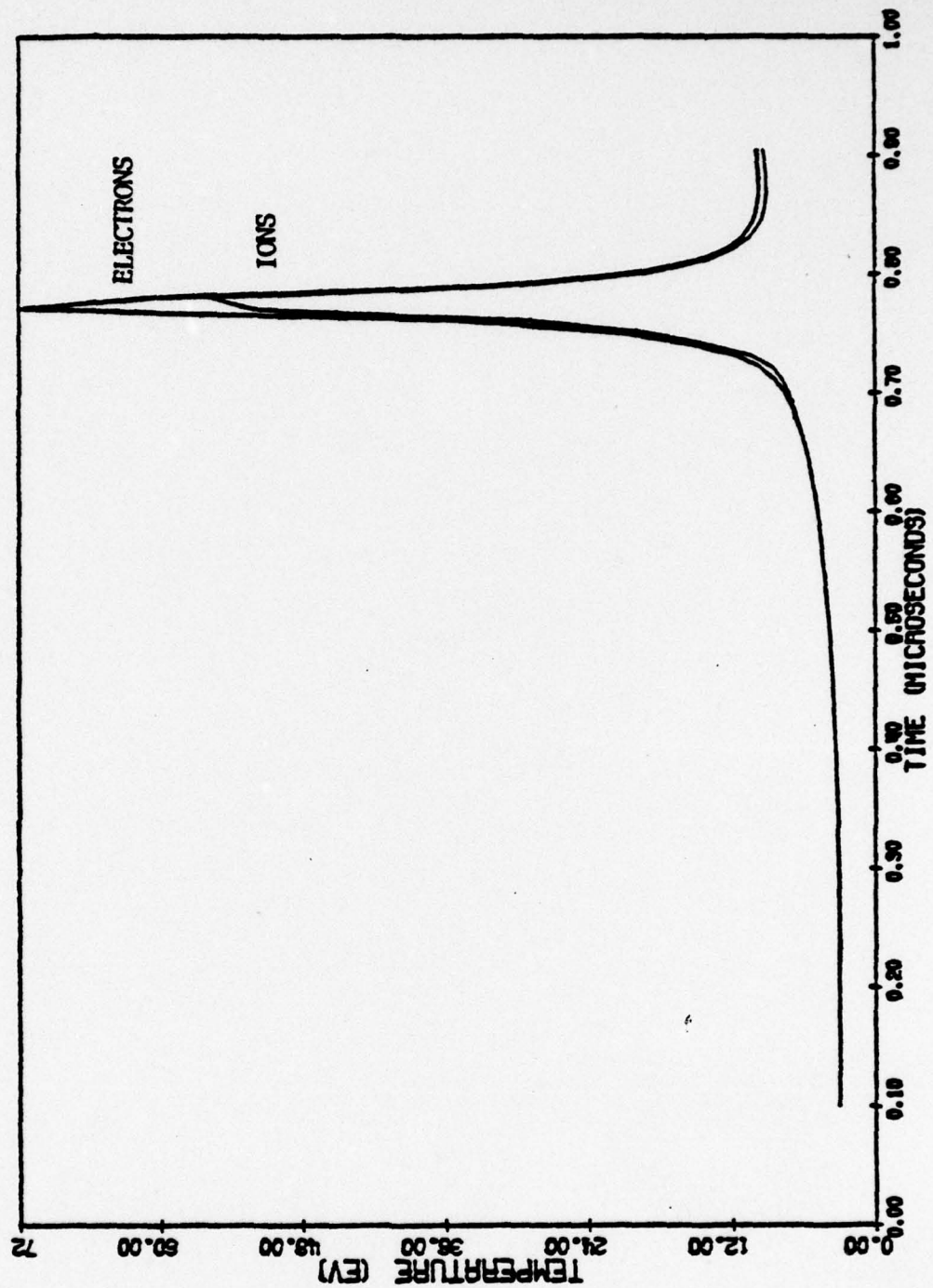


FIGURE 5.19 AVERAGE ELECTRON AND ION TEMPERATURES VS.
TIME (MHD CODE)

the discussion, has been equated to "time of peak optical emission."

Predicted values of the effective charge state, magnetic field as a function of radius, and electron and ion temperatures as a function of radius are shown in Figures 5.15 through 5.17. Particularly interesting was the plot of electron temperature vs. radius at pinch time, Figure 5.17. The average electron temperature at this time was about 70 eV, well above the 40 eV threshold of detection of the x-ray detector (Section 4.2). Comparison of predicted electron temperature profiles at time of pinch and just 10 nsec previous to pinch indicated that this average temperature rose from something below this 40 eV detectability threshold to the 70 eV value in a very short time (Figure 5.18). Also, the code indicated that this average temperature exceeded the 40 eV detection threshold for about 200 nsec after time of pinch (Figure 5.19). Experimentally, the plasma had disassembled for times later than 150 nsec after pinch. Thus, the difference in calculated and experimentally inferred electron temperatures was unresolved.

An often-cited model of plasma evolution in a linear dynamic pinch is the snowplow model (Uman, 1964). This model assumes that a cylindrical shell of current moves toward the center and sweeps up all charged

particles like a piston, driving them in a ring of ever-increasing density which eventually coalesces in the center and then reexpands. Temporal evolution of such a model yields a contracting ring of high electron density with a low-density center, and centerline density remains low in this model until time of minimum shell radius.

This was not the case in the results of this study. Inspection of Figure 5.9 shows that the centerline density generally increased with the density at any other radius, and peaked earlier, rather than later, than the time of density peaking at larger radii.

The snowplow analysis is actually a specific case of the planar shock model of the dynamic pinch, with γ , the ratio of specific heats, set to 1 (Roberts, 1972). The more general analysis, with $\gamma \neq 1$, allows for separation of the current piston and the density shell associated with the shock. Furthermore, low conductivity of the plasma or slow pinching allow for thickening of the current shell due to the skin effect, smoothing out the expected density shell.

Of course, the snowplow model or its more general version, the planar shock model, does not allow for variation in the z -dimension as was seen in this investigation. From examination of the manner in which a high density region propagated from bottom to top of the hologram

(Figure 5.2 and Figure 5.4), a propagation velocity of about 10^6 cm/sec was calculated. In the imaging system for the holograms, the plasma was inverted, so a motion from bottom to top was actually a motion in the direction of electron drift associated with the discharge current, that is, from bottom to top. However, the propagation velocity was about five times greater than the drift velocity for uniform current distribution across the column. A more shell-like current distribution, as predicted by the MHD code, would increase the calculated drift velocity at the outer edge of the column, and could bring it up to the observed velocity of this density wave.

A surprising observation was made concerning the time in the dip in the time-rate-of-change of current through the plasma, as monitored by the coil windings around the copper current return path, and the time of peak optical emission. The dip in the current trace occurred about 200 nsec before time of optical peak. A series of experiments was undertaken to confirm and further understand this discrepancy. Holograms taken 200 nsec before optical peak, at time of dip, showed no evidence of a plasma. Because the holograms viewed a 1 cm portion of a 17 cm long discharge column, the possibility of pinching above or below the field of view was studied. By drilling small holes near the

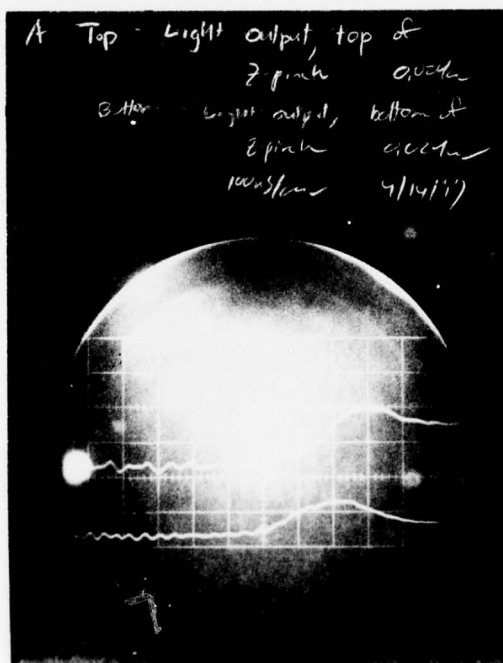
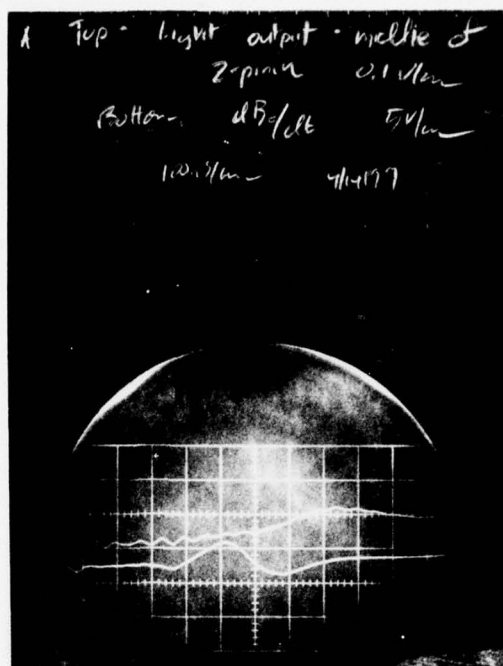


FIGURE 5.20 LIGHT PULSE VS. TIME AND AXIAL
 POSITION; dI/dt VS. TIME (100 nsec/div)

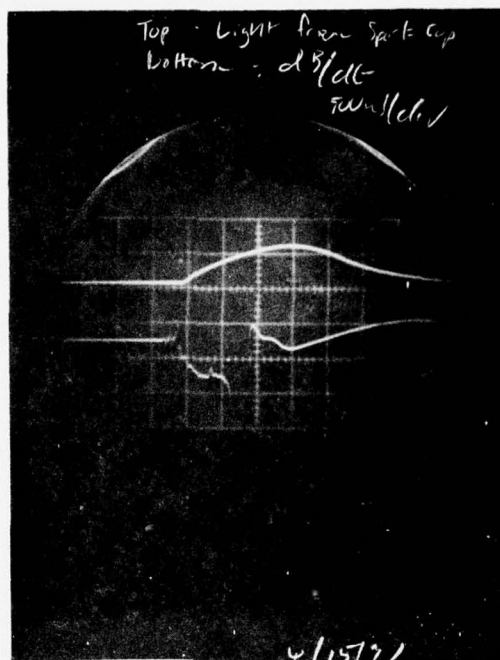


FIGURE 5.21 SPARK GAP OPTICAL EMISSION (TOP) AND dI/dt (BOTTOM) VS. TIME (500 nsec/div)

top and bottom of the copper current return cylinder of an early prototype Z-pinch, light output at the top, middle, and bottom of the column, as well as the dip in dI/dt , was monitored with PIN diode light detectors mounted at the ends of fiber optic cables. The results, shown in Figure 5.20, indicated no more than 80 nsec difference in time of light output from top to bottom. Light output occurred 40 nsec later at the standard center viewing port than at the bottom port, and 80 nsec later at the top port than at the bottom, with the current dip preceding the light peak at the center by 200 nsec. This corresponded to a luminous front velocity of about 2×10^8 cm/sec from bottom to top, in the direction opposite to apparent Z-axis propagation in the holograms and also opposite to direction of the electron drift velocity.

To determine whether the early dip in dI/dt was a result of an effect in the spark gap, light emission from the gap was compared to dI/dt . Again, nothing was seen to distinguish time of current dip (Figure 5.21).

An investigation of the coupling of plasma parameters to external circuit parameters was undertaken by Steel and Mehlhorn (Steel, 1976). By solving the Leontovich-Osovets equation and the circuit equation, plasma radius vs. time and dI/dt vs. time were numerically calculated. The calculation predicted coincidence of

time of dip and time of minimum radius.

A possible interpretation of the difference of time of dip in dI/dt and optical peak, or time of pinch, was that the current was not distributed in a thin collapsing shell, but rather moved in ahead of the collapsing shell and reached a distribution of high inductance at a time before peak density was reached. This sudden high inductance caused the dip in the dI/dt trace. The analysis of the planar shock model of the Z-pinch allowed for separation of the shock and the current piston in any case except where $\gamma = 1$ (snow-plow model, used in the previously mentioned simulation). No interpretation further than that the results of the simulation may change for $\gamma \neq 1$, and that the current piston and shock need not be coincident, can be gained from this explanation.

Before concluding this section, it is noted that the central clump occurring for $t_h < -30$ nsec was not a regular feature of holograms taken at this time, although it occurred in the majority. Frequently, a distribution reminiscent of a hyperbolic-shaped cooling tower of a power plant was seen. However, nothing else in the shots distinguished one type of appearance from the other.

The main points of the preceding discussion of plasma evolution are as follows: A definite z-axis

dependence on plasma distribution was seen. Plasma evolution in the target region of the plasma was characterized by attaining critical density 50 nsec before time of pinch, and remaining critical to 80 nsec after pinch time. In the time span of the laser-plasma interaction experiments, from 35 nsec before to 35 nsec after pinch, the only time-dependent feature was the presence of a density shelf that decreased the critical scale length before pinch time from its value after pinch. Other than this feature, the plasma remained fairly constant in density and profile shape in the time period, or, more pessimistically, varied in a manner not easily characterized. The MHD code predicted electron density profile at pinch time with accuracy, although some of its other predictions did not match as well with experimental observations which, in turn, were not known with the experimental accuracy of the density profile. Of particular interest in the discharge evolution was the lack of coincidence in time of dip in dI/dt and time of peak density and plasma emission.

5.3 Holographic appearance of interaction - results

As discussed in the previous two section, the holographic interferograms provided spatially- and

temporally-resolved density profiles of the plasma in the region of CO₂ laser radiation incidence. This knowledge was essential in the physical modeling of the interaction, especially in determining the presence of a critical layer in the plasma. Holographic interferometry also provided a unique opportunity to observe the perturbation of the plasma column by the high-intensity CO₂ laser beam.

The density and scale length of the target plasma were determined by the point along discharge evolution that the CO₂ radiation impinged upon it. Use of the holographic interferogram depended upon its having been taken at a time near the peak of the CO₂ laser pulse to show signs of the interaction. Thus, the goal in these shots was to fire both the 38 nsec CO₂ laser pulse and the 16 nsec holography laser pulse within 10 nsec of the time of pinch, that is, the optical peak, of the Z-pinch discharge. Timing of the two lasers to the discharge was of extreme importance. The 40 nsec uncertainty in occurrence of the time of pinch prevented any better pre-shot timing than this, although the post-shot timing diagnostics allowed determination of the time between the two laser pulses to within 5 nsec and of the time of holography relative to the pinch to within 15 nsec.

In addition to qualitative information, one

gained quantitative information by making certain assumptions about the symmetry of the perturbation seen in interferograms. Using these assumptions, particularly on shots in which the CO₂ laser fired upon a plasma of maximum density, the large-scale density perturbation brought on by the laser was measured. This information was used in a series of hydrodynamic calculations to estimate the fraction of laser energy that was absorbed.

This section sets forth the observations made by holography of the laser-plasma interaction in a qualitative manner. A quantitative discussion occurs in the following section.

The time between firing of the holography laser and optical peak, t_h , has been mentioned in Section 5.1. Two more times must be defined in the discussion. The time between incidence of the CO₂ laser and optical peak is defined as t_i . As with t_h , positive values of t_i correspond to incidence before optical peak, and negative values, after. Furthermore, the time interval between the CO₂ laser and the holography laser pulses is defined as t_1 , with positive values referring to CO₂ laser preceding holography laser. It is suggested at this point that the conscientious reader mark the meanings of t_h , t_i , and t_1 on his shirt cuff, as the following discussion relies upon use of these symbols.

For shots in which the CO₂ laser was incident

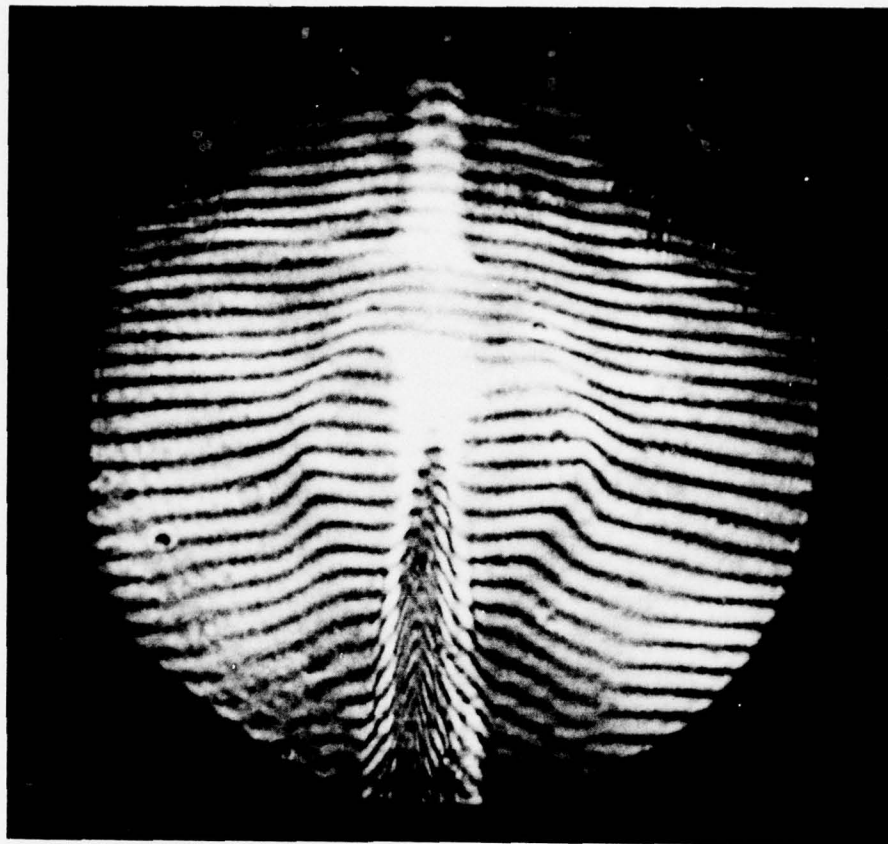


FIGURE 5.22 BLOW-OUT OF UNDERDENSE TARGET
PLASMA BY LASER ($t_h = 66$ nsec;
 $t_i = 76$ nsec; $t_l = 10$ nsec)

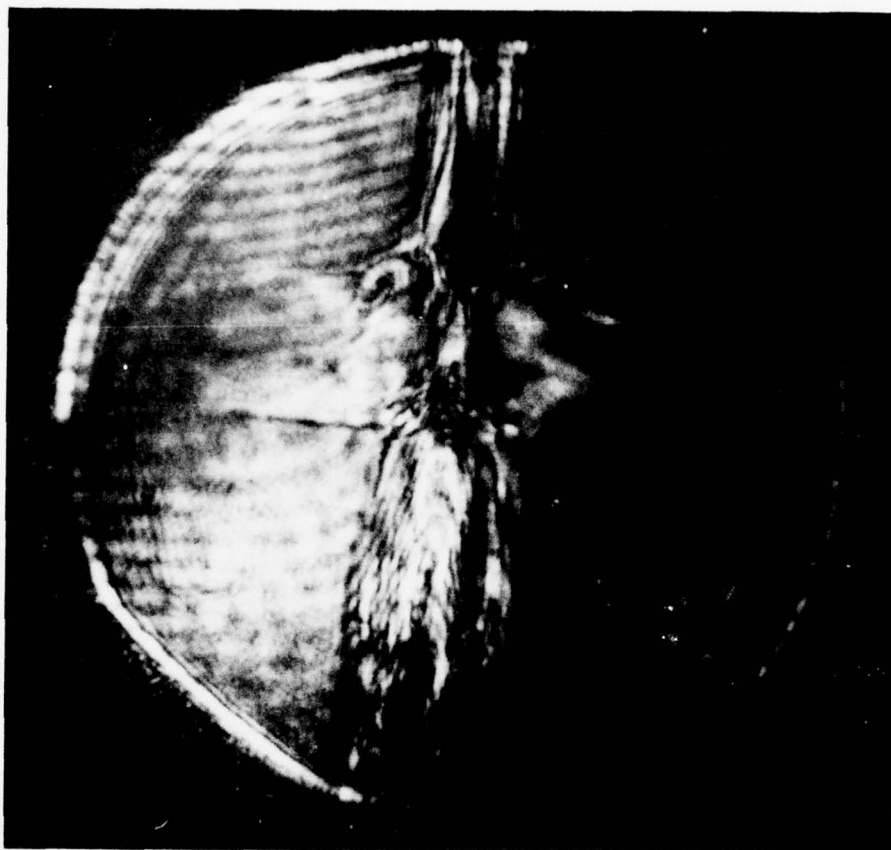


FIGURE 5.23 CONstriction OF MARGINALLY-OVERDENSE
TARGET PLASMA BY LASER ($t_h = 32$ nsec;
 $t_i = 36$ nsec; $t_l = 4$ nsec)



FIGURE 5.24 BEGINNING OF PERTURBATION BY LASER -
TWITCH AT RIGHT OF COLUMN ($t_h = 6$ nsec;
 $t_i = 16$ nsec; $t_l = -10$ nsec)

upon an underdense plasma ($80 \text{ nsec} > t_h > 50 \text{ nsec}$) holograms taken immediately after peak CO_2 intensity ($0 \text{ nsec} < t_1 < 20 \text{ nsec}$) indicated nearly complete blowing out of the segment of plasma column which the laser hit (Figure 5.22). The blown-out segment was about 10 times the size of the diffraction-limited central disc of the focused CO_2 beam. This appearance persisted for about 20 nsec after peak CO_2 intensity ($t_1 = 20 \text{ nsec}$). At $t_1 = 20 \text{ nsec}$, laser energy was still incident upon the plasma, having dropped to about half the peak intensity reached at $t_1 = 0 \text{ nsec}$ (the laser pulse was triangular, 38 nsec FWHM and 76 nsec base width). Reading of a Moire fringe through the region indicated an electron density of less than $2 \times 10^{18} \text{ e}^-/\text{cm}^3$.

If the CO_2 laser was incident at times of marginal attainment of critical density, $50 \text{ nsec} > t_1 > 35 \text{ nsec}$, a narrowing of the column diameter was observed at the interaction height (Figure 5.23). Again, the vertical extent of the narrow region exceeded the focal spot size by about ten.

For CO_2 incidence within 35 nsec of pinch time, $35 \text{ nsec} > t_1 > -35 \text{ nsec}$, an indentation was seen on the side of laser incidence, to the right in the reconstruction. Since most of the shots were taken in this regime, more data was examined. Figure 5.24 shows the beginnings of formation of this cavity, and was taken

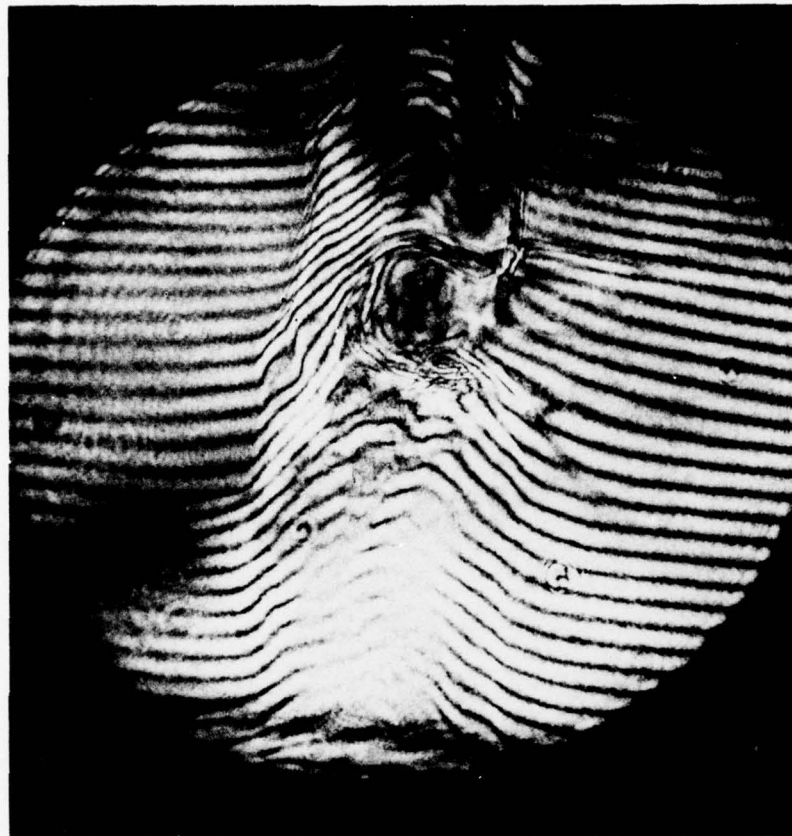


FIGURE 5.25 CAVITY-LIKE PERTURBATION FROM CO₂
LASER INCIDENT ON OVERDENSE PLASMA
($t_h = 0$ nsec; $t_i = 0$ nsec; $t_l = 0$ nsec)

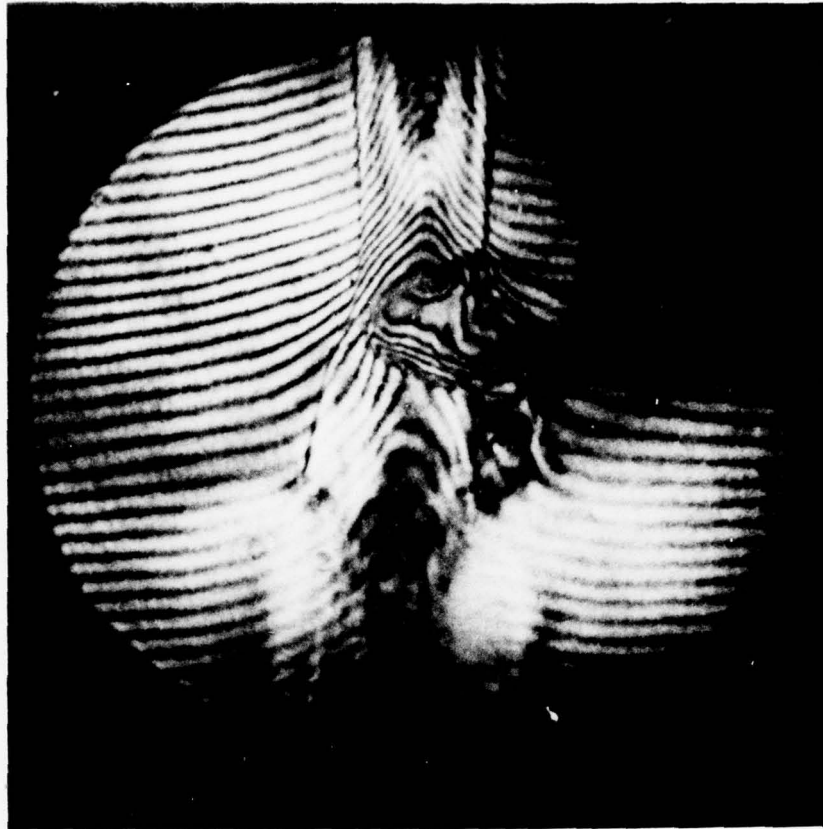


FIGURE 5.26 CAVITY-LIKE PERTURBATION FROM CO_2
LASER INCIDENT ON OVERDENSE PLASMA
BEFORE PINCH ($t_h = 24$ nsec; $t_i =$
24 nsec; $t_1 = 0$ nsec)

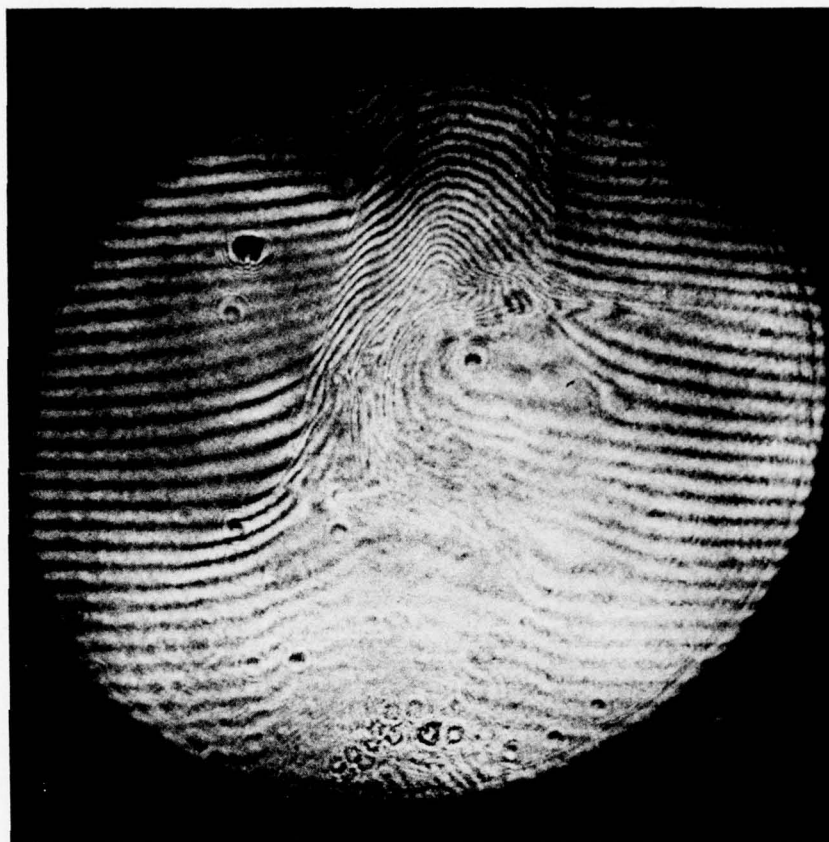


FIGURE 5.27 RELAXATION OF LASER-INDUCED PERTURBATION
($t_h = -15$ nsec; $t_i = 17$ nsec;
 $t_l = 32$ nsec)

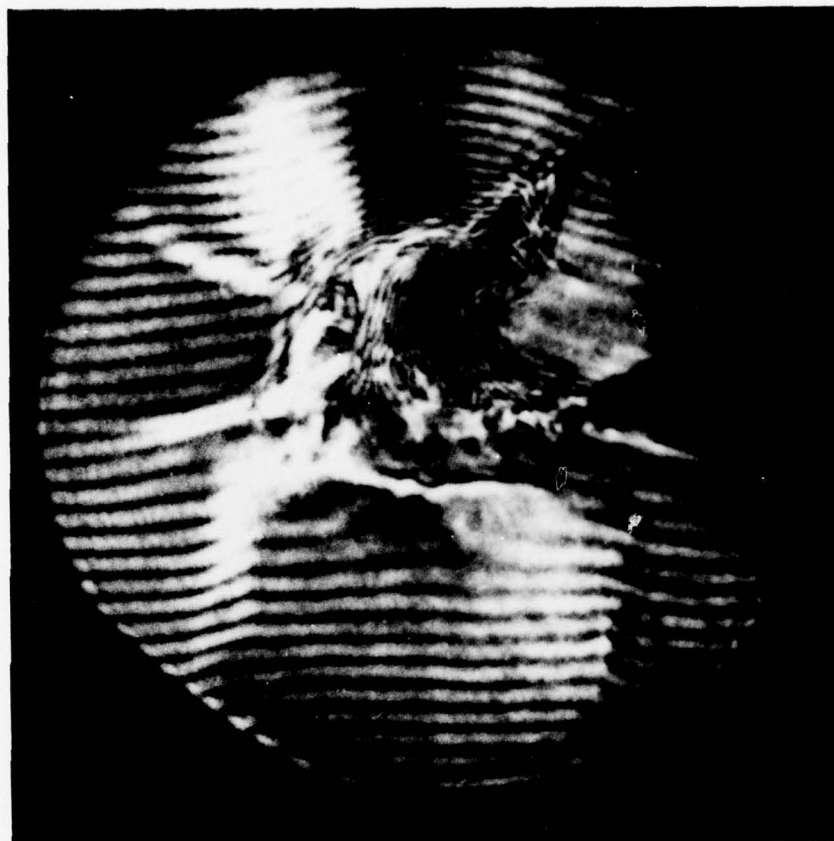


FIGURE 5.28 LASER PERTURBATION ON POST-PINCH
PLASMA ($t_h = -60$ nsec; $t_i = -27$ nsec;
 $t_l = 33$ nsec)

about 5 nsec before peak laser intensity was reached. The small twitch in the fringes at the laser height appeared as the beginning of plasma perturbation. Figure 5.25 shows the hologram associated with a shot in which the peak of both laser pulses coincided with the optical peak ($t_h = t_i = t_l = 0$ nsec). The cavity was about 1.3 mm high, again about 10 times the focal spot diameter, and was surrounded by a border of about 0.5 mm thickness. Outside this border, the plasma was unperturbed. Shots with a slightly younger target plasma (Figure 5.26, $t_h = 24$ nsec; $t_l = 0$ nsec) also displayed the cavity. After the peak of the CO_2 pulse (Figure 5.27, $t_l = 37$ nsec), the cavity was still apparent, although it had become more shallow and had expanded vertically.

If the CO_2 laser struck the plasma during post-pinch disassembly, the presence of the clump mentioned in Section 5.1 tended to obscure laser effects. However, an asymmetry of the clump, believed to be caused by the laser, was seen (Figure 5.28, $t_h = 50$ nsec).

5.4 Holographic appearance of interaction - discussion

Having set forth the qualitative appearance of the laser perturbation upon the plasma as seen in the

interferograms, a more quantitative discussion of the perturbation follows.

Underdense target plasma. - The blowing out of a segment of plasma column occurred only for an underdense target plasma ($t_i > 50$ nsec). At this time, the current through the pinch, steadily rising as pinch time was approached, was lower than its pinch value of 80 kA. Since the magnetic pressure decreases as the square of the current, at these early times, the magnetic pressure was only about 70% of its pinch value. In the absence of a critical layer, the radiation could have heated the plasma column all the way across, increasing its kinetic pressure as the temperature rose. Since the confining magnetic pressure was lower than at pinch time, this allowed hydrodynamic expansion from heating of the column segment and yielded the low densities observed in the region.

For laser incidence on a marginally overdense plasma, the same blowoff occurred at outer plasma radii, but did not extend all the way across the column. The presence of a critical layer may have prevented complete blowoff. The remaining conductor may have been further pinched by the formation of a sausage instability (Uman, 1964) due to the increased magnetic pressure from constriction of the conductor.

Overdense target plasma. - Of extreme interest was

the appearance of a cavity associated with the CO₂ beam. As noted in Figure 5.25, three regions seemed apparent. Within the cavity, there was little sign of Moire fringes. Around the edge of the cavity, there appeared to be fringes of much closer spacing than outside the region. Outside this border, the plasma column appeared unperturbed. As in the earlier cases, the size of the cavity was about ten times the focal spot size.

The disappearance of the Moire fringes in the cavity might have been due to several things. Small-scale density gradients, smaller than the 160 μ resolution of the interferometer, might have broken up the object beam in the region. Also, rapid directed motion of the plasma could have caused fringe blurring if appreciable motion occurred during the time of the holography pulse. Rockett (Rockett, 1977a) has estimated that plasma motion must approach 2.5×10^6 cm/sec to produce fringe blurring by this means. Another reason for fringe disappearance in the region could have been that there was no difference in optical pathlength through the different regions of the cavity. Careful inspection of the reconstruction shown in Figure 5.25 indicated that the fringes did not approach the cavity and stop, but rather moved either above or below the

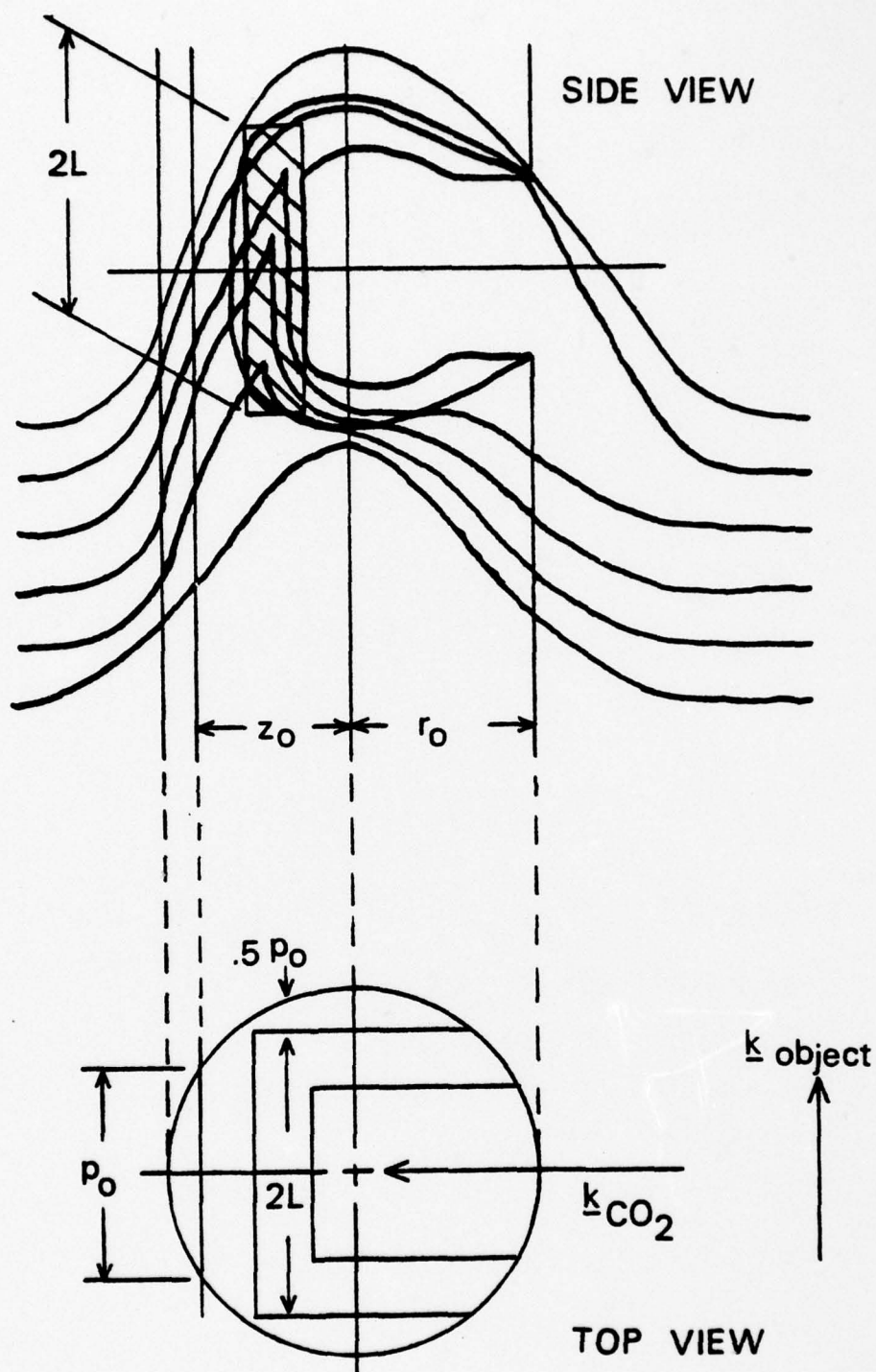


FIGURE 5.29 GEOMETRY OF SHOCK FRONT IN RECONSTRUCTION

region. This effect would be associated with the latter explanation.

Density profile in shock. - To obtain electron density information in the portion of the plasma perturbed by the laser, some symmetry was assumed in the perturbation region. The hologram shown in Figure 5.25 is sketched at the top of Figure 5.29, and a top view with direction of CO_2 incidence is shown at the bottom of the figure. As suggested by the rather rectangular shape of the cavity and its border, the cavity and border were modeled as bounded by rectangles revolved about the axis of laser incidence. Thus, the cavity-border interface was treated as a cylinder, or more accurately, a tin can with top off and bottom on, nested within the larger cylinder or can that formed the interface between the border and the unperturbed plasma. The radius of this larger cylinder is designated as L . The sketch at the top of Figure 5.29 shows the region between the bottoms of the two cylinders as shaded, and contains the region of decreased fringe spacing. The bottom sketch shows the idealized border rotated about the axis of laser incidence. Referring to the tin can analogy, the cavity was the region within the smaller can, the border formed the spacing situated between the bottoms and walls of the two cans, and the unperturbed region of the plasma was outside the larger

can.

The fraction fringe shift seen in the holograms, p , is given by

$$p = \frac{1}{\lambda} \int_{-L}^L dl(\eta - 1)$$

λ = wavelength of holography

η = index of refraction

L = boundary of region

Looking at a particular object ray that passes through the shaded region corresponding to the border ahead of the CO₂ beam, it is seen to pass first through an unperturbed region of the plasma, then through the border region, and then again through an unperturbed portion (bottom sketch of Figure 5.29). The fractional fringe shift may be subdivided into the contribution from each region:

$$p = p_0 + p'$$

p_0 = fractional fringe shift imparted to object beam from passage through unperturbed region

p' = fraction fringe shift imparted to object beam from passage through density border

The pathlength along a chord at a distance d from the center of a circle of radius r_0 is given by

$$l = 2r_0 \sin \left(\cos^{-1} \frac{d}{r_0} \right)$$

Using this and choosing d through the perturbed region, the distance of an object ray through the unperturbed portion of the plasma is given by the difference in the chord length at d and the extent of the perturbation, L :

$$l_0 = 2r_0 \sin \left(\cos^{-1} \frac{d}{r_0} \right) - 2L$$

For some z_0 toward the edge of the column in the unperturbed region, the path length across the associated chord is the same as l_0 above. This z_0 is approximately given by

$$z_0 \approx r_0 \cos \left(\sin^{-1} (1 - L/r_0) \right)$$

By the assumption of cylindrical symmetry in the unperturbed region, the fringe shift along the path at z_0 equals p_0 . Thus, p' may be determined by reading the fringe shift associated with a ray through the border which yields p , and then subtracting p_0 whose value is determined by reading a fringe at z_0 .

Knowing the fringe shift contribution of the border region and having an idea of its extent by use

of the symmetry assumptions invoked earlier, the density may be estimated in the perturbed region. The index of refraction in the region is assumed to be only a function of horizontal position, designated as z in this analysis. The fractional fringe shift in the slab-like region of Figure 5.29 is given by

$$p' = \frac{1}{\lambda} \int_{-L}^L dz (n(z) - 1) = \frac{2L}{\lambda} (n(z) - 1)$$

Using the approximation to the cold collisionless dispersion relation,

$$n = \sqrt{1 - n(z)/n_c} \approx 1 - n(z)/2n_c ; n < n_c$$

the density in the perturbed front can be extracted:

$$n(z) = \frac{p'(z)}{L} n_c \lambda$$

By using the half-integer fringe reading method and moving from the left edge inward along the line through the center of the front (Figure 5.29, top), the fringe shift p at points in the perturbed front is obtained. Care must be taken to note whether the peak of the fringe has been passed, as p decreases as one moves in beyond this point.

The error associated with the densities thus

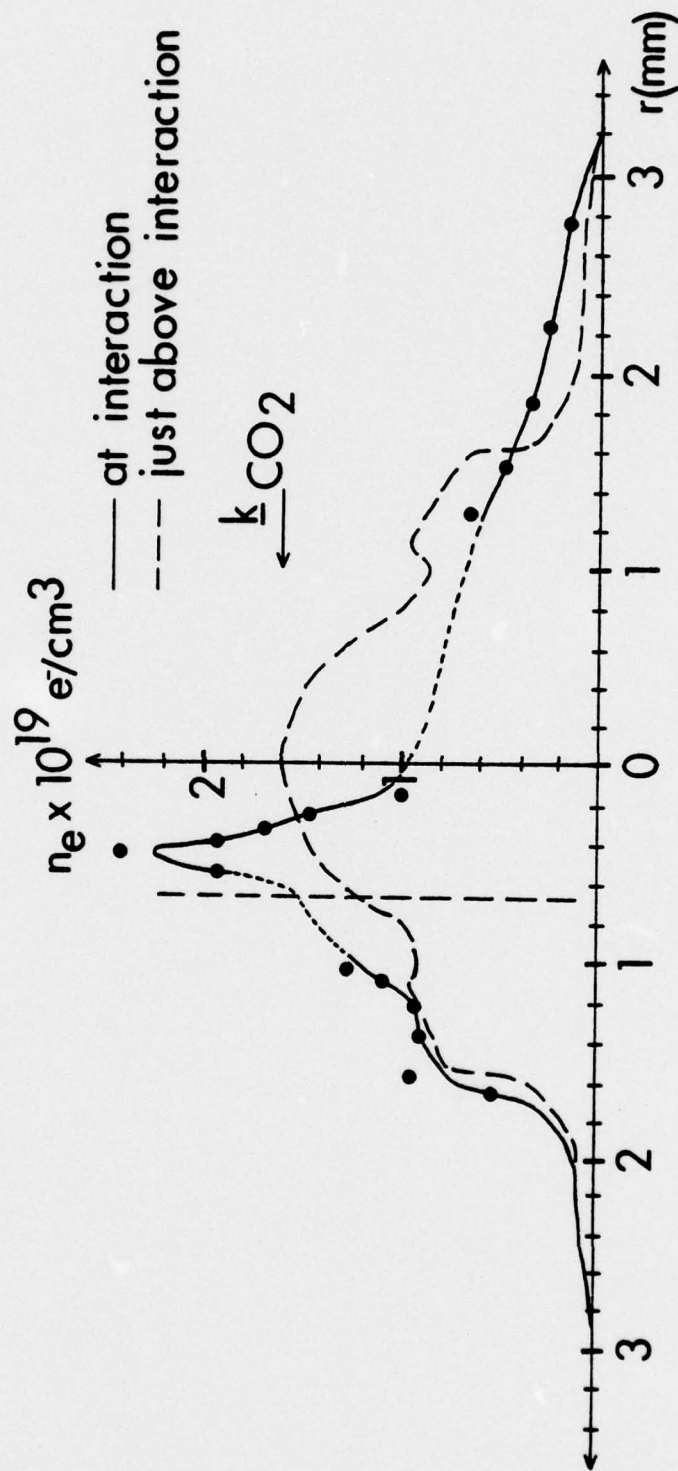


FIGURE 5.30 LASER-PERTURBED AND UNPERTURBED PLASMA DENSITY PROFILES AT PEAK LASER INTENSITY

obtained was rather large, as the method depended upon the assumption of symmetry described. An error analysis similar to the one described in Section 3.4 indicated that the densities thus obtained may exceed the actual values by 30%, and may fall short by 15%. However, for an estimate of the density in the perturbed region, this was considered adequate. Also, these values of error affected the magnitude of the density. The slope of the profile in the region was better determined, as it depended upon the fringe spacing in the region and not on the absolute fringe shift leading up to the region.

Figure 5.30 shows the density profiles obtained from the hologram in Figure 5.25. The dashed profile occurs from reading a fringe just above but outside the perturbed region of the plasma, and represents the unperturbed density profile. The dots are data points obtained at the height of the perturbed region by half-integer fringe reading techniques. For $r > 1$ mm on the left of the plot, and $r > 1.2$ mm on the right, densities were extracted by Abel inversion in these unperturbed regions. For the six data points just left of $r = 0$, the combined slab and cylindrical geometry was used. The transition regions between the two methods have no data points, as the symmetry is not clear. A curve connecting these points is dotted in

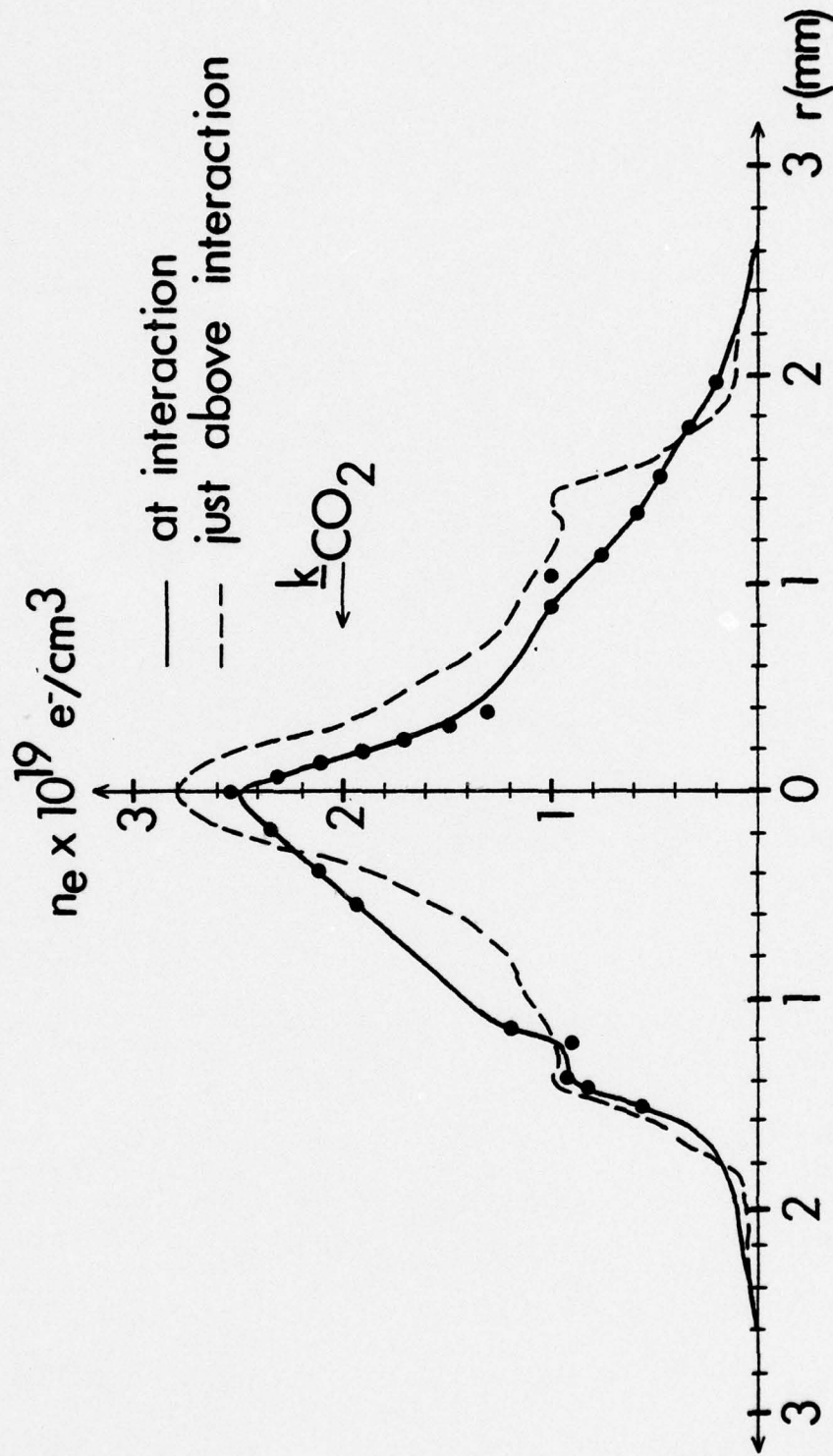


FIGURE 5.31 LASER-PERTURBED AND UNPERTURBED PLASMA DENSITY PROFILES 20 NSEC AFTER PEAK LASER INTENSITY

these transition regions.

The first item noted in comparing the two plots was the pushing of the plasma in the direction of the laser beam propagation, with a corresponding density drop behind. The density profile was suggestive of a shock front followed by a region of low density. This was physically reasonable from looking at the thick border around the perturbed region in Figure 5.25. The interface between border and unperturbed plasma seen in the hologram is marked by the vertical dashed line in Figure 5.30. The density profile in the unperturbed region at the left of the plot compared reasonably with the unperturbed reading taken above the interaction region. On the right, the density profile at the interaction exceeded the unperturbed profile, indicating some blowoff of particles in the cavity into this region. Figure 5.30 corresponds to a hologram taken at time of peak CO_2 laser intensity. Figure 5.31 is a plot attained by the same methods for a hologram taken 20 nsec after peak CO_2 intensity. The asymmetry is still seen, as is the steeper profile on the laser side, but some relaxation toward the unperturbed shape has occurred.

The plots in the perturbed region indicated that electron density exceeded critical in spite of the effect of perturbation by the laser. Furthermore, the border seen around the region exhibited the density profile

associated with a shock front propagating in the direction of the laser beam propagation.

Hydrodynamic estimate of energy absorption. -

Having obtained a plot of density in the shock front, the hydrodynamic models described in Section 2.3 were used to estimate the fractional energy absorption. The region between the vertical line at the discontinuity and the peak density in the front (Figure 5.30) was treated as a shock front of thickness Δx and peak density n_1 propagating into a homogeneous medium of density n_0 . The shock had a relaxation region behind it in which the electron temperature equilibrated with the ion temperature in a region of thickness Δx_R (Figure 5.32).

To treat the inhomogeneous plasma as a homogeneous medium, the unperturbed electron density was averaged between the two critical layers to produce a flat distribution whose total number of particles corresponded to the number contained between the two critical radii in the unperturbed density plot. The average density, \bar{n} , was determined by

$$(\pi r_c^2) \bar{n} = \int_0^{r_c} n(r) r dr$$

For the case of Figure 5.30, \bar{n} was found to be 1.14×10^{19}

e^-/cm^3 . The critical radius was chosen as the boundary for the averaging because the laser energy absorption length was at a minimum in this vicinity.

The maximum density ratio across a planar shock is given by

$$\frac{n_1}{n_0} = \frac{\gamma + 1}{\gamma - 1}$$

γ = ratio of specific heats

For $\gamma = 5/3$, for a fully ionized monatomic gas, this maximum ratio is four. The density ratio across the shock in the plot was found by setting $\bar{n} = n_0$ and using the peak density observed in the front as n_1 . The ratio n_1/n_0 was approximately two, less than the strong shock limit of four, so this shock was treated as a weak shock.

For a weak shock in a medium of zero viscosity, the front thickness is given by

$$\Delta x \approx \frac{\ell_{th}}{n_1/n_0 - 1}$$

ℓ_{th} = thermal mean free path

In this analysis, the viscosity mean free path is set to zero, since calculations indicated that it was about a factor of 40 smaller than the thermal mean free path. Thus, for $n_1/n_0 = 2$, the front thickness is on the order of the thermal mean free path. The formula for ℓ_{th} ,

$$\ell_{th} \approx \frac{\kappa(\theta_e)}{\rho c_p v_{th}}$$

was used to find what temperature was required to put ℓ_{th} equal to Δx . The shock front thickness measured in Figure 5.30 was about 180 μ , which required a temperature of about 67 eV. If both the electron and ion temperatures were equal in this region (in general not true in a plasma shock front, but treated so in this estimate), then the internal energy in this region,

$$E = \frac{3}{2} (n + n_i) V_f \theta_e$$

V_f = volume of shock front

was about 0.33 J. For an initial temperature of 20 eV before laser incidence, internal energy was about 0.10 J, so an increase in internal energy of 0.23 J was indicated in this region.

In the relaxation region behind the shock, the thickness, Δx_R , was determined by the scale over which electron heat conduction occurred. Thus,

$$\Delta x_R \approx D \tau_{eq}$$

D = average shock velocity

τ_{eq} = electron-ion equipartition time

In the particular shot under consideration, the hologram

was taken coincident with the peak intensity of the CO₂ laser, or halfway into the 38 nsec FWHM laser pulse. The distance of the shock front from the right-hand critical layer in Figure 5.30 was 1.7 mm, so a propagation velocity of 9×10^6 cm/sec was calculated for D. The equipartition time was a function of temperature (Section 3.6) and so τ_{eq} , and then the temperature, was found from the thickness of the relaxation region. Again equating the electron and ion temperatures, a temperature of 35 eV was obtained, which corresponded to an energy increase in the relaxation region of 0.11 J.

To determine the internal energy increase in the cavity region behind the relaxation region (to the right of $r = 0$ in Figure 5.30), it was assumed that the cavity was of the same temperature as the relaxation region, 35 eV. The density in the region was rather uncertain, but was taken to be an intermediate value characteristic of the transition region. The internal energy increase in the region was calculated to be 0.09 J.

An estimate of the kinetic energy associated with driving particles out of the cavity in a time corresponding to half the CO₂ laser pulse time was needed. To obtain this, an idea of the fraction driven toward the center of the plasma (into the shock

front) relative to the portion blown off toward the laser beam was needed. By comparing the number of electrons in the shock front at the time of the hologram to the number that were originally there before laser incidence, the increase in the number of particles in the shock front was compared to the number of particles available in the cavity region. Such a particle conservation calculation, using the density and the dimensions in the shock front as determined holographically, and the averaged unperturbed density \bar{n} , indicated that within the accuracy of the calculation, all particles from the cavity region were pushed into the shock front by the laser. The small amount of blowoff toward the laser indicated that this was not entirely correct, but the result compared well to the self-similar motion from a point impulse of finite duration on the surface of a gas (Zel'dovich & Raizer, 1966). That calculation arrived at less than two percent of the mass density being blown toward the source of the impulse.

Thus, in the kinetic energy calculation, all particles were treated as moving into the shock front from the cavity region in the 19 nsec associated with half of the FWHM of the CO₂ pulse. The average distance traveled by the particles was half the depth of the cavity - some travelled from the right edge of the plasma, but others were initially near the shock front.

The kinetic energy associated with this motion was found to be 0.08 J.

Both the internal and kinetic energy have been accounted for; the radiated energy was expected to be small and was set to zero. Summing up the various energy increases, an estimate of 0.51 J energy absorption was made. For the shot under consideration, the energy available from the first half of the CO₂ laser pulse was 0.7 J. Thus, an estimate of 70% energy absorption was gained by this analysis, distributed as shown:

Energy available	0.70J
<u>Thermal energy increase</u>	<u> </u>
in shock front	0.23J
Thermal energy increase	
in relaxation region	0.11J
Thermal energy increase	
in deflagration region	0.09J
<u>Kinetic energy</u>	<u>0.08J</u>
Total energy absorbed	0.51J

The preceding estimate equated electron and ion temperatures in the shock front, which in a plasma is not true, since the ions are heated by the shock and in turn heat the electrons after the relaxation

region arrives. Furthermore, the theory of weak shocks begins to break down as front thickness approaches the mean free path, as was the case in the preceding analysis. Also, the densities used in the estimate were not within the usual accuracy associated with holographic interferometry due to the uncertainty of the geometry, so the above absorption fraction is presented with the caveat that it is only an estimate.

Other hydrodynamic estimates of absorption. -

Other hydrodynamic estimates of temperature increase were possible. The most elementary was to suppose that all of the laser energy available at the time of holography, 0.7 J, was deposited in the perturbed region. For this case of 100% absorption, the temperature increase was calculated to be 38 eV, giving a final temperature of 58 eV. This temperature increase was between the temperature obtained by the previous analysis in the shock front and in the relaxation region, as was expected.

Another estimate of absorption used the ratio of densities across the front, n_1/n_0 , and assumed that the ion and electron temperatures were equal in the shock. The equation of the Hugoniot curve is just a statement of conservation of particles, momentum, and energy across a shock discontinuity in the frame of reference moving with the discontinuity. The Hugoniot equation

including an external energy source, Q , in the case of a perfect gas with constant specific heats, states

$$\frac{p_1}{p_0} = \frac{(\gamma+1)v_0 - (\gamma-1)v_1 - 2Q/p_0}{(\gamma+1)v_1 - (\gamma-1)v_0}$$

$$v_0 = 1/\rho_0$$

$$v_1 = 1/\rho_1$$

Solving this for Q in terms of pressures and specific volumes,

$$Q = \frac{-p_0}{2} \left\{ \frac{p_1}{p_0} [(\gamma+1)v_1 - (\gamma-1)v_0] - (\gamma+1)v_0 + (\gamma-1)v_1 \right\}$$

If the temperatures on either side of the shock are assumed equal to some average value, then $p_1/p_0 = v_0/v_1$ and the energy deposited by the laser is given by the ratio of densities:

$$Q = \frac{n_0 \theta_0}{2} \left\{ \frac{v_0}{v_1} [(\gamma+1)v_1 - (\gamma-1)v_0] - (\gamma+1)v_0 + (\gamma-1)v_1 \right\}$$

In obtaining this expression, the equation of state,

$$p_0 = n_0 \theta_0$$

has been used.

Continuing by using the initial temperature of 20 eV as θ_0 and using the experimentally determined values of n_0 and n_1 to get V_0 and V_1 , an estimate of the absorbed energy, in units of energy/volume, was found. When multiplied by the volume of the shock front, an estimate of 0.4 J was obtained as the absorbed energy. The estimate was about 20% lower than the absorbed energy calculated previously, but still fell within the accuracy associated with the previous calculation. An absorption fraction of 60% of the incident 0.7 J was indicated by this number, which was rather close to the 70% fraction calculated before.

Another method of estimating absorbed energy used the shock velocity and the theory of a point explosive energy deposition in an infinite homogeneous medium (Zel'dovich & Raizer, 1966). This method has been used in finding the absorption fraction in laser fusion experiments performed in a background gas (Leonard & Mayer, 1975). Though this geometry was very applicable to spherical illumination of pellet targets, it was quite different from the planar tendencies of this geometry, but is discussed here for completeness. By the dimensional arguments discussed in Appendix C, the Taylor-Sedov expression for velocity of shock wave propagation is obtained in terms of the absorbed energy and the initial mass density:

$$R(t) = \xi_0 (Q/\rho_0)^{1/5} t^{2/5}$$

$$\xi_0 = \left(\frac{75}{16\pi} \frac{(\gamma-1)(\gamma+1)^2}{3\gamma-1} \right)^{1/5} = 1.12$$

R = radius of shock

The radius of the shock at the time of the hologram was taken to be the distance from the (former) position of the critical radius to the peak of the front density, 1.5 mm. The mass density of the plasma as calculated for the average electron density of $1.14 \times 10^{19} \text{ e}^-/\text{cm}^3$ was $3.81 \times 10^{-2} \text{ kg/m}^3$, and the time was again taken to be half the CO₂ pulse width, or 19 nsec. The value of Q in this case was found to be 0.45 J, corresponding to 65% energy absorption.

Some cautions about this last analysis are necessary. The assumptions in the derivation were for a strong shock, that is, $n_1/n_0 = 4$, which was not the case. Furthermore, energy deposition was assumed to be explosive, that is, short compared with the acoustic time of propagation to the shock front. In this case, the CO₂ laser was still depositing energy at the time of this analysis. Since absorbed energy is a function of the shock radius to the fifth power in the formula, even a small change in R corresponded to a large change in Q. This placed a small tolerance upon R.

Yet another hydrodynamic argument was used to estimate energy absorbed (Brueckner & Jorna, 1974). By equating the energy incident upon the region with the increase in temperature of the region, with a region spatial extent of Δx , an energy balance equation was written:

$$I \Delta t = \frac{3}{2} n \Delta x \Delta \theta_e$$

I = laser intensity

Δt = energy deposition time

Using the steady-state version of Fourier's law of heat conduction,

$$I = \kappa(\theta_e) \frac{\Delta \theta_e}{\Delta x}$$

the energy flux into the region was equated with energy flow outward. Equating the two expressions for I and placing the thermal conductivity on the left,

$$\kappa(\theta_e) = \frac{3/2 n (\Delta x)^2}{\Delta t}$$

The Spitzer thermal conductivity is a function of $\theta^{5/2}$:

$$\kappa(\theta_e) = \kappa_0 \theta^{5/2}$$

The temperature was expressed as

$$\theta_e = \left(\frac{3/2 n (\Delta x)^2}{\Delta t \kappa_0} \right)^{2/5}$$

Again, 19 nsec was taken as Δt . The value of Δx , the spatial extent of the heated region, was taken to be the diameter of the cavity. A temperature estimate of 74 eV was obtained, corresponding to an increase in internal energy of 0.15 J (Rockett et al., 1977). This estimate was low compared to the previous ones, but it also ignored the presence of the border about the cavity which was seen in the earlier calculations to contain appreciable internal energy.

The estimates of absorption using shock structure thicknesses, the Hugoniot relation, and the expression for a strong explosion yielded similar absorption fractions, all within the range from 60% to 70%.

Another mechanism of shock wave production is the propagation of a thermal wave. The time derivative of the radius of a thermal wave, r_f , expanding spherically from a point of energy deposition is given by

$$\frac{dr_f}{dt} = \frac{a \xi^n}{r_f^{3n+1}}$$

$$\xi \approx Q/\rho_0$$

in the general case of a medium with a temperature-dependent thermal conductivity of the form $\kappa = a\theta_e^n$.

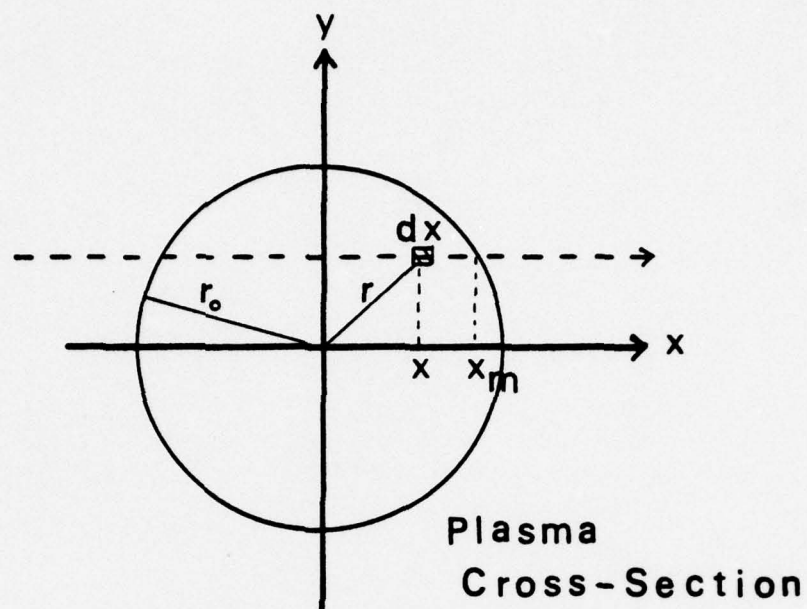
In the case of a plasma, $n = 5/2$ and $a = \kappa_0$, so

$$\frac{dr_f}{dt} \approx \frac{\kappa_0}{r_f^{17/2}} (Q/\rho)^{5/2}$$

As the radius of the thermal wave increases, its velocity decreases, until at some radius, the velocity of the thermal front equals the sound velocity. At this radius, the fluid can follow the thermal wave as a shock.

Using the expression to reflect the case at hand, it was found that r_f , the thermal front radius, had increased to a radius of 0.5 cm before the front velocity slowed to the acoustic speed. This radius was well beyond the size of the plasma. Thus, the time scale associated with this experiment did not fall into this regime, if hydrodynamics, rather than profile modification, is applicable.

By a series of hydrodynamic arguments, an estimate of 60% to 70% energy absorption was attained from quantification of the features of the interaction as seen in the interferograms. Before leaving the discussion of the holographic analysis of the perturbed region, the effect of a perturbation in profile density in a small segment along the z-axis upon a Moire fringe path is treated.



$$\Delta\phi = 2 \int_0^{x_m} \left(\frac{2\pi}{\lambda} \right) [\eta(r) - 1] dx$$

FIGURE 5.33 CYLINDRICAL GEOMETRY FOR CALCULATION OF FRINGE SHIFT

Effect of small z-axis perturbation on fringe path. - By an adaptation of the technique described by Rockett (Rockett, 1977b), an explanation for the doubling over of a Moire fringe, often seen in the CO₂ laser interaction region of the plasma, is offered. The fringe inflection at the laser height at the right of Figure 5.24 is an example.

The interferogram is located in a y-z plane with the angle between the object and reference beams lying in a plane that extends in the z-direction. Exposure vs. position is given by (Rockett, 1977a):

$$W(y,z) \propto 2 + 2\cos(\Delta\phi + kz\delta\cos\theta)$$

$\Delta\phi$ = phase shift imparted by object;

$$\Delta\phi = \frac{2\pi}{\lambda} \int_{-L}^L dl (\eta(r,z) - 1)$$

δ = change in reference angle between interferometry exposures

θ = angle between object and reference beam

The phase shift introduced by the object is represented in the axisymmetric case by

$$\Delta\phi = \frac{4\pi}{\lambda} \int_y^{r_0} (\eta(r,z) - 1) \frac{rdr}{\sqrt{r^2 - z^2}}$$

(Figure 5.33)

The expression for $\Delta\phi$ is the Abel transform of $\eta(r,z) - 1$ (Bracewell, 1965).

The cold collisionless dispersion relation for electromagnetic waves in an unmagnetized plasma relates the index of refraction, $\eta(r,z)$ to the density, $n(r,z)$:

$$\eta(r,z) = \sqrt{1 - n(r,z)/n_c(\lambda)} \approx 1 - n(r,z)/2n_c$$

Along a bright fringe on the interferogram, $W(y,z)$ is a maximum, so a bright fringe corresponds to the curve defined by

$$\Delta\phi(y,z) + kz\delta\cos\theta = 2\pi m$$

on the film plate, where m is an integer that determines the order of the fringe.

To understand the effect of a perturbed segment along the usually uniform plasma column, the density is represented as a separable function of r and z . A readily invertible function similar to the r -dependence of the density profiles is the Gaussian:

$$n_r(r) = n_0 \exp(-r^2/\sigma^2)$$

$$\sigma = \text{halfwidth}$$

$$n_0 = \text{peak density}$$

If this form of r -dependence is multiplied by a second Gaussian of a very narrow half-width, this one a function of z , a segment of z -variation in the column is

incorporated:

$$n_z(z) = 1 + \epsilon \exp(-z^2/s^2)$$

$s \ll$ column length

Taking the product of the r -dependent portion and the z -dependent portion yields the density distribution to be used:

$$\begin{aligned} n(r,z) &= n_r(r) \cdot n_z(z) \\ &= n_0 \exp(-r^2/\sigma^2) (1 + \epsilon \exp(-z^2/s^2)) \end{aligned}$$

If this density function is placed in the expression for $\eta(r,z)$, and this is then placed in the expression for $\Delta\phi(y,z)$, the equation of a bright fringe becomes

$$-\kappa\sigma\pi^{\frac{1}{2}} \exp(-y^2/\sigma^2) = \frac{\alpha z + \frac{\lambda}{2}m}{1 + \epsilon \exp(-z^2/s^2)}$$

$$\kappa = \frac{n_0}{2n_c}$$

$$\alpha = -\frac{1}{2}\delta\cos\theta$$

after evaluation of the integral. The locus of points (y,z) that meet the above equation forms the fringe path.

If n_0 and δ are chosen to match the Gaussian to a density profile and s is chosen to be comparable to the size of the vertical density perturbation, in particular, the size of the CO_2 laser focal spot, then the

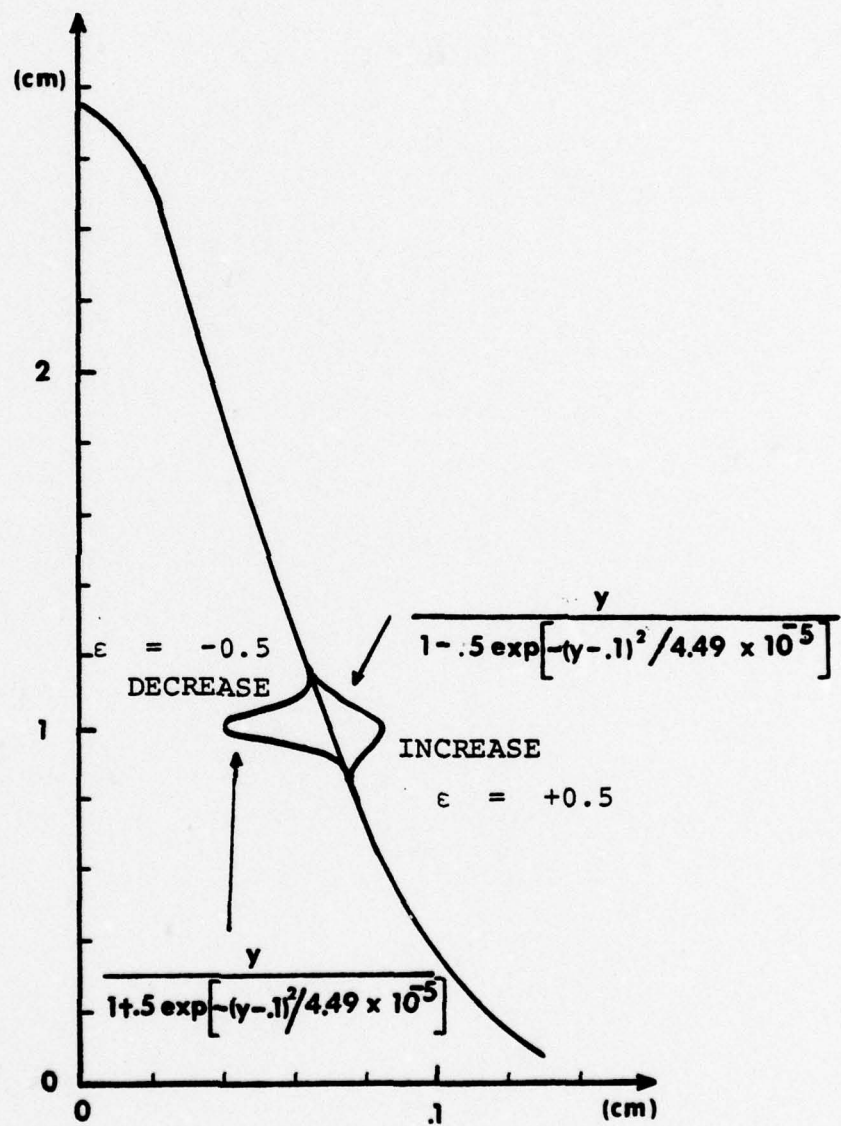


FIGURE 5.34 FRINGE PLOT FOR SMALL AXIAL SEGMENT OF DENSITY PERTURBATION

equation represents a fringe for an axisymmetric plasma column with a small segment of perturbed density centered about $z = 0$. If ϵ is set to 0.5, then the perturbed z -segment corresponds to an increase in density by 1.5 times the unperturbed density at $z = 0$, with a half-width comparable to the focal spot size.

By solving the transcendental equation graphically, the fringe may be plotted. Figure 5.34 is a plot of such a fringe for $\epsilon=0$, $\epsilon=+0.5$, and $\epsilon=-0.5$. The plot for $\epsilon=+0.5$ shows a fringe perturbation similar to that seen in the hologram shown in Figure 5.24. Thus, some density increase is seen at the laser height before the cavity is formed.

The preceding discussion has described the holographic appearance of the effect of the laser on the plasma at different stages along the plasma evolution, and at different times relative to time of peak intensity. By accounting for the non-axisymmetric geometry of the interaction, density estimates in the perturbed region of the plasma were obtained. The macroscopic scale of the perturbed region suggested hydrodynamic effects, and such calculations provided an idea of the energy absorption fraction, about 60% - 70%. No intensity-dependent effects in the perturbed region were noted in the holograms.

5.5 Transmitted 10.6 μ radiation - results

In this section and the next, the observations of the transmission of high-intensity 10.6 μ radiation through the overdense plasma are described. The previous sections have shown that near the time of optical emission from the plasma, electron densities well exceeded the critical value of $1 \times 10^{19} \text{ e}^-/\text{cm}^3$. Classical electromagnetic theory predicts reflection of electromagnetic radiation incident on a plasma of electron density greater than critical (Section 2.1). Gross hydrodynamic perturbation due to energy absorption from incident radiation within a short length and subsequent shock waves and thermal expansion can modify the plasma on a large scale.

At high intensities, the oscillating magnetic field of the incident radiation begins to contribute to the motion of electrons at the laser-plasma interface, and a radiation pressure, the "ponderomotive force," begins to appear in the direction of radiation propagation (Section 2.2). This force, which becomes important at sufficient intensity where the kinetic pressure of the plasma does not overwhelm the radiation pressure, can modify the plasma density profile. The force is distinguished from the hydrodynamic effects from local heating. The hydrodynamic effects could just as well

be brought on by an appropriately tailored chemical explosive, whereas profile modification specializes to the presence of an intense beam of radiation. Another mechanism of density perturbation can take place on a small scale. The effect of thermal self-focusing results in density decrease in the focal volume due to thermal expansion of the plasma. The low-density region causes the beam to converge in the region, due to the gradient in the refractive index, and the process continues.

The spatial resolution of the holography system only allowed detection of large hydrodynamic perturbation from the laser beam, and small scale effects of the size of the focal spot were not observable in the manner.

A diagnostic mechanism that provided information on a spatial scale the size of the focal spot was the transmitted beam from the incident CO_2 radiation passing through the plasma. The idealized case of low-intensity electromagnetic radiation incident on a semi-infinite homogeneous plasma predicted no such transmission; however, this plasma was neither semi-infinite nor homogeneous, nor was the laser intensity low.

Both the temporal and spatial shape of the transmitted pulse were monitored in the experiment. Shots were made at various incident intensities, ranging from

0.1 to 4×10^{11} W/cm², and were timed so that, in most cases, the CO₂ laser radiation struck the plasma within 35 nsec of the optical peak. The highest electron densities occurred within this range and were generally three times critical density on the plasma centerline. By the calibration procedure mentioned in Section 3.5, the transmitted pulse, recorded by the pyroelectric detector, was compared to the incident pulse in both shape and intensity. The use of exposed Polaroid black-and-white prints to record the burnspot of the beam transmitted through the plasma provided a spatial distribution. The temporal structure will first be discussed, followed by the observed spatial structure. The following section discusses the observation set forth in this section.

A few shots were taken before critical density was reached in the discharge. The transmitted pulse in this case was seen to be identical in duration to the incident pulse, and indicated an intensity transmission of about 6%. Transmission through the underdense plasma was linear with incident intensity.

Intensity threshold for transmission. - The bulk of the data was taken for laser incident upon an overdense plasma. The most interesting result was an intensity dependence of the transmission through the overdense plasma. The mundane case of intensity-independent transmission preserves a constant transmission

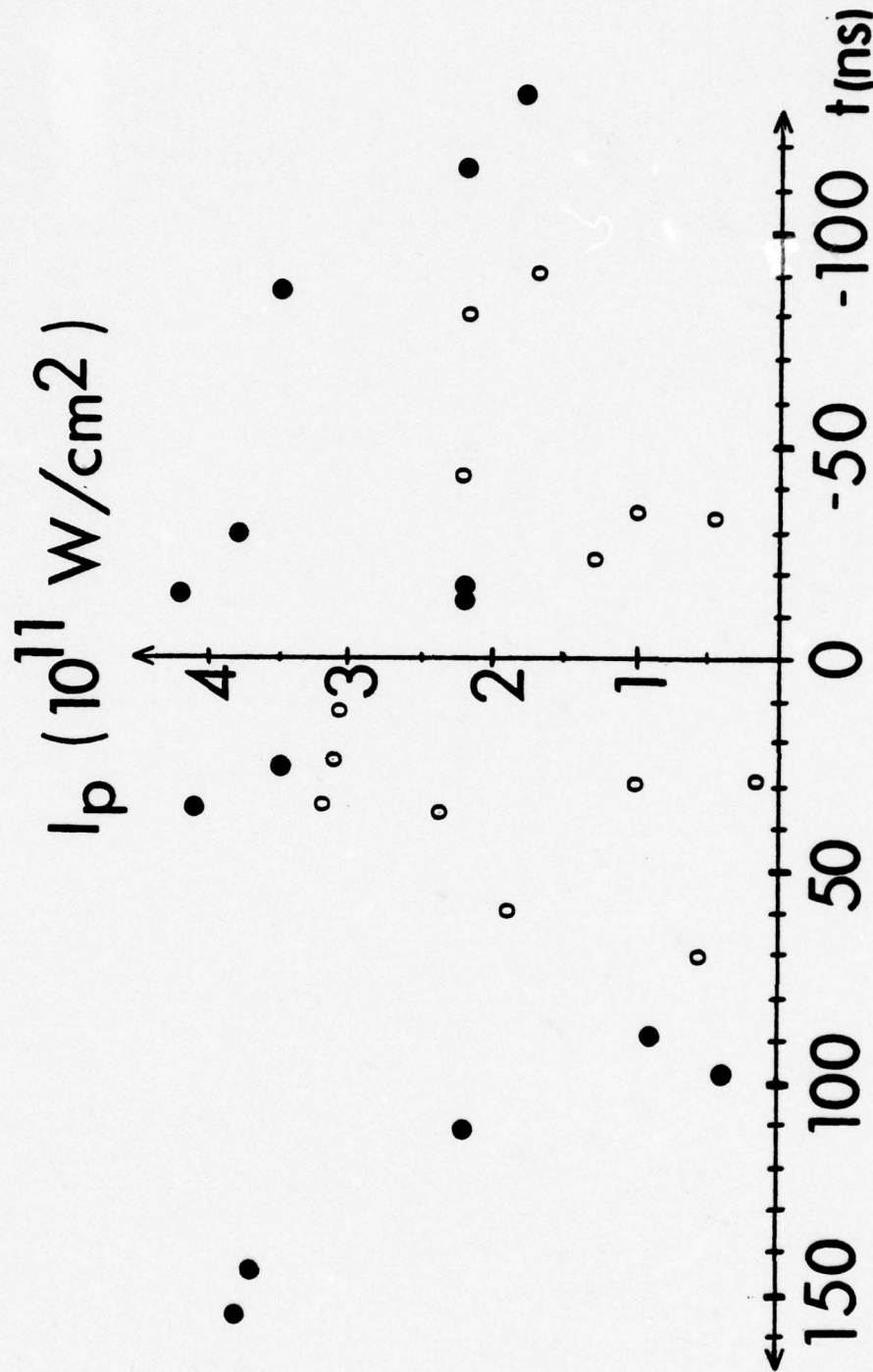


FIGURE 5.35 PLOT OF TRANSMISSION VS. INCIDENT INTENSITY AND TIME OF INCIDENCE OF

10.6 μ RADIATION - SOLID DOTS \rightarrow TRANSMISSION; HOLLOW CIRCLES \rightarrow NO

TRANSMISSION

fraction, regardless of intensity. Thus, for the case of intensity-independent transmission, a doubling of incident intensity requires a doubling of transmitted intensity to maintain a constant fractional transmission. However, the surprising observation in this experiment was quite different. In the experiment, with an increase in incident intensity over a particular threshold by a factor of only 1.6, the transmitted intensity increased by more than a factor of five. This sudden jump in transmission for a small change in intensity was the most unusual observation in this experiment.

The threshold was discovered when it was noted that for incident radiation intensity of less than 2×10^{11} W/cm², no transmission was seen on the pyroelectric detector or on the film for shots incident within 35 nsec of time of pinch. For an intensity of greater than 3.5×10^{11} W/cm², transmission was always detected. A plot of the more recent shots shows shots for which CO₂ transmission through the overdense plasma occurred as solid dots, and shots for which no detection of transmission occurred as circles (Figure 5.35). Since the plasma was continuously changing as the discharge evolved, the shots are plotted along a horizontal axis according to the time of CO₂ laser incidence relative to the optical peak associated with maximum plasma density. The left side of the plot corresponds to

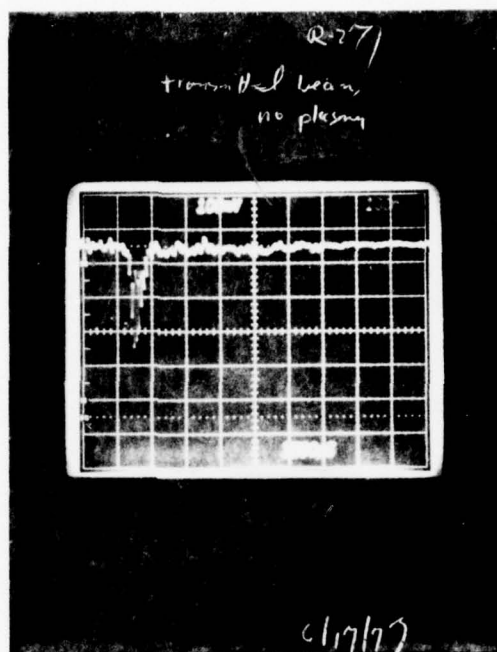


FIGURE 5.36 INCIDENT LASER PULSE SHAPE (100 nsec/div)

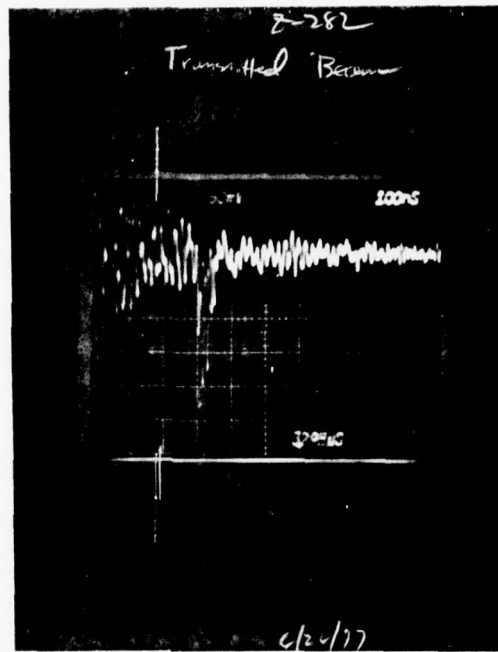


FIGURE 5.37 TRANSMITTED LASER PULSE SHAPE,
MODERATE INTENSITY (100 nsec/div)

incidence before time of pinch. The vertical axis represents the incident intensity within the central disc of the focal spot. For CO₂ laser incidence more than 80 nsec before time of pinch, transmission was detected regardless of incident intensity. For the time from 35 nsec before pinch to time of pinch, no transmission was seen unless incident intensity exceeded $3.5 \times 10^{11} \text{ W/cm}^2$. From pinch time to 35 nsec after, transmission was seen if the incident intensity exceeded $2.2 \times 10^{11} \text{ W/cm}^2$.

Temporal modification of transmitted pulse. - For laser incidence within 35 nsec of time of pinch, another important intensity-dependent effect was observed. As the intensity was increased, the temporal shape of the transmitted laser pulse was distorted. The incident laser pulse shape is displayed as Figure 5.36. For incident intensity of $2.2 \times 10^{11} \text{ W/cm}^2$, the transmitted pulse exhibited a very rapid rise (less than 10 nsec) and was highly modulated (Figure 5.37). The modulation frequency corresponded to the frequency of self-mode-locking in the incident pulse, as seen in Figure 5.36, but the percentage of modulation was seen to have increased to nearly 100%. Also, the peak of the transmitted pulse was seen to occur about 30 nsec later than would have been expected when firing through a vacuum instead of the plasma. This fact, when taken with

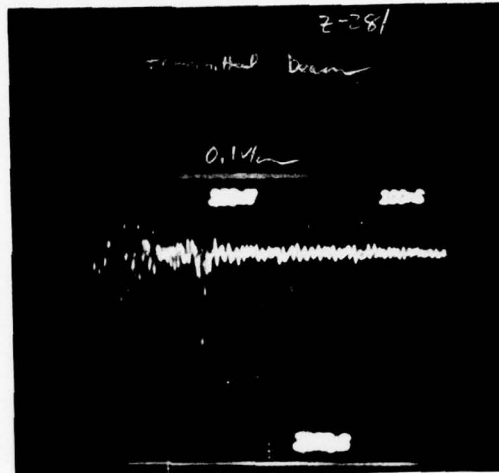


FIGURE 5.38 TRANSMITTED LASER PULSE SHAPE, HIGH
INTENSITY (100 nsec/div)

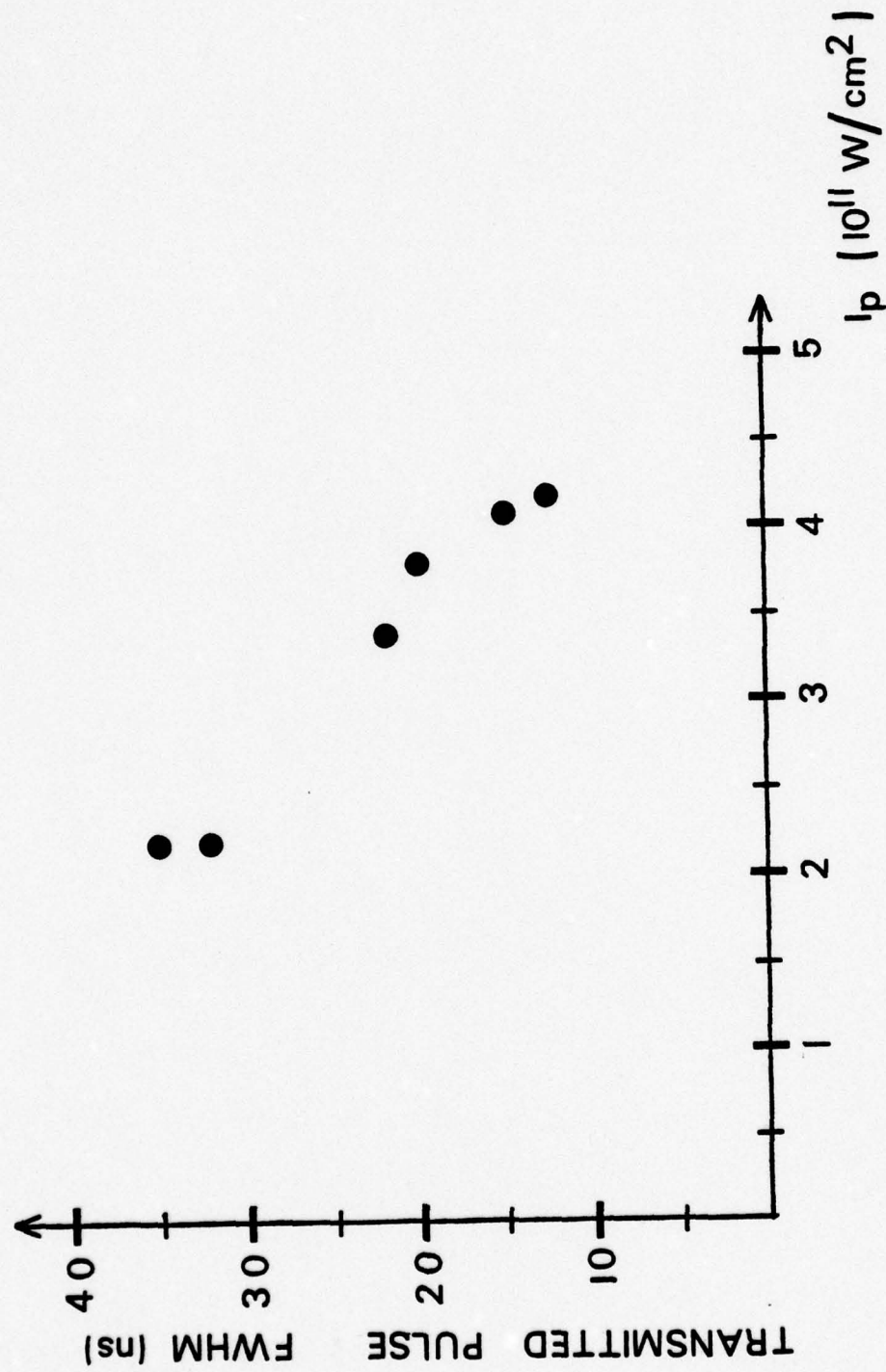


FIGURE 5.39 TRANSMITTED PULSE WIDTH VS. INCIDENT INTENSITY

the very rapid rise on the transmitted pulse, indicated that the first portion of the incident pulse was not transmitted.

For the highest intensity used, 4.2×10^{11} W/cm², the transmitted pulse was much shorter (Figure 5.38) and reached a lower peak intensity. The time of CO₂ laser incidence, t_i , was -15 nsec (after pinch), the same as in Figure 5.37. The FWHM of the transmitted pulse at the lower intensity was 35 nsec, and for the transmitted pulse taken at the higher intensity, was 15 nsec. Other shots within 35 nsec of pinch time indicated this same pulse-compression with high intensity. A plot of the full-width-at-half-maximum of transmitted pulse vs. incident intensity appears as Figure 5.39. The half-width of the transmitted pulse decreased as the incident intensity was raised.

Before leaving the description of results from temporal study of the transmitted beam, description of transmission of a tail on the incident laser pulse is presented. On some shots, no pyroelectric signal was seen, but a burnspot appeared on the film placed to record beam transmission. This led to the observation that on a time scale much longer than the incident 38 nsec pulse, another pulse of comparable energy content was occasionally transmitted. In Figure 5.40, a 38 nsec pulse at the left of the trace corresponded to the

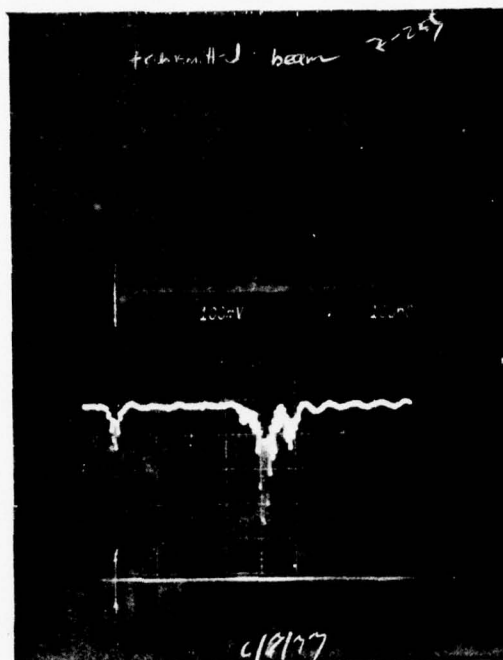


FIGURE 5.40 ENHANCEMENT OF TAIL OF CO₂ LASER PULSE
IN TRANSMISSION (100 nsec/div)

gain-switched spike. Following this pulse by 400 nsec were two more pulses of greater intensity and energy than the first. The incident pulse shape was carefully reexamined, and a 100 nsec tail was occasionally found to occur on the pulse leaving the laser. Intensity in the tail was a factor of 13 lower than intensity in the gain-switched spike, but the greater pulse width implied an energy content of 8% - 10% of the gain-switched spike. Since the gain-switched spike was used as the pulse synchronized with pinch time, and since the tail was well-separated from the spike in time, the tail was ignored except in the interpretation of the pulse-integrating burnspot. No reproducibility was seen in the occurrence of the tail on the incident pulse, which was seen to varying extents in about 1/3 of the laser shots examined. No regularity was observed in the appearance of this tail on the beam transmitted through the plasma, and the irregularity was attributed to the irregular occurrence of the tail on the incident pulse.

Spatial modification of transmitted pulse. -

The results reported by Steel (Steel, 1976) indicated the appearance of a series of concentric rings on the burnspot of the beam transmitted through the overdense plasma, as recorded by the Polaroid film. He noted that the rings had the appearance of a Fresnel diffraction pattern of a beam through a circular aperture. His

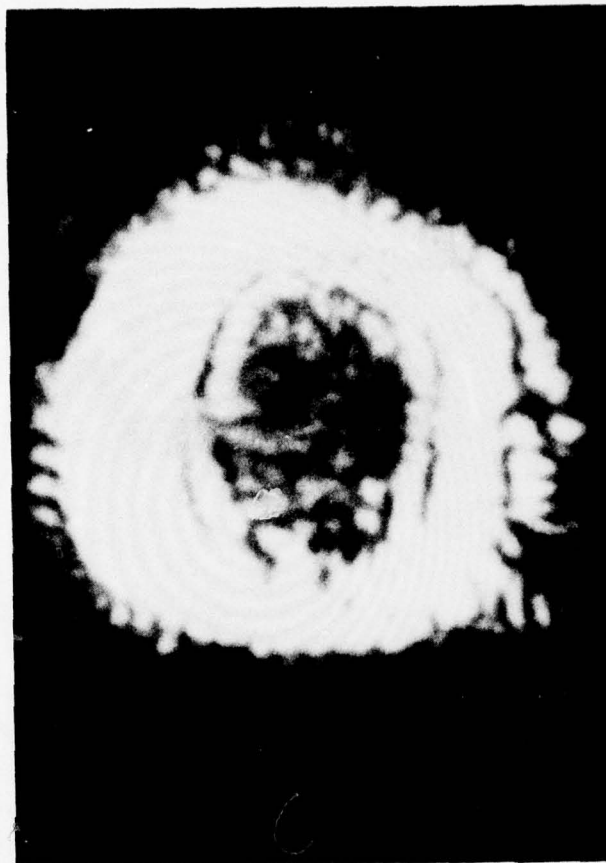


FIGURE 5.41 ANNULAR DISTRIBUTION OF TRANSMITTED
BEAM - NO PLASMA IN CHAMBER



FIGURE 5.42 CONCENTRIC RINGS ON PULSE TRANSMITTED
THROUGH OVERDENSE PLASMA



FIGURE 5.43 HOT-SPOT IN TRANSMISSION BURNSPOT FROM
HIGH INCIDENT INTENSITY THROUGH OVER-
DENSE PLASMA

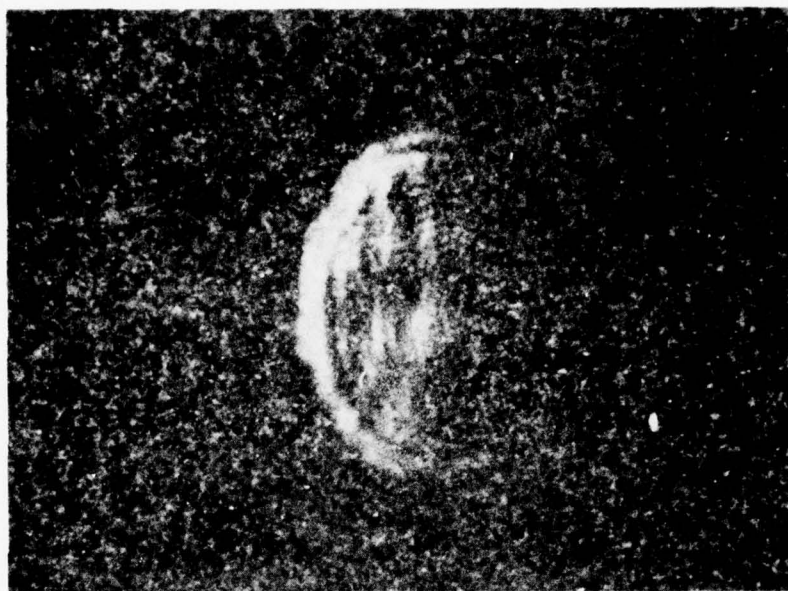


FIGURE 5.44 VERTICAL BARS ON TRANSMISSION
BURNSPOT THROUGH OVERDENSE PLASMA

geometrical argument related the size of the burnspot to an aperture in the plasma approximately of the size of the CO₂ focal spot.

This pattern was reproduced in this investigation. Figure 5.41 is a photograph of a burnspot of the CO₂ beam through the chamber with no plasma present. The annular region of illumination is typical of the unstable resonator laser cavity used. Figure 5.42 displays the burnspot produced by transmission through the overdense plasma, and the burnspot has the thick border and concentric rings associated with the Fresnel diffraction pattern. The high-contrast rings are a feature of diffraction through a smooth-walled aperture; as the aperture border becomes more irregular, ring contrast decreases (Judd, 1973). The rings appeared on the burnspot for laser incidence generally within the time that the plasma discharge was overdense. For incident intensity greater than $3.5 \times 10^{11} \text{ W/cm}^2$, the pattern was seen to exhibit hot spots, or small areas of intense illumination, upon occasion. In these cases, non-uniform spot illumination prevented observation of the rings, since only the small hot spot was illuminated (Figure 5.43). Some shots with laser incidence within 15 nsec of pinch time, and of moderate intensity (less than $2.5 \times 10^{11} \text{ W/cm}^2$) displayed vertical bars on the burnspot (Figure 5.44).



FIGURE 5.45 MULTIPLE TRANSMISSION BURNSPOTS
DUE TO SEVERAL TRANSMITTED PULSES

Study of a number of burnspots indicated that for all shots with laser incidence within 50 nsec of time of pinch, those that did not have the ring structure were either produced at very high intensity (greater than 3.3×10^{11} W/cm²) or were the result of a tail on the transmitted pulse as shown in Figure 5.40. In fact, some burnspots had the appearance of multiple exposure of a slightly displaced ring pattern (Figure 5.45). This was attributed to the transmission of several separate pulses through the plasma, possibly one gain-switched spike and several tail pulses, as shown in Figure 5.40.

Laser incidence upon an underdense plasma well before time of pinch produced an evenly illuminated spot with no ring structure (Steel, 1976).

5.6 Transmitted 10.6 μ radiation - discussion

Error analysis. - This section begins with a discussion of possible errors in the experimental determination of transmission. Many experimental parameters entered into the measurement of intensity transmission. The time of laser incidence relative to the time of plasma pinch determined the density profile of the target plasma. This time was measured by comparing the time of peak light emission seen by a PIN diode

monitoring the plasma to the time that a photon drag detector marked as time of CO₂ laser firing. The two signals were displayed on a Tektronix 555 oscilloscope on a common time base, at a sweep rate of 200 nsec/div. The photon drag detector signal was combined with a PIN diode monitoring the time of the holography pulse and separated by a passive delay line by a fixed, well-known amount. Between every second shot, a reference shot was taken by synchronizing the two PIN diode traces with a common laser pulse. This ensured that coincident signals were seen on the oscilloscope as such. Timing information was obtained from photographs of scope traces by use of a magnifying comparator that afforded 4 nsec resolution on the trace photos. The optical peak was determined within a 10 nsec range with the comparator. So with care, timing of the CO₂ laser to time of pinch was determined to within 10 nsec.

It was found important that the entire spatial distribution of the transmitted beam be collected by the pyroelectric detector. Earlier shots in which only a portion of the beam was incident upon the detector displayed temporal structure that could be caused by various portions of the spot being illuminated at different times in a search-light manner (R. Stern, 1977). In these earlier shots, the detector was not at the focus of the KCl collecting lens, but inside

the focus by about 2 cm. By placing the detector at the focus of the lens, as was done in these most recent experiments, any CO_2 ray that passed through the focal region in the plasma was imaged on the pyroelectric detector. Care was taken to determine the focus of the KCl lens by experiments at 10.6μ , since the dispersion of the KCl altered position of focus from that seen at visible wavelengths. The diameter of the focal spot on the detector was less than 1 mm, and was centered on the 4 mm diameter active surface. The transmitted beam hitting the detector was split off from the beam leaving the plasma by a 0.5 cm thick NaCl flat. The two images resulting from the two surfaces of the beam-splitter were sufficiently separated at the focus of the collecting lens to allow only one to hit the detector. Output signals were at least a factor of two below amplifier saturation, and linearity of the detector amplifier was verified with a pulse generator during the course of the investigation. Linearity of the detector was also checked over the range of use. The limit on bandwidth was imposed by the pulse amplifier. Its 150 MHz bandwidth may be conservatively transformed to a 7 nsec risetime (the relationship between bandwidth, BW, and risetime, τ , is given by $\tau = \alpha/\text{BW}$, where the value of α depends upon the manufacturer -

Tektronix places $\alpha = 0.35$, Hewlett Packard, the manufacturer of the amplifier, places $\alpha = 0.16$; this discussion sets it equal to one). The rise time of the pyroelectric detector was published as less than one nanosecond. The pyroelectric signal was displayed on a new Tektronix 7904 oscilloscope at a sweep speed of either 50 nsec/div or 100 nsec/div.

Calibration of the pyroelectric detector sensitivity was determined by the reference shots taken every two shots. By firing a beam of known intensity through the optical system, the measured voltage from the pyroelectric detector provided a reference point for one hundred percent transmission. By comparing the photon drag signal time to the pyroelectric signal time, these reference shots also provided signal coincidence information useful in measuring a delay in transmitted pulse peak relative to incident pulse peak. Such a calibration technique allowed for differences in optical and electrical path lengths as well as attenuation of various optical elements. The frequent checks in calibration and timing rarely showed any variation, so no variation between shots in timing or sensitivity was expected. Additionally, the position of the focal spot upon the plasma was frequently checked during a run, and was maintained constant to within 60 μ .

Overall system calibration was performed with a Lumonics Model 50D Large-Area CO₂ Radiation Detector, which was itself calibrated by Lumonics, Inc., using an NBS-calibrated standard. This overall calibration was checked before and after each run of shots.

The threshold of detectability of the transmitted beam detection system was 1×10^9 W/cm², a factor of 300 below typical incident intensities, and over a factor of four below the lowest transmitted intensity seen in this experiment. This threshold was set by the requirement of sufficient dynamic range on the oscilloscope to allow faithful reproduction of the transmitted pulse shape.

Shot-to-shot reproducibility of the discharge appeared to be excellent from holography, streak camera photographs, dI/dt, and every other diagnostic method used.

Absorption by underdense target plasma. -

Before continuing with further examination of the CO₂ transmission through the overdense plasma, some points about the transmission through the underdense plasma are worth noting. For laser incidence more than 100 nsec before time of pinch, a transmission of about 6% intensity was noted.

This investigation utilized a ray-tracing computer code that calculated both the refraction and the ab-

sorption along a ray of a specified impact parameter through an axisymmetric plasma of a specified density profile (DeBoo, 1973; Rockett & DeBoo, 1975). The refractive index was found by use of the cold collisionless dispersion relation for electromagnetic waves, and absorption was calculated by the use of the inverse bremsstrahlung absorption coefficient at a specific temperature.

By fitting the holographically-determined density plot for an underdense Z-pinch plasma to a Lorentzian,

$$n(r) = \frac{n_0}{r^2 + b^2}$$

a functional form of the profile was obtained. For a Lorentzian fit to an underdense profile, a transmission of 14% was calculated for an electron temperature of 20 eV, and a transmission of 5% was derived for a temperature of 15 eV. These values were felt to match acceptably with the observed transmission of 6% through the underdense plasma, allowing for the inaccuracy inherent in fitting the density profile to an analytical expression.

For a ray along the diameter of a cylindrically-symmetric plasma, no refraction was expected, since the ray was always at normal incidence to density gradients.

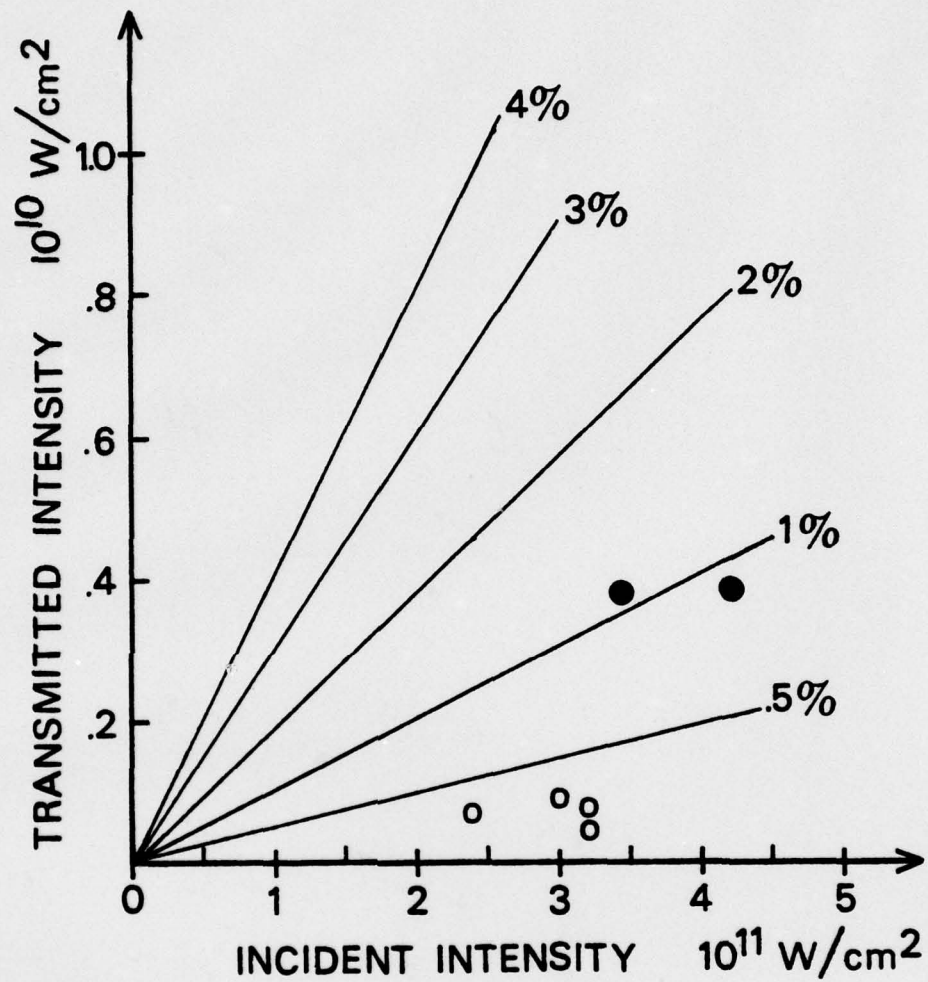


FIGURE 5.46 TRANSMITTED INTENSITY VS. INCIDENT INTENSITY -
 PRE-PINCH OVERDENSE PLASMA - HOLLOW CIRCLES -
 UPPER LIMIT ON TRANSMITTED INTENSITY

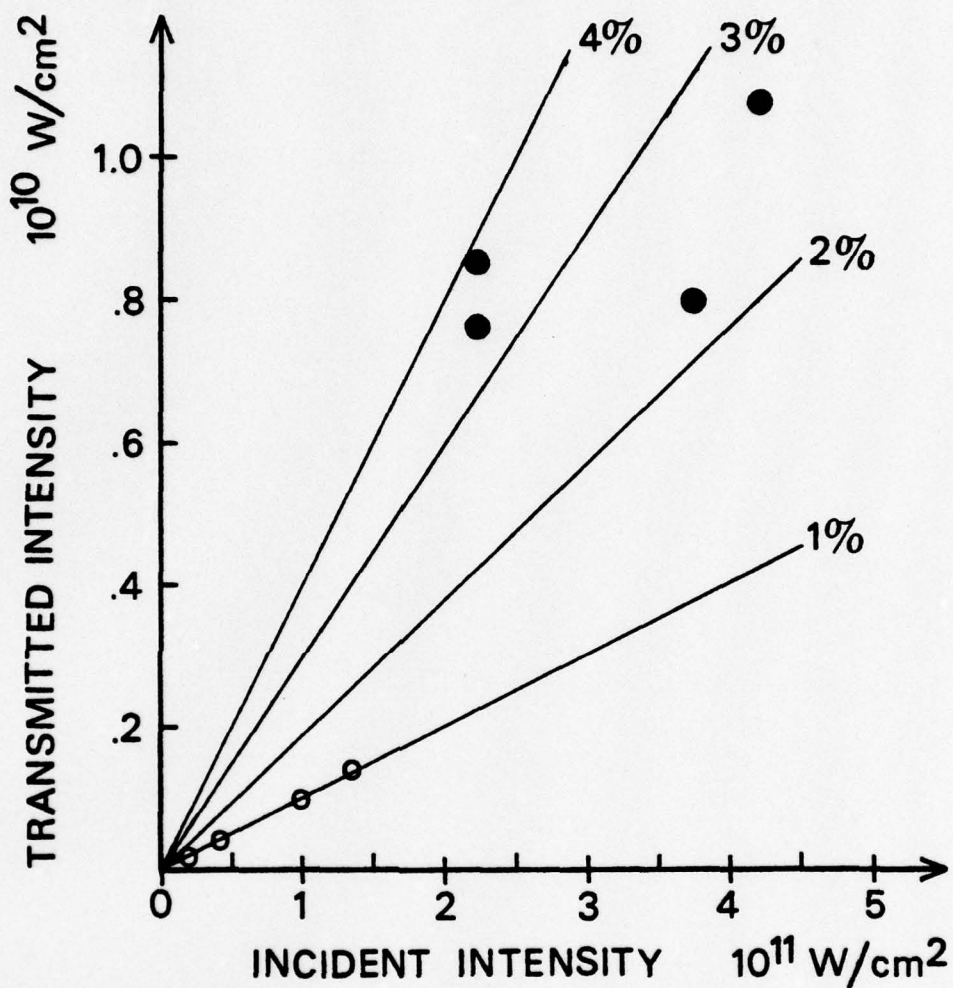


FIGURE 5.47 TRANSMITTED INTENSITY VS. INCIDENT INTENSITY -
 POST-PINCH OVERDENSE PLASMA - HOLLOW
 CIRCLES -- UPPER LIMIT ON TRANSMITTED INTENSITY

For the experimental case, then, only deviations in alignment to the center of the plasma or asymmetries in the axial or azimuthal direction contributed to refraction. Since the Abel inversion density extraction process also assumed cylindrical symmetry, these deviations from symmetry were ignored.

Intensity threshold for transmission. - Returning to the discussion of transmission through the overdense plasma, the main features observed were the intensity threshold for transmission and the increased modulation and compression of the transmitted pulse for high intensities. A striking view of the threshold effect is presented in Figures 5.46 and 5.47. The figures display transmitted intensity vs. incident intensity for $35 \text{ nsec} > t_i > 0 \text{ nsec}$ in the first figure, and $0 \text{ nsec} > t_i > -35 \text{ nsec}$ in the second. Solid dots denote intensity transmitted, and lines of constant fractional transmission are drawn. The circles represent shots for which no transmission was seen, and are vertically placed to represent the upper limit on transmission as determined by the lower limit on detector sensitivity. Thus, rather than setting shots with no observed transmission to zero, they were conservatively moved to the highest transmission that was consistent with the lack of observed signal. The

sudden increase in transmitted intensity over a small change in incident intensity is readily seen. The threshold in the first plot, for CO_2 laser incident before pinch time, is about $3.5 \times 10^{11} \text{ W/cm}^2$, and for the second, taken after time of pinch, is about $2 \times 10^{11} \text{ W/cm}^2$. In the plot indicating the higher threshold, transmission was seen to be about 1%, and in the lower threshold case, about 3%.

In interpreting the data, one can conservatively place the intensity threshold somewhere in a band between $2 \times 10^{11} \text{ W/cm}^2$ and $3.5 \times 10^{11} \text{ W/cm}^2$. This treatment makes no distinction between shots taken before pinch time and those taken after pinch time, and explains the three data points indicating no transmission at $3 \times 10^{11} \text{ W/cm}^2$ for $t_1 > 0 \text{ nsec}$ as being due to experimental error, either from non-reproducibility in the discharge or timing and analysis error. The discussion at the first of this section detailed the possible experimental errors and discussed the reproducibility of the plasma source. The known sources of error do not appear to be large enough to allow this sort of discrepancy.

Another explanation is that the plasma was in some way different before time of pinch than after time of pinch. Figure 5.9 indicates that plasma evolution was not symmetric about pinch time - plasma

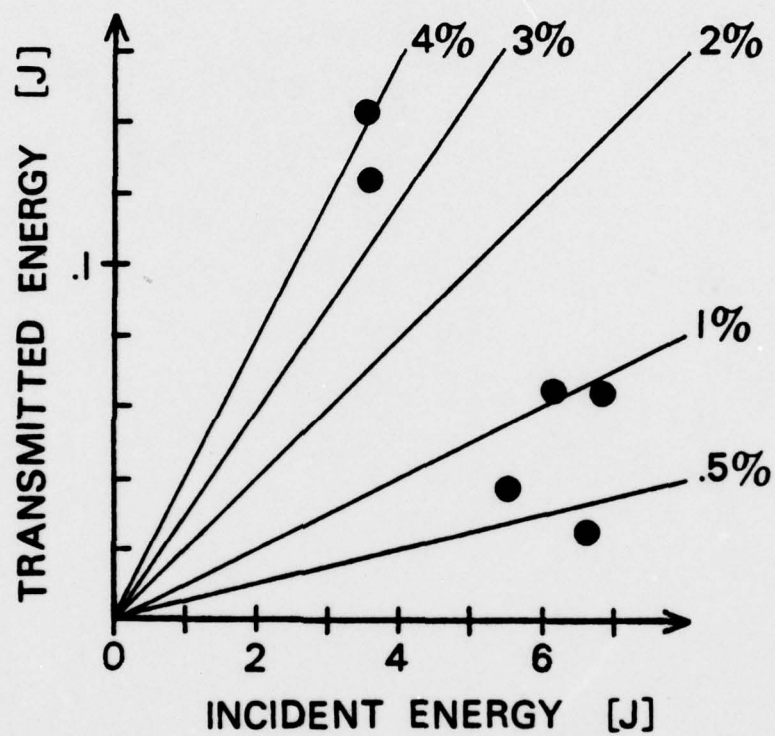


FIGURE 5.48 TRANSMITTED ENERGY VS. INCIDENT ENERGY FOR OVERDENSE PLASMA

compression and disassembly were not the reverse process of one another. The presence of a shelf in the density profile was noted as unique to times before pinch. The density slope near the critical density was seen to be much steeper as the plasma approached pinch than afterwards. An important difference between a plasma approaching pinch and one relaxing from pinch is the direction of overall plasma motion. As the plasma is pinching down, motion is directed inward, and might fill in a laser-induced perturbation more than when the radial motion is outwardly directed as the plasma disassembled. Thus, a higher laser intensity would be needed to perturb a contracting plasma sufficiently to allow transmission.

The pulse width of the transmitted beam decreased as incident intensity was increased (Figure 5.39). Using the transmitted pulse width and peak intensity, an estimate of energy transmission was obtained. Figure 5.48 shows energy transmitted vs. energy incident in the gain-switched spike for shots taken within 35 nsec of time of pinch. A noticeable decrease in fractional energy transmission with increased incident energy is seen in the plot.

Effect of intensity-dependent transmission on transmitted pulse shape. - The observation of the intensity

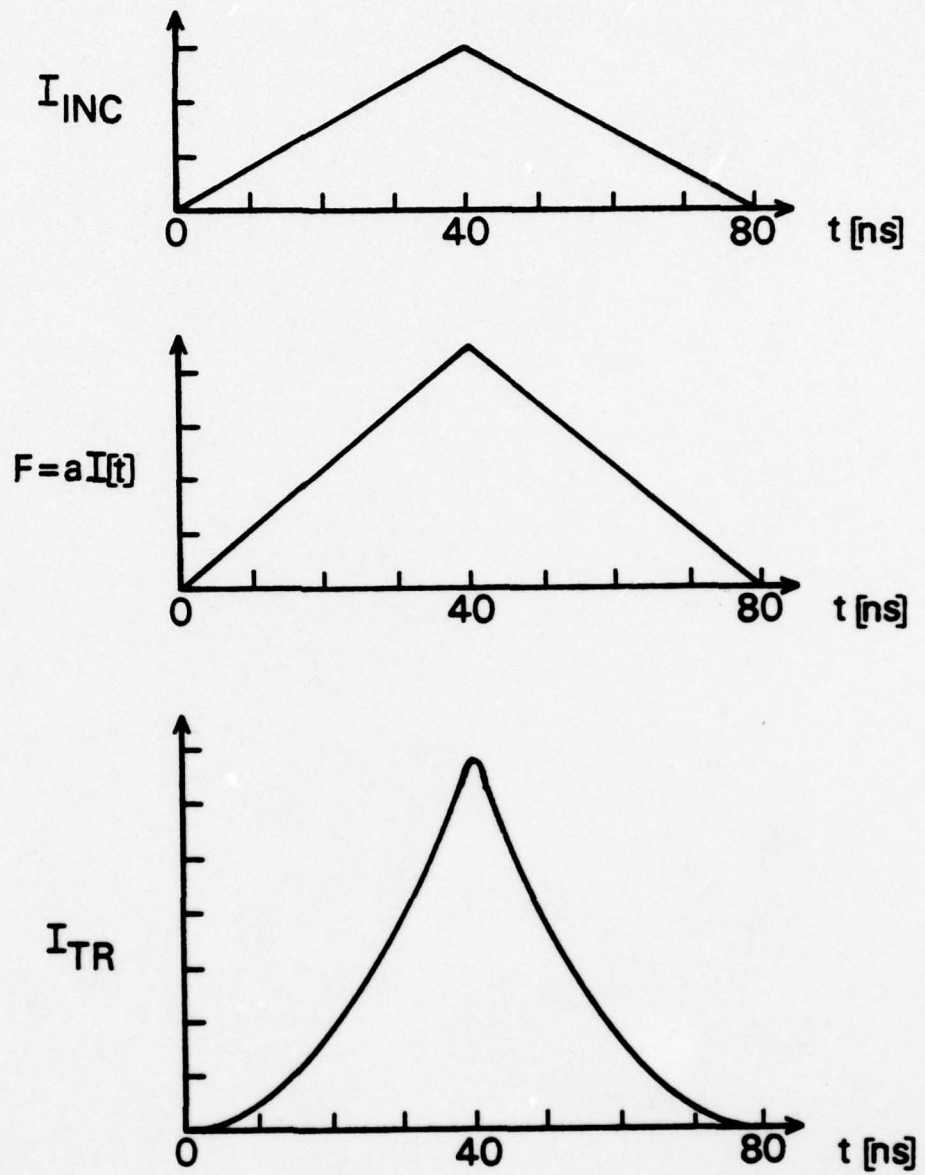


FIGURE 5.49 PULSE-SHAPE DISTORTION FROM TRANSMISSION
THROUGH AN INTENSITY-DEPENDENT ABSORBER

threshold suggests an intensity-dependent transmission mechanism in the laser-plasma interaction. Further evidence of this is seen in the distortion of the transmitted pulse shape. An intensity-dependent effect which allows higher transmission percentage for higher intensity could transmit the high-intensity peak of the incident laser pulse at a higher fraction than the low-intensity wings, resulting in shortening of the transmitted pulse. Intensity-dependent transmission of this sort would also predict the enhanced high-frequency oscillations on the transmitted pulse as being the result of enhanced transmission at peaks of the modelocking structure on the incident pulse. A transmission fraction that is a steadily increasing function of incident intensity does not explain the observation of pulse width shortening as intensity was increased. A threshold model would predict the narrowest pulses at a point just above threshold intensity, when only the high-intensity peak of the pulse would be passed. Figure 5.49 presents the pulse shape distortion that can be produced from the transmission of an originally triangular pulse through a medium whose transmission is linearly proportional to intensity. This transmitted pulse shape is the result of taking a triangular incident pulse of 40 nsec FWHM, $I(t)$ (top),

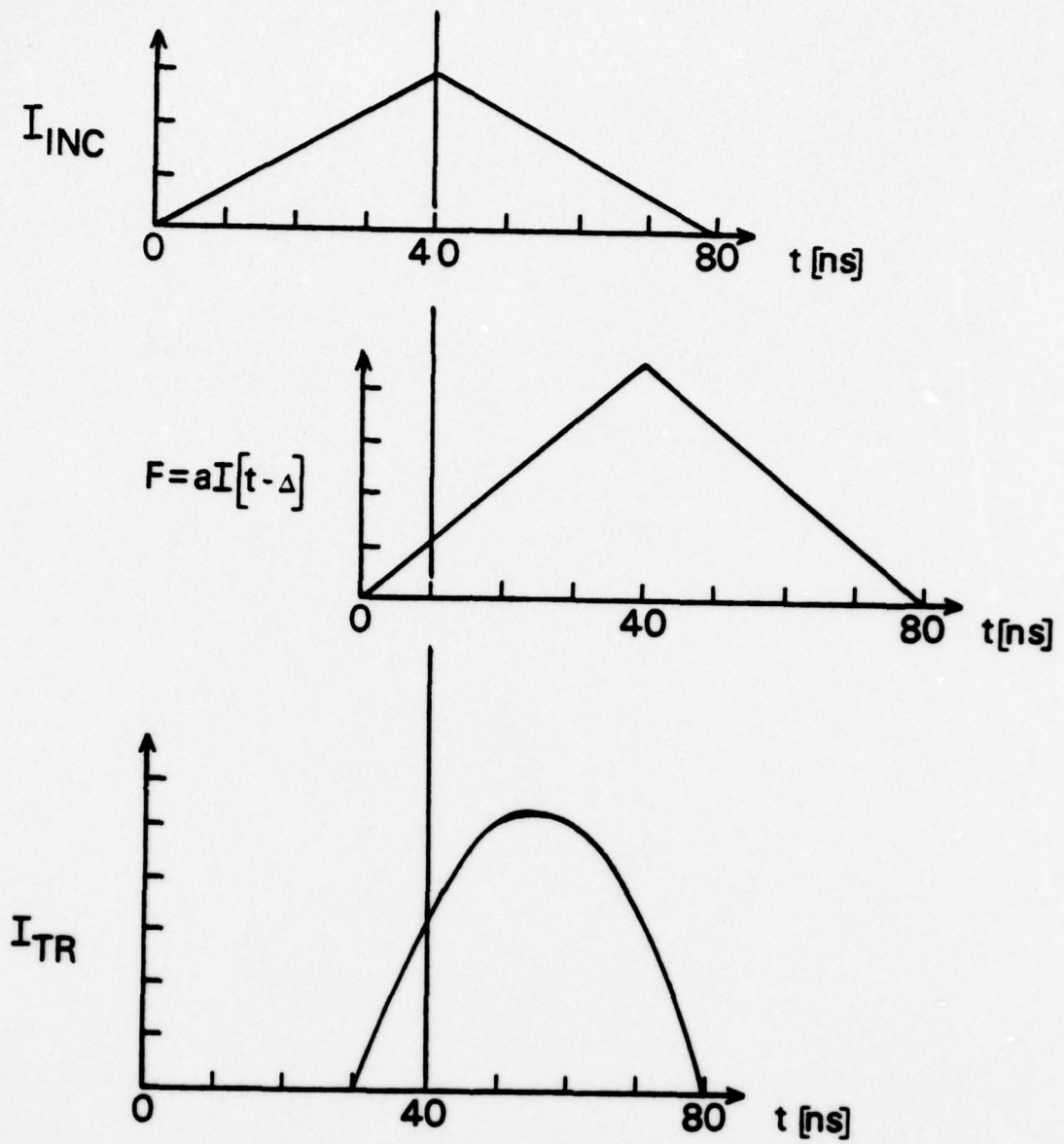


FIGURE 5.50 PULSE-SHAPE DISTORTION FROM TRANSMISSION
THROUGH AN INTENSITY-DEPENDENT ABSORBER
WITH DELAYED RESPONSE

and multiplying it by a transmission fraction, F , that is linear with intensity, $F = aI(t)$ (middle), to get a sharper transmitted pulse, $I_{TR}(t)$ (bottom). The transmitted pulse is of 25 nsec FWHM, compared to 40 nsec FWHM incident, in this model.

The model as stated does not predict a temporal difference between the time of incident peak intensity and transmitted peak intensity. However, a difference of about 30 nsec was observed between the incident peak and transmitted peak. To incorporate this delay into the model, a certain time lag in change of transmission fraction after a change in incident intensity may be introduced. By shifting the instantaneous transmission curve, $F(t)$, at the middle sketch of Figure 5.49, 30 nsec later than as shown, a time lag is incorporated. This 30 nsec time lag is the approximate time of propagation of an acoustic disturbance across the plasma column. The results are shown in Figure 5.50. The transmitted pulse is narrower than the incident pulse, and has a later peak.

The purpose of the preceding graphical sequence was to display the possible pulse-shape modification due to transmission through an intensity-dependent absorber. Simple functions were used to demonstrate an effect, and no claim of applicability of a particular

functional form to the experiment at hand is intended.

Possible physical mechanisms. - Some physical reasons for an intensity-dependent transmission fraction can be presented. One such mechanism is intensity-dependent inverse bremsstrahlung, which provides for a decrease in absorption by this mechanism at high intensities. The coherent electron velocities in the laser field introduce an intensity-dependent factor in the inverse bremsstrahlung absorption coefficient, as described by Shearer (Shearer, 1970).

A thermal wave can propagate in a medium with a temperature-dependent thermal conductivity, such as a plasma. The classical absorption coefficient due to inverse bremsstrahlung by electrons in the presence of ions is inversely proportional to the electron temperature to the $3/2$ power, so as the temperature goes up, absorption goes down. This can give rise to a bleaching wave whereby successive layers of plasma are heated to transparency (Steinhauer & Ahlstrom, 1971). The specifics of this interaction include diffusion from the heated region, plasma motion during heating, and the absorption length over which the energy is deposited. Expressions have been derived for the propagation velocity of this wave (Burnett & Offenberger, 1974; Yuen, Lax, & Cohn, 1975) in the infinite homogeneous

case. Ignoring these idealizations, the expressions when applied to this experiment yield transit times across the column in tens of nanoseconds.

This experiment was in the regime in which profile modification by the ponderomotive force is expected (Giovanielli, 1976). The oscillatory velocity of the electrons in the laser field was calculated to be near their mean thermal velocity (Section 3.6), and thus the incident radiation was expected to alter the density distribution of the plasma in the region of the focal spot. As a result, the pushing out of a portion of the plasma from the focal volume and into regions of lower field strength might be expected (Marhic, 1975). Shearer (Shearer, 1970) calculates a deconfinement time in which the plasma expands in the focal region due to the ponderomotive force on the critical surface. At an intensity of 3×10^{11} W/cm² and a scale length of 250 μ , this time is less than a nanosecond, so a density perturbation may be expected for most of the laser pulse time. An effect producing similar density depression in the focal volume is the thermal expansion of the heated plasma from the focal volume. By the removal of the plasma from the region in either of these manners, subsequent beam propagation through the region may occur.

Hydrodynamic expansion of the plasma from the heated region could also occur, and this effect was

observed on a spatial scale much larger than the laser focal spot. The holographic analysis of the density perturbation, however, found that a critical layer was present on this large scale.

The sharp rise on the transmitted beam suggested a sudden increase in transmission after an initial delay. This delay, about 30 nsec, was about the same as the acoustic propagation time across the column. It was also (much more roughly) similar to the theoretically-derived time for propagation of a thermal bleaching front across the column. It appeared, then, that the first portion of the laser pulse conditioned the plasma in some manner to allow the second portion of the pulse to be transmitted. The delay in transmission could result in wide-angle backscattering of 10.6μ radiation from the critical layer during the first portion of the pulse. After the critical layer was modified to allow transmission, the second portion of the pulse might be seen in transmission as a delayed pulse. The shorter transmitted pulse seen at high intensities exhibited both a rapid rise and a rapid fall. This implied some intensity-dependent cutoff mechanism that occurred at high intensity, since the fall time of the pulse was much more rapid than that of either the incident pulse or the transmitted pulse observed at lower intensity.

The appearance of a Fresnel diffraction pattern on the burnspot has been attributed to the formation of a hard aperture within the plasma by the beam (Steel, 1976). Such an aperture was expected to be approximately the size of the focal spot to produce the diffraction rings, and was expected to remain stationary during time of beam transmission to produce the high-contrast fringes.

In preparation for a parameter study of the appearance of a Fresnel diffraction pattern produced by a spherical wavefront through a circular aperture, a computer code was written to calculate the intensity distribution that resulted from application of the Fresnel approximation to the Huygens-Fresnel diffraction formula. By Romberg integration of the resulting expression, the intensity was calculated for an arbitrary distribution of illumination on the aperture. The resulting program proved extremely costly to run, so the study was postponed. A description of the code and the relevant physics is placed in Appendix G. Correct operation of the code was verified by calculation of the intensity distribution at the center of curvature of the wavefront, which yielded the Fraunhofer pattern associated with a focal point, and could be checked with an analytical representation.

Refraction effects could not be eliminated as

a possible cause of the ring structure. A decrease in plasma density along the beam axis would refract the beam into the focal region. If the intensity near the center of the focal spot was great enough to cause this self-focusing, and the intensity at the edge was not, the resulting transmitted beam could display interference effects from the two portions of the beam. It would seem highly coincidental, however, that the resulting pattern would have the circular structure, the thick bright border, and the increasing ring spacing toward the edge of the spot as seen in a Fresnel pattern.

This and the preceding section have described both the temporal and spatial modulation on the CO_2 beam transmitted through the overdense plasma. The most unusual observation was of an intensity threshold requirement for beam transmission. This intensity threshold was about $3.5 \times 10^{11} \text{ W/cm}^2$ for incidence before pinch time, and was about $2 \times 10^{11} \text{ W/cm}^2$ for incidence after pinch. The transmitted pulse was compressed from its original width of 38 nsec to about 15 nsec at an incident intensity of $4 \times 10^{11} \text{ W/cm}^2$, and was seen to peak about 30 nsec later in intensity than the incident pulse. This was indicative of the removal of the first portion of the transmitted pulse by a shutter effect in the plasma. Possible errors in the experiment were dealt with. A model that

explained some features of the pulse distortion in terms of an intensity-dependent transmission fraction was discussed, and some physical mechanisms for the intensity dependence were proposed. The appearance of a Fresnel diffraction pattern on the transmitted burnspot suggested the creation of an aperture in the plasma by the beam.

5.7 Radiation from the interaction region

The largest part of the information was a result of the holographic information and the transmitted beam diagnostics. However, a look at the results of the associated diagnostics is useful. The remainder of this chapter sets forth the observations concerning optical emission from the laser-heated plasma, the search for x-ray emission, and the measurements obtained with the backscatter detector.

Optical emission was monitored from the region of the plasma column that coincided with the focal volume of the CO₂ laser. By imaging this region with a magnification of three upon a 1 mm diameter aperture, and then reimaging this spatially filtered image on a PIN diode detector, optical emission from a 300 μ region of the plasma was selected. By selectively viewing the focal volume in this manner, any change in optical

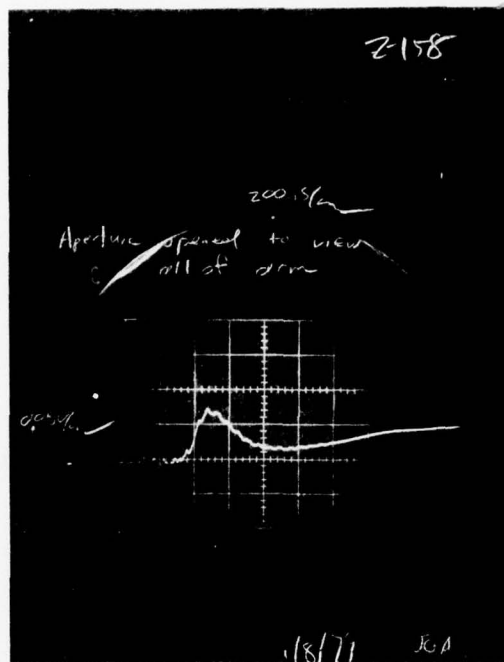


FIGURE 5.51 OPTICAL PULSE FROM PLASMA AT PINCH
 TIME - NO APERTURE OR IMAGING
 (200 nsec/div)

AD-A050 773

MICHIGAN UNIV ANN ARBOR LASER PLASMA INTERACTION LAB
CRITICAL LAYER PENETRATION IN A COLD Z-PINCH PLASMA BY HIGH-INT--ETC(U)
SEP 77 J G ACKENHUSEN

F/G 20/9

AFOSR-77-3349

UNCLASSIFIED

LPIL-TR-100

AFOSR-TR-78-0352

NL

4 OF
AD
A050773



END
DATE
FILMED

4-78

DDC

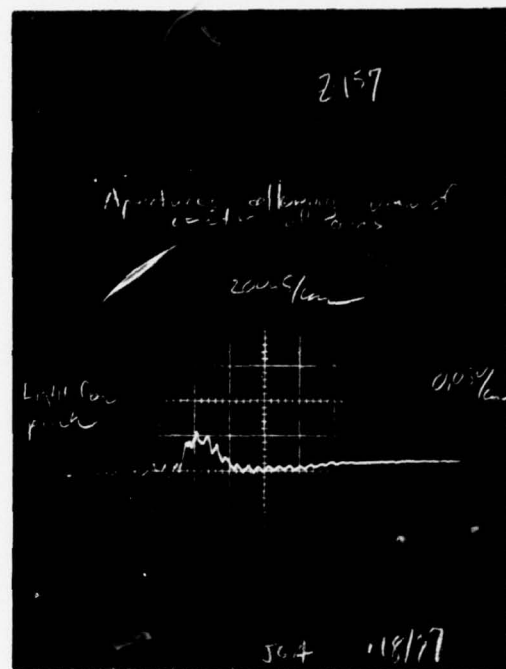


FIGURE 5.52 OPTICAL PULSE FROM PLASMA
 TIME - APERTURE, NO IMAGE
 (200 nsec/div)

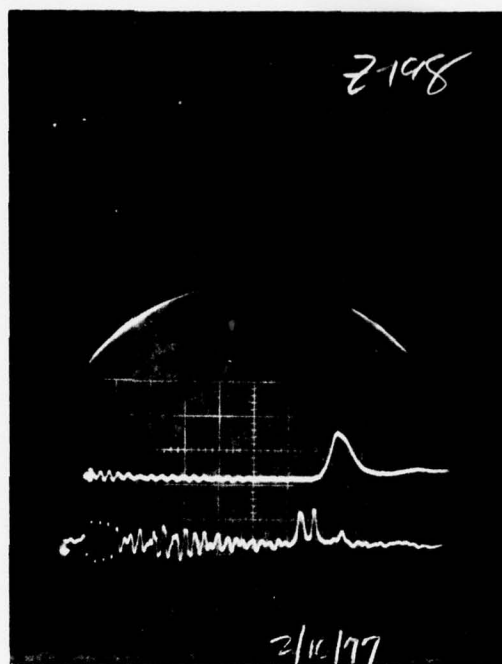


FIGURE 5.53 OPTICAL PULSE FROM PLASMA AT PINCH
TIME - APERTURED AND IMAGED
(200 nsec/div)

emission brought on by the laser was separated from the background emission of the rest of the plasma.

Earlier shots were taken with no imaging system at all; the detector was placed near a viewing port and monitored emission from the entire chamber. The light pulses observed in this fashion were characteristically 300 nsec FWHM pulses followed by a slowly-rising pulse that reached the same intensity as the first after about 1.4 μ sec (Figure 5.51). With an aperture in place to allow view of only the center of the chamber, but with no imaging, the first pulse was decreased to 200 nsec FWHM, and the second slower pulse was barely detectable (Figure 5.52). With the plasma column imaged on the aperture and reimaged on the detector, the half-width of the light pulse was decreased to 80 nsec and the slower second pulse did not appear at all (Figure 5.53). In this manner, a short, sharp pulse with a well-defined maximum was obtained for use as a marker of the time of pinch. The maximum of this pulse could be located to within 10 nsec by careful use of a comparator. Alignment of the optical detector to the focal volume is described in Section 3.5.

An approximate two-fold increase in light output from the focal volume was seen for laser incidence upon the plasma within 15 nsec of time of pinch. The

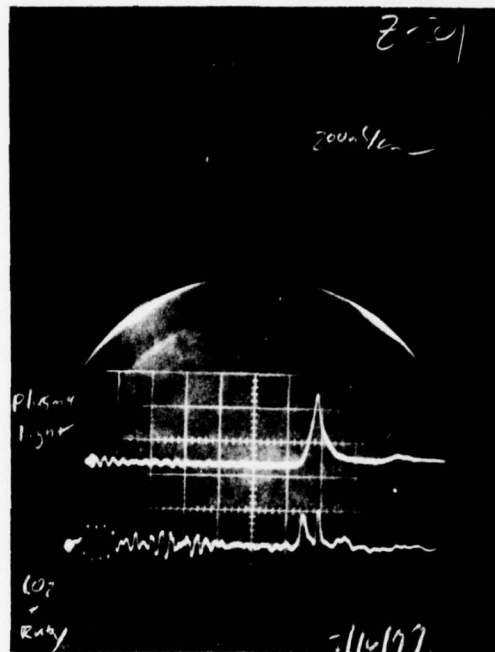


FIGURE 5.54 ENHANCED, NARROWED OPTICAL PULSE
FROM LASER-HEATED PLASMA

light pulse was also much sharper than in the case of no laser incident (compare Figure 5.54, with laser incident 10 nsec before pinch, to Figure 5.53, with no laser effect). The FWHM of the pulse with laser incident on pinch was only about half that seen for late laser incidence. This enhanced radiation burst gave evidence of plasma heating by the laser beam.

In Section 4.1, the results of looking for x-ray emission from the Z-pinch plasma were mentioned, and may be reviewed briefly. No x-ray emission was seen, implying an upper bound to electron temperature of about 40 eV. X-ray emission from the plasma was also investigated when fired upon by the CO₂ laser to determine whether sufficient heating had occurred for x-ray detection. By use of the x-ray analysis code discussed earlier, it was estimated that the focal volume would have to reach a temperature of 200 eV before detectable x-ray bremsstrahlung emission would be expected. If thermal conduction out of the focal spot region were set to zero, deposition of only 0.02 J in the region would raise the temperature enough to allow x-ray detection. This was only a small fraction of the available energy incident in the laser beam. However, if the laser energy diffused out of the focal volume, the result would be the same amount of energy distributed among many more

particles, which would greatly reduce the electron temperature increase.

The results of the investigation of continuum emission are summarized: Some heating from the CO₂ laser was evident from the enhanced optical continuum emission from the region and the sharpening of the optical pulse to a shape more indicative of the laser pulse. However, not enough heating occurred to move sizeable continuum emission into the X-ray spectrum. The 40 to 70 eV temperature in the larger perturbed region calculated in Section 5.4 was not sufficient to produce enough x-ray emission for detection. If all the energy incident in a typical 3 J pulse were confined to heating electrons and ions in the focal region, a temperature of 27 keV would result, entirely sufficient for x-ray detection. Thermal conduction out of the region, lowering the temperature below 200 eV, explained the lack of X-ray observation and was compatible with the hydrodynamically-estimated temperature.

5.8 Backscattered 10.6 μ radiation

The final diagnostic to be described is the backscatter measurement. Although the exceedingly small detector area and the long optical path made these results very sensitive to alignment, and although the

preamplifier for the detector had a 70 nsec rise time which allowed only measurements integrated over the 38 nsec laser pulse width, there were some observations worth noting.

Steel found that backscatter energy was much less than would be predicted to occur by stimulated Brillouin scattering (Steel, 1976). The backscatter that he observed was linear with incident energy, which was not predicted for the SBS mechanism. However, classical backscatter from a critical layer would be linear in many cases. Since an infinite homogeneous plasma was expected to produce stimulated Brillouin scattering at the high laser intensity used, he concluded that the finite interaction length and steep density gradients in the plasma prohibited achieving the wave-matching conditions over sufficient lengths to produce appreciable stimulated backscatter.

In this investigation, a small amount of backscatter, linear with incident energy, was also seen. As detailed in Section 3.3, room vibrations picked up by the backscatter pellicle caused motion of the spot across the face of the backscatter detector, so the backscatter pellicle was replaced by a salt wedge for a portion of the investigation. The wedge was optically flat on its reflecting surface, so a smaller focal spot was obtained, which could be better positioned on the

detector. Furthermore, room vibrations did not cause motion of the spot as before.

With the wedge in place, an attempt was made to quantify the fractional backscatter seen by the detector. Alignment was attempted with a helium-neon laser beam reflected from a mirror in a manner so as to retrace the incident beam path. This met with only moderate success, as the accuracy in retro-reflecting the beam was not sufficient to reposition the spot on the detector reproducibly.

More success in alignment was achieved in maximizing the backscattered radiation from an air-break-down plasma produced by the CO_2 beam focused into the air-filled chamber. Since reflection was occurring from a laser-produced plasma, the beam was backscattering in a manner believed representative of backscatter off the plasma. By adjusting the backscatter mirror to maximize signal from a number of air-breakdown shots, alignment was achieved.

To calibrate absolutely the backscatter detector proved very difficult. The method of placing a mirror to simulate plasma backscatter did not afford sufficient accuracy over the long path lengths and small detector area to provide confidence that the beam was reproducibly positioned. An attempt at calibration in this manner

was made by maximizing a HeNe alignment laser signal by adjustment of the mirror that was simulating plasma backscatter. Once this was done, an attenuated CO₂ beam was fired upon the back-reflecting mirror and to the detector. Measurement of this backscattered energy with a Gentec energy monitor and subsequent attenuation of the CO₂ beam with the calibrated attenuating cell provided a signal of known energy upon the detector, thus affording calibration.

A completely different method of calibration, using air-breakdown backscatter, was also used. An experiment determined that energy transmission through an air-breakdown plasma was 75% at an intensity of 1.2×10^{11} W/cm². It was then assumed that all energy not transmitted was backscattered. This value of 25% backscatter was within a factor of two of the 45% reported by the Osaka University group for reflection off a polyethylene target at this CO₂ intensity (Osaka University, 1976). Since the goal was only order-of-magnitude accuracy, this was felt to be a reasonable assumption (more realistically, it was the only possible assumption). The response of the backscatter detector to this signal yielded a sensitivity within a factor of four (lower) of that obtained by the previous method.

The integrated backscatter energy was found to be 2×10^{-4} of the incident using the air-breakdown

calibration, or 0.5×10^{-4} using the mirror calibration scheme. The intermediate value of 10^{-4} is taken in the following discussion.

Unfortunately, the slow response of the backscatter detector preamplifier prohibited any of the fine temporal resolution possible with the transmitted beam. Researchers have seen enhancement of laser mode structure on a backscattered pulse, similar to that seen on the transmitted pulse in this investigation (Donaldson, Hubbard, & Spalding, 1976). This fine structure was far outside the time response of this detector system.

A backscatter fraction of about 10^{-4} was seen to be independent of intensity. The backscatter collection optics only gathered a fraction of the 2π associated with the backward direction. In fact, the ratio of solid angle of the detector to 2π was 2.7×10^{-3} . So if some mechanism uniformly distributed backscattered radiation over 2π , only a small portion would appear in the detector. Recalling the hydrodynamic estimate of absorption of 60% - 70%, only about 30% of the incident radiation remained to be backscattered, refracted, or transmitted. Thirty percent backscattered uniformly over 2π yields about 8×10^{-4} at the detector. Furthermore, collisional absorption of the radiation on its way to the turning point in the plasma, and additional absorption on the way out would reduce backscatter intensity

by about

$$\exp\left(-\frac{32}{15} \frac{v_{ei}L}{c}\right)$$

(Section 2.1)

For the collision frequency and scale length of the experiment, this factor was about 0.01.

Therefore, while stimulated scattering could increase fractional backscatter, many mechanisms could greatly reduce it. The spreading of the backscatter into 2π could result from rippling of the critical surface by the incident laser radiation (Kindel, 1977). This rippling has been predicted to be of length comparable to the laser wavelength on the critical surface, and would specularly reflect incident light over a variety of angles into 2π .

CHAPTER SIX

CONCLUSIONS AND IMPLICATIONS

The experiment may be briefly summarized: A 38 nsec FWHM pulse of high-intensity $10.6\ \mu$ radiation was focused radially upon an overdense low-temperature Z-pinch plasma. Holographic interferometry at 347.2 nm provided density information and monitored the evolution of the laser-plasma interaction. A series of auxiliary experiments suggested an average electron temperature of about 20 eV, which, when coupled to the high incident intensity (up to $4 \times 10^{11}\ \text{W/cm}^2$) and short density scale length (100 - 200 μ), placed the ratio of electron oscillatory velocity to thermal velocity near one. Optical emission and backscattered radiation from the focal volume were monitored. A series of Z-pinch shots with no laser incident provided a holographic cinema of target plasma evolution.

The most significant observation was an intensity threshold for transmission of the $10.6\ \mu$ radiation through the overdense portions of the plasma. Thresholds of $3.5 \times 10^{11}\ \text{W/cm}^2$ for incidence before pinch time and $2 \times 10^{11}\ \text{W/cm}^2$ for incidence after pinch time were observed. The difference in thresholds was attributed to the difference in the density profile and radial velocity

direction before and after pinch. Increasing the incident intensity above the threshold value resulted in the shortening of the transmitted pulse to a minimum FWHM of 15 nsec at peak intensity of 4×10^{11} W/cm².

The burnspot of the beam transmitted through the overdense plasma exhibited the concentric rings of a Fresnel diffraction pattern from a hard circular aperture.

Transmission of 1% incident intensity typified shots with laser incidence before pinch time, and 3% transmission was indicated in post-pinch shots above the intensity threshold.

In interpretation of the data, comparison of holographically-determined features of plasma evolution to a one-dimensional MHD simulation obtained agreement of the density profile at time of pinch. However, the interferograms suggested multidimensional effects in the evolution. A temporal difference in the dip of the time-derivative of the current through the discharge, associated with a momentary high impedance, and time of peak compression was attributed to a separation of the current piston and shock (density shell) in the contracting plasma.

Holographic interferograms provided density information concerning the interaction on a hydrodynamic scale. The appearance of a shock wave expanding from the

point of laser incidence on the column provided information used in a hydrodynamic calculation of energy absorption. This calculation, relating density ratio across the shock, shock front thickness, and shock velocity to energy deposition and temperature increase, provided an estimate of fractional energy absorption of about 60% - 70%. Heating of the interaction region was also indicated by enhanced optical emission.

The temporal modulation of the transmitted beam of 10.6μ radiation was interpreted in terms of a model of intensity-dependent transmission through a nonlinear medium. This model, however, was not adequate to account for the pulse-width compression at increasing intensity.

Backscatter radiation was linear with intensity and was about 10^{-4} of incident energy. The small solid angle sampled by the backscatter detector was only 0.27% of the general 2π of the backward direction.

Comparison of some of the observed effects to other results reported in the literature is limited to those publications encountered in the course of this research, and is not complete.

Apparently, the published literature contains no accounts of experimental investigation of the evolution of the Z-pinch discharge, as was performed in this experiment. In fact, only one Z-pinch has

been reported that approaches the densities of the LPIL Z-pinch (Neufeld et al., 1976), and these densities are at least a factor of two lower.

Also, the interferometric investigation of laser interaction with an independently-produced plasma is not described in the literature. However, holographic interferometry of CO₂ laser-produced plasmas has been reported (Donaldson & Spalding, 1976a) to exhibit signs of caviton formation. The interferometric investigation of laser-solid target interaction has been performed at several institutions (Reintjes et al., 1976; Maher & Hall, 1975). Many of these results, as well as some theoretical efforts (Fauquignon & Floux, 1970; Bobin, 1971), have indicated the occurrence of laser-supported detonation waves when the target is surrounded by a gaseous medium. The observation of a shock wave, followed by a deflagration wave, which was discussed in the reports just mentioned, was confirmed in this research. The phenomenon of "cratering," that is, the occurrence of a damage site much larger than the incident beam spot, has been reported by Dyer (Dyer, 1973) as well as by Reintjes et al. The latter study also exhibited high plasma expansion velocity that was believed to have caused fringe blur in this study.

Transmission of a CO₂ laser pulse through an underdense plasma has been studied (DeBoo & Bach, 1975;

Burnett & Offenberger, 1976; Fabre & Stenz, 1974). The first study was performed on an independently-produced plasma at low intensity and exhibited inverse bremsstrahlung absorption. The second study utilized the laser for plasma production as well as for transmission studies and reported complete absorption of the latter portion of the tail of the laser pulse, but showed no modification of the gain-switched spike. The work of Fabre and Stenz utilized an independently-produced ruby laser-breakdown plasma which was irradiated with a rather high-intensity CO_2 pulse ($4 \times 10^{11} \text{ W/cm}^2$ peak). The transmitted pulse exhibited a dip where plasma density had reached a maximum of about $9 \times 10^{18} \text{ e}^-/\text{cm}^3$. Their absorption measurements vs. intensity showed a dependence associated with inverse bremsstrahlung up to an incident intensity of $1 \times 10^{10} \text{ W/cm}^2$. Above this point, absorption was higher than expected by inverse bremsstrahlung calculations. This they attributed to an undetermined form of anomalous absorption. Their calculation of inverse bremsstrahlung absorption included a mechanism of heating in the focal region due to absorption. The investigation was carried out on a marginally-underdense plasma at peak intensity that was a factor of ten lower than used in this experiment. Similar studies at higher densities and intensities are not reported.

An observation of enhanced modelocking structure,

similar to that seen on the transmitted pulses in this investigation, was reported on backscatter radiation from a laser-produced plasma (Donaldson & Spalding, 1976b). The other observations of the present study, such as the abrupt threshold, the narrowing of transmitted pulse with increasing power, and the ring pattern on the transmitted pulse, are not reported elsewhere.

Some implications of the primary experimental results are worth noting. The investigation provided an experimental view of several unique effects which could result from an assortment of physical mechanisms. An intensity-dependent transmission fraction may be analytically modeled in a number of ways. One explanation includes the increased heating and associated increased transparency of the plasma at high powers. Alternative analysis in terms of profile modification at high intensities is possible. In addition, the thermal expansion of plasma from the focal volume due to heating could result in intensity-dependent transmission. Similarly, hydrodynamic motion in the laser-heated plasma is apparent and could contribute to non-linearity. The abrupt intensity threshold and the subsequent modification of the transmitted pulse shape, both temporally and spatially, do not appear to be interpretable in terms of just one of the above mechanisms, and thus may arise from a combination of factors.

Many effects, such as the pulse-shape modification and transmission threshold, were only seen when firing into an overdense target plasma. The theoretical picture of radiation interaction at a critical layer contains predictions unique to the overdense regime, such as very short absorption lengths, increased ponderomotive force, and critical surface instabilities. The contribution of a single physical mechanism seems unlikely.

Further experiments to distinguish between the possible mechanisms are to begin with a higher resolution holographic system able to record density perturbations of the focal spot size. However, even with the increased resolution, the observation of such small perturbations is not certain, as the path length of the holographic beam through the unperturbed plasma greatly exceeds the pathlength through the small focal volume for holography perpendicular to the direction of laser incidence. High-resolution holography down the axis of the CO_2 beam is expected to alleviate this partially, although other experimental problems arise, such as separating the holographic scene beam from the CO_2 beam and getting both wavelengths through the port windows. The transmission of a low-power probe beam through the focal volume, collinear with the CO_2 laser axis, would also clarify the nature of the perturbation.

A more complete inventory of the CO₂ radiation is also needed. With about 60% energy absorption and 3% transmission, with a small fraction of a percent backscatter into the focusing optics, a sizable amount of CO₂ energy is left unaccounted for. This energy is expected to have been deflected into angles other than directly forward or backward. The appearance of this energy at angles not collinear with the CO₂ beam may not be monitored with the present target chamber because of the geometric limitations imposed by the arms. The redesign of the Z-pinch to a device affording observation over more angles could also be useful in allowing more incident intensity, because present intensity limitations are set by the optics rather than by the laser.

Time resolution of backscatter and wide-angle scattering analysis would provide interesting comparison to the temporal modification observed on the transmitted beam. In particular, if radiation was seen at non-forward angles during the 30 nsec delay in transmission, an explanation for the clipping of the transmitted pulse would favor scattering rather than absorption during this delay time. The backscatter of radiation over the entire 2π of backward angle could be attributed to the rippling of the critical surface by the beam.

The development of a 1 to 2 nsec pulse-length

CO₂ laser system is proceeding in this laboratory. Replacing the present 38 nsec system with the short-pulse system would allow experiments in which hydrodynamic effects are not as large a contributor. This would also provide closer simulation to laser-pellet experiments, which occur at shorter pulse lengths.

Further theoretical modeling should include a detailed treatment of a plasma shock in an inhomogeneous medium with a time-dependent external energy source. A numerical modeling of the laser-plasma interaction at right angles to the axis of cylindrical symmetry would prove useful in a calculation of transmission vs. time through the overdense plasma. Extension of the photon transport picture of the laser-plasma interaction to include an estimate of reflectivity would provide an alternative to the WKB calculations of reflectivity mentioned here, and the further inclusion of time dependence of the reflected signal would provide a prediction readily verified in the laboratory.

As with many experiments with plasmas or other complicated physical systems, this investigation has raised at least as many questions as it has addressed. The observation of an intensity threshold for transmission through an overdense plasma has indicated a number of possible physical mechanisms that can only be differentiated by further experimental and theoretical work.

APPENDIX A

PROPAGATION OF EM WAVE THROUGH A HOMOGENEOUS PLASMA

A basic analysis of the propagation of electromagnetic waves through a homogeneous plasma begins with the two Maxwell curl equations. These are written in the one-dimensional case of propagation down the z -axis, with the electric field polarized in the iy direction and the magnetic field in the ix direction:

$$\nabla \times \mathbf{E} = -\frac{1}{c} \frac{\partial \mathbf{B}}{\partial t} \quad \rightarrow \quad \frac{\partial \mathbf{E}}{\partial z} = -\frac{1}{c} \frac{\partial \mathbf{B}}{\partial t}$$

$$\nabla \times \mathbf{B} = \frac{4\pi}{c} \mathbf{J} + \frac{1}{c} \frac{\partial \mathbf{E}}{\partial t} + \frac{\partial \mathbf{B}}{\partial t} = \frac{4\pi}{c} \mathbf{J} + \frac{1}{c} \frac{\partial \mathbf{E}}{\partial t}$$

(Gaussian units)

Taking the derivative of the first equation with respect to z and the derivative of the second with respect to t , the wave equation is obtained for a plane wave:

$$\frac{\partial^2 \mathbf{E}}{\partial z^2} = \frac{1}{c^2} \left(4\pi \frac{\partial \mathbf{J}}{\partial t} + \frac{\partial^2 \mathbf{E}}{\partial t^2} \right)$$

For a linearly polarized wave, $\mathbf{E}(z,t)$ may be represented as

$$\mathbf{E}(z,t) = E_0 e^{j(\omega t - kz)}$$

To obtain the real quantity E , the exponential and its

complex conjugate are added. Substituting this form of E into the wave equation,

$$-k^2 E = \frac{4\pi}{c^2} \frac{\partial J}{\partial t} + \omega^2 E$$

The current, J , is not yet known, and is found from the equation of motion of an electron in an oscillating electric field. The current is defined by

$$J = n e v$$

n = electron density

e = charge on electron

v = velocity of electron

To find the electron velocity in the oscillating field, the equation of motion is written:

$$m\ddot{y} + m\nu_{ei}\dot{y} = -e(E + \dot{y} \times B)$$

$$v \equiv \dot{y}$$

$\nu_{ei}\dot{y}$ = effective force due to collisions
at frequency ν_{ei}

In this low-intensity limit, the magnetic field associated with the wave is set to zero. This approximation removes most of the high-intensity effects of interest in the experiment, and is only temporary. Solving for v by using the assumed form of E , the velocity is expressed in complex form similar to E :

$$v(z,t) = v_o e^{j(\omega t - kz)}$$

$$v_o = \frac{eE}{m} \frac{(v_{ei} - j\omega)}{\omega^2 + v_{ei}^2}$$

Substitution of this velocity into the expression for J yields:

$$J = \frac{1}{4\pi} \frac{\omega_p^2}{\omega^2 + v_{ei}^2} (v_{ei} - j\omega) E$$

$$\omega_p^2 = \frac{4\pi n e^2}{m}$$

The plasma frequency, ω_p , is a very basic parameter in the study of electromagnetic radiation with a plasma, and is conveniently expressed in terms of the electron density, n (cm^{-3}), as

$$\omega_p = 5.64 \times 10^4 \sqrt{n} \text{ rad/sec}$$

This expression for the current may be differentiated with respect to time and placed in the wave equation to obtain:

$$-k^2 E = \frac{1}{c^2} \frac{\omega_p^2 (\omega^2 - j\omega v_{ei})}{\omega^2 + v_{ei}^2} E - \omega^2 E$$

This expression readily simplifies to the dispersion relation for electromagnetic waves in the plasma:

$$k^2 = \frac{\omega^2}{c^2} \left(1 - \frac{\omega_p^2 (1 - jv_{ei}/\omega)}{\omega^2 + v_{ei}^2} \right)$$

The refractive index of a medium is defined as the ratio of the phase velocity of radiation in a vacuum, c , to its phase velocity in the medium, ω/k . The index of refraction of the plasma is thus given by

$$\eta = \operatorname{Re}(ck/\omega) = \left(\frac{\beta}{2} + \frac{1}{2} \sqrt{\beta^2 + (1-\beta^2)(v_{ei}/\omega)^2} \right)^{1/2}$$

$$\beta = 1 - \frac{\omega_p^2}{\omega^2 + v_{ei}^2}$$

If ω is taken to be real, then the dispersion relation indicates that k must be complex. The imaginary part of k , when substituted into the expression for E , indicates that the electric field is attenuated. More traditionally, since the intensity is what is experimentally observed, attenuation of the intensity is expressed in terms of $\operatorname{Im}(k)$ as

$$\frac{I}{I_0} = \frac{E^2}{E_0^2} = \exp(-2\operatorname{Im}(k)z)$$

Therefore, an attenuation constant, K , may be defined by

$$K = 2\text{Im}(k) = 2 \frac{\omega}{c} \left(-\frac{\beta}{2} + \frac{1}{2} \sqrt{\beta^2 + (1-\beta^2)(v_{ei}/\omega)^2} \right)^{1/2}$$

and so the ratio of intensity after to before propagation through an extent of plasma of length z is

$$\frac{I}{I_0} = \exp(-Kz)$$

In obtaining the above expressions for the attenuation constant and the refractive index, the square root of a complex quantity, $z = x + jy$, was taken, and is expressed in polar form as

$$z = r e^{j\theta}$$

$$z^{1/2} = r^{1/2} e^{j\theta/2}$$

$$r = \sqrt{x^2 + y^2}$$

$$\theta = \tan^{-1}(y/x)$$

One may simplify the expression for the refractive index and the attenuation constant by assuming that $\omega_p < \omega$ and $v_{ei} \ll \omega$. The ratio of laser frequency, ω , to typical electron-ion collision frequency, v_{ei} , in this experiment was about 0.02, so the second assumption is reasonable. Since for the overdense plasma, $\omega_p > \omega$ in much of the plasma, the first assumption is not reasonable, but some relevant physics may be obtained. However, in the regions near critical density, the entire

expressions for η and K must be used.

The simplifying assumptions provide the cold collisionless expression of the refractive index, which is found from the previous expression in the limit $\nu_{ei} = 0$.

$$\eta = \sqrt{1 - (\omega_p/\omega)^2}$$

The attenuation constant is given in this approximation by

$$K = \left(\frac{\omega_p}{\omega} \right)^2 \frac{\nu_{ei}}{nc} .$$

APPENDIX B
REFRACTION IN A CONTINUOUS MEDIUM

For a medium with density gradient scale lengths that are long compared to the radiation wavelength, the scalar wave equation,

$$\nabla^2 u + k^2 u = 0$$

$$k = 2\pi/\lambda$$

$$\lambda = \text{wavelength of radiation in medium}$$

may be assumed to have solutions of the form

$$u = A e^{jk_0 S}$$

(Sommerfeld, 1949)

$$k_0 = 2\pi/\lambda_0$$

$$\lambda_0 = \text{wavelength of radiation in vacuum}$$

The quantity S is called the eikonal. The surfaces defined by

$$S(r) = \text{constant}$$

correspond to the propagating wavefronts, and the unit normal to these surfaces form the rays of geometrical optics. If the proposed solution is substituted into the scalar wave equation, the differential equation for the eikonal is defined:

$$(\nabla S)^2 = \eta^2(r)$$

$$\eta = \text{refractive index; } \eta = \lambda_0/\lambda$$

In the particular case of η being only a function of distance from a point, r , the formula of Bouguer relates the angle between the direction of the ray at some point in the medium and the ray from the origin to that point, ϕ , by (Born & Wolf, 1975):

$$\eta r \sin\phi = \text{constant}$$

This formula may be applied to determine the amount of refraction that a ray experiences as a result of passing through a cylindrical plasma with an axisymmetric density distribution (Schreiber & Hunter, 1973). A computer code based on this technique was used in various parts of this investigation.

A formula more useful for estimates of refraction in a spherically- or cylindrically-symmetric medium relates the radius of curvature of a ray, ρ , to the scalar product of the unit normal to the ray, \mathbf{v} , and the gradient of the refractive index:

$$1/\rho = \mathbf{v} \cdot \nabla(\ln \eta(r))$$

In the special case of small-angle refraction by a plasma of radius r_0 for radiation whose critical density is n_c ,

$$n_c = \frac{1.1 \times 10^{21}}{\lambda^2 (\mu)}$$

the angle of refraction, θ , is approximately given by

$$\sin \theta = \frac{r_o}{n_c} \frac{dn}{dr}$$

APPENDIX C

HYDRODYNAMIC ENERGY TRANSFER AND SHOCK WAVES

This discussion of hydrodynamics begins with a brief treatment of gas dynamics in general. The equations from which most of the effects to be discussed arise are the equations stating the conservation of mass, conservation of momentum, and conservation of energy:

$$\frac{D\rho}{Dt} + \rho \nabla \cdot \mathbf{u} = 0$$

$$\rho \frac{D\mathbf{u}}{Dt} + \nabla p = 0$$

$$\frac{D\varepsilon}{Dt} + p \frac{D\mathbf{u}}{Dt} = 0$$

$$\frac{D}{Dt} \equiv \frac{\partial}{\partial t} + \mathbf{u} \cdot \nabla$$

$$\rho = \text{density}$$

$$\mathbf{u} = \text{velocity}$$

$$p = \text{pressure}$$

From these equations may be derived a wave equation (Zel'dovich & Raizer, 1966) which allows solutions in the form of right- or left-traveling waves propagating at the sound speed, c_0 , given by

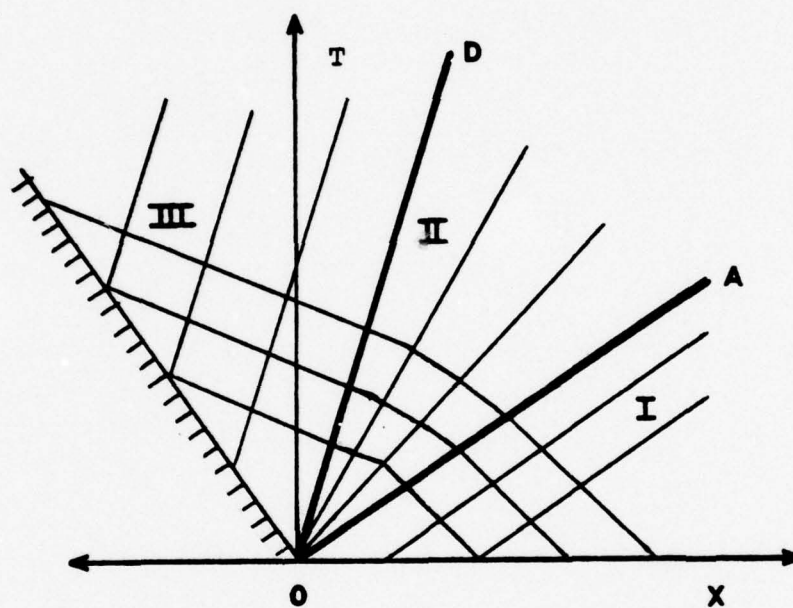


FIGURE C.1 THE X,T DIAGRAM FOR A CENTERED RAREFACTION WAVE

$$c_o^2 = \left(\frac{\partial p}{\partial \rho} \right)_s .$$

These waves may arise from propagating pressure or density disturbances of small amplitude. For a fluid moving with a local velocity u and having a local sound velocity c_o , a family of characteristics may be drawn on a plot of x vs. t for plane isentropic flow. These characteristics are given by one of two equations:

$$\frac{dx}{dt} = u + c_o ; \quad \frac{dx}{dt} = u - c_o$$

The two characteristics through a point x_o, t_o are paths along which a small disturbance at a location x_o and time t_o propagates in the x, t plane. The two curves correspond to propagation in opposite direction.

A problem that illuminates some concepts is the situation of a one-dimensional extent of gas (for example, gas contained in a cylinder) which is bounded on one end by a movable piston. If the piston is instantaneously accelerated to a velocity w and is thence withdrawn from the gas at this constant velocity, an x, t diagram may be drawn with the origin, $(0,0)$, located at the original position of the piston at the time it first begins motion (Figure C.1). The slope of the

receding boundary in the figure for $t > 0$ is given by the piston velocity, w . The characteristics may be drawn as shown. In Region I, the slope of the characteristics is just $1/c_0$, and corresponds to the state before piston motion begins.

In Region III, the sound velocity is lowered at the moving piston face. Thermodynamical considerations show that the new sound velocity in the lower-pressure region, c , is related to the sound velocity in the undisturbed region by

$$c(w) = c_0 - \frac{\gamma-1}{2} |w|$$

γ = ratio of specific heats

The characteristics in this region take on a different slope:

$$\frac{dx}{dt} = c_0 - \frac{\gamma+1}{2} |w|$$

In Region II, the characteristics of positive slope originate from the point $(0,0)$. The heavy lines between the regions in the diagram define the "head" (A) and the "tail" (D) of the rarefaction wave that moves into the original volume as a result of the receding piston. The head of the rarefaction wave moves with the original speed of sound, c_0 , into the region $x > 0$, and the tail of the wave moves at the lower sound speed of the low-

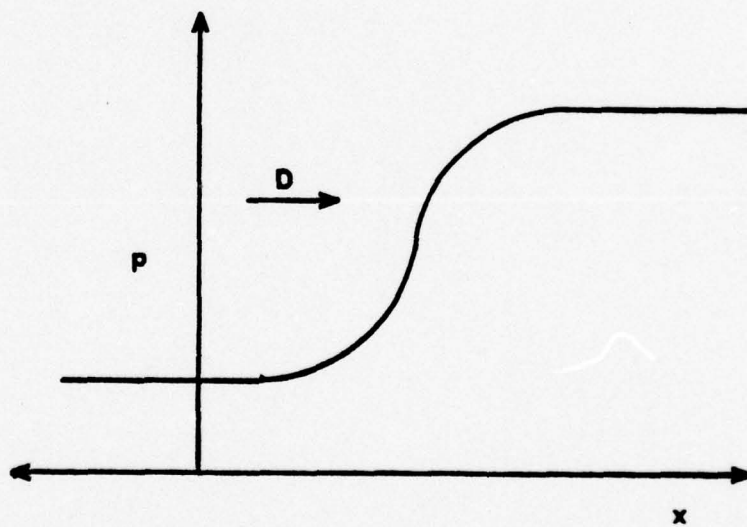
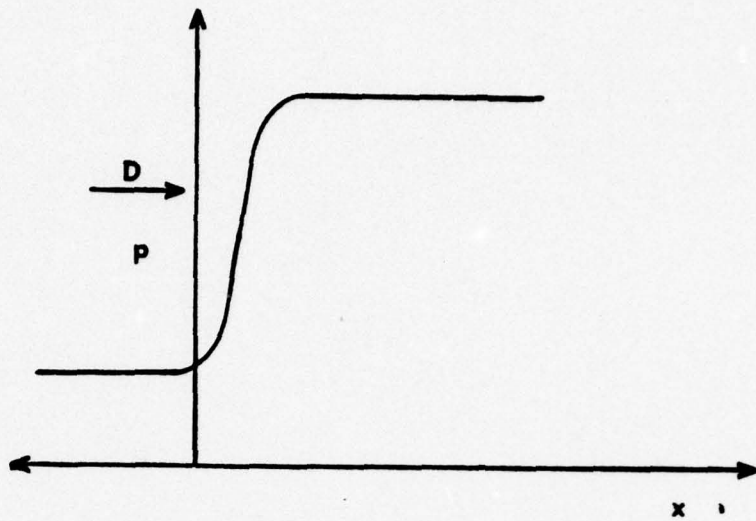


FIGURE C.2 RAREFACTION WAVE AT TWO DIFFERENT TIMES

pressure region in front of the piston, c.

A plot of pressure vs. position at successive times indicates a pressure rarefaction moving to the right (Figure C.2). By inspection of the x, t diagram, the pressure rarefaction has a thickness that increases with time as a result of the difference in propagation speeds of the head and tail of the wave.

If a similar plot were made of pressure vs. the ratio x/t , the shape of the wave would not change as a function of time. The type of motion whereby the dynamic quantities (pressure, density, etc.) may be frozen on a plot with the ratio x/t^α as the abscissa is given the name "self-similar motion," and simplifies the solution of the gas dynamic equations considerably. The case of the receding piston is a particular example for which $\alpha = 1$. The motion for which the head and the tail of the resulting wave originate from the zero-point, as in the case of the instantaneously-accelerated piston, is described as being "centered." Thus, a description has been given of a centered, self-similar rarefaction wave.

It would seem reasonable that imparting a sudden, constant velocity to the piston in the opposite direction, to move it into the gas, would also provide a centered, self-similar wave. However, the speed of sound in a

high-pressure region is greater than in a low-pressure region. Thus, the speed of propagation of the tail of such a wave will be at the sound speed associated with the compressed gas at the piston face, and the propagation speed of the head of the wave will occur at the lower sound velocity of the undisturbed gas. Thus, the tail of the wave will overtake the head of the wave, producing a non-physical condition. The analytical result of this evaluation is the overshooting of the wave, with subsequent multi-valued thermodynamic quantities.

The physical solution to this problem is a discontinuous change in the flow variables. The compression wave takes the form of a thin layer that propagates in the direction of piston motion, with the initial values of density and pressure on one side, and the final, higher values on the other. This discontinuity is a shock wave.

The equations of gas dynamics may be transformed to a reference frame moving with the shock. In this frame, the regions may be separated into Region 0, the undisturbed region in front of the shock, and Region 1, the region of higher density behind the shock. If D is the shock velocity in the laboratory frame, then the velocities of gas on either side of the front are given in the frame of the shock front by

$$u_0 = -D$$

$$u_1 = v_1 - D$$

where v_1 is the (laboratory) gas velocity behind the shock. The transformed gas dynamic equations express conservation of mass, momentum, and energy on either side of the shock in the frame of the shock front:

$$\rho_0 u_0 = \rho_1 u_1$$

$$p_0 + \rho_0 u_0 = p_1 + \rho_1 u_1$$

$$\epsilon_0 + \frac{p_0}{\rho_0} + \frac{u_0^2}{2} = \epsilon_1 + \frac{p_1}{\rho_1} + \frac{u_1^2}{2}$$

$$\epsilon_{0,1} = \text{internal energy}$$

$$\epsilon = \frac{1}{\gamma-1} \frac{p}{\rho}$$

Also, an additional energy term may be placed in the energy balance equation to represent energy deposition from an external source, such as a laser.

If both a thermodynamic property of the gas, such as the internal energy expression, $\epsilon = \epsilon(p, \rho)$, and one variable behind the shock, characterizing its strength, are known, the remaining flow variables may be calculated. The Hugoniot equation relates the internal energy on either side of the shock front to the pressures, p_0 and p_1 , and the specific volumes, $V_0 = 1/\rho_0$, $V_1 = 1/\rho_1$. The Hugoniot curve is a plot of p vs. V , as determined by the initial conditions of the gas. From such a plot, the

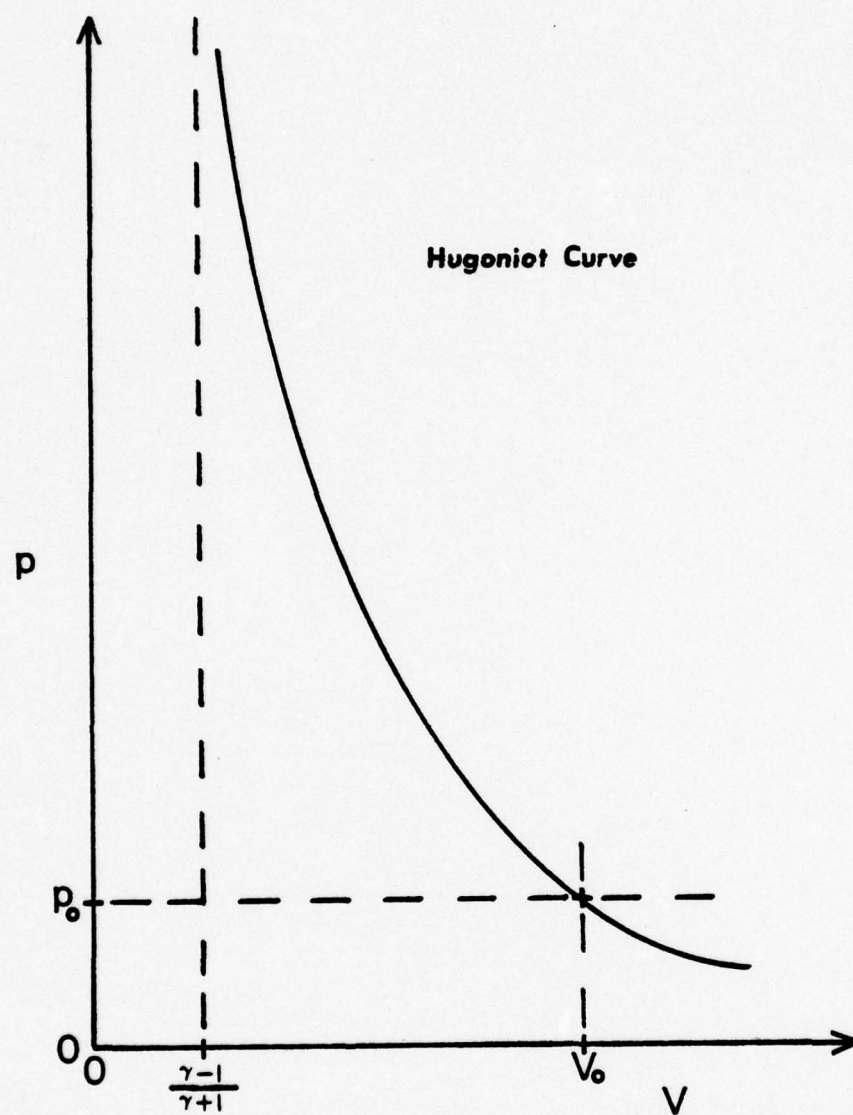


FIGURE C.3 HUGONIOT CURVE

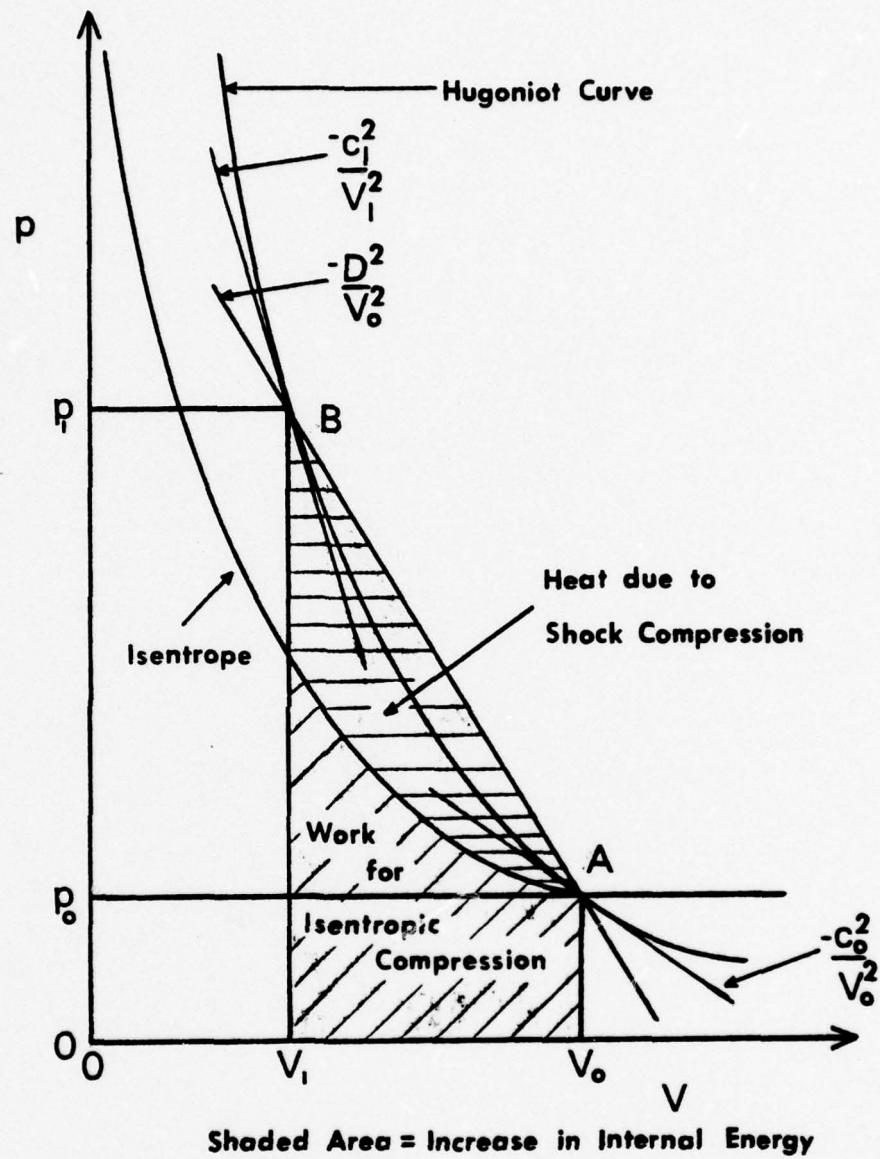


FIGURE C.4 HUGONIOT CURVE - GEOMETRIC INTERPRETATION

thermodynamically-determined pressure in a shock front as a function of its specific volume may be found. For an ideal gas, where $\varepsilon(p, \rho) = pV/(\gamma-1)$, an explicit solution of the Hugoniot relation may be obtained. The equation of the Hugoniot curve in this case is

$$\frac{p_1}{p_0} = \frac{(\gamma+1)V_0 - (\gamma-1)V_1 + 2Q/p_0}{(\gamma+1)V_1 - (\gamma-1)V_0}$$

where an external energy source, Q , has been included. For the case $Q = 0$, the expression reduces to the usual Hugoniot relation for a normal shock in an ideal gas with ratio of specific heats of γ . The curve for a normal shock ($Q = 0$) is plotted in Figure C.3. The maximum specific volume ratio across the shock is given by $V_1/V_0 = (\gamma-1)/(\gamma+1)$. The initial conditions of the gas are at the point $V = V_0$, $p = p_0$. A shock wave increases the pressure and decreases the specific volume in a path along the Hugoniot curve passing through the initial conditions.

A geometric interpretation is useful in obtaining velocities and energy increases from the curve (Zel'dovich & Raizer, 1966). The Hugoniot curve is redrawn in Figure C.4. Below the Hugoniot curve, which corresponds to shock compression, is drawn the curve corresponding to isentropic compression, $p \propto V^{-\gamma}$. The initial state is

denoted by A, and the final state, after shock compression, is labelled B. The isentrope intersects the Hugoniot curve at A and is tangent to it. The slope of the isentrope at A determines the sound velocity in the undisturbed region by the relation

$$(\text{slope})_A = - \frac{c_0^2}{V_0^2}$$

The slope of the Hugoniot curve at B provides the sound velocity in the region after shock compression by a similar relationship:

$$(\text{slope})_B = - \frac{c_1^2}{V_1^2}$$

The slope of the line joining the initial and final states yields the propagation velocity of the shock:

$$(\text{slope})_{AB} = - \frac{D^2}{V_0^2}$$

As the plot indicates, the shock propagation velocity is greater than the acoustic velocity in the unperturbed region, and less than the acoustic velocity behind the shock.

The area of the parallelogram $(V_1, 0) (V_0, 0) A B$ is just the increase in internal energy due to shock compression. Similarly, the area under the isentrope between

V_1 and V_0 is the work associated with isentropic compression. This work is less than that due to shock compression, which indicates additional heating as a result of shock compression over that by isentropic compression.

The inclusion of dissipative mechanisms, ignored so far, lessens the gradients across the shock front from the steep jump described thus far. The final and initial values of the quantities across the shock remain unchanged. Inclusion of dissipative effects, such as thermal conduction out of the region and viscosity within the region, introduce a finite (non-zero) thickness to the shock front.

For the case of a weak shock, in which the limiting ratio $(\gamma-1)/(\gamma+1)$ is not approached, the solution of the gas dynamic equations with the inclusion of heat conduction or viscosity provides an approximate front thickness, Δx :

$$\Delta x \approx \frac{\ell}{\frac{n_1}{n_0} - 1}$$

The mean free path, ℓ , is determined by heat conduction or viscosity as follows:

$$\ell_{th} \approx \frac{\kappa}{\rho c_p v_{th}} \qquad \ell_{vis} \approx \frac{\mu}{\rho v_{th}}$$

κ = thermal conductivity

c_p = specific heat at constant pressure

μ = viscosity

Self-similar motion has been described as flow whose parameters depend only on the ratio $1/t^\alpha$. The problem of calculating the velocity of propagation of the spherical shock from a strong explosion in a homogeneous atmosphere serves to illustrate the use of self-similar motion to simplify a relevant problem. The only parameters that determine the gas motion are the initial density of the gas and the energy deposited in the explosion. To combine these quantities to obtain a variable of the self-similar form $1/t^\alpha$, the ratio is needed:

$$\left(\frac{E}{\rho_0} \right) = \left(\frac{ml^2}{t^2} / \frac{m}{l^3} \right)^{1/5} = \frac{1}{t^{2/5}}$$

Thus, $\alpha = 2/5$. A plot of any flow variable vs. $1/t^{2/5}$ would remain frozen in time, so a time dependence of $t^{2/5}$ is indicated. The radius of the front increases as $t^{2/5}$, but to convert $t^{2/5}$ to the dimension of length, the multiplicative factor $(E/\rho_0)^{1/5}$ must be used:

$$R(t) \propto (E/\rho_0)^{1/5} t^{2/5}$$

Thus, the radius of the spherical shock as a

function of time has been found to within a multiplicative constant as a function of time, density, and deposited energy. The dimensionless constant, ξ_0 , may be determined by a more complete analysis that puts the ratio of specific volumes on either side of the shock at the strong-shock limit and assumes that the entire mass of gas encountered by the expanding wave is collected in a shell at the shock front. The result is the Taylor-Sedov expression:

$$R(t) = \xi_0 (E/\rho_0)^{1/5} t^{2/5}$$

$$\xi_0 = \left(\frac{75}{16\pi} \frac{(\gamma-1)(\gamma+1)^2}{3\gamma-1} \right)^{1/5}$$

For the common case of $\gamma = 5/3$, ξ_0 is about 1.1.

This problem falls into the broad category of self-similar processes in gas dynamics. In general, if the length and time scales cannot be constructed separately from the initial parameters of the problem, the solution will not depend on length or time alone, but on a combination of the two, l/t^α . The parameter α may be defined in one of two ways. In the case of the point explosion, α was determined by the initial specifications before the problem was solved. Another sort of self-similar motion does not allow determination of α until the problem is solved. In this case, α is determined by conditions on the final equations. A particular example is the implosion of a spherical shock wave, of great interest in laser

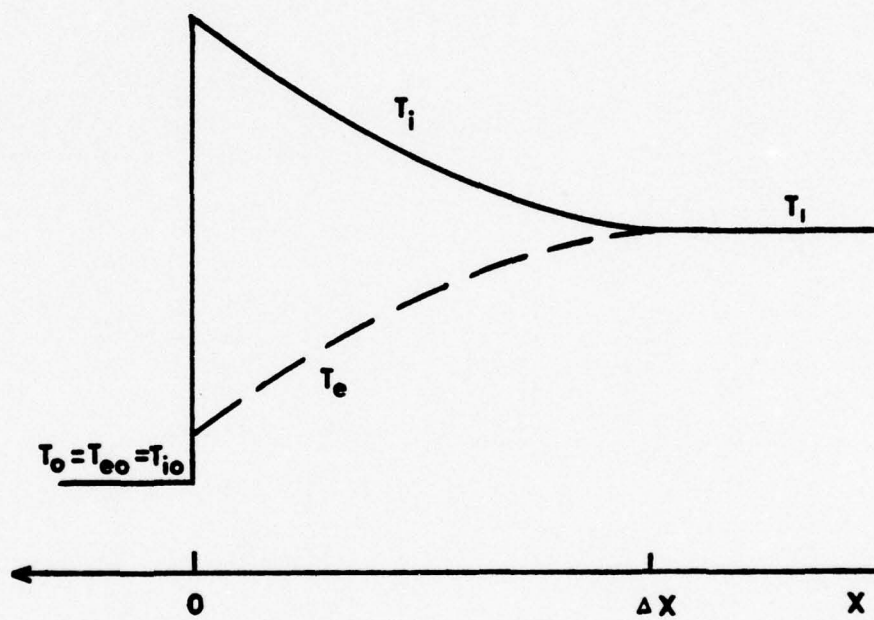


FIGURE C.5 TEMPERATURE DISTRIBUTION OF SHOCK WAVE
IN PLASMA

fusion. In this case, α is determined by the condition of single-valuedness of the thermodynamic parameters.

The preceding discussion has not been specialized to shock waves in a plasma. In a fully-ionized plasma, the ions are quickly heated by a shock wave due to the high viscosity of the ion fluid; however, the electrons, due to their high mobility, have a lower viscosity and are only heated by electron-ion collisions behind the shock front. This leads to a relaxation region behind the shock front in which the electron temperature equilibrates with the ion temperature in a region of thickness D_{Teq} (Figure C.5). The electron-ion equilibration time is given by

$$\tau_{\text{eq}} = \frac{3.8 \times 10^8 A \theta^{3/2} (\text{eV})}{n_i Z^2 \ln \Lambda}$$

Another feature that distinguishes a fully-ionized plasma from a neutral gas in hydrodynamic analysis is the temperature dependence of the thermal conductivity. The thermal conductivity of Spitzer is given by

$$\kappa = 4.67 \times 10^{-12} \frac{\theta^{5/2} \cdot \epsilon(Z) \cdot \delta(Z)}{Z \ln \Lambda} \frac{\text{cal}}{\text{sec} \cdot \text{deg} \cdot \text{cm}}$$

For the plasma under analysis, $Z = 2$ and $\epsilon = .410$ and $\delta = .356$. Changing the units on the thermal conductivity,

$$\kappa = 2.85 \times 10^{-11} \theta^{5/2} \frac{J}{\text{sec} \cdot ^\circ\text{K} \cdot \text{m}}$$

In standard analyses of heat conduction in media of constant thermal conductivity, the temperature distribution usually decays exponentially from the heat source. However, in a nonlinear medium, a sharp boundary in temperature moving away from the heat source may occur. This propagating boundary forms a thermal wave in the medium, whose velocity of propagation may be calculated. For example, an instantaneous point source of energy in a medium for which the thermal conductivity depends on temperature as θ^n produces a spherically-expanding thermal front whose radius is expressed as a function of time:

$$r_f \propto t^{\frac{1}{3n+2}}$$

The thermal wave generally starts out at a velocity far above the acoustic velocity in the medium, and slows as it expands. When the wave has slowed to a point where its velocity is equal to the acoustic velocity, it can cause fluid motion in the manner of a shock wave, which then moves ahead of the thermal wave.

APPENDIX D

OPTICAL DESIGN OF ALIGNMENT COMPENSATING WEDGE

The path of a ray in an optical system may be characterized by its lateral position from the axis of the system, δ , and the angular direction of propagation with respect to the axis, ψ . To determine analytically the effect of a wedge placed in a beam, a formula was derived from Snell's law and geometric arguments to relate the path of a ray after passing through a wedge, (ψ', δ') to its path at point of entrance to the wedge, (ψ, δ) . Because the images reflected off either wedge surface, one to the energy monitor and one to the back-scatter focusing mirror, were directed out of the incident beam axis, the wedge required placement so that its entrance face formed an angle ϕ with the plane normal to the axis of the system (Figure D.1). For a wedge of refractive index η , minimum thickness t , and wedge angle α , the exit angle of the beam with the optical axis is

$$\psi' = \phi + \alpha - \sin^{-1} \left\{ \eta \sin \left\{ \sin^{-1} \left(\frac{1}{\eta} \sin(\phi - \psi) \right) + \alpha \right\} \right\}$$

$$\psi = \text{entrance angle}$$

The total lateral deflection imparted by the wedge to the beam, a , is given by

$$a = \frac{t + l \tan \alpha}{\cos\{\sin^{-1}(\frac{1}{n} \sin(\phi - \psi))\}} \cdot \sin\{\phi - \sin^{-1}(\frac{1}{n} \sin(\phi - \psi))\}$$

l = distance along face from thinner edge to
ray entrance point

In application of the two formulas, the signs of the angles are important, and are as indicated in the figure.

After leaving the NaCl wedge, a 10.6 μ ray was calculated to have a path defined by (0.75873°, 0.160 cm) for entrance at (0°, 0 cm). The helium-neon alignment beam had a path given by different values of ψ' and δ' due to the difference of n of NaCl at 10.6 μ and .6328 μ ($n_{\text{NaCl}}(10.6 \mu) = 1.49$; $n_{\text{NaCl}}(.6328 \mu) = 1.53$). In fact, for the HeNe alignment beam entering the wedge at (0,0), the exit ray was characterized by (0.82054°, 0.147 cm). Thus, the compensating wedge had to impart a $\Delta\psi$ to the HeNe beam of 0.00618°. The difference in lateral deflection, $\Delta\delta$, between the two wavelengths was less than 0.2 mm and was ignored as being beyond the accuracy of the alignment technique.

Using the above considerations, a wedge of BK-7 glass placed 13 cm down the beam path from the NaCl beamsplitter would match (ψ, δ) of the CO₂ beam (in the absence of the compensator) and the HeNe beam (in the presence of the compensator), if it had a wedge angle of 9.5 min and a thickness of 0.75 in.

APPENDIX E

SOURCE LISTING OF X-RAY ANALYSIS CODE

```

ROMBERG INTEGRATION OF H(E) TIMES SPECTRAL DIST. A PLOT
THIS PROGRAM REQUIRES AS INPUT THE FOIL DENSITY, GRAF
RHOFOI, THE THICKNESS OF THE TWO ABSORBED FOILS WITHIN
THE RATIO CALCULATION, T1 AND T2, IN CM, THE THICKNES
SCINTILLATOR IN CM, X, AND XI AND ETA, THE FIRST OF WHI
SLOPE OF THE FOIL ATTENUATION CONSTANT, K(CM**2/GRAM)
PLOT OF LOG10K VS WAVELENGTH IN ANGSTROMS, AND ETA IS
Y-INTERCEPT OF THE SAME PLOT. A AND B ARE RESPECTIVE
SAME REQUIRED QUANTITIES FOR THE SCINTILLATOR ON A PLO
ATTENUATION CONSTANT VERSUS WAVELENGTH. THE PRECEDIN
INPUT IN NAMELIST FORM ON INPUT DEVICE 4. THE TEMPERE
BREMSSTRAHLUNG SOURCE, THETA, IS READ FROM INPUT DEVIC
DEVICE 7 IS USUALLY ASSIGNED TO *DUMMY* AND CONTAINS C
APPROXIMATIONS TO THE INTEGRALS USING THE ROMBERG METH
DEVICE 6 YIELDS THE FINAL INTEGRALS FOR THE TWO THICKN
AS WELL AS THE RATIO.
A K-EDGE, MARKED BY A DIFFERENT Y-INTERCEPT, KETA, TO
USED FOR ENERGIES LESS THAN K, IS ALLOWED FOR IN
THE FOIL. DEVICE 7 ALSO CONTAINS A PLOT OF RESPONSE
FUNCTION VS. WAVELENGTH, FOR ENERGIES AS DETERMINED BY
INPUT VALUE OF THE VARIABLE ITER. THE ENERGY DOMAIN,
0 TO 25 KEV, IS DIVIDED INTO 2** (ITER + 4) SUBDIVISIO
WHEN LISTING H(E) VS. E.
CAN REPRESENT THE SCINTILLATOR CROSS SECTION ON A LOG
WAVELENGTH AS TWO STRAIGHT LINES INTERSECTING AT ENER
AS BREAK, THE FIRST WITH SLOPE A1 AND INTERCEPT B1, AND
SECOND WITH SLOPE A2 AND INTERCEPT B2.

IMPLICIT REAL*8(A-H,K,O-Z)
REAL*8 FINT
NAMELIST/INPUT/RHOFOI,XI,ETA,A,B,A1,B1,BREAK,T1,T2,X,XI
COMMON THETA,RHOFOI,XI,ETA,A,B,A1,B1,BREAK,X,K,KETA
DIMENSION TRAP(3,3)
READ(4,INPUT)
WRITE(6,208)
208 FORMAT(' ENTER TEMPERATURE IN KEV. ')
READ(5,209) THETA
WRITE(7,212)
209 FORMAT(1D5.4)
NC=0
T=T1
777 DO 50 I=1,3

```

```

NODIV=2**I(I+4)
AREA=0.
WIDTH=.25D02/(DFLOAT(NODIV))
SAVEA=A
SAVEB=B
DO 40 J=1,NODIV
EL=(DFLOAT(J-1))*WIDTH
ER=(DFLOAT(J))*WIDTH
IF(EL.GT.BREAK)A=A2
IF(EL.GT.BREAK)B=B2
IF(EL.EQ.0.)GO TO 69
IF(ER.GT.K)GO TO 70
GO TO 80
70 IF(EL.LT.K)GO TO 71
L=R
R=KFINT(ER,T)
AR=(WIDTH/2.)*(L+R)
GO TO 39
71 L=R
R=FINT(K,T)
AR=((K-EL)/2.)*(L+R)
AREA=AREA+AR
L=KFINT(K,T)
R=KFINT(ER,T)
AR=((ER-K)/2.)*(L+R)
GO TO 39
80 L=R
R=FINT(ER,T)
AR=(WIDTH/2.)*(L+R)
GO TO 39
69 R=FINT(ER,T)
AR=(WIDTH/2.)*R
39 P=ER/THETA
IF(P.GT.170)GO TO 37
AITCH=R*DEXP(P)
36 IF(I.EQ.ITER)WRITE(7,213)ER,AITCH
212 FORMAT(' ENERGY',10X,'H(E)')
213 FORMAT(D9.4,7X,D26.20)
GO TO 40
37 AITCH=0.0
GO TO 36
40 AREA=AREA+AR
TRAP(I,1)=AREA
A=SAVEA
B=SAVEB
50 CONTINUE
C ROMBERG CORRECTION OF SEQUENCE OF TRAPEZOIDAL INTEGRATION
DO 100 J=2,3
DO 100 I=1,3
100 TRAP(I,J)=(4.**(J-1)*TRAP(I,J-1)-TRAP(I-1,J-1))/(4**J)
C PRINT VALUES AND THEN REPEAT THE ABOVE FOR SECOND TOTAL
DO 200 I=1,3

```



```

200 WRITE(7,210)(TRAP(I,J),J=1,I)
210 FORMAT('0',3D30.20)
      T=T2
      NC=NC+1
      IF(NC.EQ.1) GO TO 776
      BOTTOM=TRAP(3,3)
      GO TO 900
776 TOP=TRAP(3,3)
      GO TO 777
900 RATIO=TOP/BOTTOM
      WRITE(6,211)TOP,BOTTOM,RATIO
211 FORMAT('0INTEGRAL FOR T1 IS ',D36.20,' INTEGRAL FOR T
      ! RATIO IS ',D36.20)
      RETURN
      END
      REAL FUNCTION KFINT*8(E,T)
      IMPLICIT REAL*8(A-H,G-Z)
      COMMON THETA,RHOFOL,XI,ETA,A,B,A2,B2,BREAK,X,K,KETA
      KFINT=E*DEXP(-E/(THETA))*DEXP(-RHOFOL*((12.4/E)**XI)*
      #DEXP(2.303*ETA)*T)*(1-DEXP(-(12.4/E)**A)*DEXP(2.303*B
      RETURN
      END
      REAL FUNCTION FINT*8(E,T)
      IMPLICIT REAL*8(A-H,K,O-Z)
      COMMON THETA,RHOFOL,XI,ETA,A,B,A2,B2,BREAK,X,K,KETA
      FINT=E*DEXP(-E/(THETA))*DEXP(-RHOFOL*((12.4/E)**XI)*
      #DEXP(2.303*KETA)*T)*(1-DEXP(-(12.4/E)**A)*DEXP(2.303*
      RETURN
      END

```

APPENDIX F
CHECKLIST FOR EXPERIMENTAL PROCEDURE

Pre-run checklist

1. Check holography floating tables
2. Check each holography beam - normal to plate
3. Check ultimate pressure in Z-pinch
4. Fill backscatter detector reservoir with liquid N₂
5. Align backscatter detector
6. Fill backscatter attenuator cell with propylene
7. Fill CO₂ attenuator cell with propylene (26")
8. Fire CO₂; check for signal presence on transmitted beam diagnostics
9. Fill Z-pinch with helium to desired pressure
10. Put up clean film at transmitted beam monitor
11. Put up CO₂ laser beamstop
12. Synchronize the two PIN diodes with common laser pulse
13. Check coincidence of holography and CO₂ lasers
14. Set CO₂ laser output energy as desired
15. Check synchronization of Z-pinch trigger
16. Time all other signal channels with pulser
17. Check all scope sensitivities
18. Check all cable connections

19. Remove light-tight flags from scope cameras
20. Activate "Caution" warnings
21. Load holography plate
22. Align CO₂ laser to center of plasma column

Intra-shot checklist

1. Check film in scope cameras
2. Photograph scope gratings
3. Turn off scope gratings
4. Turn on liquid N₂ cooling Z-pinch arms
5. Check Z-pinch pressure
6. Check liquid N₂ level in backscatter detector
7. Check both holography and CO₂ optical paths
for obstructions
8. Peak the UV output from the frequency-doubler
9. Turn on and check Z-pinch charging and trigger
voltages
10. Turn off all room lights but one
11. Turn on CO₂ laser charging circuits and ascertain
that triggering mode is set to "External"
12. Reset, clear, and enable storage scope for CO₂
energy monitor
13. Reset all single sweep scopes
14. Check that all scope gratings are off and all
scope camera viewing ports are closed

15. Open all scope camera shutters on "time" exposure
16. Start timer at 1 minute
17. At 38 sec, begin charging Z-pinch
18. Turn final room light off
19. Open film box containing holography plate
20. At 13 sec on timer, begin charging holography laser
21. Check that all scopes are still enabled
22. At 0 sec, Z-pinch and two lasers fire
23. Close all camera shutters
24. Turn up graticle on holography timing scope
25. Advance camera on this scope
26. Turn off CO₂ charging circuits
27. Turn off Z-pinch charging circuits
28. Move mirror in holography reference arm
29. Begin charging holography laser
30. After 11 sec, open shutter on holography timing camera
31. After laser fires, close shutter
32. Turn Z-pinch supply voltages off
33. Turn off Z-pinch liquid nitrogen
34. Change holography plates and close film box
35. Reset holography reference mirror
36. Turn on room lights
37. Develop and mark scope pictures
38. Check Z-pinch pressure

39. Record storage scope reading; clear scope
40. Replace film at transmitted beam burnspot monitor
41. Make all necessary timing and sensitivity changes
42. Record changes on log sheet
43. Iterate

APPENDIX G
FRESNEL DIFFRACTION THROUGH CIRCULAR APERTURE
NUMERICAL ANALYSIS

The distribution of the scalar field at a point (x_0, y_0) which results from the illumination of an aperture with boundaries defined by Σ and illuminated with a wavefront spatial distribution given as a function of x_1 and y_1 at the aperture, $U(x_1, y_1)$, is expressed by the Huygens-Fresnel diffraction formula. With r_{01} expressing the distance between the aperture point (x_1, y_1) and the observation point (x_0, y_0) , and with \mathbf{n} the unit vector normal to the aperture, the field strength at a point (x_0, y_0) is expressed as the sum of Huygens spherical wavelets over the aperture:

$$U(x_0, y_0) = \iint_{\Sigma} h(x_0, y_0; x_1, y_1) U(x_1, y_1) dx_1 dy_1$$

$$h = \frac{1}{j\lambda} \frac{e^{jkr_{01}}}{r_{01}} \cos(\mathbf{n}, \mathbf{r}_{01})$$

$$k = \frac{2\pi}{\lambda}$$

$$\lambda = \text{wavelength of illumination}$$

The magnitude of the vector \mathbf{r}_{01} between the aperture point and the field point is given by

$$r_{01} = \sqrt{(x_0 - x_1)^2 + (y_0 - y_1)^2 + z^2}$$

in which z is the distance from the aperture plane to the observation plane. In many cases, z is much greater than x_0 , y_0 , x_1 , or y_1 . In these cases, the expression for r_{01} , which is alternatively expressed by factoring out z ,

$$r_{01} = z \sqrt{1 + \frac{(x_0 - x_1)^2}{z^2} + \frac{(y_0 - y_1)^2}{z^2}}$$

is approximated by the simplification $\sqrt{1+\delta} \approx 1 + \frac{\delta}{2}$

$$r_{01} \approx z \left[1 + \frac{1}{2} \left(\frac{x_0 - x_1}{z} \right)^2 + \frac{1}{2} \left(\frac{y_0 - y_1}{z} \right)^2 \right]$$

Then,

$$h(x_0, y_0; x_1, y_1) \approx \frac{e^{jkz}}{j\lambda z} \exp\left\{ \frac{jk}{2z} ((x_0 - x_1)^2 + (y_0 - y_1)^2) \right\}$$

and the Fresnel approximation is obtained. Setting $\cos(n, r_{01})$ to one

$$U(x_0, y_0) = \frac{e^{jkz}}{j\lambda z} \exp\left\{ \frac{jk}{2z} (x_0^2 + y_0^2) \right\} \times$$

$$\mathcal{F} \left\{ U(x_1, y_1) \exp\left(\frac{jk}{2z} (x_1^2 + y_1^2) \right) \right\} \bigg|_{\substack{f_x = x_0/\lambda z \\ f_y = y_0/\lambda z}}$$

(Goodman, 1968)

In this expression, \mathcal{F} represents the two-dimensional Fourier transform, given by

$$\mathcal{F}(g) = \iint_{-\infty}^{\infty} g(x,y) \exp(-j2\pi(f_x x + f_y y)) dx dy$$

If in addition to the Fresnel assumptions,

$$z \gg \frac{k(x_1^2 + y_1^2)}{2}$$

then

$$\frac{jk}{2z} (x_1^2 + y_1^2) \rightarrow 0$$

and the Fraunhofer expression is obtained:

$$U(x_0, y_0) = \frac{e^{jkz}}{j\lambda z} \exp\left(\frac{jk}{2z}(x_0^2 + y_0^2)\right) \mathcal{F}\{U(x_1, y_1)\} \Big|_{\substack{f_x = x_0/\lambda z \\ f_y = y_0/\lambda z}}$$

The Fourier transform of a function of circular symmetry is sometimes more conveniently expressed in one dimension. The two-dimensional Fourier transform of a function of circular symmetry is expressed in cylindrical coordinates as the Fourier - Bessel transform, \mathcal{B} :

$$\mathcal{B}(g(r)) = 2\pi \int_0^{\infty} r g(r) J_0(2\pi \rho r) dr$$

The variables f_x and f_y in the two-dimensional Fourier transform, and ρ in the Fourier-Bessel transform, represent the frequency component of interest; to obtain the amplitude of a particular frequency, the desired value is substituted for f_x , f_y , or ρ .

It was desired to find the field distribution, $U(x_0, y_0)$ for a converging wave passing through a circular aperture. The problem has an inherent cylindrical symmetry, suggesting the use of the Fourier-Bessel transform to obtain the field distribution as a function of radial position on the observation plane, r_0 :

$$U(r_0) = \frac{e^{jkz}}{j\lambda z} \exp\left(\frac{jk r_0^2}{2z}\right) \int \left(U(r_1) \exp\left(\frac{jk}{2z} r_1^2\right) \right) \Big|_{\rho=r_0/\lambda z}$$

Because the aperture illuminator was a spherical wavefront, the aperture illumination function incorporated a phase factor indicative of convergence to a point s along the z axis:

$$U(r_1) = U_0(r_1) \exp\left(-\frac{jk r_1^2}{2s}\right)$$

Observation at the center of wavefront curvature, $s = z$, provides the Fraunhofer expression for the field distribution associated with the Fraunhofer pattern at a focus of a lens.

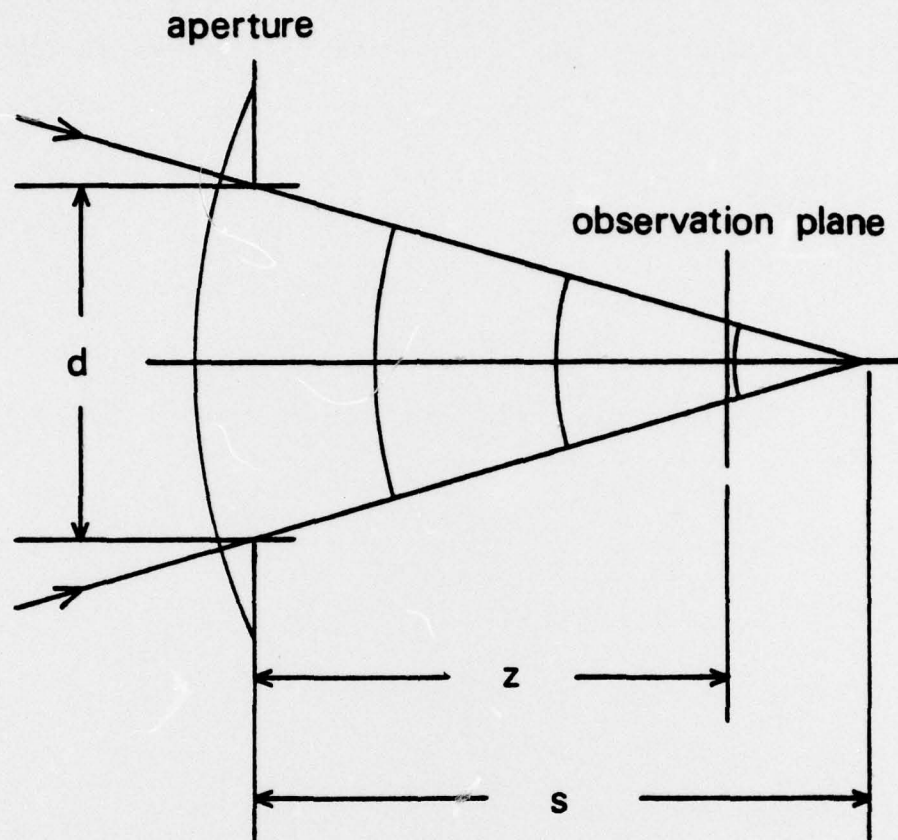


FIGURE G.1 CALCULATIONAL GEOMETRY OF FRESNEL DIFFRACTION

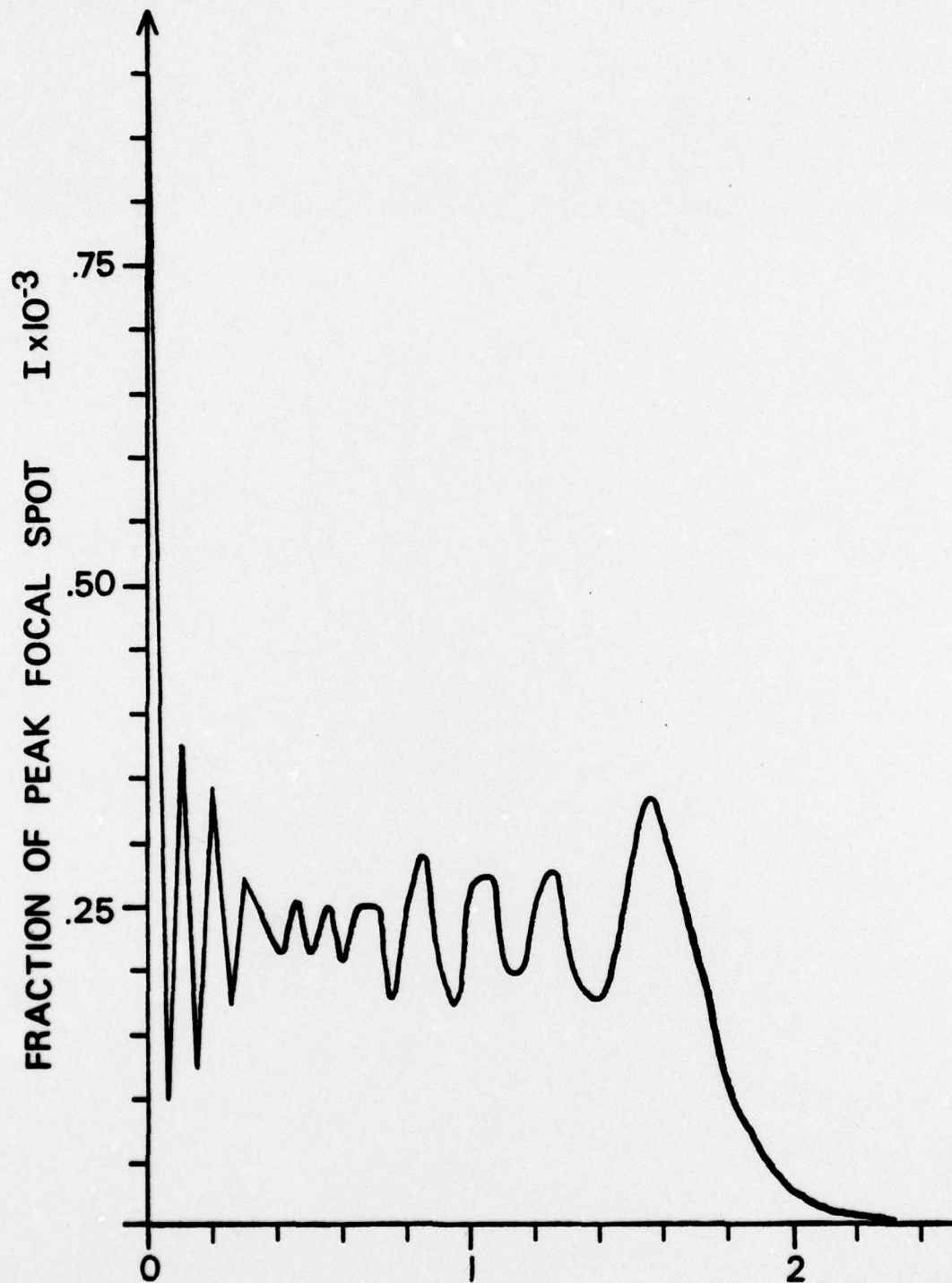


FIGURE G.2 INTENSITY VS. RADIUS FOR FRESNEL DIFFRACTION
PATTERN FROM CIRCULAR APERTURE

The computer code that was written solved the Fourier-Bessel transform of an arbitrary aperture illumination function, $U_0(r_1)$. The particular case of uniform aperture illumination gives rise to the analysis of Lommel as discussed in Born and Wolf.

To verify correct operation of the code, the field distribution at the center of wavefront curvature was calculated and found to match the analytical expression.

Figure G.1 shows the geometry associated with the calculation. The diffraction pattern from an aperture of diameter d , illuminated by a wave converging to a point s , with an arbitrary distribution across the aperture plane, was calculated at the plane z as a function of the radial position r_0 .

A sample non-trivial calculation for $s = 19.5$ cm, $z = 17.5$ cm with uniform aperture illumination, and an aperture diameter of 4 cm, was performed. The resulting intensity distribution, $(U(r_0))^2$, is shown as a function of r_0 in Figure G.2. Of interest is the increased spacing of the rings toward the edge of the pattern, very similar to the pattern seen in transmission through the overdense plasma.

A listing of the source code follows:

2
3
4
5
6
7
8
9
10
11
12
13
14
15
16
17
18
19
20
21
22
23
24
25
26
27
28
29
30
31
32
33
34
35
36

FRESNEL DIFFRACTION BY CIRCULAR APERTURE
JOHN G. ACKENHUSEN---UNIVERSITY OF MICHIGAN DEPARTMENT OF NUCLEAR ENGINEERING
JULY 20, 1977

THIS PROGRAM FINDS THE INTENSITY DISTRIBUTION, ALSO, AS A
FUNCTION OF R_0 , THAT RESULTS FROM APPLICATION OF THE FRESNEL
APPROXIMATION TO THE HUYGENS-FRESENL DIFFRACTION FORMULA FOR
A CIRCULAR APERTURE OF RADIUS "RCNEMX". THE FORMULA USED FOR THE FIELD
DISTRIBUTION IS $U = 1/2(C + IS)$, WHERE C AND S ARE SIMILAR TO
THOSE DEFINED IN RCN AND WOLF, PRINCIPLES OF OPTICS, SEC. 8.8,
EQ 14. WITH THEIR U AND V SLIGHTLY REDEFINED AND A FACTOR UAPERT(R0)
INCLUDED TO ALLOW FOR ARBITRARY APERTURE ILLUMINATION. ALSO,
INTEGRATION LIMITS ARE FROM 0 TO ROMAX. BY ROMBERG INTEGRATION
OVER THE SOURCE PLANE RADIAL COORDINATE R1, AND BY SQUARING
THE RESULTING FIELD DISTRIBUTION, THE INTENSITY PATTERN UPON
A SCREEN A DISTANCE Z FROM THE APERTURE FOR A WAVE CONVERGING
TO A POINT S FROM THE APERTURE IS CALCULATED FOR DESIRED INCREMENTS
IN RADIUS. DELRO, FROM 0 TO ROMAX AT WAVELENGTH LAMRDA.

INTERMEDIATE RESULTS (RCMBERG ARRAY AND REAL AND IMAGINARY
VALUES OF FIELD AT EACH R0) ARE STORED IN DEVICE 7, AND DEVICE 6,
THE MAIN OUTPUT, RESTATES INPUT DATA AND GIVES INTENSITY AS
A FUNCTION OF R0.

INPUT IS ENTERED IN NAMELIST MANNER ON DEVICE 5, WITH ALL
DIMENSIONS IN CM. REQUIRED ARE:

DELPC -- INCREMENTS OF THE INDEPENDENT VARIABLE R0, THE
OBSERVATION PLANE RADIAL COORDINATE

RCMAX -- MAXIMUM R0 DESIRED IN CALCULATION

LAMRDA -- WAVELENGTH

S -- AXIAL POSITION OF CENTER OF CURVATURE OF WAVEFRONTS--
POSITIVE VALUES CORRESPOND TO SIDE OF APERTURE OF
OBSERVATION PLANE

```

37 C      Z      -- AXIAL POSITION OF CRSERVATION PLANE
38 C      RCNEMX-- RADIUS CF APERTURE
39 C
40 C
41 C
42 C      IMPLICIT REAL*8(A-T,L,C-Z)
43 C      DIMENSION TRAP(3,3),AI(2)
44 C      NAMELIST/INPUT/DELRO,ROMAX,LAMBDA,S,Z,RCNEMX
45 C      READ(5,INPUT)
46 C      WRITE INPUT VALUES
47 C      WRITE(6,109) DELRO,ROMAX,LAMBDA,S,Z,RCNEMX
48 C      199 FCRMAT(' DELRO (SPACING BETWEEN SUCCESSIVE VALUES OF RO) = ',
49 C      1D16.10/'ROMAX (MAXIMUM RO) = ',D16.10/'LAMBDA (WAVELENGTH)
50 C      2 = ',D16.10
51 C      3/'S (WAVEFFONT CENTER CF CURVATURE) = ',D16.10/
52 C      4'Z (CRSERVATION PLANE) = ',D16.10/
53 C      9'RCNEMX (RADIUS OF APERTURE) = ',D16.10/
54 C      5'*****
55 C      6/'ALL DIMENSIONS IN CM/'*****')
56 C
57 C      WRITE COLUMN HEADINGS
58 C
59 C      WRITE(6,201)
60 C      201 FORMAT(' ',4X,'RO',30X,'UO(RO)')

61 C
62 C      INITIALIZE AND SET UP DESIRED RO VALUES
63 C
64 C

```

```

65 R0=0.0
66 AN=(ROMAX/DELRO)+1.
67 NUMIT=IFIX(SNGL(AN))
68 ALPHA=3.14159*((1.C/Z)-(1.0/S))/LAMBDA
69
70 THIS LOOP ITERATES OVER R0 FROM 0 TO ROMAX.
71
72 DO1 IRC=1,NUMIT
73 NN=0
74 RETA=(6.28319*R0)/(LAMBDA*Z)
75
76 POMBERG INTEGRATION OVER APERTURE, R1, FOR GIVEN R0 -- DO ONCE
77 FOR COS INTEGRAND, ONCE FOR SIN
78
79 30 NN=NN+1
80 DO50 I=1,2
81 L=0.0
82 MODIV=2*((I+5)
83 AREA=0.0
84 WIDTH=RONEMX/(DFLOAT(NODIV))
85 DO40 J=1,NODIV
86 FL=(DFLOAT(J-1))*WIDTH
87 ER=(DFLOAT(J))*WIDTH
88
89 THE ARBITRARY APERTURE FIELD DISTRIBUTION, U1, IS CALCULATED
90 IN A FUNCTION SUBROUTINE.
91
92 U1=UAPERT(ER)
93
94 TEST FOR FIRST (COS) OR SECOND (SIN) INTEGRAND AND EVALUATE INTEGRAND.
95
96 IF(NN.EQ.1)R=F1(ER,ALPHA,BETA,U1)
97 IF(NN.EQ.1)GC TO 45
98 R=F2(ER,ALPHA,BETA,U1)
99

```



```

100 45 AR=(WIDTH/2.)*(L+R)
101 L=R
102 40 AREA=AREA+AR
103 TRAP(I,1)=AREA
104 50 CONTINUE
105
106 C RCMBERG CORRECTION
107 C
108 C
109 J=2
110 DO100 I=J,3
111 100 TRAP(I,J)=((4.**(J-1))*TRAP(I,J-1)-TRAP(I-1,J-1))/(4.**(J-1)-1.)
112
113 C PRINT INTEGRATION ARRAY ON 7
114 C
115 C
116 DO200 I=1,2
117 200 WRITE(7,210)(TRAP(I,J),J=1,1)
118 210 FORMAT('O',3D30.20)
119
120 C THE FINAL RCMBERG RESULT IS SELECTED
121 C
122 C
123 AI(NN)=TRAP(2,2)
124
125 IF(NN.NE.1)GO TO 7C
126 GO TO 30
127
128 C THE INTEGRALS OF F1 AND F2 ARE SQUARED AND ADDED, GIVING A FACTOR
129 C THAT IS PROPORTIONAL TO THE INTENSITY AT R0.
130 C
131 70 AISORC=((AI(1)**2))+((AI(2))**2)
132
133 C THE COMPLEX FIELD IS PRINTED ON 7.
134 C
135 C
136 WRITE(7,2C8)R0,AI(1),AI(2)
137 208 FORMAT(' AT R0= ',D16.10,2X,'U(R0)= ',D16.10,2X,'+ I',D16.10)
138
139 C

```

```

134 C
135 C
136 C
137 P0 AND ITS INTENSITY ARE PRINTED, AND THE PROCEDURE MOVES
138 ON TO THE NEXT R0.
139
140 WRITE(6,202)R0,AISCRO
141 202 FORMAT(D26.20,4X,D26.20)
142 R0=R0+DELRO
143 1 CONTINUE
144 RETURN
145 END
146 PEAL FUNCTION UAPERT*8(X)
147 IMPLICIT REAL*8 (A-H,O-Z)
148 UAPERT=1.
149 RETURN
150 END
151 REAL FUNCTION F1*8(ER,ALPHA,BETA,U1)
152 IMPLICIT REAL*8(A-H,O-Z)
153 X=BETA*ER
154 Y=ALPHA*(ER**2)
155 IF(X.LT.0.1D-10)GO TO 5
156 CALL BESJ(X,0,RX,0.001,IER)
157 GO TO 6
158 5 RX=1.0
159 6 F1=((DCOS(Y))*RX)*U1*ER
160 RETURN
161 END
162 PEAL FUNCTION F2*8(ER,ALPHA,BETA,U1)
163 IMPLICIT REAL*8(A-H,O-Z)
164 X=BETA*ER
165 Y=ALPHA*(ER**2)
166 IF(X.LT.0.1D-10)GO TO 5
167 CALL BESJ(X,0,RX,0.001,IER)
168 GO TO 6
169 5 RX=1.0
170 6 F2=((DSIN(Y))*RX)*U1*ER
171 RETURN
172 END

```

LIST OF REFERENCES

- Abramowitz, M. & Stegun, I. (1965). Handbook of Mathematical Functions. New York: Dover.
- Ackenhusen, John G. and Steel, D. G. (1977). Optical Alignment Procedure for an Unstable Resonator High-Power Laser. to be published by Rev. Sci. Instr.
- Billman, K. W. & Stallcop, J. R. (1976). Appl. Phys. Lett., 28:704.
- Bobin, J. L. (1971). Phys. Fluids, 14:2341.
- Born, M. & Wolf (1975). Principles of Optics, 5th ed. New York: Pergamon.
- Bracewell, R. M. (1965). The Fourier Transform and its Applications. New York: McGraw-Hill.
- Brueckner, K. A. & Jorna, S. (1974). Rev. Mod. Phys., 46:311.
- Burnett, N. H. & Offenberger, A. A. (1974). J. Appl. Phys., 45:623.
- Chapin, D. L., Duderstadt, J. J., & Bach, D. R. (1974). J. Appl. Phys., 45:1726.
- Chen, F. F. (1974). Laser Interaction and Related Plasma Phenomena, Hora & Schwartz, eds., Vol. 3A, p. 291. New York: Plenum.
- Craxton, R. S. & Haines, M. G. (1975). Phys. Rev. Lett., 35:1336.
- DeBoo, J. C. (1973). "Laser Absorption in a Dense Lithium Plasma" (Ph. D. dissertation, Department of Nuclear Engineering, University of Michigan).
- DeBoo, J. C. & Bach, D. R. (1975). J. Appl. Phys., 46:2496.
- Donaldson, T. P. & Spalding, I. J. (1976a). Phys. Rev. Lett., 36:467.

- Donaldson, T. P., Hubbard, M., & Spalding, I. J. (1976b). Phys. Rev. Lett., 37:1348.
- Drake, J. F. et al. (1974). Phys. Fluids, 17:778.
- Drawin & Felenbok (1965). Data for Plasmas in Local Thermodynamic Equilibrium. Paris: Gauthier-Villars.
- DuBois, D. F. (1974). Laser Interaction and Related Plasma Phenomena, Hora & Schwartz, eds., Vol. 3A, p. 267. New York: Plenum.
- Duston, D. P. (1977). "Theoretical Studies of the Radiation-Hydrodynamics of Dense, Laser-Heated Plasmas" (Ph. D. dissertation, Department of Nuclear Engineering, University of Michigan).
- Duston, D. P. & Duderstadt, J. J. (1977). Ionization and Radiation Dynamics of Dense MHD Plasmas. submitted to J. Appl. Phys.
- Duston, D. P. et al. (1977). Characterization of an Ultradense Reproducible Z-Pinch. submitted to Appl. Phys. Lett.
- Dyer, P. E. et al. (1974). Laser Interaction and Related Plasma Phenomena, Hora & Schwartz, eds., Vol 3A, p. 191. New York: Plenum.
- Estabrook, K. G., Valeo, E. J., & Kruer, W. L. (1975). Phys. Fluids, 18:1151.
- Fabre, E. & Stenz, C. (1974). Phys. Rev. Lett., 32:823.
- Fauquignon, C. & Floux, F. (1970). Phys. Fluids 13:386.
- Forslund, D. W., Kindel, J. M., & Lindman, E. L. (1975). Phys. Fluids, 18:1002.
- Frank, A. M. et al. (1976). A Laser Start-Up System for Magnetic Mirror Fusion. University of California Report UCRL 78235.
- Freidberg, J. P., et al. (1972). Phys. Rev. Lett., 28:795.
- Ginzburg, V. L. (1960). Propagation of Electromagnetic Waves in Plasma. New York: Gordon and Breach.

- Giovanielli, D. V. (1976). Bull. Am. Phys. Soc., 21:1047.
- Goodman, J. W. (1968). Introduction to Fourier Optics. San Francisco: McGraw-Hill.
- Hora, H. (1969). Phys. Fluids, 12:182.
- Jahoda, F. C. et al. (1960). Phys. Rev., 119:843.
- Judd, O. P. (1973). Diffraction from Circular and Irregular Apertures. Los Alamos Scientific Laboratory Report LA-5391-MS.
- Judd, O. P. (1974). Diffraction from an Annular Aperture. Los Alamos Scientific Laboratory Office Memorandum.
- Karzas, W. J. & Latter, R. (1961). Astrophys. J., Supplement 55, 6:167.
- Kolodner, P. & Yablonovitch, E. (1976). Phys. Rev. Lett., 73:1754.
- Kruer, W. L. (1976). University of California Class Notes.
- Kruer, W. L. et al. (1976). Proceedings of the Sixth Annual Symposium on the Anomalous Absorption of Intense High-Frequency Waves. Vancouver.
- Landau, L. D. & Lifshitz, E. M. (1960). Course of Theoretical Physics, Vol. 8: Electrodynamics of Continuous Media. Oxford: Pergamon.
- Leonard, T. A. (1972). "Laser Interaction with a High Density Lithium Plasma" (Ph. D. dissertation, Department of Nuclear Engineering, University of Michigan).
- Leonard, T. A. & Mayer, F. J. (1975). J. Appl. Phys., 46:3562.
- Lindl, J. D. & Kaw, P. K. (1971). Phys. Fluids, 14:371.
- Maher, W. E. & Hall, R. B. (1975). J. Appl. Phys., 46:761.
- Marhic, M. E. (1975). Phys. Fluids, 18:837.
- Meyerott, A. J., Fisher, P. C., & Roethig, D. T. (1964). Rev. Sci. Instr., 35:669.

- Neufeld, C. R. et al. (1976). Bull. Am. Phys. Soc., 21:1139.
- Nishikawa, K. & Liu, C. S. (1975). Advances in Plasma Physics, Simon, ed., Vol. 6, p. 3. New York: Wiley.
- Oktay, E. (1969). "Absorption of HeNe Laser Radiation in an Exploded Lithium Wire Plasma" (Ph. D. dissertation, Department of Nuclear Engineering, University of Michigan).
- Osaka University. (1976). Annual Progress Report on Laser Fusion Program. Institute of Laser Engineering Report.
- Osborn, R. K. (1975). IEEE Trans. on Plas. Sci., PS-3:3.
- Phillion, D. W. (1976). Bull. Am. Phys. Soc., 21:1046.
- Reintjes, J. F. et al. (1976). J. Appl. Phys., 47:4461.
- Rehm, R. G. (1970). Phys. Fluids, 13:921.
- Roberts, D. E. (1972). Phys. Fluids, 15:192.
- Rockett, P. D. & DeBoo, J. C. (1975). IEEE Conference Record Abstracts, p. 120.
- Rockett, P. D. (1977a). "Pulsed Holographic Interferometry of High Density Z-Pinch and Exploding Lithium Wire Plasmas" (Ph. D. dissertation, Department of Nuclear Engineering, University of Michigan).
- Rockett, P. D. (1977b). Axial Electron Density Profiles Gained from Axisymmetric Plasma Phase Objects. submitted to Appl. Opt.
- Rockett, P. D. et al. (1977). Anomalous Transmission of Intense CO₂ Laser Radiation Through an Overdense Plasma. submitted to Phys. Rev. Lett.
- Schreiber, P. W., Hunter, A. M., & Smith, D. R. (1973). Plasma Physics, 15:635.
- Shearer, J. W. (1970). A Survey of the Physics of Plasma Heating by Laser Light. University of California Report UCID 15745.

- Smith, H. M. (1975). Principles of Holography, 2nd ed. New York: Wiley.
- Stark, E. et al. (1976). Progress Report on Laser-Fusion Program at LASL - January 1 - June 30, 1976. Los Alamos Scientific Laboratory Report LA-6510-PR.
- Steel, D. G. (1976). "Intense CO₂ Laser Interactions with a Dense Helium Z-Pinch Plasma" (Ph. D. dissertation, Department of Nuclear Engineering, University of Michigan).
- Steel, D. G. et al. (1977). An Ultra-Dense Reproducible Z-Pinch Suitable for CO₂ Laser-Pellet Simulation Experiments. submitted to Rev. Sci. Instr.
- Steinhauer, L. C. & Ahlstrom, H. G. (1971). Phys. Fluids, 18:541.
- Stern, R. (1977). personal communication. Bell Telephone Laboratories.
- Uman, M. A. (1964). Introduction to Plasma Physics. New York: McGraw-Hill.
- Valeo, E. J., & Estabrook, K. G. (1975). Phys. Rev. Lett. 34:1008.
- Yuen, S. Y., Lax, B., & Cohn, D. R. (1975). Phys. Fluids 18:829.
- Zel'dovich, Y. B. & Raizer, Y. P. (1966). Physics of Shock Waves and High-Temperature Hydrodynamic Phenomena. New York: Academic.